N° d'ordre NNT : 2018LYSEE005

THESE de DOCTORAT DE L'UNIVERSITE DE LYON

opérée conjointement

au sein de l'Ecole centrale de Lyon
et de l'Ecole Nationale d'Ingénieurs de Saint-Etienne

Ecole Doctorale N° 488 Science Ingénierie Santé

Spécialité
Mécanique et Ingénierie

Soutenue publiquement le 16/07/2018, par :

Iñaki Mirena ARRIETA GALDOS

Study of microstructural aspects when broaching ferritic-pearlitic steels: influence on cutting mechanisms, tribological and material properties

---

Devant le jury composé de :

M. Franci PUSAVEC	*Professeur, University of Ljubjlana*	*Président*
M. Guénaël GERMAIN	*Professeur, ENSAM (Angers)*	*Rapporteur*
M. Oscar MARTIN	*Professeur, Université de Valladolid (Espagne)*	*Rapporteur*
M. Vincent FRIDRICI	*Professeur, École Centrale de Lyon*	*Examinateur*
M. Daniel SOLER	*Professeur, Université de Mondragon (Espagne)*	*Examinateur*
M. Patxi Aristimuño	*Professeur, Université de Mondragon (Espagne)*	*Examinateur*
M. Joël Rech	*Professeur, ENISE (Saint-Étienne)*	*Directeur*
M. Cédric COURBON	*Professeur, ENISE (Saint-Étienne)*	*Co-directeur*
M. Pedro J. ARRAZOLA	*Professeur, Université de Mondragon (Espagne)*	*Co-directeur*

Spécialités doctorales :
SCIENCES ET GENIE DES MATERIAUX
MECANIQUE ET INGENIERIE
GENIE DES PROCEDES
SCIENCES DE LA TERRE
SCIENCES ET GENIE DE L'ENVIRONNEMENT
MATHEMATIQUES APPLIQUEES
INFORMATIQUE O.
IMAGE, VISION, SIGNAL

Responsables:
K. Wolski Directeur de recherche
S. Drapier, professeur
F. Gruy, Maître de recherche
B. Guy, Directeur de recherche
D. Graillot, Directeur de recherche
O. Roustant, Maître-assistant
Boissier, Professeur

EMSE : Enseignants-chercheurs et chercheurs autorisés à diriger des thèses de doctorat (titulaires d'un doctorat d'Etat ou d'une HDR)

AVRIL	Stéphane	PR2	Mécanique et ingénierie	CIS
BATTON-HUBERT	Mireille	PR2	Sciences et génie de l'environn	FAYOL
BENABEN	Patrick	PR1	Sciences et génie des matéria	CMP
BERNACHE-ASSOLLAN	Didier	PR0	Génie des Procédés	CIS
BIGOT	Jean Pierre	MR(DR2)	Génie des Procédés	SPIN
BILAL	Essaid	DR	Sciences de la Terre	SPIN
BOISSIER	Olivier	PR1	Informatique	FAYOL
BORBELY	Andras	MR(DR2)	Sciences et génie de l'environn	SMS
BOUCHER	Xavier	PR2	Génie Industriel	FAYOL
BRODHAG	Christian	DR	Sciences et génie de l'environn	FAYOL
BURLAT	Patrick	PR2	Génie Industriel	FAYOL
COURNIL	Michel	PR0	Génie des Procédés	DIR
DARRIEULAT	Michel	IGM	Sciences et génie des matéria	SMS
DAUZERE-PERES	Stéphane	PR1	Génie Industriel	CMP
DEBAYLE	Johan	CR	Image Vision Signal	CIS
DELAFOSSE	David	PR1	Sciences et génie des matéria	SMS
DESRAYAUD	Christophe	PR2	Mécanique et ingénierie	SMS
DOLGUI	Alexandre	PR0	Génie Industriel	FAYOL
DRAPIER	Sylvain	PR1	Mécanique et ingénierie	SMS
FEILLET	Dominique	PR2	Génie Industriel	CMP
FOREST	Bernard	PR1	Sciences et génie des matéria	CIS
FORMISYN	Pascal	PR0	Sciences et génie de l'environn	DIR
FRACZKIEWICZ	Anna	DR	Sciences et génie des matéria	SMS
GARCIA	Daniel	MR(DR2)	Génie des Procédés	SPIN
GERINGER	Jean	MA(MDC)	Sciences et génie des matéria	CIS
GIRARDOT	Jean-jacques	MR(DR2)	Informatique	FAYOL
GOEURIOT	Dominique	DR	Sciences et génie des matéria	SMS
GRAILLOT	Didier	DR	Sciences et génie de l'environn	SPIN
GROSSEAU	Philippe	DR	Génie des Procédés	SPIN
GRUY	Frédéric	PR1	Génie des Procédés	SPIN
GUY	Bernard	DR	Sciences de la Terre	SPIN
GUYONNET	René	DR	Génie des Procédés	SPIN
HAN	Woo-Suck	CR	Mécanique et ingénierie	SMS
HERRI	Jean Michel	PR1	Génie des Procédés	SPIN
INAL	Karim	PR2	Microélectronique	CMP
KERMOUCHE	Guillaume	PR2	Mécanique et Ingénierie	SMS
KLOCKER	Helmut	DR	Sciences et génie des matéria	SMS
LAFOREST	Valérie	MR(DR2)	Sciences et génie de l'environn	FAYOL
LERICHE	Rodolphe	CR	Mécanique et ingénierie	FAYOL
LI	Jean Michel		Microélectronique	CMP
MALLIARAS	Georges	PR1	Microélectronique	CMP
MOLIMARD	Jérôme	PR2	Mécanique et ingénierie	CIS
MONTHEILLET	Franck	DR	Sciences et génie des matéria	SMS
PERIER-CAMBY	Laurent	PR2	Génie des Procédés	DFG
PIJOLAT	Christophe	PR0	Génie des Procédés	SPIN
PIJOLAT	Michèle	PR1	Génie des Procédés	SPIN
PINOLI	Jean Charles	PR0	Image Vision Signal	CIS
POURCHEZ	Jérémy	CR	Génie des Procédés	CIS
ROUSTANT	Olivier	MA(MDC)		FAYOL
STOLARZ	Jacques	CR	Sciences et génie des matéria	SMS
SZAFNICKI	Konrad	MR(DR2)	Sciences et génie de l'environn	CMP
TRIA	Assia		Microélectronique	CMP
VALDIVIESO	François	MA(MDC)	Sciences et génie des matéria	SMS
VIRICELLE	Jean Paul	MR(DR2)	Génie des Procédés	SPIN
WOLSKI	Krzystof	DR	Sciences et génie des matéria	SMS
XIE	Xiaolan	PR0	Génie industriel	CIS

ENISE : Enseignants-chercheurs et chercheurs autorisés à diriger des thèses de doctorat (titulaires d'un doctorat d'État ou d'une HDR)

BERGHEAU	Jean-Michel	PU	Mécanique et Ingénierie	ENISE
BERTRAND	Philippe	PU	Génie des procédés	ENISE
DUBUJET	Philippe	PU	Mécanique et Ingénierie	ENISE
FEULVARCH	Eric	MCF	Mécanique et Ingénierie	ENISE
FORTUNIER	Roland	PR	Sciences et Génie des matéria	ENISE
HAMDI	Hédi	PU	Mécanique et Ingénierie	ENISE
LYONNET	Patrick	PU	Mécanique et Ingénierie	ENISE
RECH	Joël	PU	Mécanique et Ingénierie	ENISE
SI LARBI	Amir	PU	Mécanique et Ingénierie	ENISE
SMUROV	Igor	PU	Mécanique et Ingénierie	ENISE
TOSCANO	Rosario	PU	Mécanique et Ingénierie	ENISE
ZAHOUANI	Hassan	PU	Mécanique et Ingénierie	ENISE

Mise à jour : 03/11/2015

PR 0 Professeur classe exceptionnelle
PR 1 Professeur 1ère classe
PR 2 Professeur 2ème classe
PU Professeur des Universités

Ing. Ingénieur
MCF Maître de conférences
MR (DR2) Maître de recherche
CR Chargé de recherche

SMS Sciences des Matériaux et des Structur SPIN Sciences des Processus Industriels et N FAYOL aturels
Institut Henri Fayol
CMP Centre de Microélectronique de Proven ce

École Nationale d'Ingénieurs de Saint-Etienne de Saint-Étienne

Ecole Centrale de Lyon

N° d'ordre : 2018LYSEE005

Iñaki Mirena ARRIETA GALDOS

STUDY OF MICROSTRUCTURAL ASPECTS WHEN BROACHING FERRITIC-PEARLITIC STEELS: INFLUENCE ON CUTTING MECHANISMS, TRIBOLOGICAL AND MATERIAL PROPERTIES

Speciality : Mechanical engineering

Keywords : Ferritic-Pearlitic Steel , Tribology, Broaching, Simulation

Abstract :

The Ferritic-Pearlitic (FP) steels are widely used in automotive and generally in engineering industry. Even if steels with FP structure are among the most common materials, they are not at the very least the easiest materials to machine. Many study researches have been undertaken on the inclusion contribution in the machining processes, but further investigation is required. More precisely, the machining performance appears to be highly dependent on the microstructural parameters. That is why in this research project this kind of steels were analysed in terms of its microstructural features. Five steel grades have been manufactured in four different microstructure variants regarding ferrite and pearlite percentage, hardness, interlamellar space of pearlite, grain size of ferrite and the aspect of pearlite (band or globular). The main goal of this research work is to understand the influence of FP steels microstructure in the broaching process. To do so, several specific goals have been defined: (i) characterization of the FP steels obtaining their microstructure, mechanical features (including flow stress) and thermal characteristics, (ii) friction identification depending on the microstructural parameters, (iii) experimental results of forces, roughness and chip thickness depending on the FP steel microstructure and (iv) development of a Finite Element Model able to simulate the broaching process and predict the experimental outputs.

École Nationale d'Ingénieurs de Saint-Etienne de Saint-Étienne

Ecole Centrale de Lyon

N° d'ordre : 2018LYSEE005

Iñaki Mirena ARRIETA GALDOS

ETUDE DES ASPECTS MICROSTRUCTURAUX LORS DU BROCHAGE D'ACIERS FERRITO-PERLITIQUES: INFLUENCE SUR LES MECANISMES DE COUPE, LA TRIBOLOGIE ET LES PROPRIETES DES MATERIAUX

Spécialité: Mécanique et Ingénierie

Mots clefs : Acier ferritique-perlitique, tribologie, brochage, simulation

Résumé :

Les aciers de type ferrite-perlite sont largement utilisés dans le secteur automobile et dans l'industrie en général. Même si les aciers à structure FP sont parmi les matériaux les plus courants, ils ne sont pas au moins les matériaux les plus faciles à usiner. De nombreuses recherches ont été menées sur l'influence des inclusions dans les procédés d'usinage, mais d'autres recherches sont nécessaires. Précisément, les performances d'usinage semblent fortement dépendantes des paramètres microstructuraux. C'est pourquoi dans cette thèse, ce type d'aciers sera analysé en termes microstructuraux. Cinq types d'acier ont été fabriqués dans quatre variantes différentes de microstructure en ce qui concerne la taille des grains, le rapport ferrite-perlite, l'espacement interlaminaire et l'aspect perlite (bande ou globulaire). L'objectif principal de cette thèse est de comprendre l'influence de la microstructure des aciers ferrite-perlite tant dans la tribologie que dans l'usinage. À cette fin, Pour ce faire, plusieurs objectifs spécifiques ont été définis: (i) caractérisation des aciers FP obtenant leur microstructure, leurs caractéristiques mécaniques (tension de fluage compris) et leurs caractéristiques thermiques, (ii) l'identification du frottement en fonction des paramètres microstructuraux (iii) des forces, de la rugosité et de l'épaisseur des copeaux en fonction de la microstructure de l'acier FP et (iv) de la mise en place d'un modèle d'éléments finis capable de simuler le processus de brochage et de prédire les résultats expérimentaux.

DECLARATION OF ORIGINALITY

I declare through these lines that this PhD and the work presented in it with its results, has been done by me, both in the mechanical and manufacturing department in Mondragon Unibertsitatea's Engineering Faculty (hereinafter MU) and the École nationale d'Ingénieurs de Saint-Étienne (hereinafter ENISE).

ACKNOWLEDGMENTS

The author acknowledges to Mondragon Unibertsitatea and École Nationale d'Ingénieurs de Saint-Étienne for the aid granted for the research training, as well as the financial grant from the Research Fund for Coal and Steel (RFCS) of the European Community under the project named as IMMAC (grant agreement num. RFSR-CT-2014-00020).

The research team is also grateful to EKIN S. Coop. Company for providing the tools and the technical support for the broaching tests. In the same line the author would like to thank ASCOMETAL and SIDENOR for supplying the steel used in this study and technical support provided during the performance of work.

The author is grateful to the research supervisors Pedro José Arrázola and Joël Rech, as well as to Cédric Courbon for his invaluable help and assistance during the whole PhD.

Finally, I could not finish the acknowledgment thanksgiving to my workmates both in Mondragon and in Saint-Étienne with special mention to those with which I have been in the research group with.

From ENISE side mainly Rafal Kaminski, Sintya Davin, Maxime Dumas and the rest of the PhD students, Dorian Fabre, Alexis Giovenco, Maysa Guediche, Vipul Vigiri, Jian Cao and Han. I could not leave behind the students who have been to Saint-Étienne each year to finish their master degree, Jon Duarte, Iker Arrien, Amaia Peñalba and Irati Malkorra.

From MU side Patxi Aristimuño teaching very patiently how to use the Lagun CNC machining center. I would like also to remember, Andoni Villar, Javier Aperribai, Endika Gandarias, Dani Soler, Aitor Madariaga, Raúl Fernandez, Ainhara Garay, Mikel Cuesta, Mikel Saez de Buruaga, Ariane Iturbe, Irantzu Sacristan, Aitor Kortabarria, Xabi Badiola, Gorka Ortiz, Andres Sela and Harry Otalora. Not least the workshop technicians in Saint-Étienne: Patrick Polly, Mehmet Cici, Herve Seux, Floriant Dumont, Maryane Jacquier, Frederic Cabanettes and Christophe Claudin due to their assistance performing the experimental tests.

LABURPENA

Ferrita-perlita motako altzairuak oso erabiliak dira automozioan eta industrian oro har. Nahiz eta mekanizatzeko errazenak ez diren FP egitura duten altzairuak, material arrunten artean daude. Ikerketa asko egin dira inklusioen eraginaren inguruan mekanizazio prozesuetan, baina ikerketa gehiago behar direla argi dago. Hain zuzen ere, mekanizazio-errendimendua parametro mikroegituraren menpe dagoela dirudi. Horregatik, tesi honetan, altzairu mota hau aztertuko da mikroegitura. Bost altzairu mota lau mikroegitura aldaera desberdinetan fabrikatu dira alearen tamaina, ferrita-perlita-ratioa, perlitaren tarte interlinarra eta perlita mota (banda edo globularra) kontutan hartuta. Ikerketa-lan honen helburuak ondokoak dira (I) FP altzairuen karakterizazioa hauen mikroegitura, propietate mekanikoak (fluentzi tentsioa barne) eta propietate termikoak lortuz, (II) frikzioa identifikatu mikroegituraren arabera (III) indarrak, zimurtasunak eta txirbilaren zabalerak lortu eta aztertu mikroegituraren arabera eta (iv) mekanizazio mozketa simulatu eta emaitza esperimetalak aurreikusteko gai izango den eredu birtual bat garatu.

RÉSUMÉ

Les aciers de type ferrite-perlite sont largement utilisés dans le secteur automobile et dans l'industrie en général. Même si les aciers à structure FP sont parmi les matériaux les plus courants, ils ne sont pas au moins les matériaux les plus faciles à usiner. De nombreuses recherches ont été menées sur l'influence des inclusions dans les procédés d'usinage, mais d'autres recherches sont nécessaires. Précisément, les performances d'usinage semblent fortement dépendantes des paramètres microstructuraux. C'est pourquoi dans cette thèse, ce type d'aciers sera analysé en termes microstructuraux. Cinq types d'acier ont été fabriqués dans quatre variantes différentes de microstructure en ce qui concerne la taille des grains, le rapport ferrite-perlite, l'espacement interlaminaire et l'aspect perlite (bande ou globulaire). L'objectif principal de cette thèse est de comprendre l'influence de la microstructure des aciers ferrite-perlite tant dans la tribologie que dans l'usinage. À cette fin, Pour ce faire, plusieurs objectifs spécifiques ont été définis: (i) caractérisation des aciers FP obtenant leur microstructure, leurs caractéristiques mécaniques (tension de fluage compris) et leurs caractéristiques thermiques, (ii) l'identification du frottement en fonction des paramètres microstructuraux (iii) des forces, de la rugosité et de l'épaisseur des copeaux en fonction de la microstructure de l'acier FP et (iv) de la mise en place d'un modèle d'éléments finis capable de simuler le processus de brochage et de prédire les résultats expérimentaux.

RESUMEN

Los aceros ferrito perlíticos (FP) son ampliamente utilizados en el sector del automóvil y en la industria en general. Aunque su uso es bastante común, no son considerados como los materiales más fáciles de mecanizar. Se han realizado muchos trabajos de investigación sobre la influencia de las inclusiones en el mecanizado, pero la realidad es que se requiere más investigación. Esto se debe a que el comportamiento de estos aceros en mecanizado está altamente relacionado con la microestructura. Esto es por lo que en este proyecto de investigación se van a estudiar estos aceros en función de su microestructura. Para ello se han fabricado cinco calidades de acero con cuatro variantes de microestructura considerando el tamaño del grano, la relación de ferrita-perlita, el espaciado interlaminar y el aspecto de la perlita (banda o globular). El objetivo principal de esta tesis es comprender la influencia de la microestructura de los aceros ferrita-perlita tanto en la tribología como en el mecanizado. Para ello, se han establecido los siguientes objetivos específicos (i) caracterización de los aceros FP obteniendo su microestructura, propiedades mecánicas (incluyendo la tensión de fluencia) y las propiedades térmicas, (ii) identificar la fricción dependiendo de la microestructura, (iii) obtener fuerzas, rugosidades y espesores de viruta dependiendo de la microestructura y (iv) desarrollo de un modelo numérico de corte capaz de simular y predecir los resultados experimentales.

ABSTRACT

The Ferritic-Pearlitic (FP) steels are widely used in automotive and generally in engineering industry. Even if steels with FP structure are among the most common materials, they are not at the very least the easiest materials to machine. Many study researches have been undertaken on the inclusion contribution in the machining processes, but further investigation is required. More precisely, the machining performance appears to be highly dependent on the microstructural parameters. That is why in this research project this kind of steels were analysed in terms of its microstructural features. Five steel grades have been manufactured in four different microstructure variants regarding ferrite and pearlite percentage, hardness, interlamellar space of pearlite, grain size of ferrite and the aspect of pearlite (band or globular). The main goal of this research work is to understand the influence of FP steels microstructure in the broaching process. To do so, several specific goals have been defined: (i) characterization of the FP steels obtaining their microstructure, mechanical features (including flow stress) and thermal characteristics, (ii) friction identification depending on the microstructural parameters, (iii) experimental results of forces, roughness and chip thickness depending on the FP steel microstructure and (iv) development of a Finite Element Model able to simulate the broaching process and predict the experimental outputs.

INDEX

1 INTRODUCTION 27

1.1 Industrial context 27
1.2 Scientific approach 29
1.3 Objectives 30
1.4 Methodology and document's structure 30

2 INTRODUCTION TO BROACHING 35

2.1 Broaching process 35
2.2 Broaching scientific studies 43

3 MATERIAL CHARACTERIZATION 73

3.1 Introduction to the ferritic-pearlitic steels 73
3.2 Ferritic-pearlitic steels manufacturing 75
3.3 Thermal characterization 84
3.4 FP steel's flow stress 99
3.5 Conclusions 109

4 ANALYSIS OF FRICTION AND WEAR IN FP STEELS 113

4.1 Introduction 113
4.2 Tribological study setup 126
4.3 Friction results in fundamental study 130
4.4 Tribological study focused on the broaching process 145
4.5 Conclusions 153

5 BROACHING TESTS 159

5.1 Experimental Setup 159
5.2 Results & Discussion 162
5.3 Conclusions 194

6 FEM SIMULATIONS IN BROACHING 199

6.1 Introduction 199
6.2 Numerical tests 205
6.3 Results and comparison with the experiments 208
6.4 Scientific discussion 212
6.5 Conclusions 217

7 CONCLUSIONS AND FUTURE LINES 221
8 ORIGINAL CONTRIBUTIONS 227
8.1 Published articles 227
8.2 Conferences 227
9 BIBLIOGRAPHIC REFERENCES 231
10 APPENDICES 243
10.1 Material Characterization 243
10.2 Analysis of the friction in the FP steels 251
10.3 Broaching tests 252

LIST OF FIGURES

Figure 1. Car engine parts manufactured with ferritic-pearlitic steels. 27
Figure 2. Turning, drilling and broaching processes. 28
Figure 3. Scheme of the outputs obtained in the tool-workpiece interaction inspired from (Fabre et al. 2016). 29
Figure 4. C45 steel in its four different variants with same magnification. From left to right: Standard, Coarse grain, Globular Pearlite & Wide Bands. 30
Figure 5. Broaching machine patented by (Stephens 1873). 35
Figure 6. Inner broaching examples (left side) external broaching examples (right side). 36
Figure 7. a) Correct length of a pulled broach scheme b) Too long broach pulled suffering a buckling (Fabre 2016). 37
Figure 8. Usual broach with its parts (Fabre 2016). 38
Figure 9. Usual broaching moving motion (Fabre 2016). 38
Figure 10. Elemental broach shape and teeth (Fabre 2016). 39
Figure 11.Influence of the coating on the cutting radius R, schematization of a section of the broaching tooth, final state after manufacturing. 40
Figure 12. Influence of the sulphur and the chlorine in the friction coefficient (Byers 2006). 43
Figure 13. Broaching parameter inputs and corresponding outputs. 44
Figure 14. Kishawy's multi-teeth study set-up (Kishawy et al. 2012). 46
Figure 15. One tooth external broaching setup (Vogtel et al. 2013). 47
Figure 16. Experimental setup developed by (Ducobu et al. 2016). 48
Figure 17. Schematisation of the cutting area (AC). 49
Figure 18. Comparison of simulated and experimental cutting forces during a broaching operation (Kishawy et al. 2012). 50
Figure 19. ANOVA study of the variation of cutting force (Fz) and feed (Fy) by (Mo et al. 2005). 51
Figure 20. Influence of cutting speed (left) and feed (right) on broaching forces (Forst 1973). 52
Figure 21. Cutting and feed forces in a wide range of speeds and same RPT on a stainless steel (Fabre et al. 2016). 52
Figure 22. ANOVA study of the Ra variation performed by (Mo et al. 2005). 55
Figure 23. Influence of the rake angle on the surface condition (Forst 1973). 55
Figure 24. Evolution of roughness Rz with cutting speed (Weule et al. 2005). 56

Figure 25. Roughness evolution with cutting speed (Forst 1973). 58
Figure 26. Evolution of hardness versus temperature of high-speed steels (Handbook 1990). 59
Figure 27. Influence of cutting speed, progression and mode of lubrication on the temperatures of the cutting zone in broaching (Forst 1973). 60
Figure 28. Serrated chip example by (Duan, Zhang 2012). 62
Figure 29. Shear angles observed for various depths (from shallow to deep left to right) (Schulze et al. 2013). 63
Figure 30. Chips observed in dry (left) and whole oil (right) cutting tests (Schulze et al. 2012). 64
Figure 31. Influence of cutting speed and microstructure on the chip curling (Forst 1973). 65
Figure 32. SEM image of the clearance of a tool after alloy wear tests nickel (left) and titanium (right) (Mo et al. 2005)]. 66
Figure 33. Wear curves of a HSS tool over a C45 for two cutting speeds (Weule et al. 2005). 67
Figure 34. Wear levels observed for a high-speed steel and carbide tool (Forst 1973). 68
Figure 35. Ferrite and pearlite (Callister, Rethwisch 2011)..... 74
Figure 36. Hardness versus pearlite's interlamellar spacing (Clayton, Danks 1990).... 75
Figure 37. Schematic representation of the heat treatment performed to obtain the variants. 77
Figure 38. Microstructures obtained for standard grades 16MnCr5 (up) and 27MnCr5 (down). 77
Figure 39. Examples of lamellar/globular perlite observed in 16MnCr5. 78
Figure 40. ASTM pearlitic grain size obtained with the different heat treatments for 45CG variant. 79
Figure 41. ASTM grain size obtained for 60CG steel variant. 79
Figure 42. Microstructures obtained for grades 16MnCr5 (up), 27MnCr5 (middle) and C45 (down) in the surface, mid-radius and core of the bar for the With more Bands steel variants. 80
Figure 43. Fully pearlitic C70R image (280HB) 81
Figure 44. Method used at ASCO for measuring the interlamellar spacing 83
Figure 45. Example of lamellar pearlite on the 27R variant 83
Figure 46. Thermo-electric pyrometer device developed by Roberts-Austen (Roberts-Austen 1899). 85

Figure 47. Thermal conductivity and specific heat of a C45 provided by (Woo, Lee 2015). 86
Figure 48. Picture showing the zones where the samples are taken from in mm. 87
Figure 49. Density characterization sample (left) and Vertical Dilatometer L75PT device (right). 88
Figure 50. FP steel variant's density versus T, a) 16MnCr5, b) 27MnCr5, c) C45 & d) C60 & C70. 89
Figure 51. FP steel variant's density versus temperature split in variants, a) Standard (R), b) Coarse Grain (CG), c) Globular Pearlitic (GP) & d) With Bands (WB). 90
Figure 52. Tool materials' density variations versus temperature: a) M35-HSS b) H13A. 90
Figure 53. Specific Heat characterization sample (left) and the Laser Linseis LFA 1000 device (right). 91
Figure 54. FP steel variant's specific heat versus temperature split in grades, a) 16MnCr5, b) 27MnCr5, c) C45 & d) C60 &C70 92
Figure 55. FP steel variant's specific heat versus temperature split in variants, a) Standard (R), b) Coarse Grain (CG), c) Globular Pearlitic (GP) & d) With Bands (WB) 92
Figure 56. Tool's materials specific heat versus temperature 93
Figure 57. Thermal diffusivity characterization sample (left) and device for its calculation (right) 93
Figure 58. FP steel variant's diffusivity versus temperature split in grades, a) 16MnCr5, b) 27MnCr5, c) C45 & d) C60 &C70 94
Figure 59. FP steel variant's diffusivity versus temperature split in variants, a) Standard (R), b) Coarse Grain (CG), c) Globular Pearlitic (GP) & d) With Bands (WB) 95
Figure 60. Tool materials' diffusivity variations versus temperature. 95
Figure 61. FP steel variant's diffusivity versus temperature split in grades, a) 16MnCr5, b) 27MnCr5, c) C45 & d) C60 &C70. 96
Figure 62. FP steel variant's specific heat versus temperature split in variants, a) Standard (R), b) Coarse Grain (CG), c) Globular Pearlitic (GP) & d) With Bands (WB) 97
Figure 63. The conductivity variations of tool materials versus temperature. 98
Figure 64. Gleeble 3800M machine used for the experimental strain stress tests at low strain. 100
Figure 65. Complete description of the behaviour of C70 steel. 101
Figure 66. Behaviour curves for the C45 at the lowest strain rate and room temperature and highest strain rate and highest tested temperature. 101

Figure 67. Comparison of the influence of variants for the different grades at 20°C, 0.5 s^{-1}..... 102
Figure 68. Evolution of flow stress as a function of pearlite content. 103
Figure 69.Split Hopkinson pressure bar (SHPB) system schema and strain gage signal (KIMAB). 104
Figure 70. SHPB flow stress curves for C45 in its four extreme conditions T=22ºC-680ºC and ε=500 s^{-1} / 4000 s^{-1}..... 105
Figure 71. Pearlite content influence on flow stress at high strain rate tests..... 107
Figure 72. Comparison between the model and the experiment for 27MnCr5 R at room temperature. 107
Figure 73. Comparison between the model and the experiment for C70 at room temperature. 108
Figure 74. Tool-chip contact interface showing the primary and secondary shear zones (Rech et al. 2008). 114
Figure 75. Experimental setup developed by (Grzesik, Nieslony 2004)..... 115
Figure 76. Right: Experimental set-up considering the radial feed direction and left: cutting FE model used by (Franchi et al. 2016). 116
Figure 77. New experimental setup developed by (Puls et al. 2012). 117
Figure 78. Pin on disc measure system used by (Bahrudin et al. 2013). 118
Figure 79. A scheme of the tribo-pair configuration used in the investigation performed by (Grzesik et al. 2002). 118
Figure 80. The SRV wear system developed by (Su et al. 2004). 119
Figure 81. Schematic illustration of the modified pin-on-disc test geometry with test pin (A), workpiece (B), cutting tool (C) and argon gas inlet (D) (Olsson et al. 1989)..... 121
Figure 82. Test mode A: same surface roughing performing wear tests, Test mode B: new contact surface in air atmosphere & Test mode C: new contact surface in argon atmosphere. (Olsson et al. 1989) 121
Figure 83. Illustration of the tribometer installed on a lathe (Zemzemi et al. 2007). ... 122
Figure 84. Orthogonal cutting system developed by (Smolenicki et al. 2014)..... 122
Figure 85. a) The pin-on-ring test set-up pin holder (A), loading mechanism (B) and counter material (C). (b) Schematic drawing of the test set-up, with test pin (D) and counter material (E) (Hedenqvist, Olsson 1991)..... 123
Figure 86. Open tribometer setup on a turning CN machine (Mondelin et al. 2011). . 124
Figure 87. Polishing device and paste used to clean the pins. 126
Figure 88. Detailed view of the setup: a) tribometer and workmaterial, b-c) view of the tribometer on the turret, d-e) existing instrumentation and f) close view on the sliding configuration. 127

Figure 89. Friction versus speed in C45R material using HSS-M35 as tool material for the comparison of 300 N and 1000 N. 129
Figure 90. Broach tooth coated on the flank face and uncoated on the rake face. 130
Figure 91. FP steel's friction coefficient versus sliding speed with carbide pins..... 131
Figure 92. Standard FP steel's friction coefficient versus sliding speed. 131
Figure 93. Coarse Grain FP steel's friction coefficient versus sliding speed. 132
Figure 94. Globular Pearlitic FP steel's friction coefficient versus sliding speed. 132
Figure 95. With more Band FP steel's friction coefficient versus sliding speed. 133
Figure 96. Friction coefficient comparison between reference and the modified variants. 134
Figure 97. FP steel's friction coefficient versus ferrite content with carbide pins..... 135
Figure 98. FP steel's friction coefficient versus hardness with carbide pins. 135
Figure 99. FP steel's friction coefficient versus the grain size of the ferrite. 136
Figure 100. Examples of contact zones observed on the friction pins at different sliding velocities and for some variants – WC-Co+TiN pins. 137
Figure 101. Examples of contact tracks observed on the workmaterial at different sliding velocities and for some selected variants – WC-Co+Tin pins. 138
Figure 102. EDX analyses performed on the contact zone of the friction pins showing material transfer (iron in red) and wear of the coating (tungsten in blue). Extracted covered area based on image processing to assess material transfer tendency. 139
Figure 103. Evolution of material coverage on the pins with the microstructural parameters. a) Ferrite content, b) Pearlite content c) Interlamellar spacing and d) Hardness. 140
Figure 104. Wear mechanisms observed on some variants: a) 16MnCr5 Globular Pearlite (GP), b) 16MnCr5 banded structure (WB), c) C45 and d) C60. 141
Figure 105. Wear tendency towards the different variants: a) wear ranking proposed b) image processing example to extract the worn area and c) worn area extracted for each variant (sorted from the less to the most worn). 142
Figure 106. Friction coefficient plotted against ferrite-pearlite microstructural parameters: a) ferrite content, b) pearlite content, c) interlamellar spacing and d) macro hardness. 143
Figure 107. Frictional model curves depending on the steel's ferrite percentage. 144
Figure 108. Comparison between the experimental data and the proposed models (continuous lines) in terms of friction coefficient for the standard variants are presented. 145
Figure 109. FP steel's friction coefficient versus sliding speed with uncoated HSS M35 pins. 146

Figure 110. FP steel’s friction coefficient versus sliding speed TiN coated HSS-M35 pins. 147
Figure 111. FP steel’s friction coefficient versus ferrite content with uncoated HSS-M35 pins. 148
Figure 112. FP steel’s friction coefficient versus ferrite content TiN coated HSS-M35 pins. 148
Figure 113. FP steel's friction coefficient versus hardness with uncoated HSS-M35 tools. 149
Figure 114. FP steel’s friction coefficient versus hardness with TiN coated HSS-M35 tools. 149
Figure 115. Effect of lubrication and comparison on coated and uncoated pins. 150
Figure 116. Friction coefficient plotted against ferrite-pearlite microstructural parameters using the uncoated HSS steel pin: a) ferrite content, b) pearlite content, c) interlamellar spacing and d) macro hardness. 151
Figure 117. Frictional model curves depending on the steel’s ferrite percentage. 152
Figure 118. Comparison between the experimental data and the proposed models (continuous lines) in terms of friction coefficient for the standard variants are presented. 153
Figure 119. Scheme of the broaching system and devices used mounted on the CNC. 159
Figure 120. Overview of the experimental setup with a) the laboratory-broaching tool, b) the workpiece specimen. 160
Figure 121. Cutting forces of all variants at all the nine cutting conditions in broaching. 163
Figure 122. Penetration forces of all variants at all the nine cutting conditions in broaching. 163
Figure 123. Cutting broaching forces versus cutting speed on standard FP steels. 164
Figure 124. Cutting broaching forces versus sliding speed on Coarse Grain FP steels. 165
Figure 125. Cutting broaching forces versus sliding speed on Globular Pearlitic FP steels 165
Figure 126. Cutting forces comparison between reference and variants. 166
Figure 127. Broaching cutting forces versus ferrite content on FP steels changing RPT. 167
Figure 128. Broaching cutting forces versus ferrite content on FP steels changing speed. 168
Figure 129. Cutting broaching forces versus IS changing RPT. 168

Figure 130. Cutting broaching forces versus hardness changing RPT. 169
Figure 131. Cutting broaching forces versus IS changing speed keeping RPT constant. 170
Figure 132. Cutting forces versus grain size keeping constant the speed and changing RPT. 170
Figure 133. Cutting forces versus grain size keeping constant the speed and changing RPT. 171
Figure 134. Scheme of the roughness measurements zone and direction. 171
Figure 135. Ra roughness obtained in the fundamental broaching campaign. 172
Figure 136. Rz roughness obtained in the fundamental broaching campaign. 172
Figure 137. Ra roughness versus ferrite content on FP steels changing RPT. 173
Figure 138. Ra roughness versus ferrite content on FP steels changing speed. 174
Figure 139. Ra roughness versus hardness changing RPT. 174
Figure 140. Ra roughness versus hardness changing speed keeping RPT constant. 175
Figure 141. Ra roughness versus grain size keeping constant the speed and changing RPT. 176
Figure 142. Ra roughness versus grain size keeping constant the speed and changing RPT. 176
Figure 143. Cutting forces in one sole cutting condition over different tooth state and lubrication. 178
Figure 144. Material selection campaign broaching cutting forces versus ferrite content. 179
Figure 145. Cutting forces obtained in the selection campaign versus hardness. 179
Figure 146. Ra roughness obtained in the material selection campaign. 180
Figure 147. Material selection campaign Ra roughness versus ferrite content. 181
Figure 148. Material selection campaign Ra roughness versus hardness. 181
Figure 149. Scheme of the cutting focused on the tool tip. 182
Figure 150. Material selection campaign chip compression ratio versus ferrite content. 183
Figure 151. Material selection campaign chip compression ratio versus hardness. 183
Figure 152. Examples of chip micrographs showing the deformed microstructure (a) 184
Figure 153. Broaching setup vertically mounted showing the wear tests sample and sued tooth. 185
Figure 154. Cutting forces evolution while broaching C45 steel variants. 187
Figure 155. Ra roughness evolution while broaching C45 steel variants. 187
Figure 156. Zone of the tooth photographed. 188
Figure 157. Evolution of the tool edge state after broaching each 5 meters. 188

Figure 158. Cutting forces and friction coefficient comparison versus ferrite content. 189
Figure 159. Cutting forces and friction coefficient comparison versus hardness..... 190
Figure 160. Ra roughness and friction coefficient comparison versus ferrite content. 191
Figure 161. Ra roughness and friction coefficient comparison versus hardness. 192
Figure 162. Chip compression ratio and friction coefficient versus ferrite content. 193
Figure 163. Chip compression ratio and friction coefficient versus hardness. 193
Figure 164. Two-stage modelling approach adopted for machining processes (P. Arrazola et al. 2013)..... 200
Figure 165. FEM models for ALE formulation with (a) Eulerian and Lagrangian boundary conditions, and (b) pure Lagrangian boundary conditions, and the predicted temperature fields, respectively ((c) and (d) (P. J. Arrazola 2010)..... 201
Figure 166. Lagrangian simulation of the broaching operation carried out by (Kong et al. 2011). 202
Figure 167. Orthogonal cutting numerical simulation (ALE) by Bonnet et al. (Bonnet et al. 2008)..... 203
Figure 168. (a) the elementary Lagrangian model and (b) the Iterative Lagrangian Model (ILaM) (Fabre et al. 2017). 204
Figure 169. SPH simulation of an orthogonal machining process (Xi et al. 2014)..... 204
Figure 170. Boundary conditions of the last developed 2D ALE broaching model..... 207
Figure 171. Experimental cutting and feed forces comparison with modelling forces. 209
Figure 172. Experimental and numerical cutting forces obtained at different teeth state and lubrication versus ferrite content. 210
Figure 173. Experimental chip compression ratios comparison with numerical chip compression ratios..... 211
Figure 174. Experimental and numerical chip compression ratios obtained at different tooth state and lubrication versus ferrite content. 212
Figure 175. Temperature fields computed with the ALE model: on the left without the tool on the right with the tool (C45GP with the Uncoated tooth in dry conditions at 2 m/min and 40 µm). 213
Figure 176. Temperature gap assessment in model results comparing versus the experimental cutting forces. 214
Figure 177. Numerical and experimental forces comparison at 20 m/min assessing the viscosity and the influence of the temperature dependency on the flow stress..... 214
Figure 178. Cutting forces comparison experimental under lubrication versus numerical in dry conditions..... 215
Figure 179. Illustration of the scale effects to consider when cutting a) a standard C45R and b) a coarse grain C45CG with a RPT of 50µm. 216

LIST OF TABLES

Table 1. HSS classification according to ISO 4957. 40
Table 2. Cutting speeds in broaching V_c (values in m / min) (BELLAIS 1997). 41
Table 3. Typical steel and alloy compositions (Callister, Rethwisch 2011). 73
Table 4. Physical properties of each phase (Handbook 1990, Abouridouane et al. 2012). 75
Table 5. Codification of the different studied steel variants. 76
Table 6. ASTM grain size conversion to mm. 78
Table 7. Chemical composition of steel grades. 81
Table 8. Measured ferrite content (%). 82
Table 9. Ferrite grain size (µm). 82
Table 10. Interlamellar spacing - average ± standard deviation (nm). 83
Table 11. Hardness HB (average). 84
Table 12. Design of experiments for the flow stress model development. 99
Table 13. Summary of the impact of variant compared to reference grade strain (ε = 0.2). 102
Table 14. Summary of the impact of variant compared to reference grade's stress at a given strain (ε = 0.2) 106
Table 15. Friction coefficient (CoF) values obtained by (Rech 2006) using WC-Co over 27MnCr5 steel. 115
Table 16. Volume fraction of ferrite and pearlite and mean linear intercept grain sizes of as-received, sand and air-cooled samples (Gündüz et al. 2008). 120
Table 17. Tribology studies summary table. 125
Table 18. Selected design of experiments for the fundamental study. 128
Table 19. Selected design of experiments for the broaching focused tribological study. 129
Table 20. Dominant wear mechanisms observed depending on the variant. 142
Table 21. Selected design of experiments for the fundamental study. 161
Table 22. Selected design of experiments for the broaching focused tribological study. 162
Table 23. Steel selection for the focused campaign. 177
Table 24. Tool life tests cutting conditions. 186
Table 25. Cutting conditions selected for the modelling part. 208

NOMENCLATURE

Cutting conditions

a_p	mm	Depth of cut
f	mm	Feed
$RPT\ (h)$	µm	Rise per tooth
V_c	m/min	Cutting speed

Geometrical aspects

A_{min}	mm	Minimum section of the broach
d	mm	Pin's diameter
D_B	mm	Base diameter of the broach
D_G	mm	Diameter of the broach before the cutting part
H_D	mm	Height of the tooth
L_{Aar}	mm	Backside fixing length
L_{Aav}	mm	Frontside fixing length
L_{Gar}	mm	Backside guiding length
L_{Gav}	mm	Frontside guiding length
L_C	mm	Length of the cutting part of the broach
L_D	mm	Length machined
L_T	mm	Total length of the broach
L_U	mm	Machined material length
P	mm	Tooth pass
R_β	mm	Cutting edge radius
α	°	Rake angle
γ	°	Clearance angle

Material's and tool's properties

c_t	J/(kg·K)	Tool's specific heat
c_p	J/(kg·K)	Workpiece's specific heat
k_t	J/(m·K·s)	Tool's condictivity
k_p	J/(m·K·s)	Workpiece's conductivity
R	N/m^2	Yield strength
α_t	m^2/s	Tool's diffusivity
α_p	m^2/s	Workpiece's diffusivity
ρ_t	kg/m^3	Tool's density
ρ_p	kg/m^3	Workpiece's diffusivity

Thermomechanical loads

F	N	Force
F_c	N	Cutting forces
F_{max}	N	Maximum admissible tensile force
F_μ	N	Friction forces
F_f	N	Feed force
k_{sec}	-	Safety coefficient

K_s	N/mm^2	Specific cutting force
M_z	N·m	Torque
Q	J	Heat
T	K	Temperature
μ		Friction coefficient

Abbreviations

ALE	Arbitrarian Lagrangian Eulerian
BUE	Built Up Edge
CAD	Computer Aided Design
CEL	Coupled Eulerian Lagrangian
CG	Coarse Grain
CNC	Computer Numerical Control
COA	Coated
CoF	Coefficient of Friction
CVD	Chemical Vapour Deposition
DOE	Design of Experiment
DSA	Dynamic Strain Aging
EDM	Electrical Discharge Machining
FE	Finite Element
FEM	Finite Element Modelling
FP	Ferritic-Pearlitic
GP	Globular Pearlite
HB	Brinell Hardness
HSS	High Speed Steel
IND	Industrially coated tooth
JC	Johnson-Cook
LOM	Light Optical Microscopy
PSZ	Primary Shear Zone
R	Reference
SHPB	Split Hopkinson Pressure Bar
SSZ	Secondary Shear Zone
t	s time
TiN	Titanium carbon nitride
UNC	Uncoated
WB	With more Bands
WC-Co	Tungsten carbide with cobalt

Chapter 1

INTRODUCTION

1 INTRODUCTION

Industrial context

Nowadays, in a context of globalization, companies have to work with additional economic constraints. In this globalized industry, manufacturers are directly concerned with the idea of reducing the development steps i.e. define the optimal process parameters. Recent and increasing evolutions in materials are tending to make it more and more difficult. Steels, even if they appear as common materials in mechanical or automotive industries, are not always the easiest one to machine. They can exhibit very different material properties leading to various machining performances. In this, ferritic-pearlitic steels are especially concerned as they can cover a wide range of mechanical properties due to the numerous variants that their microstructure can enable.

The automotive industry represents a considerable amount of complex products engineered and manufactured with just in 2015 more than 65 million cars. Each car requires around 900 kg of steel, with around 20% used in a ferritic pearlitic state (FP). Therefore, only in 2015, it can be easily calculated that 12 million tons of ferritic pearlitic steels were sold to manufacture car engine parts such as crankshafts, pinions or common rail injection system (Figure 1).



Figure 1. Car engine parts manufactured with ferritic-pearlitic steels.

The car parts shown in the Figure 1 are machined after forging using mainly three different cutting processes: turning, drilling and broaching. Briefly, turning (Figure 2a) is a machining process in which a cutting tool (typically a non-rotary tool) describes a helix toolpath by moving more or less linearly while the workpiece rotates. Drilling (Figure 2b) consists on making circular holes in one piece by the use of a drill. Broaching (Figure 2c) uses a toothed tool with a linear or rotary movement to remove material.

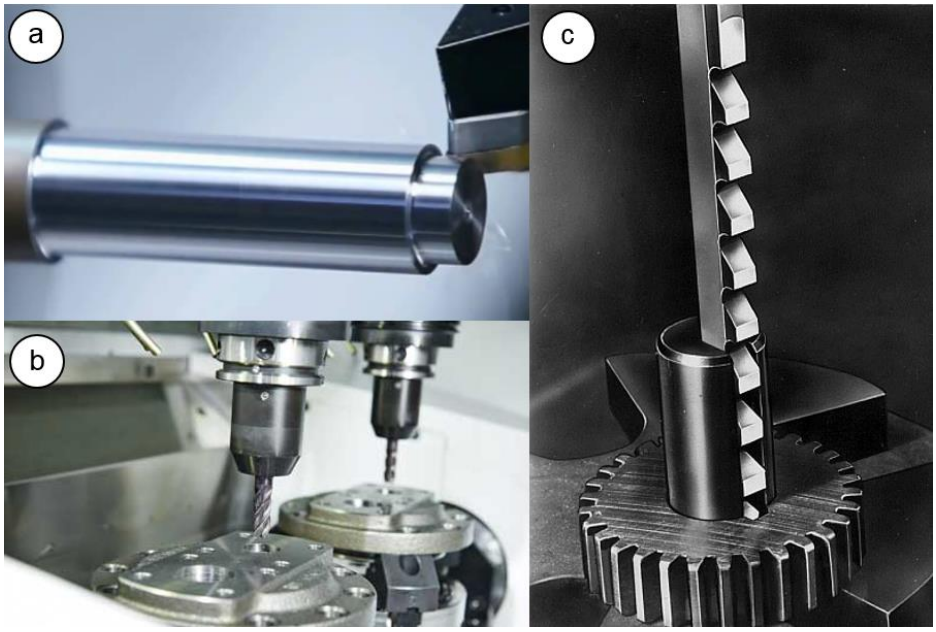

Figure 2. Turning, drilling and broaching processes.

If these processes might be considered as conventional, variations in terms of microstructure can significantly affect their performance. This is especially true for broaching. This machining technique reaches almost the limits of conventional cutting as (i) very low cutting speed, commonly between 1 and 5 m/min with high speed steel tools (Kishawy et al. 2012) and up to 60 m/min with carbide tools (Meier et al. 2014), as well as (ii) small uncut chip thickness from 0.1 to 0.25 mm in the roughing section of the tool or down to 0.0015 mm in the finishing one, are typically used. These values can take it somehow in the range of micro machining (Simoneau et al. 2006).

Today, the main issues for steelmakers as well as end-users can be summarized by the following questions:

- In broaching, which is the steel variant leading to the best results in terms of roughness, machining forces and tool wear? i.e. which of the steel provides the best machinability?
- Based on the previous question, could be the cutting conditions optimized to improve the machinability?
- Could it be possible to design and tailor a steel grade with a defined microstructure for a specific cutting process?

This PhD will try to answer these questions by analysing the influence of the steel's microstructure on the broaching process from an experimental, tribological and numerical point of view.

Scientific approach

This study is part of a larger EU project proposing an approach to improve the understanding of how steel's microstructure can affect the machining performance of a component. In broaching, the key process outputs are the resulting forces (Fc & Ff), surface roughness (Ra & Rz) and chip morphology (Figure 3). To date, it is really difficult to predict the effect of the FP microstructural parameters on them and how to adapt the processing conditions to alleviate the various issues. Numerical modelling can be seen as a promising tool but there is still a lack of microstructural considerations in the currently developed model. Constitutive models remain at the macroscopic scale and are usually homogenised ones whereas tribological interactions are rather limited by a single constant friction coefficient. The latter is mainly seen as a "fitting" parameter depending on the type of workmaterial. The scientific approach proposed in this work aims at introducing a more physical dimension to these primary input data, i.e. material and frictional behaviours, keeping in mind the constraints of the industrial environment.

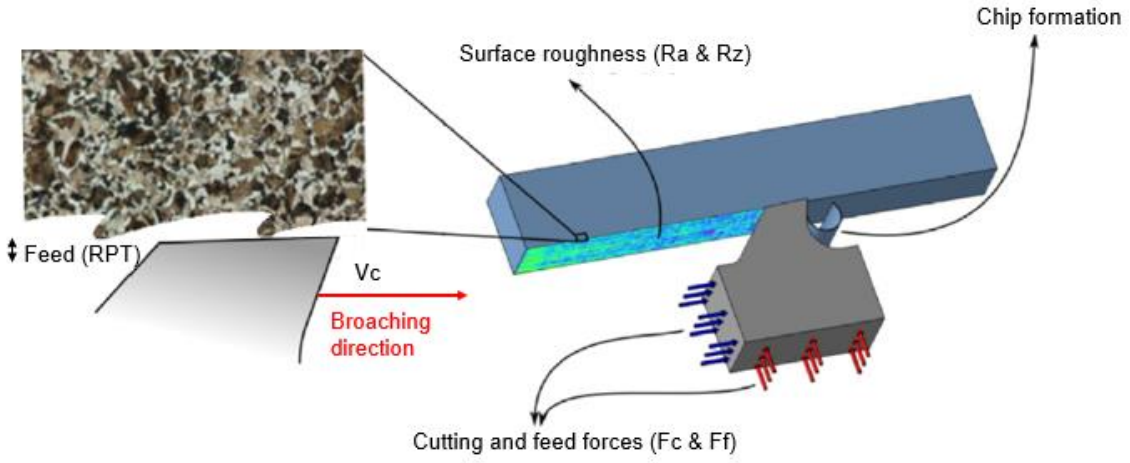

Figure 3. Scheme of the outputs obtained in the tool-workpiece interaction inspired from (Fabre et al. 2016).

In order to dissociate the effect of each microstructural parameter, five steels grades (16MnCr5, 27MnCr5, C45, C60 & C70) have been developed with four different microstructures: standard, globular perlite, coarse grain & wide bands (Figure 4). The different grades provide a large range of carbon content, i.e. ferrite-pearlite ratios and hardnesses, and their variants guarantee various grain sizes, microstructure morphologies, interlamellar spacings etc.

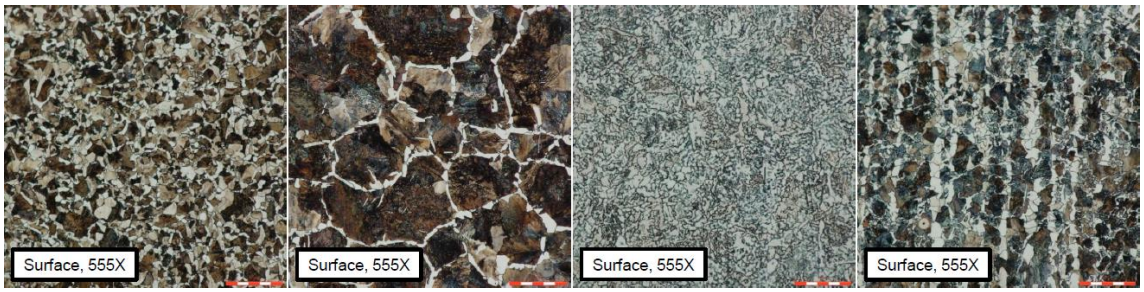

Figure 4. C45 steel in its four different variants with same magnification. From left to right: Standard, Coarse grain, Globular Pearlite & Wide Bands.

Several experimental techniques have been applied at different scales to assess the contribution of each microstructural parameter on:

- The process outputs via an intensive experimental broaching campaign;
- The frictional behaviour via a tribological approach using different tool/coating systems;
- Local data and overall process performance by the development of a numerical model and the implementation of the identified input data.

Objectives

The main goal of this PhD is to understand the influence of FP steels microstructure on the broaching process. To this end, several specific goals have been defined:

1. Provide knowledge about the machinability of FP steels so as to lead the industry in future developments by improving productivity and profitability simultaneously.
2. Thermal characterization (conductivity, density, specific heat and the thermal diffusivity) all the ferritic pearlitic steel variants related to the project.
3. Understand how the microstructural parameters affect to the tribological behaviour and broaching process, assessing the importance of coating and lubrication.
4. To develop a numerical model for broaching that will provide a further analysis possibility once compared with the experimental data.

Methodology and document's structure

This PhD thesis has been split with the following structure in order to browse all the key aspects of the project.

Chapter 1 – INTRODUCTION

Introduction to the PhD, explaining its industrial context, the scientific approach conducted in this work as well as the objectives.

Chapter 2 – BROACHING CUTTING PROCESS

An introduction to the broaching process is presented introducing its basics and identifying the key parameters driving the cutting mechanisms. A literature review is then

performed in order to assess the existing work on the related topic and emphasize the contribution this thesis may have for the scientific community.

Chapter 3 – MATERIAL CHARACTERIZATION

Introduction to the materials used throughout the PhD and explanation on how their metallurgical characterizations were carried out. Then, the steel's thermal characterization and their flow stress will be presented.

Chapter 4 – ANALYSIS OF THE FRICTION AND WEAR IN THE FP STEELS

A tribology study using the FP steels, obtaining their friction coefficient in two clearly differentiated campaigns will be detailed. Two types of studies have been carried out: a fundamental study on a wide range of speeds using carbide pins and a second one focused on low speeds using pins made of High Speed Steels.

Chapter 5 – CUTTING TESTS (BROACHING)

Experimental broaching tests performed with the 16 FP steels variants in order to record the machining forces, surface roughnesses and analysing the generated chips.

Chapter 6 – NUMERICAL TESTS AND COMPARISON WITH THE EXPERIMENTAL

Numerical simulation is developed in order to model the broaching process itself and a comparison with the previously obtained experimental results is carried out.

Chapter 7 – CONCLUSIONS AND FUTURE LINES

The overall conclusions drawn from all the work done in the PhD as well as the future lines in which further work will be required.

Chapter 8 – ORIGINAL CONTRIBUTIONS

The papers submitted to journal and papers presented in conferences are mentioned during the development of the PhD thesis are exhibited.

Chapter 9 – BIBLIOGRAPHIC REFERENCES

The bibliographic references cited through this entire document are presented.

Chapter 10 – ATTACHMENTS

Additional information that is not presented through the document is exposed: all the graphs related to each of the FP steel variant, etc.

Chapter 2

INTRODUCTION TO BROACHING

2 INTRODUCTION TO BROACHING

Broaching process

2.1.1 Introduction

Broaching is a machining process that was originated in the 1860s in the United States and was originally used for the pulley grooves or gears production. The first broaching operations were carried out manually, the operator pushed the broaching tool in the hole by the repeated application of hammer strokes on the tool. The term broaching appeared for the first time in 1873 and was patented by Anson P. Stephens during a broaching machine improvement project (Stephens 1873).

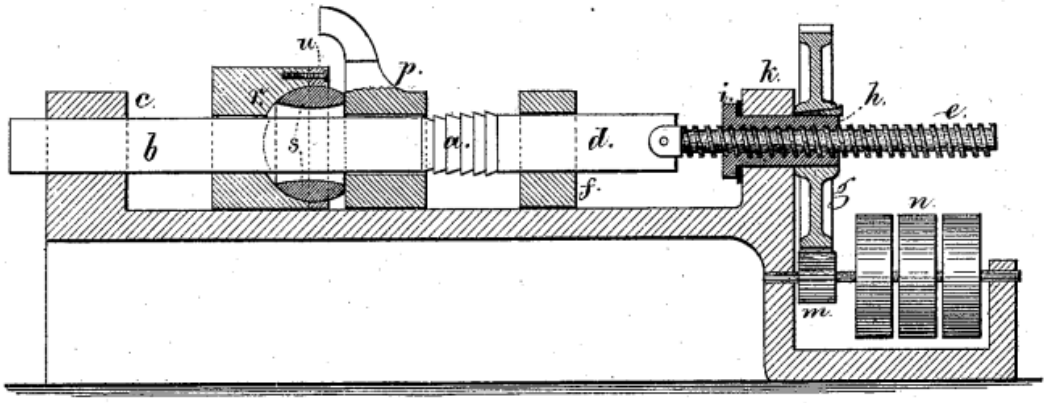

Figure 5. Broaching machine patented by (Stephens 1873).

Between 1898 and 1902, the Canadian Francis J. Lapointe used industrially this process for the first time, by means of a horizontal stapler driven by screw mechanism. He patented this version in 1914 (Lapointe 1914) and improved it in 1920 (Lapointe 1920). In 1921, the company Oilgear Co. started selling the first hydraulic puller.

The broaching consists in machining of internal and external surfaces by rectilinear cutting movement. The cutting mechanisms implemented during a broaching operation are very similar to those generated by a slotting operation unlike the tool used consists of several successive and loose teeth.

Some examples of holes made by means of broaching are shown in Figure 6:

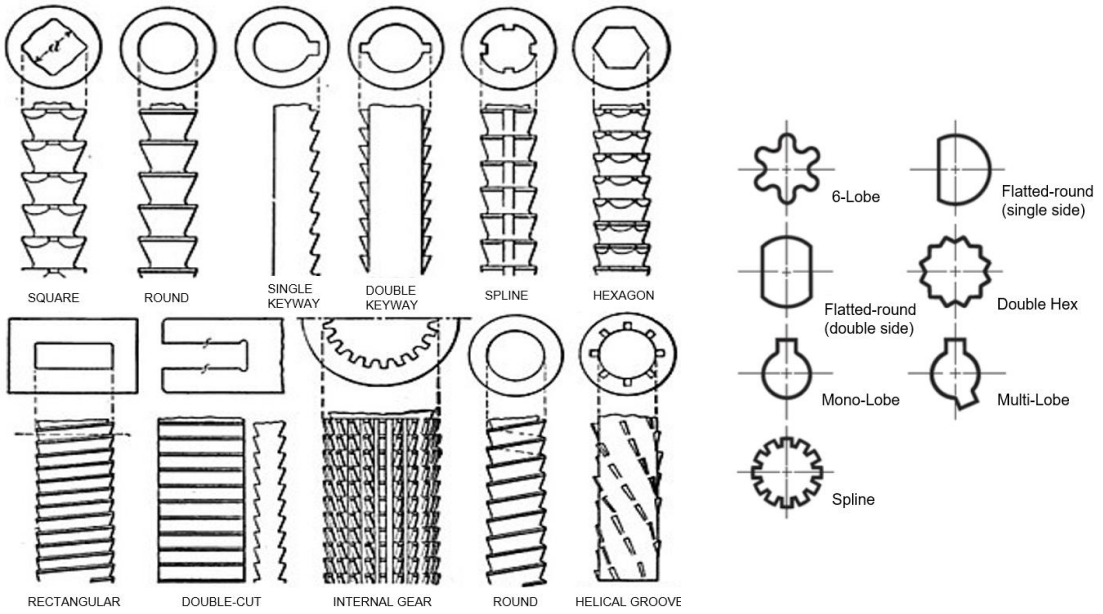

Figure 6. Inner broaching examples (left side) external broaching examples (right side).

Application fields

The use of broaching is generally considered in two cases. It has one of the best productivities observed in machining, and therefore fits perfectly to the production of parts in large or medium-sized series. It is usually more cost-effective than boring or milling operations, and the execute time is from 3 to 4 times inferior to those generated by these latter processes (Cubberly 1989, Masseglia 2009).

Besides it allows a very high chip flow, it is also able to generate high precision surfaces, with a dimensional ISO ranging from 7 to 9, and arithmetic roughness extending over a range of 3.2 to 0.4 µm. The generation of these surfaces being made in a single pass, each broach has teeth for roughing, the semi finishing and the finishing.

The cutting kinematic is quite simple (translational motion), the broaching therefore requires the use of relatively simple machines (cycle machines). However, this process leads to consistent cutting forces, providing a large cutting area and the simultaneous work of several cutting sections. Moreover, the cutting speeds are generally very low in broaching (mostly inferior to 6 m/min), that is why hydraulic actuator machines are generally preferred. This process is really profitable as it is useful for long batches as well as of course short batches.

2.1.2 Design of a broach

One of the key elements of the quality of a broaching operation is the care provided in the production of the broach. In fact, in most machining operations the number of cutting edges is limited (less than a dozen in the case of milling), and their geometry is simple and easily characterizable. On the other hand, the tools possess multitude of cutting

sections (up to 200) composed of arcs whose geometry is generally as complex as variable. These specifications make considerably complicate the design, manufacture and control of these tools.

There is a very large diversity of broaches which differ as well by their application, their geometry, their metallurgical composition or their coating. It is common to distinguish the internal broaching and the external broaching as the implementations and applications are very different. The internal broaching is mainly intended for the realization of various holes (with or without complex shapes…, internal gears…), from the simple circular hole up to the groove through the keyway (Figure 6). External broaching is used a lot in automotive or aeronautic applications, for the manufacture of racks and pinions or anchorages of turbine blade feet.

Broach overall structure

The realization of an internal broaching operation can involve a tool to be pulled or pushed. This last mode of action is used marginally at the industrial level, generally on presses to broach. The broaching length of a pushed tool is limited as there is a risk of buckling inherent to the mode of application of the effort. Checking the Figure 7, maximum ratio of 25 between the length of the broach and its diameter must be respected so as to limit this risk. These broaches are mainly used for operations requiring only a small amount of material removal or a very good surface condition, such as calibration works.

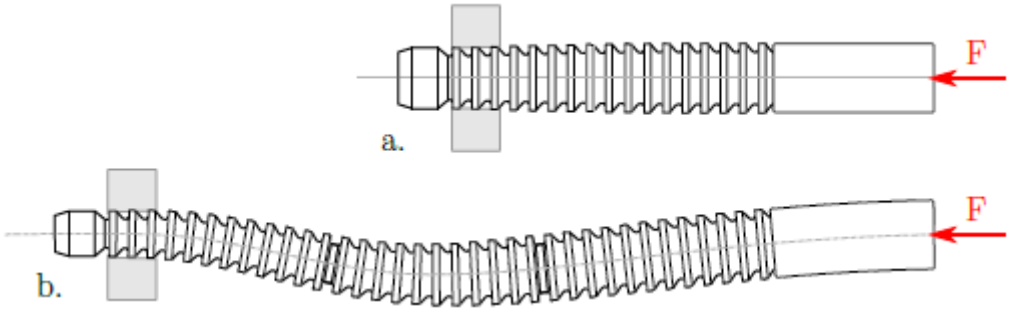

Figure 7. a) Correct length of a pulled broach scheme b) Too long broach pulled suffering a buckling (Fabre 2016).

The pulled broaches can measure up to several meters, and they are essentially limited by the area of the minimum section (A_{min}) of the broach, and thus the basic diameter for a circular broach. It is indeed at this level that the break will occur in a privileged manner. The standard DIN 1417 proposes a standardization of the maximum allowable tensile stress on the broaches according to the nominal diameter and the length of these. The Forst handbook proposes for its part a mechanical tensile strength calculation of this

broach, presented by the equation below. This is to limit the maximum tensile force F_{max} (Eq. 2.1) so as not to exceed the R elastic limit.

$$F_{max} < \frac{R\ x\ A_{min}}{k_{sec}} \qquad (Eq.\ 2.1)$$

with a $1.2 \leq k_{sec} \leq 1.4$ and a $R = 250\ {}^{N}/_{mm^2}$ for a HSS tool, which is indeed our case.

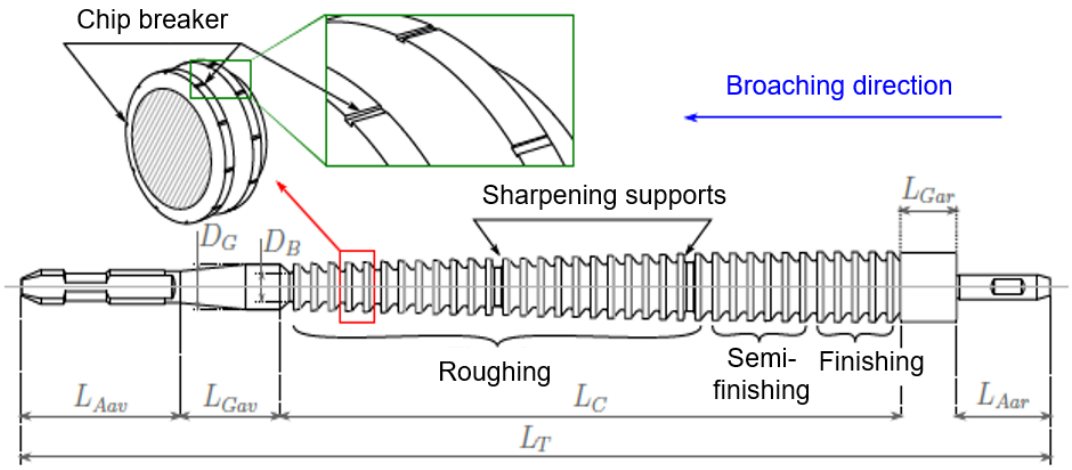

Figure 8. Usual broach with its parts (Fabre 2016).

Figure 8 shows the typical structure of a broach. To better understand the function of each element of this tool, it is interesting to look at the flow of a broaching cycle, based on the schema of Figure 9.

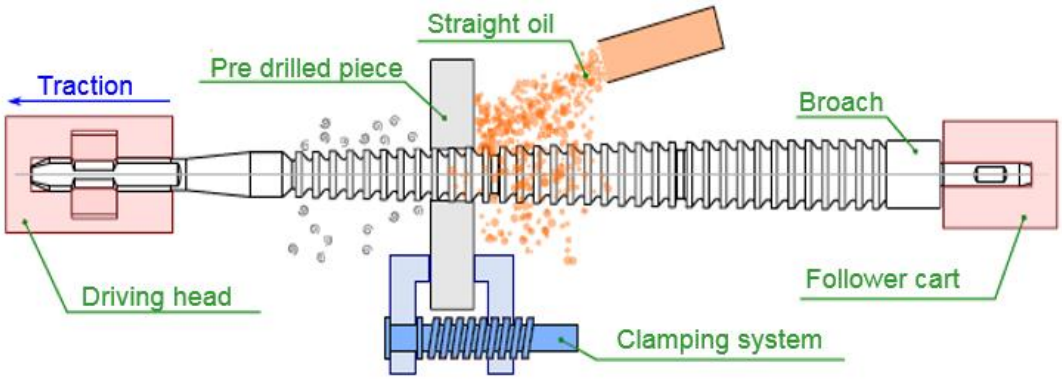

Figure 9. Usual broaching moving motion (Fabre 2016).

First, the piece to broach must be drilled or even bored in some cases and positioned on a support (driving head and follower cart) sustaining the cutting force of the broach (Figure 9). The piece can also be maintained by a clamping system improving in this way the rigidity of the assembly. At the beginning of the cycle, the tool is only held by the tail by means of a follower carriage which at first passes the coupling head into the bored hole.

Once passed, the head of traction grasps the broach by the hitch head, the spindle then centres in the hole thanks to the front guide, and the material removal begins. The

carriage remains attached to the broach backside during the operation (follower cart in Figure 9), to avoid the phenomenon of whipping characterized by an oscillation of this part. This phenomenon is responsible of premature wear of cutting edges, dimensional defects or even breaking of the broach by bending in the most severe cases. This carriage can also ensure tensioning of the system, ensuring better rigidity in certain applications.

At the end of the operation, the last teeth are stabilized by the rear guide, and the broach ends its stroke maintained only by the front linkage (Figure 9 driving head). The machined piece is then removed and the follower carriage again grabs the broach to return it to the initial position.

Basic tooth of a broach

The operating conditions commonly used in broaching are far from those used in the most machining processes. For example, there cutting speeds are generally very low (V_c ≤ 8 m/min (Handbook 1990, DeGarmo et al. 1997) and the generation of chips most of the time very narrow (h ≤ 0.15 mm) (Handbook 1990).

This explains the use of geometries of very specific teeth, especially with large rake angles (γ ≥ 15º) or very sharp cutting edge radii (5 ≤ R ≤ 15 µm) (Makarov et al. 2008).

a. Overall shape of a tooth

   It is considered at first as a section with some broaching teeth. Figure 10 shows the structure of a flat elementary broach (which may for example be intended to produce keyways).

b. Broaching teeth angles

   As previously mentioned, the cutting angle (rake angle) used in broaching is generally positive (of the order of 20º), the clearance angle (α) is on the other hand very low, in the order of 1º to 2º. This is mainly due to the combination of a low chip thickness and the use of high speed steel for most broaches.

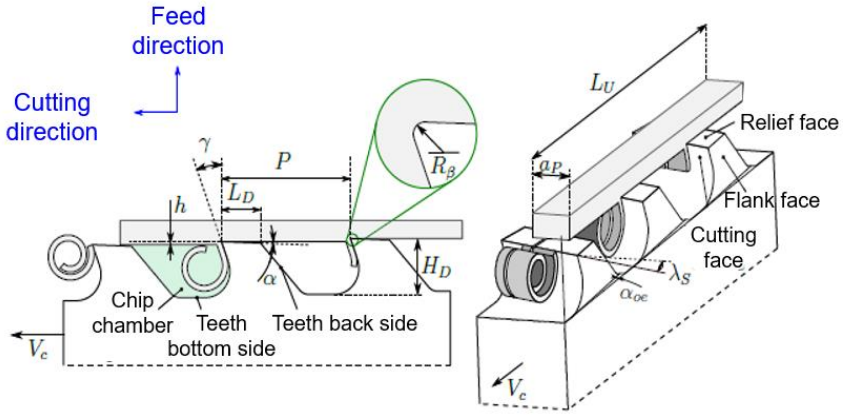

Figure 10. Elemental broach shape and teeth (Fabre 2016).

Broaching tool materials

In most cases, broaching is in general achieved by means of high speed steel (HSS) one-piece (monoblock) tools. While many HSS formulations were used early in the industrial use of broaching, a standardization effort was made that eventually led to the use of limited quantity of fast steels particularly qualified for the implementation on this process. There is a marginal use of steels strongly alloyed with chromium, just in some cases of specific applications. The use of carbide tools may also have certain advantages, in particular in terms of reduction of wear (according to the criteria described in standard NF ISO 3685), although the increased fragility of these tools limits their use in the field of broaching.

In some applications, a nitriding treatment can be applied to the high-speed steel broaches. If this one can easily be a source of a critical fragility of the cutting edge, an adaptation of this treatment to the broaching tools can be the origin of a reduction of the friction coefficient between the tool and a material that is suitable for adhesion (Forst 1973).

Table 1. HSS classification according to ISO 4957.

	HSS containing less than 4.5% Co and less than 2.6% Vn	HSS containing at least 4.5% Co and at least 2.6% Vn
Usual HSS	HSS	HSS-E
HSS from powder metallurgy	HSS-PM	HSS-E-PM

In general, the tool coating is preferred over the nitriding treatment, as it is easier to carry out and easier to control under the broaching conditions (sharp cutting edges, etc.). In terms of broaching, the most commonly encountered coatings are the TiN, TiAlN or even TiCN coatings which are generally 1 to 5 µm thick. A resharpening of the cutting face is generally carried out after coating to limit the rake radius, as shown in Figure 11.

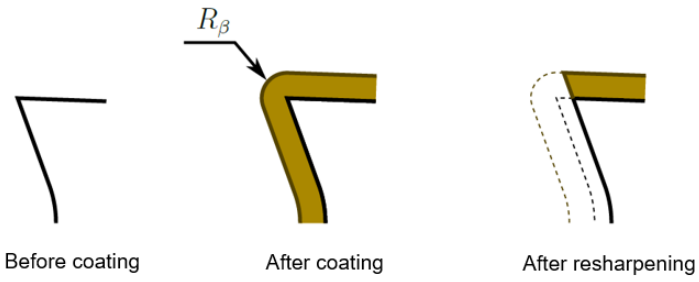

Figure 11.Influence of the coating on the cutting radius R, schematization of a section of the broaching tooth, final state after manufacturing.

Note: The coating applications shown in the Figure 11 are in fact the way in which the teeth were coated for the experimental tests. From left to right respectively, uncoated (UNC), fully coated (COA) and the industrial (IND) way of coating.

2.1.3 Process parameters

Cutting speed

Comparing with other machining processes such as turning or drilling, cutting speeds commonly used in broaching are low, of the order of 5 - 10 m/min reaching up to 34 m/min depending on the machined material. In fact, the high productivity of this process results more from important cutting areas than from cutting speeds.

Historically, the cutting forces have been consistent being this way the hydraulic broaching machines favoured. Therefore, the cutting speeds allowed by these machines rarely have exceeded 10 m/min. Nowadays, electromagnetically controlled broaching machines make it possible to increase these speeds considerably, facilitating the development of the use of carbide tools.

Table 2 summarizes the orders of magnitude of cutting speeds commonly used in broaching.

Table 2. Cutting speeds in broaching V_c (values in m / min) (BELLAIS 1997).

		HSS tool	Carbide tool
Steels	400 < R ≤ 700MPa	10-24	12-24
	700 < R ≤ 1100MPa	8	
Casts		8	30-34
Non-ferrous metals		10-40	25-30

It should be noted that the cutting speed has an influence on the heat flux generated at the tool/material interface and therefore has an influence on tool wear, also in broaching as in any other cutting process. The wear appears faster at high speed but the thermal softening taking place in the shear zones can be beneficial for the generated surface state. The velocity also plays an important role in chip formation and chip-winding mechanisms, which are critical in the case of broaching. Finally, the cutting speed is directly related to the appearance of vibrational phenomena which can occur during the

operation and to which the process of broaching is particularly prone due to the implementation of tools sometimes very long and large assemblies.

Lubrication

The lubrication mode has a direct influence on the surface state as well as on the wear of the tool.

Lubricant plays 5 major roles in machining (Byers 2006):

- It allows to reduce the friction coefficient between the tool and the material. The chip formation can thus be facilitated, reducing the heat flux generated at the interface.
- The additives present in the oil make it possible to limit the chemical nitrates between the tool and the material. This can reduce the phenomena of micro-welding and thus the risks of BUE appearance.
- The freshly machined surface is very prone to the appearance of corrosion, the cutting oil can limit the chemical reactions occurring on the surface of the broached material.
- In addition, it influences the heat source and its transmission as the lubricant allows to evacuate part of the generated heat. The choice of the lubricant (oil, emulsion, liquid nitrogen, etc.) as well as its application method (constant flow, MQL, etc.) can significantly change the temperatures at the same time in the cutting edge.
- The last point particularly useful in broaching is the evacuation of the chips. Since the cutting zone is inaccessible during broaching, a very large flow of cutting oil is generally applied to the broaches before and after broaching to evacuate the chips.

Regarding this last point, the use of oil jets under high pressure offers convincing results concerning the evacuation of the chips, but perhaps the cause of the appearance of oil mists prohibitions from a health point of view in the absence of appropriate fairings. The use of brushes may also be required to further improve chip evacuation. It will then be a question of finding a compromise between the effectiveness of evacuation and the wear of the broaches and the brushes.

The use of straight cutting oil is generally preferred in broaching due to the low cutting speeds and high pressures involved in the cutting zone. Thus, very polarized straight oils and mixed with additives at high pressure are mainly used. Note that the use of chlorine or sulphur is increasingly prohibited during the development of cutting oils for broaching.

Although their effect on the friction coefficient is recognized as presented in Figure 12, health and environmental constraints no longer permit their use.

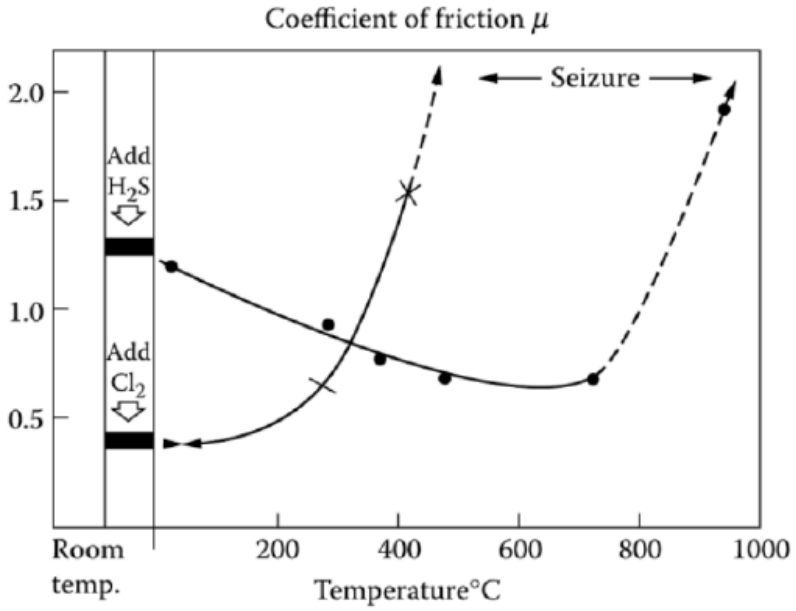

Figure 12. Influence of the sulphur and the chlorine in the friction coefficient (Byers 2006).

2.1.4 Conclusions

Broaching is an ancient cutting process that implements generally basic kinematics (linear displacement). The large diversity of broached products and the complex structure of the tools makes their design particularly delicate. Thus, broach design and manufacture, as well as the operational conditions of broaching and the machines used, have a direct influence on the broaching quality i.e. surface state, tool wear, etc.

With the aim of analysing the influence of the different steel's microstructure on the broaching outputs (such as cutting forces, roughness, or chip formation) it is important to know the scientific approach carried out up to now in this field. This work presented in the next chapter is intended to provide elements to understand and improve the understanding of the steel's microstructure impact on broaching performance.

Broaching scientific studies

2.1.5 Introduction

Although broaching is a very old process, the selection of cutting conditions relies mainly on a technical know-how. The manufacturers of broaches and broaching machines as well as some expert users essentially hold the knowledge related to the process. Very few scientific studies have been published about broaching compared to more conventional processes such as turning or milling.

The design and use norms established are proved to be relevant compared to the quantity of research works published. The understanding of the physical mechanisms responsible for cutting, allow the optimization of the efficiency of the process (improvement of the geometrical surfaces and productivity, lower costs, etc.). To do this, a scientific approach to study the cutting operation is more relevant than the phenomenological approach obtained by the experience.

It is thus necessary firstly to identify the broaching parameters to study and then their influence on the different broaching results highlighted. These are presented in the following figure (Figure 13):

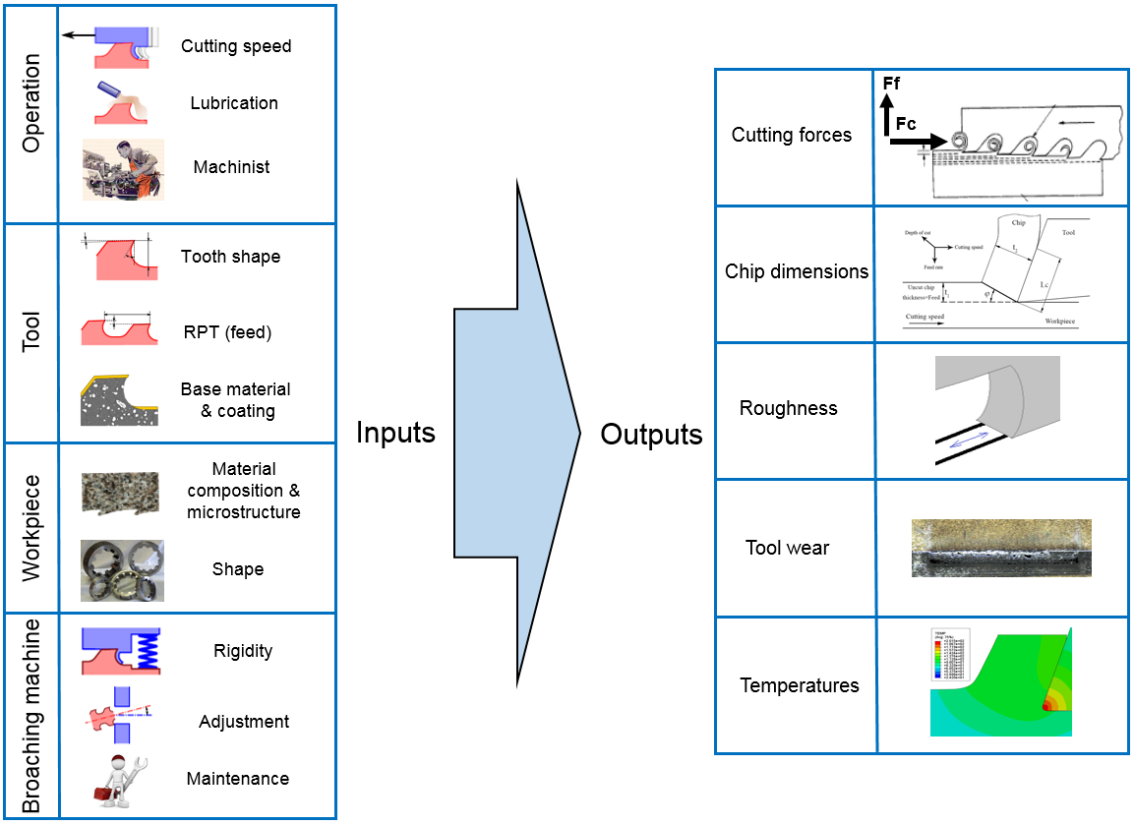

Figure 13. Broaching parameter inputs and corresponding outputs.

In the case of broaching, there are usually found four families of modifiable parameters, depending on the tool, the piece, the broaching machine or the operation itself. Regarding to the broaching output results, three large categories can be dissociated:

- The quality of the machined part: These parameters correspond to the indicators of the quality obtained after a broaching operation. They can be fixed by the specifications established by the customer; the operator will be required to respect the specified constraints.
- Physical indicators: This is to study the consequences of the thermomechanical effects occurring during the cutting operation. These parameters are often

essential for understanding the physical, chemical or thermal mechanisms involved in cutting. The monitoring of the broaching operation usually passes through the study of the evolution of these parameters.

- The quality of the broach: The indicators of the quality of a broach are observed by the worker to evaluate the capacity of a tool to perform a specific operation in an efficient way. This criteria (life, price or dimensional) related to the broaches are defined by the operator. The tool manufacturer will be then required to respect the specifications.

In order to study successfully the influence of these parameters, a certain number of tools can be involved, whether it is through an experimental approach essays or means of numerical study of the process. These setups and devices are presented in the next section.

2.1.6 Broaching process studying setups

With the aim of analysing the influence of previously discussed parameters, several scales and tools of study can be considered, from the industrial broaching operation up to the study of tribo-chemical behaviour at the tool/material interface. When it comes to represent this machining operation, two complementary approaches are commonly considered; the setting up of an experimental test bench and the representation of the cutting process by means of numerical modelling and simulation. We detail in the upcoming subsections each of these approaches and the methods used to implement them.

Experimental devices

Most of the experimental studies present in the literature have been carried out by means of broaching machines (Bejnoud et al. 2015, Schulze et al. 2011, Axinte et al. 2005, Kishawy et al. 2012) These have many advantages such as high rigidity and a working mode identical to the one it can be seen in industry. This allows to consider the work of a broach in its entirety, for example to study of the evolution of the cutting elements.

For instance, (Kishawy et al. 2012) have implemented an internal broaching tool on a broaching machine equipped with a shelf, as shown in Figure 14. This tool has 44 teeth, which makes it possible to obtain the evolution of the cutting elements throughout the broaching operation under industrial conditions. (Bejnoud *et al*. 2015) used a similar approach for the study of the deformations of a part induced by an internal broaching operation.

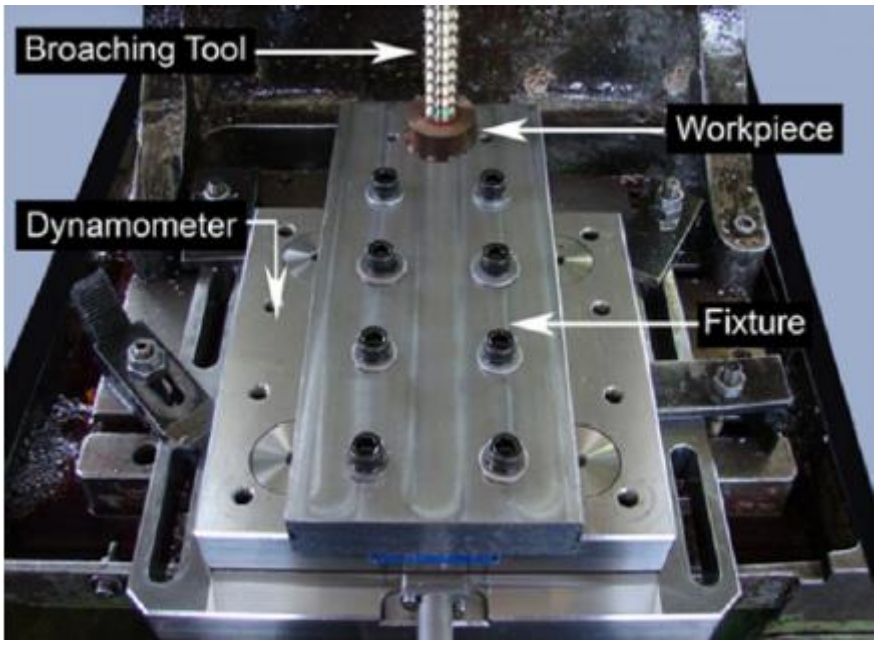

Figure 14. Kishawy's multi-teeth study set-up (Kishawy et al. 2012).

However, these two examples implement an internal broaching tool that is geometrically axial, which induces a compensation of the feed forces (only the cutting forces can be measured). However, the broaching efforts are generally more sensitive to the variations of cutting mechanisms involved at the tool/material interface. Therefore, external broaching is sometimes favoured at the scale of the laboratory study. This makes it possible to measure the feed forces in addition to the cutting forces, or even the lateral forces generated by a possible inclination of the edge or teeth.

Moreover, the use of a single tooth geometry (orthogonal cutting type) allows for a more fundamental study, compared to the use of a complex cutting edge (with variable angles, etc.), and to concentrate the study on the mechanisms of separation of the material. The results thus obtained can subsequently be extrapolated to more complex case studies.

Several studies have thus been carried out using orthogonal external broaching tools. For instance, it can be found the work of (Klocke, Kuchle 2011) with the use of a tool with 13 teeth or the one performed by (Mo et al. 2005) on a tool with 5 teeth. (Schulze, Meier et al. 2012) also investigated an external broaching operation, but with a production tool consisting of three rows of 88 teeth. The objective in the latter was to observe the work of the tool in a global way and not to focus on the work of a single tooth. The study of a broaching tool for the manufacturing of turbine blade housing was also carried out (Axinte 2007).

When it comes to study the influence of the parameters related to the structure of a broaching tooth, it may be interesting to rely on the interaction of several teeth. (Vogtel et al. 2013) for this purpose also used an external broaching machine, but this time with

a tool with only one tooth (Figure 15). In this study, the chip chamber is not present on the tool, so its effects are neglected.

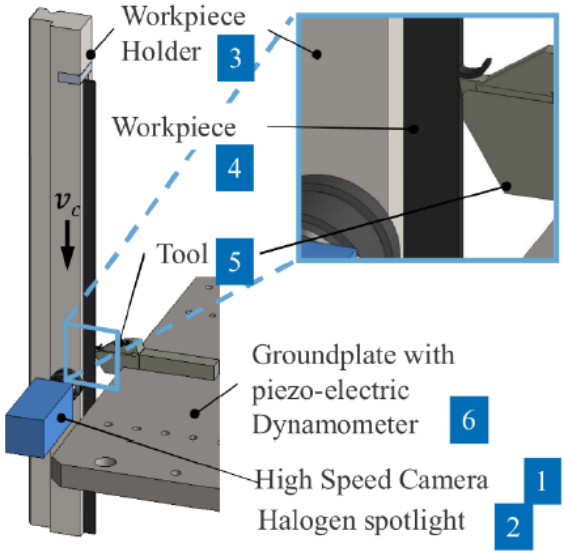

Figure 15. One tooth external broaching setup (Vogtel et al. 2013).

Thus, the implementation of a tool provided with a single tooth makes it possible to represent an orthogonal cutting operation with the particularities of broaching (low progressions, large cutting angles, very low thickness, etc.). Thus, in the literature, there are assemblies set up on CNC milling machines intended to represent an orthogonal cutting operation which is elemental micro-machining. (Malekian et al. 2012) study, for example, the results of a cutting operation with an advance of only a few microns. (Ducobu et al. 2016) uses a similar system for the study of larger advances, up to a few tenths of millimetres (Figure 16).

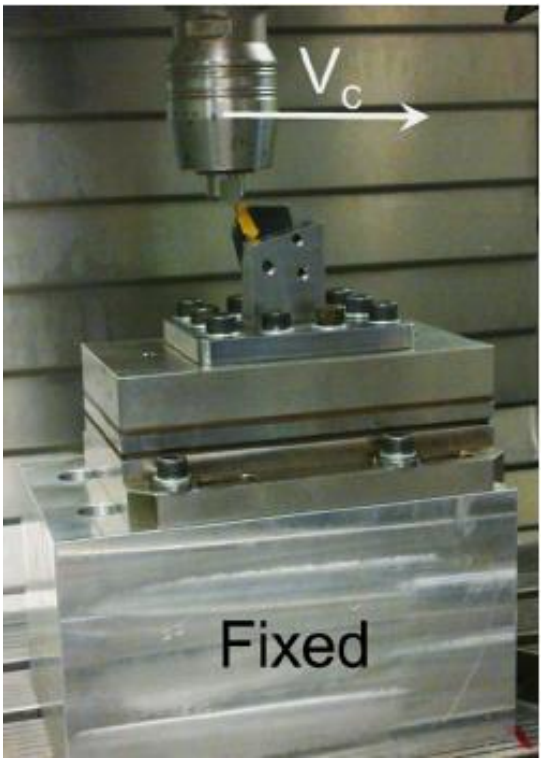

Figure 16. Experimental setup developed by (Ducobu et al. 2016).

2.1.7 Broaching process outputs

After seeing the broaching process study setups. it is important to know the physical variables studied to improve the comprehension of the cutting mechanisms involved during the broaching process. These data indicate the thermomechanical phenomena involved during the cutting operation. They give us information about the tool-material contact (efforts, temperatures, etc.) as well as the chip formation, surface roughness and wear of the tool derived from the interaction of the whole system. They are thus particularly interesting when the broaching operation is considered.

Cutting and feed forces

Most of the studies related to the broaching process presented in this bibliographic synthesis deal directly or indirectly with the characterization of the forces during cutting. Some of them present the development of prediction models more suited to the monitoring of the cutting performance while others focus on the sensitivity of the broaching efforts.

The use of analytical methods for simulation of cutting edges is common. These require little computation resources and are particularly suited to the prediction of cutting forces generated by a defined broach geometry. In addition, the prediction models thus established are easily transferable and usable in the industrial environment.

In general, the cutting force is modelled by the product of the projected cutting area ($a_p \; x \; h$ according to the parameterization described in Figure 17) with the specific force of cut $K_{c,c}$ (see equation 2.2). The variant described in equation 2.3 concerns the prediction of the specified effort in the direction of the feed.

$$F_c = K_{c,c} \; x \; A_c = K_{c,c} \; x \; (a_c \; x \; h) \tag{2.2}$$

$$F_h = K_{c,h} \; x \; A_c = K_{c,h} \; x \; (a_p \; x \; h) \tag{2.3}$$

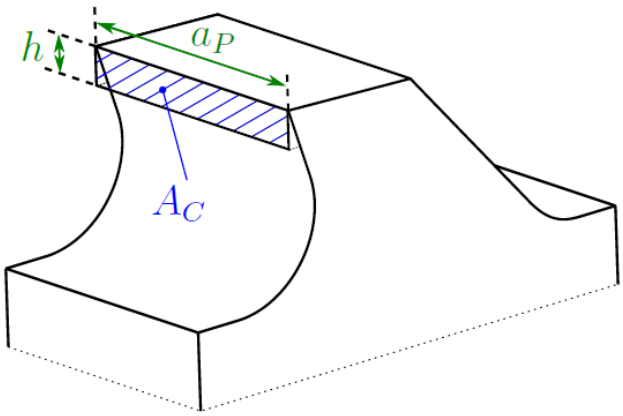

Figure 17. Schematisation of the cutting area (AC).

This method, which is widely used in machining, is for example used by (Schroeter et al. 2007, Sutherland et al. 1997), (Özlü et al. 2010) or (Vogtel et al. 2013) to compare simulated cutting forces with randomized broaching readings. Gilormini et al. used a very closely related model, which decomposes the specific cutting force $K_{c,c}$ into two components, the first fixed to represent the chip formation and the second variable as a function of time to represent its evacuation (Gilormini et al. 1984).

Note also that the specific cutting force $K_{c,c}$ is homogeneous at a pressure and therefore it can be expressed in N/mm^2. But this magnitude can also be considered from an energy point of view as an indicator of the efficiency of a process (energy spent for the removal of a specific material volume), it will then be expressed in J/m^3. A similar energy approach has been used by (Kishawy et al. 2012) in broaching (Figure 18), this one being based on a method of decomposition of the energy speculated by (Astakhov, Xiao 2008) on a filming operation. The results obtained by these latter are presented in Figure 18.

Once the force model is established and validated experimentally, it can be implemented in devices intended for broaching monitoring and aimed at detecting broaching errors. For example, (Mandrile 2014) presents a method to detect broaching errors by comparing the experimental and theoretical cutting forces. It might also be useful for broach designers for the balancing of cutting forces, i.e. performing the same effort all the teeth, like the procedure presented (Vogtel et al. 2013).

If the prediction of broaching variables is useful for the control of the process, the study of the sensitivity of these effects can also improve the understanding of the cutting mechanisms to refine the used cutting conditions to carry out this process.

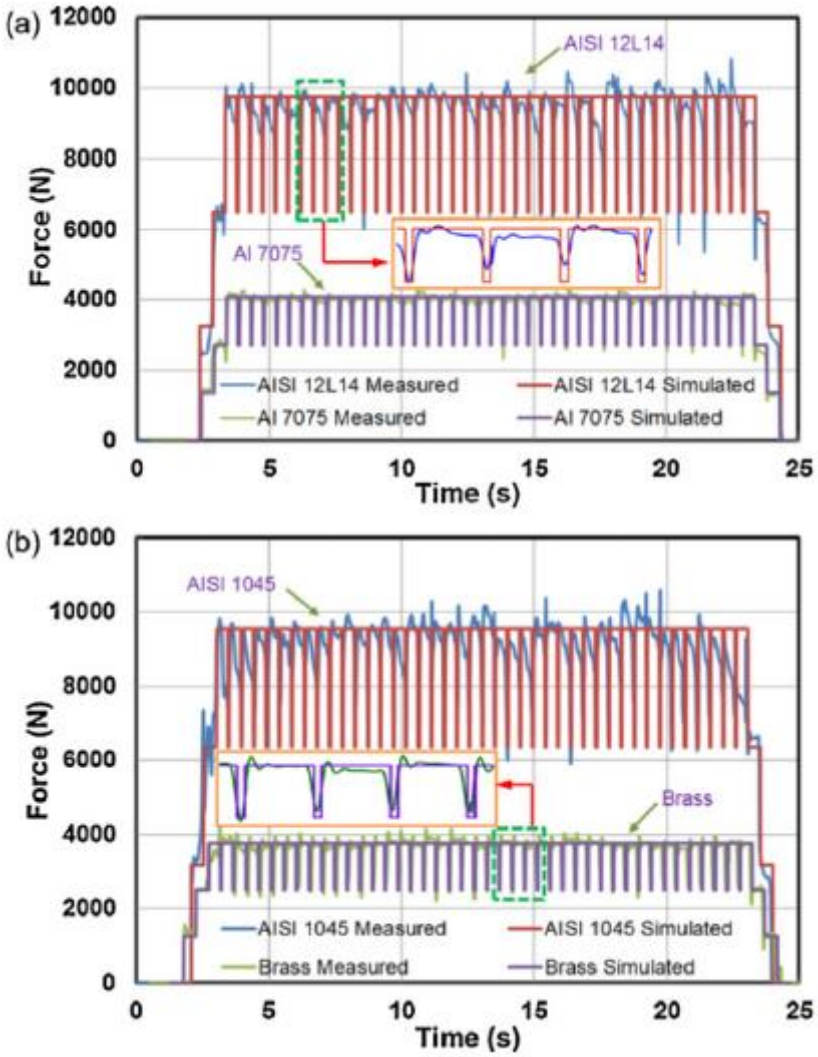

Figure 18. Comparison of simulated and experimental cutting forces during a broaching operation (Kishawy et al. 2012).

Mo et al. investigated the sensitivity of variation in cutting and peaking effects to a few parameters such as progression, velocity and angle of cut, or lubrification (Mo et al. 2005). Thus, the cutting force Fc (noted Fz in Figure 19) is essentially dependent on the progression, if not to a lesser extent, of the cutting angle in the case of titanium alloys. The penetration effort is also dependent on the progression, but also of the rake angle, the lubrication or the cutting speed. Thus, the penetration force carries more information on the movement of the cut than the cutting force, given its increased sensitivity to the variation of the different input variables studied by (Mo et al. 2005).

The importance attributed to the feed on the variation of the cutting force is clearly visible in the formulation of Equation 2.1. On the other hand, the specific cutting force depends

on the progression as defined in the NF E66-520 standard. Thus, an increase in the rise per tooth will result in a smaller increase in the cutting forces, which will result in a decrease in $K_{c,c.}$

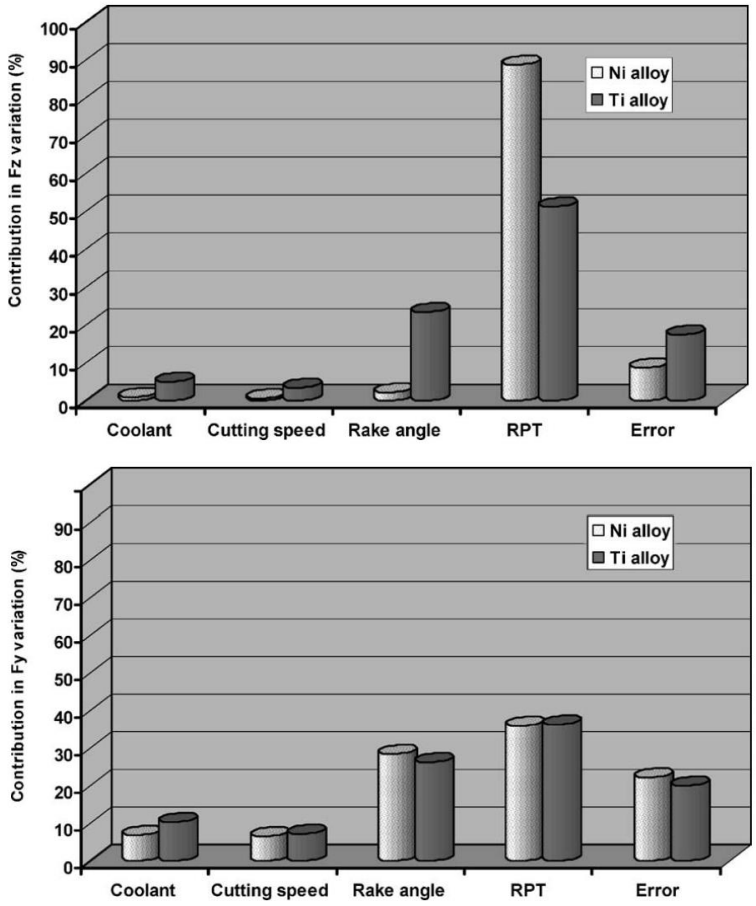

Figure 19. ANOVA study of the variation of cutting force (Fz) and feed (Fy) by (Mo et al. 2005).

The finding of this phenomenon was made by (Schulze et al. 2012) on a C45 steel. In this study, a reduction of the specific cutting force is observed during the increase of the feed. Significant sensitivity to cutting speed efforts has also been observed. The increase in speed between 7 and 50 m/min results in a reduction of the cutting force. A similar observation was made on a lower velocity range (between 1 and 6 m/min) by (Kuljanic 1975) on a 16MnCr5 steel. (Meier et al. 2014) explains this decrease in the observed cutting forces by a thermal softening of the upper brittle material caused by the high temperatures appearing at the interface at high cutting speed. (Klocke et al. 2011) carried out a study on an Inconel 718, showing that increasing the cutting speed from 3 to 10 m/min does not cause any variation in cutting forces, nor even in penetration. This deviation from the previous observations can be explained by the good conservation of the mechanical properties of the Inconel at high temperatures, despising the thermal softening effects at these low cutting speeds.

Forst presented in the broaching handbook (Forst 1973) results related to the variation of cutting and feed forces as a function of the rise per tooth, the cutting speed and also the heat treatment undergone by a C45 steel. As it has been observed in most of the previously mentioned studies, the cutting force tends to decrease slightly as the speed increases. Furthermore, the feed force increases (between 5 and 30 m/min) before decreasing again.

In this study, the higher cutting force observed on an annealed C45 steel is attributed to a higher proportion of ferrite which, although it has lower mechanical properties and this properties lead to a higher chip compression ratio.

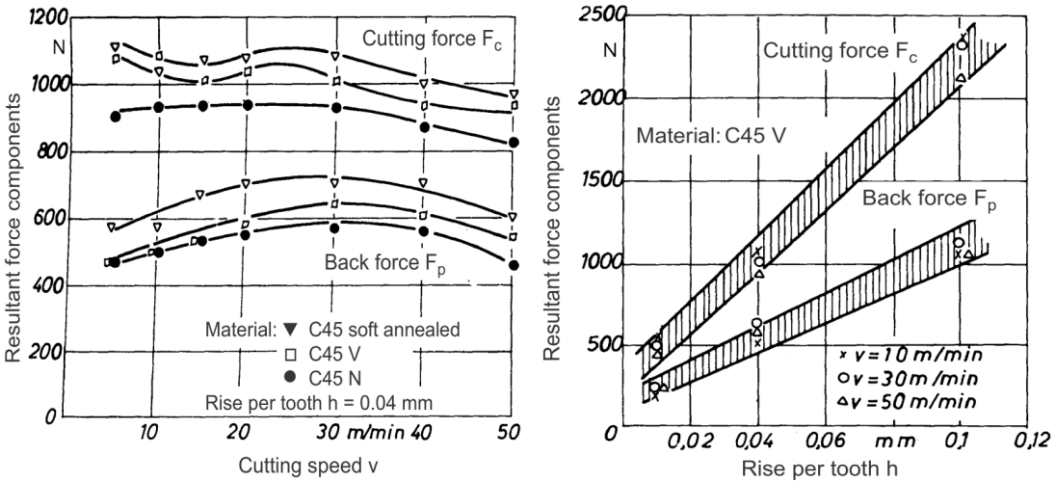

Figure 20. Influence of cutting speed (left) and feed (right) on broaching forces (Forst 1973).

On the contrary, very low differences in terms of cutting forces and high differences in feed forces were obtained by Fabre et al. in their study on the optimization of the surface roughness performed on a X12Cr13 stainless steel (ferritic-martensitic microstructure) (Fabre et al. 2016). They carried out the tests in a wide range of cutting speeds (0.5 – 60 m/min) at the same RPT (h = 0.03 mm) using a HSS tool under lubrication.

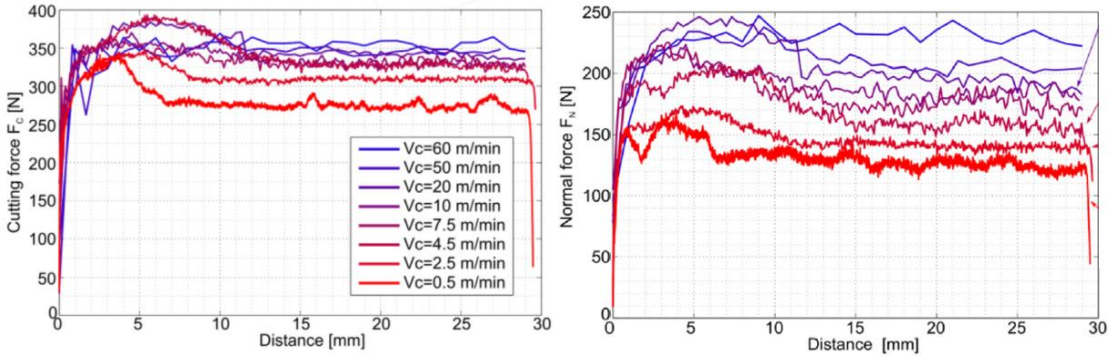

Figure 21. Cutting and feed forces in a wide range of speeds and same RPT on a stainless steel (Fabre et al. 2016).

The condition of the broached material has a significant influence on the cutting forces, the substrate as well as the coating of the tool have also been studied. For example, (Weule et al. 2005) has carried out broaching tests using tools composed of polycrystalline boron nitride (PcBN) having different PcBN concentrations. It seems that the cutting forces tends to decrease when the concentration of PcBN decreases. The influence of TiAlN and AlCrN coatings applied on a carbide tool in broaching was also studied by (Schulze et al. 2012). The cutting forces resulting from TiAlN coated tools are lower on the order of 1/3 to the forces obtained with AlCrN coating.

Thus, the analysis and comparison of average cutting forces on a certain broached length, what has been questioned until present, gives us information on the most favourable conditions for broaching. Particular attention may also be paid to the evolution of the cutting forces during a broaching operation. This work carried out by (Zanger et al. 2014) shows a first phase of generation of higher forces, followed by a stabilization of the cutting forces at a lower level, which is attributed not only to rigidity effects of the machine but also to the modification of the cutting phenomena during broaching. The plunging effect of the tool at the beginning of broaching, reducing the angle of tears and thus increasing the rubbing area is also probably a source of increased forces. (Kong et al. 2011) studied numerical simulation of the influence of chip festooning. A serrated chip is a source of more fluctuations in the cutting force, which is notably attributed to the thermoplastic instability at the secondary shear zone.

In view of the many studies and observations that the cutting efforts have been made, many trends can be identified. The first source of effort variation is progression or feed (RPT). Higher feed will be a source of higher cutting and penetration forces. Similarly, according to the literature, the increase in cutting speed over a range of between 1 and 50 m/min results in the of cases in a reduction in forces. Few works deal with the variation of feed force as a function of the cutting speed, which is partly explained by the difficulty that represents the implementation of the instrumentation effort in that direction. On a C45 steel, in a first phase, feed forces increase when working between 5 and 30 m/min, then from this point up to 50 m/min, the feed forces decrease (Forst 1973).

In the same way, the broaching forces are very sensitive to the state in which the broached material is found. It has become apparent that a material with high chip compression rates (such as ferrite) is a source of great forces, and the mechanical resistance is not the driving property of broaching forces. The material and coating of the broaching tool as well as the lubrication also influences the cutting force. For example, it has been observed that a TiAlN coating has lower cutting forces than an AlCrN coating when broaching SAE 5120 steel.

Roughness

As it is already well known by the reader, a single broaching tool allows to perform the steps of roughing, semi-finishing and finishing. The control of the surface state and roughness in particular is therefore essential in broaching. With the aim of revealing the parameters influencing the roughness resulting from broaching, (Mo et al. 2005) carried out an analysis of the variance involving parameters related to the implementation of the broaching operation. For example, the cutting speed (2 to 6 m/min), the lubricant, or tool design parameters such as progression (from 25 to 80µm, RPT for Rise per tooth in Figure 22) and rake angle (12º to 18º). This study was carried out on Ni and Ti based alloys, it shows the effect of the cutting angle on the arithmetic roughness Ra, followed by the lubricant and progression in 3rd position (Figure 22). In this case, the impact of the cutting speed on the roughness is very weak, but note the reduced range of the used cutting speed.

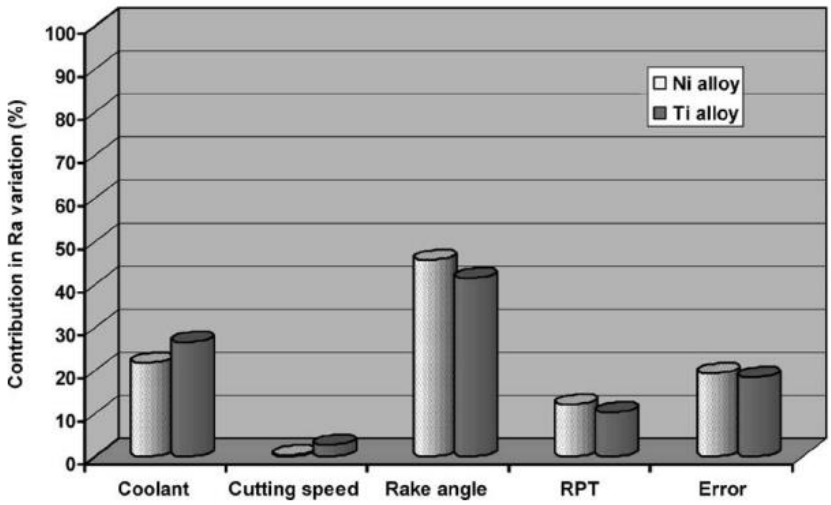

Figure 22. ANOVA study of the Ra variation performed by (Mo et al. 2005).

The sensitivity of the surface state to the cutting angle is also presented in the (Forst 1973). Figure 23 shows the link between the increase of the rake angle and the improvement of the surface state. In this work, no influence of the clearance angle or the edge inclination angle on the roughness or the mechanisms of formation of the arches is reported has not been put in evidence. In contrast, the increase of the acuity of the radius is the cause of deterioration of roughness.

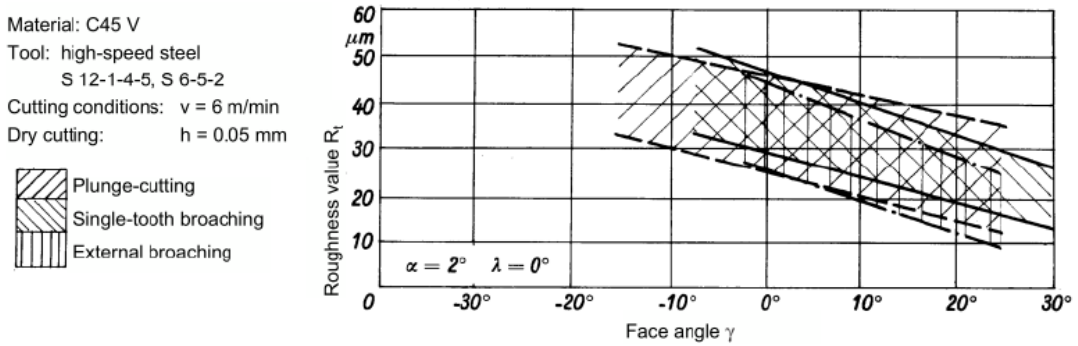

Figure 23. Influence of the rake angle on the surface condition (Forst 1973).

(Zanger et al. 2014) observed a significant influence of the progression on the obtained roughness. The average Ra observed for a progression of 40µm is more than 3 times higher than that observed for a progression of 20µm. In this same study, the profile of a machined surface is dissociated into two zones. In the first phase of broaching, a very smooth surface is generated. This is attributed to the plunging effect of the tooth in the material (and potentially to a sharp decrease in the taper angle). After a few tenths of broached millimetres, the surface state deteriorates sharply until broaching is finished. The vibration coming from the machine structure is implicated, the formation of the chip

along the cutting edge could also be a factor of degradation of the surface state (longer chip → more friction → degraded chip formation).

The negative influence of the increase of progression on the total roughness Rt is also highlighted by the (Forst 1973), especially for cutting speeds of less than 30 m/min. Beyond this, the surface state is much less progression dependent.

The influence of the cutting speed on the roughness of the broached surface has been the subject of many studies. In fact, in most machining processes, the increase in the cutting speed leads to a thermal softening of the part, which causes a decrease in the friction coefficient as shown by (Rech et al. 2013), which has a beneficial effect on the surface state. However, (Kuljanic 1975) for example observed a degradation of Ra between 1 and approximately 3 m/min, followed by an improvement when increasing the speed up to 6 m/min during the broaching of a 16MnCr5 steel. This seems to be related to the very low cutting speeds studied, which are generally proscribed in machining and appearing outside the speed ranges tested in the previously mentioned friction coefficient study.

When higher cutting speeds are studied, we find the effect of this speed increase on roughness. Weule et al. (2005) observed this when dry-grinding XC48 steel with a high-speed steel tool. They used a cutting speed range of 15 to 105 m/min (Rz parameter study shown on Figure 24). In addition, the study of the impact of the use of PcBN tools on the surface state allowed us to determine that the PcBN concentration of the tool has a significant influence on the results of surface condition although no clear trend can be demonstrated.

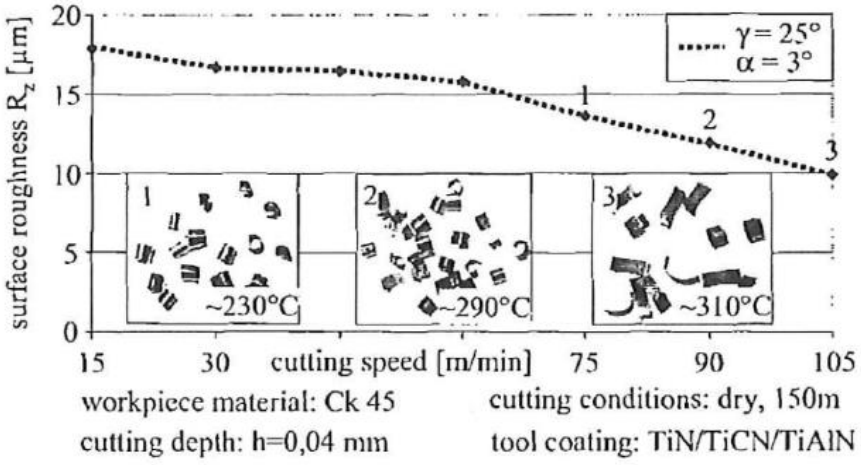

Figure 24. Evolution of roughness Rz with cutting speed (Weule et al. 2005).

Similarly, Schulze et al. showed the improvement of roughness when increasing the cutting speed from 10 to 50 m/min, with however a degradation of Ra during the transition of a speed of 7 to 10 m/min under whole oil over a 20MnCr5 steel (Schulze, Boev et al. 2012). During this study, no influence of the coating (TiAlN or AlCrN) on roughness could

be demonstrated, and the use of oil does not allow a significant improvement on the roughness compared to the dry tests. These latter findings tend even to be a source of a weaker roughness under strong progression (h = 60µm).

A study conducted by Meier et al. using carbide tools cutting at very high speeds (between 60 and 100 m/min) has brought to light the stability of the parameter of roughness Ra during the cutting speed variation in hard broaching (Meier et al. 2014). This study also highlighted the lack of effects of the thermochemical heat treatment undergone by the tool on the roughness Ra of the broached surface.

Fabre et al. performed a thorough study on the sensitivity of the evolution of the surface quality in broaching bearing in mind several parameters such as the tool design, the cutting conditions and the workpiece material (Fabre et al. 2016). They proved that the worst roughness were obtained at lowest speed and highest rise per tooth on ferritic, ferritic-martensitic and martensitic inox steels. The increase of the rake angle and the lubrication were proved positive for the surface roughness improvement.

The (Forst 1973) shows the influence of cutting edges on roughness after broaching. An increase in roughness is observed between 2 and 10 µm whereas this is significantly improved up to 50 µm (Figure 25).

In this study, a link is proposed between the sulphur content in the cobbled material and the surface state. The increase in the sulphur content is responsible for a significant improvement in the broached surface state. The improvement in machinability induced by a sulphur composition between 0.15 and 0.35% is currently accepted in machining (Le Calvez et al. 2003). In addition, an improvement in surface state has been observed during the broaching of materials having a finer microstructure (grain size, interlamellar space). The chip compression ratio also appears to be an indicator of the geometrical surface state, the higher chip compression rates coinciding with the lower roughness obtained.

To conclude, it has been seen through the previously mentioned studies the demonstration of the strong dependence of the roughness on the progression and rake angle. Numerous studies show that the influence of cutting speed have less obvious results. Generally, an increase in cutting speed tends to improve roughness. However, at a low cutting speed (less than 10 m/min) different results may appear, several studies indicate an improvement in roughness at the same time in both at high and low speeds. The few works dealing with the coating of tools or lubrication show a significant sensitivity of the roughness to these parameters. At last, there are some works analysing the contribution of the microstructure to surface state but there is not any research reporting the contribution of the FP steel's microstructure to the roughness.

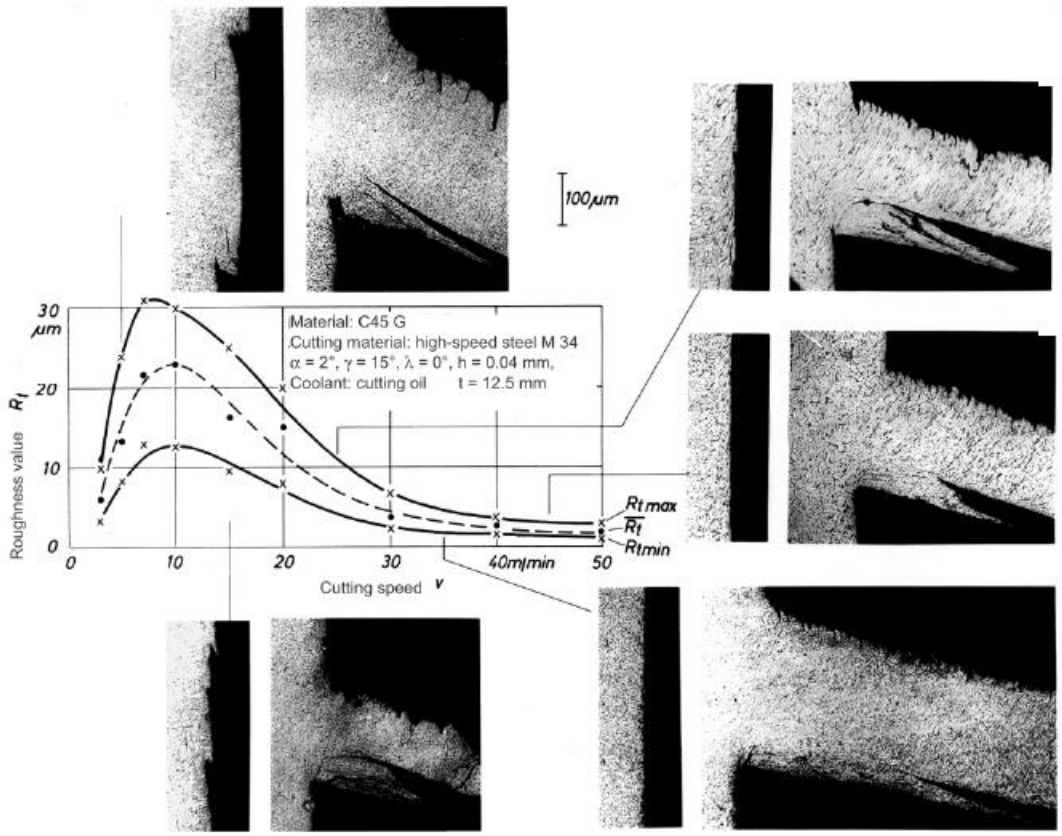

Figure 25. Roughness evolution with cutting speed (Forst 1973).

Temperatures

During the Cutting and feed forces it was seen a tendency to reduce cutting forces with the increase in speed, which is mainly due to thermal softening phenomena at the tool/material interface. The link between cutting speed and temperature at the interface is confirmed by (Kong et al. 2011) or (Vogtel et al. 2013) using experimental tests and

numerical models. This proves that the temperature has an influence on the cutting mechanisms and indirectly on the quality and productivity of the process.

Indeed, the need to maintain a limited temperature at the cutting edge is one of the fundamental reasons for the very low cutting speeds generally used. The broaches are mainly made of high-speed steel. However, their mechanical properties deteriorate rapidly as soon as their temperature reaches values that are too high, their range of use being reduced to a few hundred degrees Celsius as shown in Figure 26 from the ASM Handbook (Handbook 1990).

It is therefore necessary to control the parameters responsible for the rise in temperature during cutting. Thus, speed is indeed a factor of first order to be taken into consideration. However, other variables such as the feed or the lubrication method also influence the temperature rise in the cutting zone. The role of these parameters is presented in Figure 27 from the (Forst 1973).

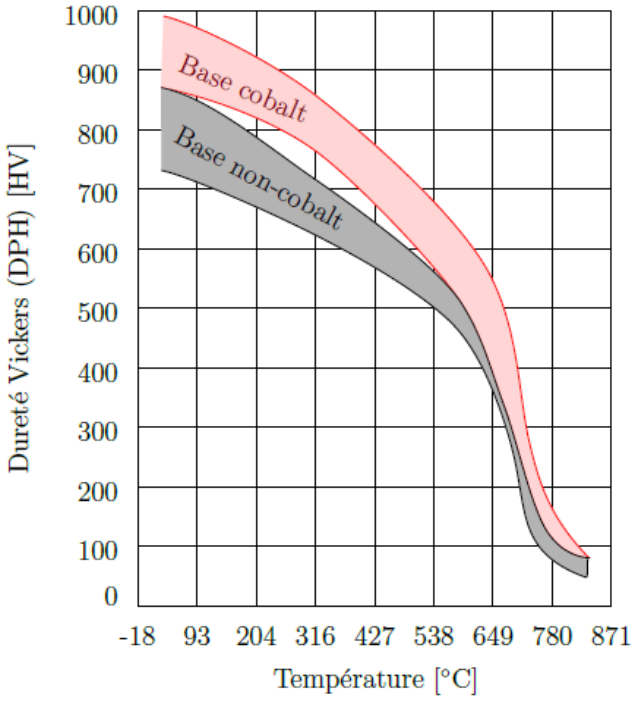

Figure 26. Evolution of hardness versus temperature of high-speed steels (Handbook 1990).

It is noted that the temperatures observed under emulsion are lower than those obtained under straight oil. The friction coefficient obtained under straight oil is inferior to that obtained by emulsion according to (Rech et al. 2013). We can deduce that the emulsion possesses a better thermal evacuation capacity than the straight oil (this being notably attributed to a better coefficient of heat exchange between the cutting zone and the water contained in the emulsion with the oil).

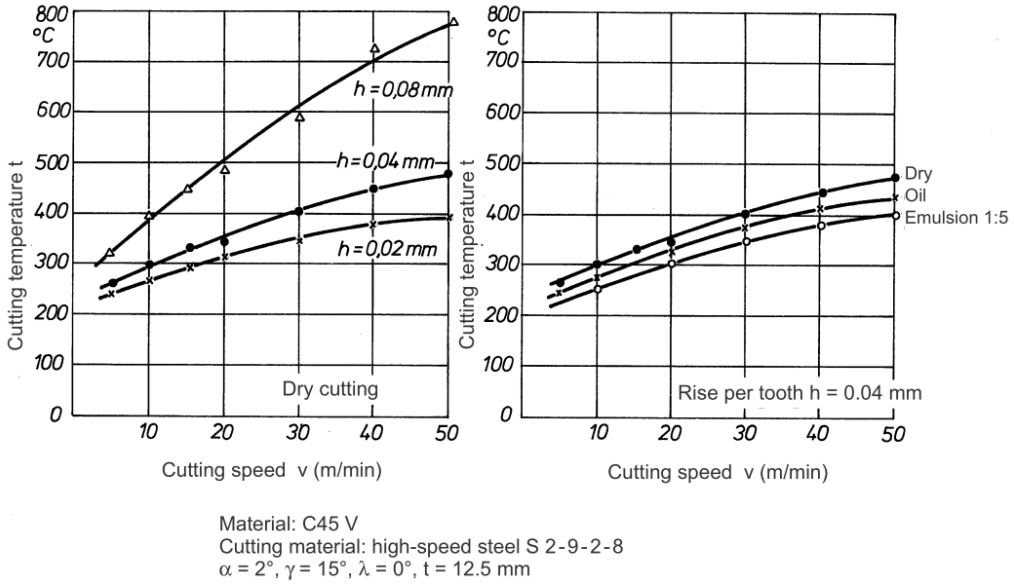

Figure 27. Influence of cutting speed, progression and mode of lubrication on the temperatures of the cutting zone in broaching (Forst 1973).

If at the local scale of the cutting area, the increase in cutting speed is synonymous with thermal evaporation, the trend can be very different when considering stitched in its entirety. In order to understand better the thermal effects induced by a cutting operation, it is more relevant to consider the notion of heat than that of temperature. Indeed, the heat flow depends on the cutting conditions; the increase in cutting speed thus results in an increase in the heat flow. However, as presented in equation 2.3, the final temperature is a function of the heat flow Φ_{heat}, but also the duration of its application Δt.

$$T_{final} = T_{initial} + \frac{\Phi_{heat}\, x\, \Delta_t}{m\, x\, C_p} \quad (2.3)$$

Thus, the increase in velocity is at the origin of a heat flux generated at the tool material interface as proved experimentally by (Courbon 2011). It also generates a reduction in the duration of application of this flux, which can result in an increase in overall temperature of the larger piece at low speed. This has been observed by (Bejnoud et al. 2015) using thermal camera measurements. Note, however, that this phenomenon is dependent on the duration of the broaching, as well as the number of passes realized in a limited time on the same piece. Indeed, (Klocke, Kuchle 2011) noticed that the temperature rise caused by the succession of teeth is more important as the cutting speed increases. Broaching in a replicated manner and with a single piece by means of tools with many teeth will probably result in a significant increase in the temperature of that piece.

To ensure that the integrity of the tool is maintained during the operation broaching, (Klocke et al. 2014) analysed the evolution of temperature on the cutting tool. In view of the very low progressions and cutting speeds, he noted significant discrepancies

between the temperature distributions calculated theoretically by the Komanduri and Hou model (Komanduri, Hou 2000, Komanduri, Hou 2001a, Komanduri, Hou 2001b), and experimental measurements by thermal camera. The author has therefore developed a new analytical model for the prediction of the temperatures encountered in the tool, adapted to the cutting conditions encountered in broaching. This model can thus be used to determine critical broaching conditions for the integrity of cutting edges.

> In conclusion, the importance of the temperature rise resulting from a broaching operation is high from the point of view of the cutting as well as the tool life. Indeed, it is favourable to the thermal softening of the material taking with it the reduction of the cutting forces. Nevertheless, it can be also harmful affecting the resistance of the high-speed steel, which is the most common material of broaches manufacturing. Thus, the literature shows the impact of the cutting speed, the feed or the lubrication on the evolution of the temperature, as well as at the level of cutting edge and on the broached piece in its entirety.

Chip morphology

A first element of study concerns the notion of formation and winding of the chip. Indeed, the broaching is a closed process, which generates a chip in a confined space that must be dimensioned to ensure proper operation of the tool. The mastering of the formation, the winding and the evacuation of the chip allows the broach manufacturer to ensure the proper geometrical dimensioning of the tool designed.

This has been already discussed in (page 39) dealing with sizing of the chip chamber. The geometry of the tool is the main element which has an impact on the formation and the winding of the chip. In the case of a nickel-based alloy GH4169, (Kong et al. 2011) studied the influence of the cutting angle on the adiabatic shear bands formation (as in the example shown in Figure 28). It represents a broaching operation at very high speed (250 m/min) and shows a higher serrated chip (Figure 28) as the cutting angle is reduced. Under these conditions, the chip is substantially continuous when the cutting angle is greater than 15°.

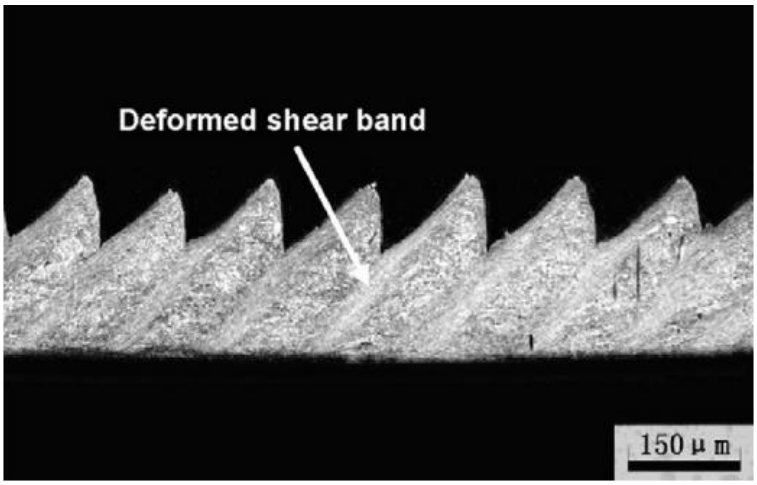

Figure 28. Serrated chip example by (Duan, Zhang 2012).

With the aim of characterizing the importance of serrated chips, Vogtel et al. (Vogtel et al. 2013) uses an indicator characterized by the ratio between the maximum thickness (peak of the chip saw) and the minimum thickness (pit of the chip saw); chip serration ratio (h_{max}/h_{min}). For a speed range between 10 and 50 m/min, if there is no clear trend identifiable, the experimental study of the feed increasing between 20 and 100 µm seems to be favourable to a serration rate increase.

Chip control is essential in broaching, its structure and shape being effective indicators of the design quality of a tool. They can also be used as physical indicators of the flow of the cut, by providing information on the thermomechanical loadings involved during the machining operation.

In broaching, a continuous and long chip is preferable as its interaction with the following teeth can be limited. Small fragmented chips could indeed be easily blocked between one of the cutting edges and the material, for example at the side of a tooth, which would have disastrous consequences on the surface state. The appearance of adiabatic shear bands may increase the propensity for chip breakage as explained (Mabrouki et al. 2008). This explains the high cutting angle values that are commonly found in broaching limiting this way the appearance of sagging.

If the continuity of the chip is essential for the proper course of the cut, its winding radius is determined by the geometry of the broach. The latter is directly related to the volume that the chip will occupy after broaching, and therefore to the volume that must be able to contain the chip chamber. No study deals directly with the volume occupied by the chip after broaching, but some of them focus on parameters strongly related to this winding such as shear angle. (Schulze et al. 2013) present for example the simulation of the evolution of this angle during the plunge of a tooth in the material at different feeds, but for the same cutting speed. This is shown in Figure 29.

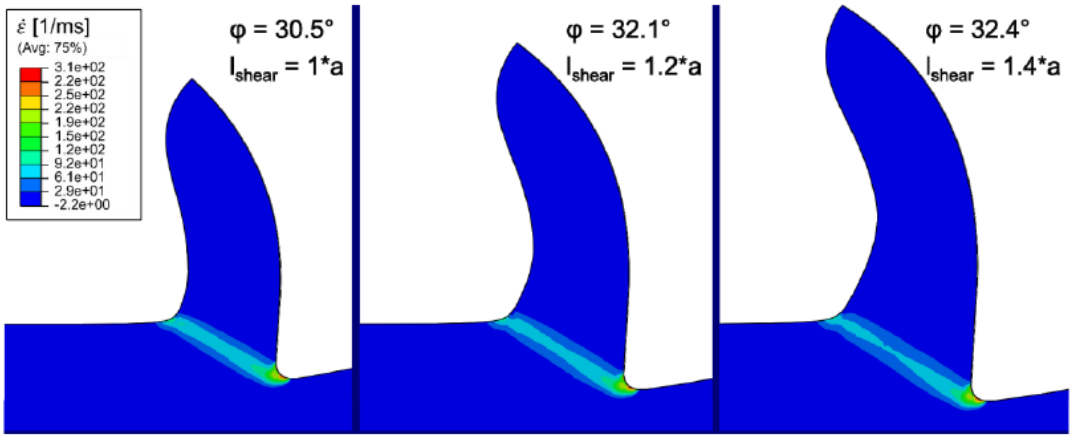

Figure 29. Shear angles observed for various depths (from shallow to deep left to right) (Schulze et al. 2013).

A greater depth is obtained in this study at a larger shear angle, and thus potentially in a larger chip winding radius. By analogy, it could be deduced that a greater progression is at the origin of a larger shear angle, and therefore of a winding radius also greater; the created chip will thus occupy more volume, requiring a larger chip chamber. The experimental observation of this increase in winding radius with the progression was carried out by (Schulze et al. 2012) on a 20MnCr5 steel between feeds of 40 and 60µm. The influence of a large chip winding radius on the cutting edge was observed by (Mandrile 2014). The latter estimates that an increase in the winding diameter is at the origin of an additional effort caused by the friction of the chip on the cutting face of the order of 40%, which encourages again to aim at a reduction of this radius of winding.
(Schulze et al. 2012) also observed an increase in chip winding radius with cutting speed increase ranging from 7 to 50 m/min. In addition, it has been found that during dry broaching, a TiAlN coated tool is a source of more coiled chips than an AlCrN tool. The same tests carried out under whole oil reveal a different trend, the dependence between winding diameter and tool coating is no longer as significant. These observations are presented in Figure 30. Based on the results presented in the section Cutting and feed forces where a decrease in cutting effort appeared when using TiAlN tools (compared to AlCrN tools), it is possible to assume that the friction coefficient is lower with TiAlN than with AlCrN. Thus, the reduction of the winding radius passes through the reduction of the coefficient of friction between the tool and the material, which can also be allowed by a lubrication adapted as it has been previously observed.

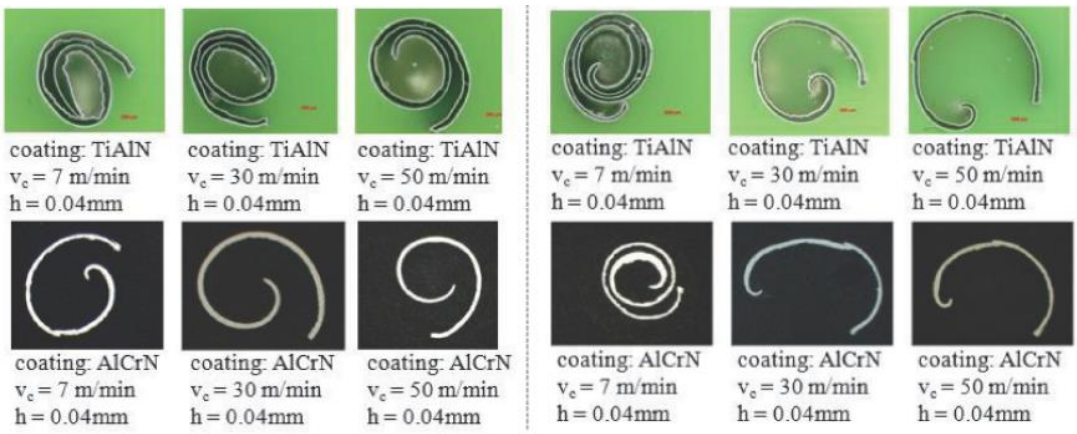

Figure 30. Chips observed in dry (left) and whole oil (right) cutting tests (Schulze et al. 2012).

Finally, the influence of both the cutting speed and the microstructural state of a C45 steel on chip formation mechanisms is presented in the (Forst 1973) (C45N: normalized, C45V: tempered). Figure 31 shows the need to reduce the cutting speed in order to reduce the curling of the chip (which is favourable for a better evacuation). Moreover, the curling is also strongly dependent on the microstructural state, a mildly annealed C45 steel (then highly concentrated in ferrite) is at the origin of poorly wound chips.

Through the studies carried out around the chip formation, it has been seen that the generation of a continuous chip is preferable in broaching. To limit the risk of chip segmentation, it is particularly appropriate to reduce the serrating phenomena, which requires the use of high cutting angles, generally greater than 15º.

Obtaining a continuous chip is essential to limit the risk of blocking what would result in surface degradation. If the chip blocking is a first order risk, the dimensioning of the chamber intended to receive this chip is also essential. It should also be noted that the diameter of the chip curling (directly related to the apparent chip volume after broaching) depends on the progression, the cutting speed and the friction at the tool/chip interface.

According to the literature, the chip will be more curled when the cutting speed, the progression and the friction coefficient are low. The microstructure of the broached material also has a significant influence on chip curling.

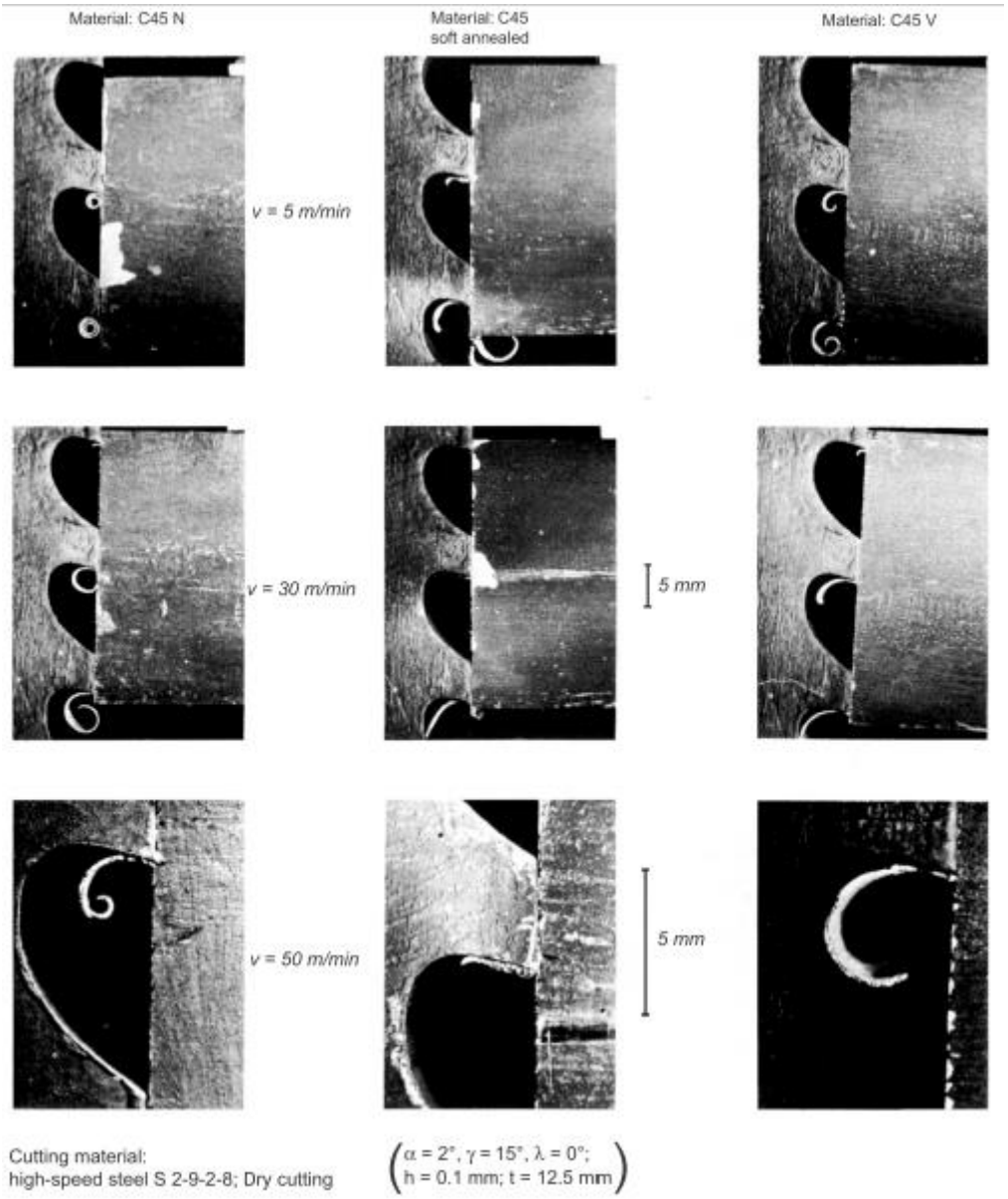

Figure 31. Influence of cutting speed and microstructure on the chip curling (Forst 1973).

Wear of the broaching tool

In broaching as in any cutting process, the resistance to wear of a tool is an essential criterion, which can even be imposed contractually by the user. from the pin manufacturer. This results for example in a minimum of broaching cycles. In machining, most tool wear simulation models are dependent on the thermomechanical loadings applied to the tool (temperature, pressure, etc.). A summary of the various current wear patterns is proposed by (Yen et al. 2004) . In broaching, the very low cutting speeds and progressions associated with the very sharp cutting angles are at the origin of wear modes.

(Mo et al. 2005), for example, investigated the evolution of tool wear when broaching nickel and titanium alloys using high-speed steel tools under two conditions; a first not

very demanding (high cutting angle, low speeds and progressions) and a second more severe. No significant differences in wear between these two conditions have been identified. However, the analysis of post-wear broaching teeth in a nickel alloy reveals the distinction of three zones (Figure 32 left):

- Very close to the edge, the tool material is worn but the tangential forces raised in this area not allowing the nickel to adhere to the tool;
- Moving slightly away, there is a zone of strong adhesion of the nickel on the tool, with a strip of nickel deposition;
- The last zone corresponds to the material that did not encounter the piece and therefore not worn.

In the case of the titanium alloy, the adhesion of the material stitched on the tool is less important; there are only a few very localized zones of adhesion of the material on the face of the tusk of the tool (Figure 32 right).

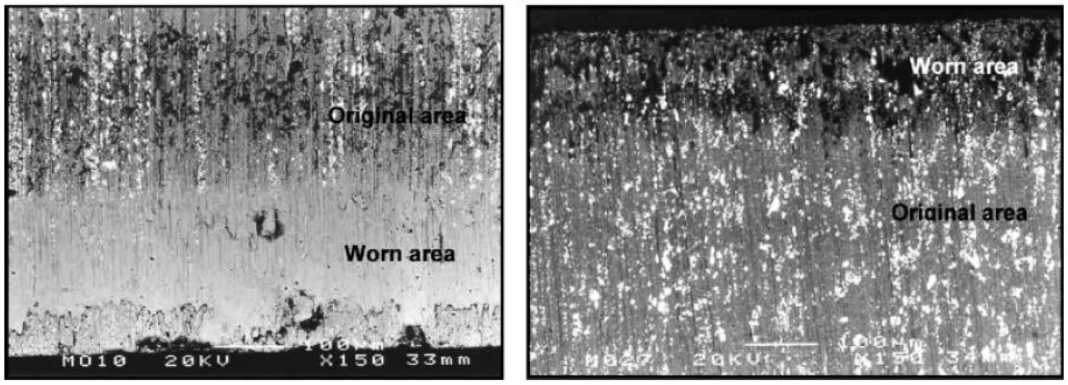

Figure 32. SEM image of the clearance of a tool after alloy wear tests nickel (left) and titanium (right) (Mo et al. 2005)].

Although little influence of loading conditions on tool wear has been observed in this study, (Weule et al. 2005) showed different wear patterns when XC48 steel was broached for two different cutting speeds, using high-speed steel tools (see Figure 33). Note that the speeds used correspond to the high range of the speeds that can be found in broaching.

Thus, during the first 5 broached meters, the wear increases very fast at low cutting speed, then this wear speed decreases and stabilizes up to about 70 m broached meters before increasing again. On the other hand, the wear speed at high cutting speed is constant, and overall higher at 80 m/min than at 30 m/min. This proves that the mechanisms of wear at low speed are different from those encountered at high speed.

The (Forst 1973) presents a comparison of wear levels observed during broaching using high-speed steel and carbide tools. It thus appears that a carbide tool has much lower

wear levels despite a higher wear rate for the carbide tool from about 70 m broaches on a C45 steel (see Figure 34).

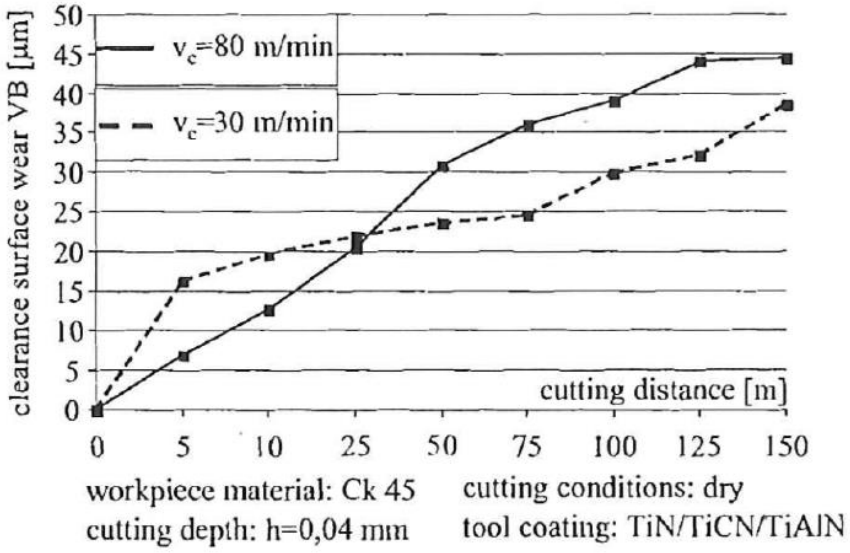

Figure 33. Wear curves of a HSS tool over a C45 for two cutting speeds (Weule et al. 2005).

To limit the influence of wear, three levels can be considered. The first one is to study the parameters influencing the wear and optimization of these parameters during experimental reference tests, then the extrapolation of these results to the broach production. This is the study level discussed in the preceding few paragraphs. The second level concerns the monitoring of forces with the aim of detecting in advance the production of these signs of wear. A third level concerns the monitoring in real time and production situation of the level of wear. If this proves to be possible with the processes involving only one cutting edge, the multiplicity of the teeth and their observed form in broaching makes this monitoring particularly complex. In addition, the wear criteria that are generally used in machining have high variability, associated with the methods and means of measurement as well as with the sensitivity of the operator carrying out the measurement.

With the aim of making the systemisation of tool wear monitoring during the production, (Loizou et al. 2015) propose the use of a different wear criterion to the VB wear generally used for the characterization of wear in machining; i.e. measurement of worn area. In fact, the various tests carried out show a much better stability and replaceability of this criterion of area used compared to the VB.

An optical measuring bench adapted to the broaches has been developed and it is presented in this work. The implemented device consists in the use of a high-resolution camera associated with a telescopic objective. This makes it possible to obtain an image of a specific tooth of the broach. This image is resized to identify the position of the

broach, then filtered, passed in grayscale and cleaned, to extract the image of the worn area.

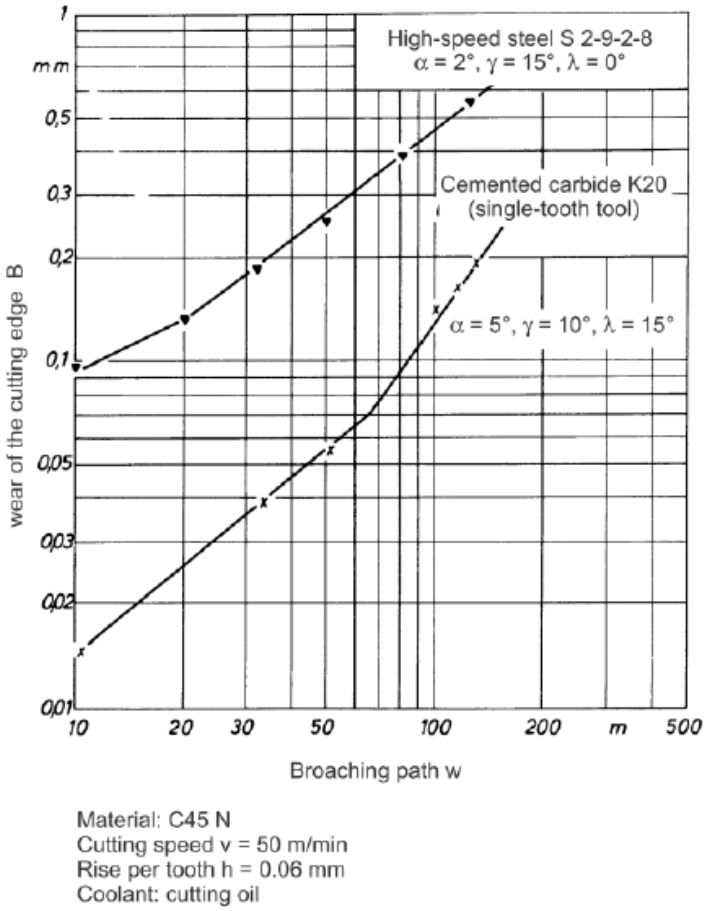

Figure 34. Wear levels observed for a high-speed steel and carbide tool (Forst 1973).

Shi and Gindy developed a method to predict the broach wear based on new techniques of automatic learning modelling (Shi, Gindy 2007). The comparison of the results obtained from this prediction method with those obtained experimentally reveals a very high degree of reliability of the developed model.

Through the presentation of these few studies dealing with broaching wear, three levels of analysis have been dissociated.

It is first possible to observe the evolution of this wear in the early stages of the production operation. This can be done on a test bench extrapolating the results to the industrial operating conditions. Thus, the studies carried out show a weak influence of the severity of the cutting conditions (speeds, progression, cutting angle, etc.) on the rapidity of evolution of the wear. However, it is observed a higher wear rate when using higher cutting speeds. In addition, the durability of carbide tools is higher than that of high-speed steel tools.

The control of wear can also be done by monitoring physical indicators such as stresses, vibrations or temperature, to identify critical levels indicative of too much wear to making the decision of changing or reusing the tool.

For cases where tool wear is a first order factor, a control of production situation of this wear can be considered. In view of the complexity of this task (many teeth with variable geometry, etc.), special and automated measuring tools have been developed. This has been done based on the measurement of wear area derived from the measurement of VB but allowing a better repetitiveness and representatively of wear of the tool. In the future, these detection methods will be able to rely on more and more reliable wear rate prediction models to detect, for example, abnormal rapid wear, which may result from defects in tool design, material composition, etc.

2.1.8 Conclusions

In this chapter, a synthesis of the results from the scientific experimental studies on broaching has been proposed. Several observations could be made according to the different output parameters studied. Thus, an improvement in roughness generally results from an increase in cutting angle or cutting speed. The results obtained at a very low speed (<5 m/min) are relatively variable and depend on the operating conditions (material and microstructural state, coating, lubrication, etc.). The mechanisms at the origin of such variations in surface state at low cutting speeds remain poorly understood. Regarding the chip forming, essential part of the broaching process, many trends have been seen throughout the read papers. Thus, an increase in progression tends to increase the curling radius of the generated chips. Likewise, a higher cutting speed will

be at the origin of less curled chips i.e. the higher is the speed the more open will be the chip. However, the studied velocity ranges remain high (>7 m/min) and the mechanisms responsible for this curling are poorly improved.

Moreover, the results observed are very dependent on the material and the operating conditions, each broaching operation therefore possesses specific characteristics.

Thus, as no study of the influence of ferrito-pearlitic steels on several broaching physical outputs (forces, roughness and chip formation) has been reported, the present work would cover an important spot in the scientific literature. Moreover, considering the microstructure at such scale appears fundamental and has to be investigated.

This study, presented in the following subsections, aims to improve the fundamental understanding of the cutting mechanisms involved when working with an elementary broaching tooth in conditions similar to those used in industrial broaching.

Chapter 3

MATERIAL CHARACTERIZATION

3 MATERIAL CHARACTERIZATION

In this chapter the 16 steels that will be used throughout the development of the PhD will be presented. After a short introduction, the analysis carried out will be explained:

1. FP steel variants manufacturing (made by ASCO and GERDAU)
2. FP steels manufacturing and Microstructure analysis.
3. Thermal characterization
4. Flow stress

Introduction to the ferritic-pearlitic steels

The material to analyse in this project is focused in the low-medium carbon content steels which microstructure is ferritic-pearlitic (hereinafter FP steel). As explained in the introduction, this kind of steels are widely used in the automotive industry where the machining is a quite habitual operation: turning, milling, drilling, broaching...

3.1.1 Composition

The FP steel is an iron alloy composed with a carbon quantity variable between 0.025% and 0.83% in mass of its composition, depending on the grade. The cooling to a hypo-eutectoid temperature generates the FP steel microstructure. This kind of microstructure consist basically on pearlite “islands” (hard phase) embedded in a ferrite matrix (soft phase). On the Table 3 are summarized the typical compositions:

Table 3. Typical steel and alloy compositions (Callister, Rethwisch 2011).

C (Carbon)	Fe (Iron)	Mn (Manganese)	P (Phosphorous)	S (Sulphur)	Ni (Nickel)	Mo (Molybdenum)	Si (Silicon)
0.025-0.83	98-99	0.45-0.75	0.01-0.02	0.01-0.025	0-3.5	0-0.25	0-0.25

Ferrite

Ferrite is, α-Fe, which is stable iron under standard conditions has BCC crystal structure as explained in Callister’s book (Callister, Rethwisch 2011). Its strength is 280 N/mm^2 and its hardness of approximately 200 HB.

Mild steels are mostly composed by ferrite (Figure 35) and as long as the carbon content is increased, pearlite content increases as well. The amount of ferrite will depend on the cooling processes; the iron-carbon alloy undergoes as it cools from liquid state.

Pearlite

Pearlite, as it can be seen in Figure 35, is a lamellar (it can be spheroidal though), two-phased structure composed by layers of alpha ferrite and cementite (under an optical microscope it can be detected due to its appearance, lamellar bands). Pearlite is formed

during sufficiently slow cooling in an iron-carbon system at the eutectoid point in the Fe-C phase diagram (723 °C, eutectoid temperature). In a pure Fe-C alloy it contains about 88% ferrite and 12% cementite. Pearlite is known for being tough and, when highly deformed, extremely strong.

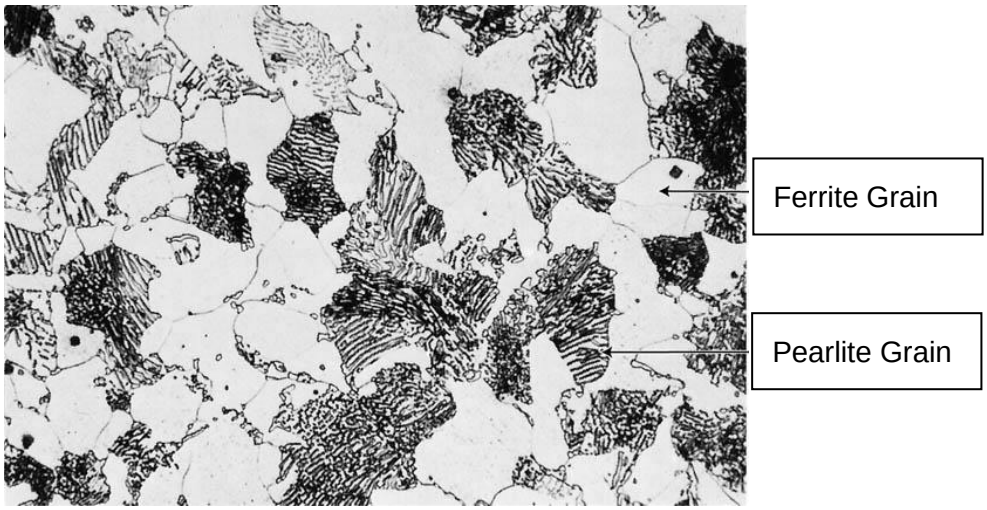

Figure 35. Ferrite and pearlite (Callister, Rethwisch 2011)

3.1.2 Mechanical and thermal properties

The mechanical properties of the steels are dependent of their microstructural features as it was found in the ASM Handbook (A. Handbook 1990). The microstructural features are dependent of the C content as well as on the heat treatment applied to manufacture the steel. From the ferrite and pearlite's point of view, this is what it has been found during the scooping of the literature review:

- The lower is ferrite's grain size yield strength and material's toughness increases. However, a bigger grain size makes the steel more ductile and improves the ductile-brittle transition (Handbook 1990).
- From the pearlite side, the main factor are the cementite lamellas which are very hard and brittle. Obtaining a lower interlamellar spacing (increasing the eutectoid cooling) it is obtained a higher yield strength and a toughness decrease.
- Pearlite's yield strength, as well as hardness, is variable depending on the cementite's interlamellar spacing. In this case, as the interlamellar spacing increases the yield strength's value increases (Clayton, Danks 1990). In the Figure 36 it can be seen how varies the hardness of an FP steel depending on the interlamellar spacing.

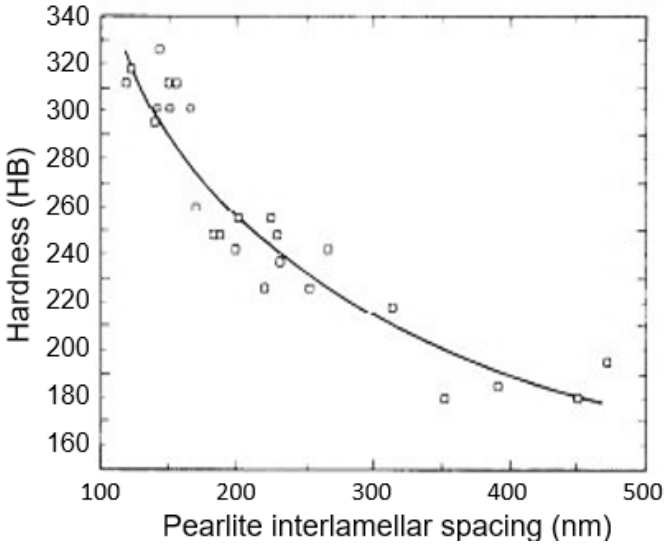

Figure 36. Hardness versus pearlite's interlamellar spacing (Clayton, Danks 1990).

Precisely, the strength in the case of the FP steels is determined by the distance between pearlite's lamellas and it becomes more and more important as the pearlite quantity is increased. With the combination of both phases, it is possible to obtain higher fracture stress values and higher hardening values due to deformation than other materials with the same creep resistance (Sandvik Coromant (Firm) 1994).

In the Table 4 there are shown each phase's properties:

Table 4. Physical properties of each phase (Handbook 1990, Abouridouane et al. 2012).

Phase	Density	Thermal conductivity	Thermal expansion	Specific heat	Yield strength	Young modulus	Hardness
	10^3kg/m^3	W/m·K	µm/m·K	J/kg·K	MPa	GPa	HB
Ferrite	7.86	70-80	11.2-15.3	461-603	546	210	80
Pearlite	7.78	50	10.6-15.3	461-603	750	210	180-320

Ferritic-pearlitic steels manufacturing

The main objective of this section is to explain how the FP steels have been manufactured by applying heat treatments. In this way, different microstructures and hardness have been obtained even if they have the same chemical composition. This step enables to carry out the experimental essays and analyse the results in terms of microstructural features. This work was completely performed by the steelmakers involved in the development of this PhD, from one side ASCOmetal (Metz, France) and from the other side Gerdau (Bilbao, Spain)**.** This part of the work is being shown to the reader, so they can see how the steels were manufactured and then better understand where the differences between variants of the same steel grade come from.

3.1.3 Metallurgical characterization

With the aim of covering a wide range of FP steels, 5 steel grades were chosen: 16MnCr5, 27MnCr5, C45, C60 and C70. The most changing composition parameters were, from steel to steel, besides the carbon content, the manganese (Mn) and the chromium (Cr). The manufacturing of the proposed grades was divided between two steelmakers: ASCO and GERDAU. The former manufactured the 16MnCr5 and the 27MnCr5 and whereas the latter manufactured the C45 and the C60. Finally, it was also added the grade C70 (97% pearlite), to the bunch of steels manufactured and heat treated by ASCO.

Due to the high carbon content of grade C60, it was not possible to manufacture the more bands variant (WB), because the ferrite amount was not enough to create the desired bands. Table 5 shows the different variants with their corresponding colour code and shape given at the time of plotting the results:

Table 5. Codification of the different studied steel variants.

Steel grades		Microstructure status			
		Standard (Reference) ○	Coarse pearlite Grain ◊	Globular Pearlite Δ	More Banded ☐
	16MnCr5	16R	16CG	16GP	16WB
	27MnCr5	27R	27CG	27GP	27WB
	C45	45R	45CG	45GP	45WB
	C60	60R	60CG	60GP	-
	C70	70R	-	-	-

3.1.4 Overview of manufactured variants

A schematic representation of heat treatments performed for obtaining the variants is given in the Figure 37 below.

- Standard variants are obtained with isothermal annealing.
- Globular perlite is obtained using a subsequent globular annealing.
- Coarse grain is obtained using an elevated austenitization temperature.
- Wide bands are obtained using a slow cooling between austenitization and isothermal annealing.

All the steel grades with its variants were supplied in bars of 0.5m length and Ø65mm diameter in except of the C70R that it came in 0.3m and Ø30mm diameter bar.

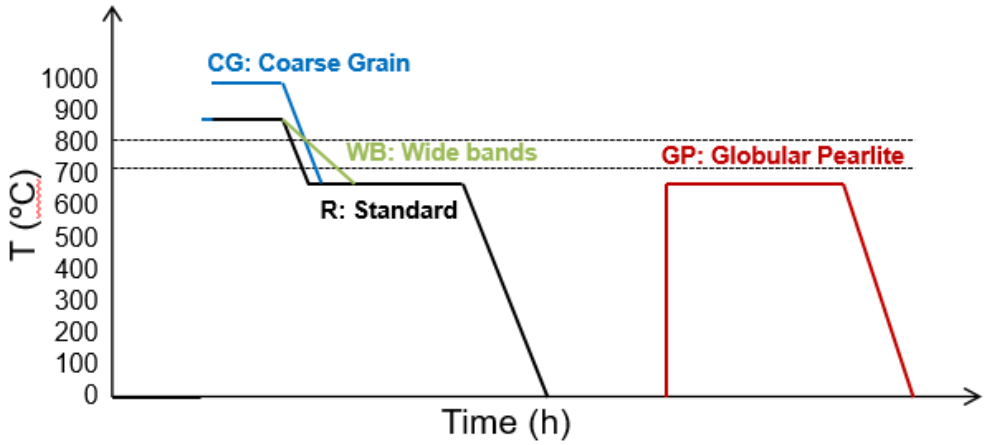

Figure 37. Schematic representation of the heat treatment performed to obtain the variants.

Manufacturing of the R (reference) variants

For grades 16MnCr5 and 27MnCr5, laboratory experiments were carried out at ASCO to determine adequate heat treatments. Indeed, the bars were delivered in Ø65mm size and the standard treatments are designed for smaller diameters. Therefore, it was not easy to obtain the desired microstructure (homogeneous ferrite-pearlite without bands) but finally this was also achieved Figure 38.

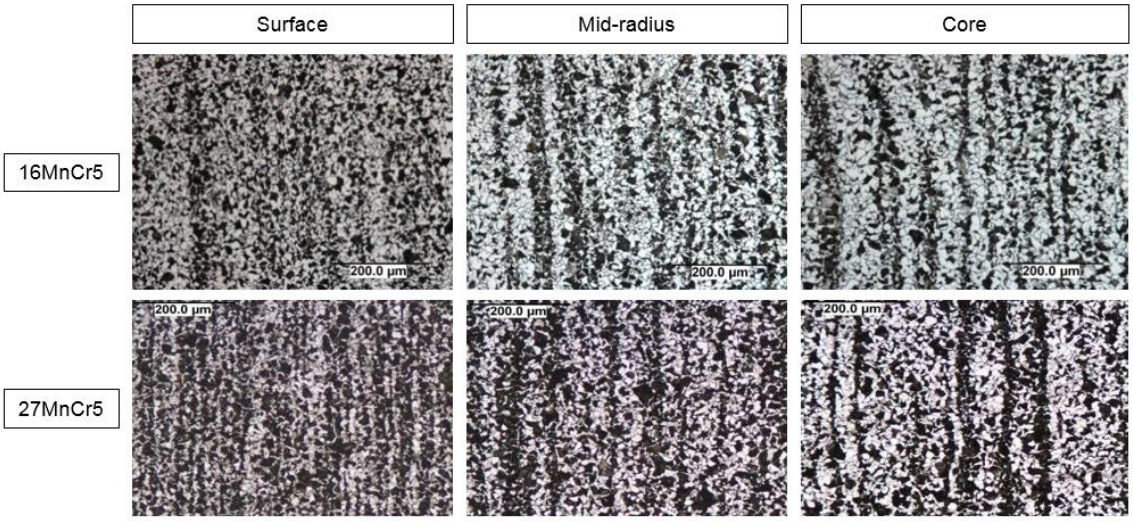

Figure 38. Microstructures obtained for standard grades 16MnCr5 (up) and 27MnCr5 (down).

As it can be seen in the Figure 38, the microstructure of the steel change depending the depth it is checked. This is something it will be considered when manufacturing the samples for the broaching study.

Manufacturing of the GP (globulized pearlite) variants

For the globular pearlite variants manufactured by GERDAU (C45 & C60), the pearlite grains globulization was achieved by a globular annealing performed with the typical parameters commonly used for these grades. As for low C content variants, some

experimental trials were carried out on grades 16MnCr5 (Figure 39) and 27MnCr5 by ASCO to determine the most adequate heat treatment. For the 16MnCr5, they found out that the most adequate structure was obtained for 700°C, 2 h 30'.

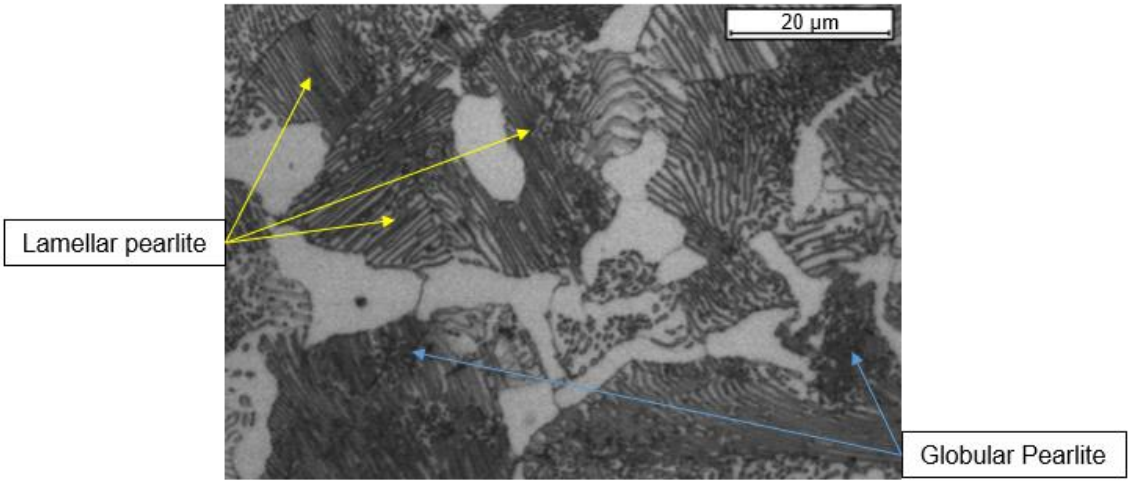

Figure 39. Examples of lamellar/globular perlite observed in 16MnCr5.

Manufacturing of the CG (coarse grain) variants

For the coarse grain variants, experimental trials were performed by ASCO and GERDAU. The austenitization conditions were tested on four grades (all but the C70). For 16MnCr5 and 27MnCr5 grades, several austenitization conditions were tested by ASCO. The samples were water quenched, and the prior austenitic grain size was observed. The fraction of coarse grains was measured for all the steels:

Table 6. ASTM grain size conversion to mm.

ASTM Number	Size (mm)
1	0.250
2	0.180
3	0.130
4	0.090
5	0.065
6	0.045
7	0.030
8	0.022
9	0.016
10	0.011
11	0.008

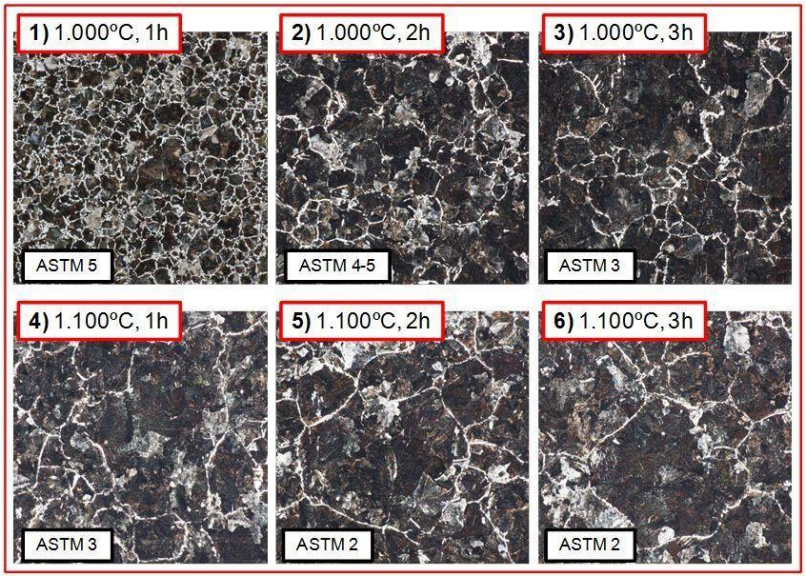

Figure 40. ASTM pearlitic grain size obtained with the different heat treatments for 45CG variant.

The condition 1000°C 45min was chosen, as they lead to about 50% of coarse grains (ASTM < 3) for the two grades 16MnCr5 and 27CrMn5. GERDAU performed some experimental trials with grade C45. The heat treatments consisted of heating at different temperatures and dwell times.

As the desired pearlitic grain size was about ASTM 3, the heat treatment number 4 (similar results than with number 3, but with clearly shorter austenization time) was chosen to manufacture the 45CG variant. In Figure 40, the microstructures obtained with each trial are shown.

For grade C60, the heat treatment number 3 was performed to check if the results were similar to the ones obtained with the 45CG. As the ASTM pearlite grain size was also 3, it was decided to apply the same heat treatment to both steel grades. The microstructure obtained in this trial is shown in Figure 41. The condition 1100°C 1h was chosen for the two grades C45 and C60.

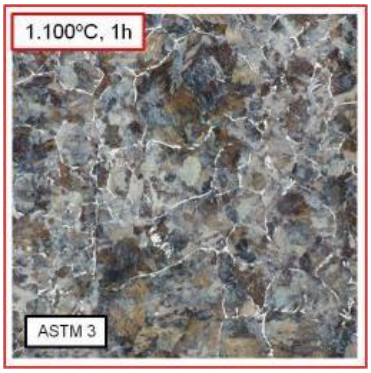

Figure 41. ASTM grain size obtained for 60CG steel variant.

Manufacturing of the WB (with bands) variants

The heat treatment performed to obtain the WB variant (with more bands) was a modified isothermal annealing. To increase the banding level, the cooling rate was decreased in the zone between the austenization and the maintenance temperatures. Increasing the transition time between these two temperatures, the ferrite-pearlite bands formation was favoured. For grades 16MnCr5 and 27MnCr5, experimental trials were conducted at ASCO. The slow cooling was obtained by setting a higher annealing temperature to 640°C (instead of 600°C).

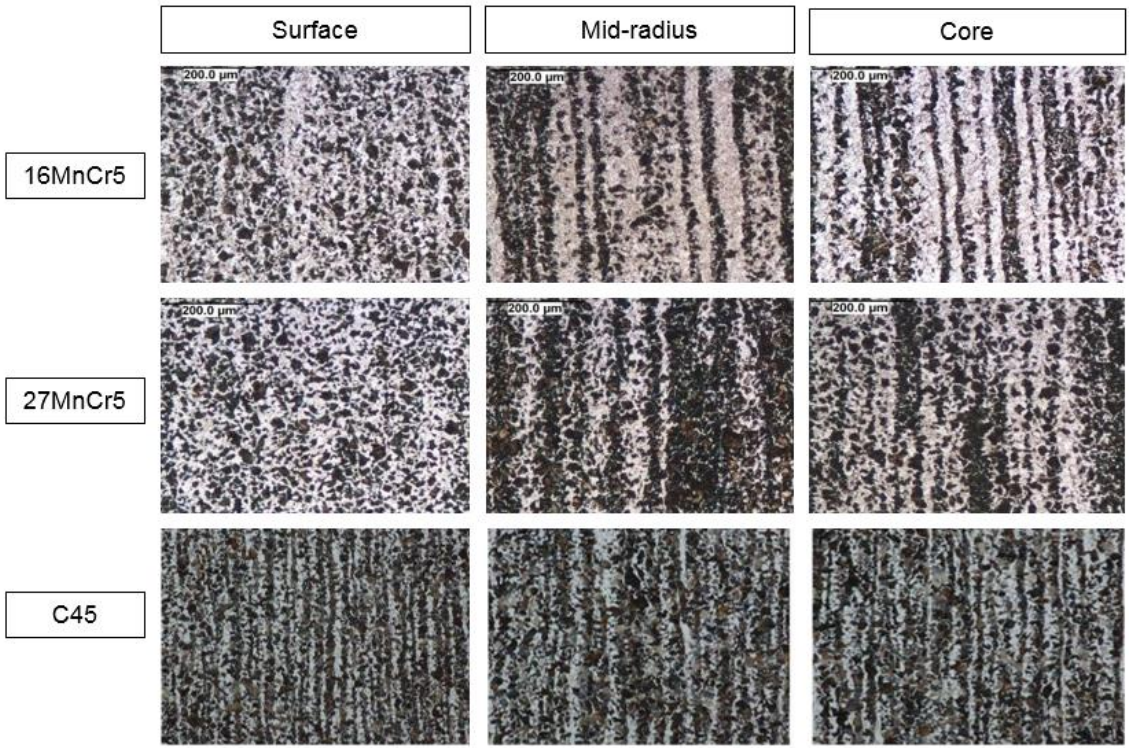

Figure 42. Microstructures obtained for grades 16MnCr5 (up), 27MnCr5 (middle) and C45 (down) in the surface, mid-radius and core of the bar for the With more Bands steel variants.

Through the pictures shown above there are clearly seen the bands much more clearly in the mid radius and in the core images.

3.1.5 Composition, microstructure and hardness analysis

Chemical composition

The chemical composition of the different heats was measured on the rolled bars (Table 7). All the variants of each grade were manufactured from the same heat.

Table 7. Chemical composition of steel grades.

Grade	C	Si	Mn	S	P	Ni	Cr	Mo	Cu	Al
16MnCr5	0.19	0.17	1.23	0.028	0.016	0.19	1.03	0.07	0.17	0.020
27MnCr5	0.25	0.24	1.19	0.033	0.009	0.09	1.06	0.04	0.11	0.032
C45	0.45	0.33	0.78	0.025	0.014	0.09	0.12	0.02	0.11	0.007
C60	0.61	0.28	0.65	0.027	0.016	0.14	0.11	0.04	0.24	0.005
C70	0.71	0.21	0.57	0.065	0.007	0.06	0.15	0.02	0.03	0.002

The carbon content was a bit high in the 16MnCr5 and a bit low in the 27MnCr5, in the rest of the grades, the carbon content was the expected one. The differences detected in the Al content were due to the different deoxidation methods used to manufacture the steels. C45, C60 and C70 were deoxidized with Si, while the rest, 16MnCr5 and 27MnCr5, were deoxidized with Al (this is the reason of their higher Al content). This higher Al content will lead to different inclusion populations which may affect on the steel machining performance. The high S content of the C70 was because ASCO does not manufacture this grade with lower S.

Microstructure analysis

In all the cases the microstructure was studied at different points of the bar section (surface, mid-radius and core). The microstructure was assessed determining the ferrite pearlite ratio, the globulization ratio, the grain size both pearlite and ferrite. For the C70 (Figure 43), besides the previous commented assessment it was also confirmed that its microstructure is fully pearlitic.

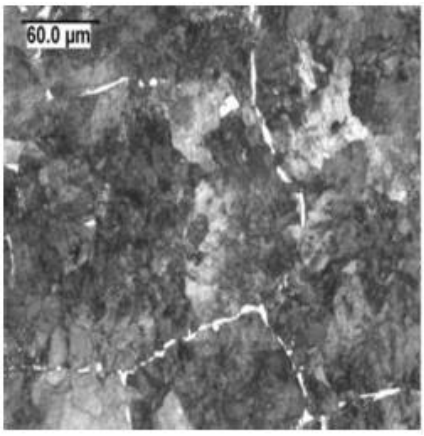

Figure 43. Fully pearlitic C70R image (280HB)

Quantitative analysis - ferrite fraction of variants:

Ferrite content percentage is measured using statistical image analysis. The values are given in the table below. Note that the pearlite content % is the complementary and the standard deviation of the measurement is about a 10% of its value for all the variants.

Table 8. Measured ferrite content (%).

	16MnCr5	27MnCr5	C45	C60	C70
Reference (R)	58	40	25	14	3
Coarse Grain (CG)	56	52	15	6	-
Globular Pearlite (GP)	53	45	10	14	-
Wide Bands (WB)	59	44	20	-	-

Quantitative analysis - ferritic grain size of variants:

The ferritic grain size is measured only when the ferrite exhibits a nodular aspect. In all the C60 variants, as well as in the 45CG, the ferrite is present at grain boundaries only therefore it was not measurable. In the globular variants 45GP and 60GP, there could not be identified ferrite nodules. In this case as well, the standard deviation of the measurement is about a 10% of its value for all the variants.

Table 9. Ferrite grain size (µm).

	16MnCr5	27MnCr5	C45	C60
Reference (R)	10	14	17	11
Coarse Grain (CG)	12	15	30	17
Globular Pearlite (GP)	12	12	10	10
Wide Bands (WB)	12	12	19	-

Pearlite interlamellar spacing of variants:

Interlamellar spacing was measured at ASCO for the 16MnCr5 and 27MnCr5 variants, and the C45 and C60 variants at GERDAU. The method used at ASCO is based on SEM images at magnification x10000. The statistical method consists in measuring the distance between 5 lamellae. This is statistically repeated on 70 images and involves up to 16 measures per image (see example below Figure 44). A comparison of the two methods were conducted on the 60R variant, and it was confirmed that both give similar

results. Average interlamellar spacing, as well as standard deviation, is given, for each variant, in the Table 10 below.

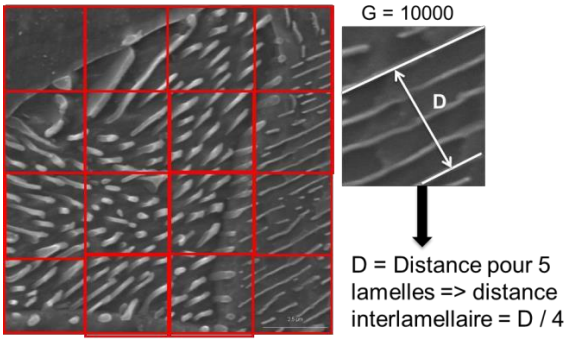

Figure 44. Method used at ASCO for measuring the interlamellar spacing

More examples of pictures taken of the pearlite lamellas are shown in the Figure 45, in this case on the standard 27MnCr5 variant.

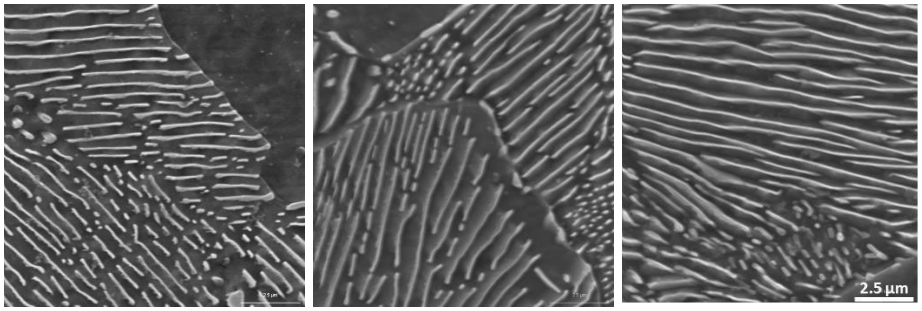

Figure 45. Example of lamellar pearlite on the 27R variant

Table 10. Interlamellar spacing - average ± standard deviation (nm).

	16MnCr5	27MnCr5	C45	C60	C70
Reference (R)	190 ± 65	285 ± 74	293 ± 82	372 ± 135	206 ± 70
Coarse Grain (CG)	222 ± 65	229 ± 59	366 ± 170	306 ± 79	-
Globular Pearlite (GP)	204 ± 69	197 ± 56	632 ± 192	623 ± 186	-
With Bands (WB)	146 ± 41	220 ± 51	326 ± 116	-	-

The values (average and standard deviation) from the Table 10 represent the “apparent value” of interlamellar spacing. So far, we can say that the higher results obtained on high globalized pearlite structure (C45 and C60) compare to Reference variants are logical.

Hardness

Table 11 shows the average hardness (HB) value obtained for each steel variant. This is not a microstructural feature, but it is tightly linked with it as it depends on each of the previous microstructural properties have been explained in the previous section.

Table 11. Hardness HB (average).

	16MnCr5	27MnCr5	C45	C60	C70
Reference (R)	162 ± 5	163 ± 5	185 ± 3	188± 2	266 ± 8
Coarse Grain (CG)	162 ± 6	168 ± 5	198 ± 5	225 ± 4	-
Globular Pearlite (GP)	160 ± 4	174 ± 4	143 ± 6	148 ± 5	-
With Bands (WB)	163 ± 7	178 ± 3	165 ± 5	-	-

The GP variants of grade C45 and C60 present a logical lower hardness compare to the Reference, due to the high level of pearlite globulized; this is not observed for low carbon steel. The hardness of CG variants increases with the carbon content. The hardness of 45R and 60R is similar despite the different percentage of pearlite.

The steels with the lowest hardness values are the variants C45GP and C60GP variants. Comparing the Table 8 with the Table 11 it could be drawn that the hardness is not directly related to the steel's ferrite content, but other features take part in it such as the ferrite and pearlite grain size, the IS or the shape of the grains.

Thermal characterization

In this chapter will be shown not only the results but also the way the conductivity of each of the FP steels was obtained i.e. it will be performed the thermal characterization of all the set of FP steels. First, it is explained briefly what it has been done around this topic after checking out the literature review. This work has been completely undertaken at MGEP.

3.1.6 Introduction

A deep study of the first and following steps made in this field is carried out by (Šesták et al. 2011). It explains how material's thermal analysis began in the early nineteenth century after Isaac Newton published the temperature scale (1701) and his law of cooling (Grigull 1984). Then, this parameter became observable and experimentally decisive quantity, which thus turned into a monitorable parameter associated with the field of thermodynamics (Šesták 2011).

One of the most important impacts came with the discovery of thermoelectric effect by Thomas J. Seebeck. It occurred in a circuit made from two dissimilar metals and the consequent development of a device called thermocouple (Hunt 1964), suitable as a more accurate temperature-measuring tool. Then, Floris Osmond investigated the heating and cooling behaviour of iron with the goal to assess the effects of carbon so that helped to the development of the metallurgy (Kayser, Patterson 1998).

In 1891, Sir William C. Roberts-Austen constructed a device (Figure 46) to give a continuous record of the output from thermocouple (Roberts-Austen 1899). In 1899, Stanfield published heating curves for gold and almost stumbled upon the nowadays idea of differential thermal analysis (DTA). Such an innovative system of measuring the temperature difference between the sample and a suitable reference material placed side-by-side in the same thermal environment initiated the development of DTA instruments.

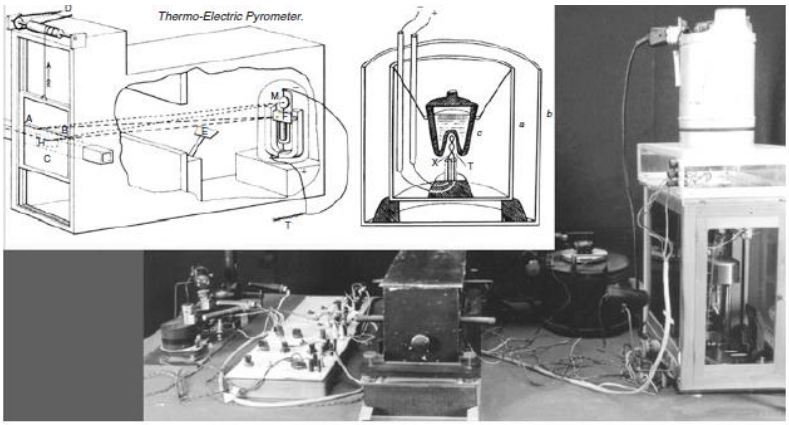

Figure 46. Thermo-electric pyrometer device developed by Roberts-Austen (Roberts-Austen 1899).

In the beginning, DTA could not be classified as a calorimetric method since no heat was measured quantitatively (Wendlandt 1964). Only the temperature was determined with the precision of the thermocouple. In the 1950s, the classical DTA and adiabatic calorimetry merged, producing a differential scanning calorimeter (DSC) originally introduced by Eyraund (EYRAUD 1954). This kind of devices monitor the difference between the counterweighing heat fluxes by two extra micro-heaters. These are respectively attached to both the sample and reference to keep their temperature difference minimal, while the samples are maintained in the pre-selected temperature program.

Nowadays the DSC type devices (sometimes combined with the DTA) are the ones normally used for the thermal characterization. Not only can be the temperature tracked and controlled but there can be also obtained such variables as specific heat, density

and thermal diffusivity (Höhne et al. 2013). Hence, the ones we need to obtain the conductivity.

Nowadays it is studied many material's thermal characterization in many fields such as pharmaceutical, organic chemistry and polymers fields (Menczel, Prime 2014). Nevertheless, as the work occupies us deals with FP steels, the literature revision's search will be focused on the materials (basically metals) used for machining operations. Scooping the researches done during the last years, in some cases there have been done full thermal characterization studies comparing the obtained data with its microstructure and composition. In some other cases these results have been published (Figure 47) not even mentioning where they obtained them from and using them to feed numerical machining models (Woo, Lee 2015, Grzesik, Nieslony 2004).

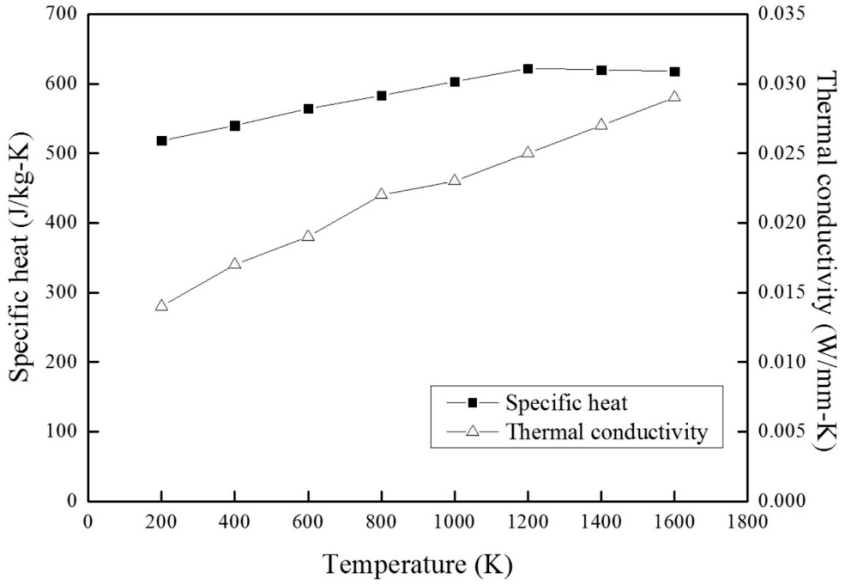

Figure 47. Thermal conductivity and specific heat of a C45 provided by (Woo, Lee 2015).

3.1.7 Experimental approach and sample preparation

It must be first identified the density, the specific heat and the diffusivity and then multiply these values getting this way the conductivity for all the bunch of FP steels. As an added work, two tool materials have also been selected for characterization: a) Carbide-H13A: is an uncoated carbide (Tungsten-carbide) grade that combines good abrasive wear resistance and toughness and b) HSS-M35: is a PVD-coated carbide grade that provides secure performance with long-lasting sharp cutting edges, keeping cutting forces low. These tools are in fact the ones will be used in the tribology study in the chapter 4. After the analysis, all this data will be implemented in the broaching cutting model so as to simulate the heat transfer occurring in the tool-workpiece interface while machining.

The following properties have been characterized:

- Specific heat (Cp): for each steel the specific heat depending on temperature has been determined with a Differential Scanning Calorimeter (sample of Ø10x3mm).
- Density (ρ): the density depending on temperature has been determined with a Vertical Dilatometer (sample of Ø6x15mm).
- Thermal diffusivity (α): thermal diffusivity depending on temperature has been determined with a Laser Flash (sample of Ø4x3mm).
- Thermal conductivity (λ): for each steel and after the previous three thermal properties the thermal conductivity depending on the temperature has been calculated (Eq. 3.3.1):

$$\lambda(T) = \alpha(T) \cdot Cp(T) \cdot \rho(T) \qquad \text{(Eq. 3.3.1)}$$

Sample preparation was carried out by milling and wire-EDM cutting operations. As the material is given in bars, first, it has to be cut a slide. Then, machining both sides of the cylinder we get the desired height (15mm). As the specific heat and diffusivity samples have to be 3mm height a zone of this cylinder is milled up to 3mm (upper side of the bar in Figure 48). Finally, this cylinder is placed into the EDM machine so as to cut the samples with the proper diameter measure for the each of the machines used for the calculation of the different properties.

In the Figure 48 are specified the regions from where the samples haven been obtained.

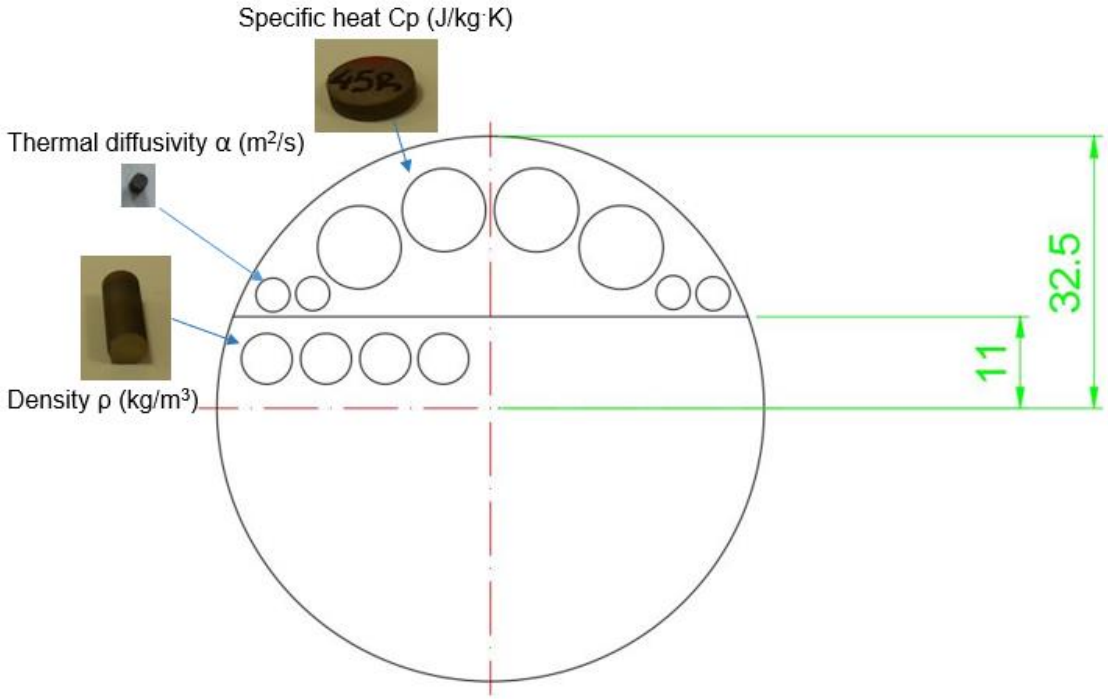

Figure 48. Picture showing the zones where the samples are taken from in mm.

A full analysis of the results is given in the following subsections. Not only there will be displayed the results versus the temperature but also versus the microstructure of each of the variants.

3.1.8 Density (ρ)

The density is a widely known material's property that gives the relationship between the mass and the volume this mass occupies. As commented previously the samples were obtained using an EDM machine that provides specimens with the exact height needed to be implemented in the dilatometer shown in the Figure 49.



Figure 49. Density characterization sample (left) and Vertical Dilatometer L75PT device (right).

FP steel's results

With the aim of obtaining the variation of the density versus the temperature increase, the samples were heated from room temperature up to 1200ºC. Three repetitions were performed per each variant so, besides the mean value a standard deviation was also extracted, being negligible in almost all the cases as you will see in the following figures. Before placing the sample in the dilatometer, the exact values of height, cylinder's diameter (Ø) and weight had to be measured and then implement this data in the machine's software.

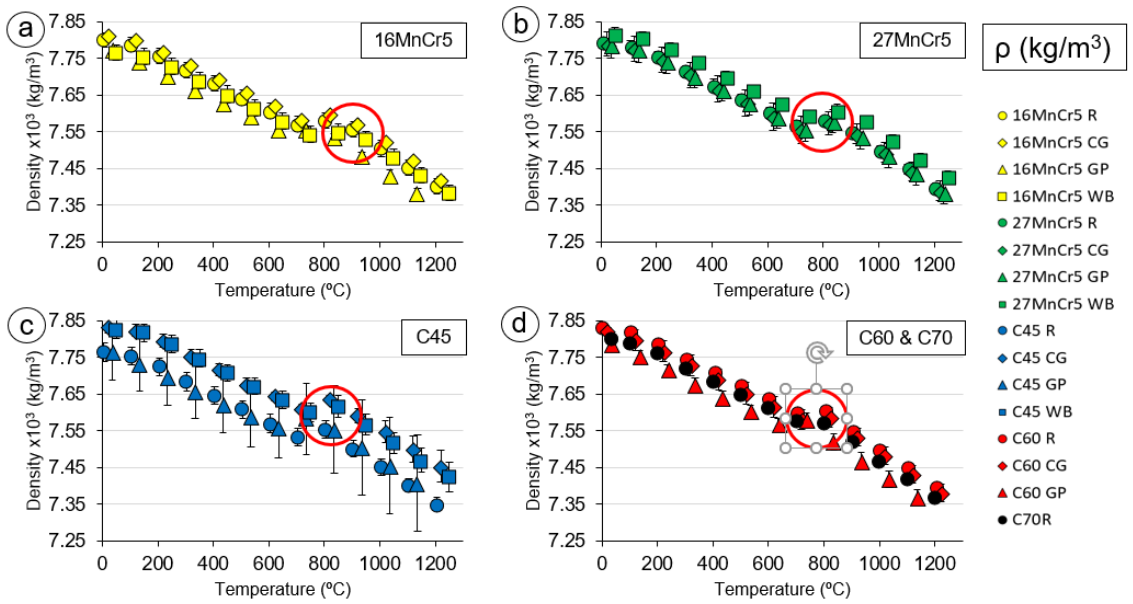

Figure 50. FP steel variant's density versus T, a) 16MnCr5, b) 27MnCr5, c) C45 & d) C60 & C70.

As it can be seen, in the Figure 50 the results are separated in variants and plotted versus the temperature. All thermal variables show a linear decrease when heating from the room temperature, but it can be detected a variation on the measured values around 700-800ºC due to a phase change; an austenite transformation (circled in red).

Going through the variants slight density differences are found between the studied grades. Taking the standard variant as reference, focusing on the trends, they seem to have lower density values for the GP variants, and slightly higher for the WB variants in comparison with the reference (R) of each grade. The density values decrease from 7800 to 7400 kg/m^3 (± 5%) when moving from room temperature up to 1200ºC.

The results have been plotted in terms of the name given to each of the variants of the different grades (Figure 51). This figure shows that the trends do not depend on the carbon content. Even the trend changes for all the variants when passing through the austenization point (circled in red). For example, analysing the Figure 51a the C60R's density is higher (1% at maximum) than the 16MnCr5R's one from the room temperature until the austenization point. Then, after reaching 800ºC, the densities values equalize being even lower in the last measured point. Sometimes this effect occurs in an inverse way what it is clear is that the difference between the values increases after the austenization point. This fact is confirmed as well if focusing the attention in the standard deviation obtained from the measurements being higher the higher is the temperature. This effect happens as well due to the difficulty of acquiring a stable temperature level. This machine required nitrogen to carry out the essays and from time to time the nitrogen tank had to be refilled to get a stable temperature signal.

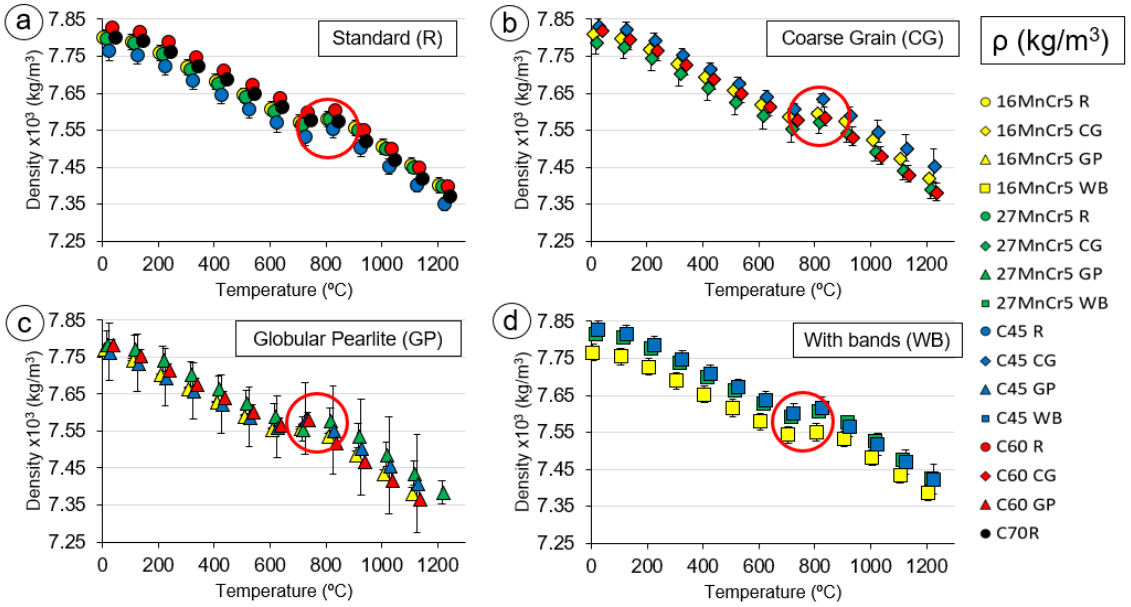

Figure 51. FP steel variant's density versus temperature split in variants, a) Standard (R), b) Coarse Grain (CG), c) Globular Pearlitic (GP) & d) With Bands (WB).

Tool's results

The variation of the density was also measured in the tool's materials, as it had to be also implemented in the cutting models. We have just two materials, so it is easy to see the differences between them. In this case, we have split the results into two graphs because of the density differences are that high and the variation that low that merging those curves in the same graph would make it difficult to differentiate the change occurring when raising the temperature. As it can be seen in the Figure 52, the behaviour of the HSS-M35 is similar to that obtained with the FP steels, which is because indeed it is a steel. On the contrary, focus the attention on the H13A it can be seen see that the variation is quite stable and there is no change when it reaches around 800ºC. It bears our attention as well that the H13A's density is quite higher than M35's. The density reduction is higher in the M35 variant that, despite the increase when reaching 900ºC, it decreases 2.75%. On the contrary, the density variation occurring in the H13A tool material is 1.3%. The fact of having lower dilatation when increasing the temperature can be related to its toughness.

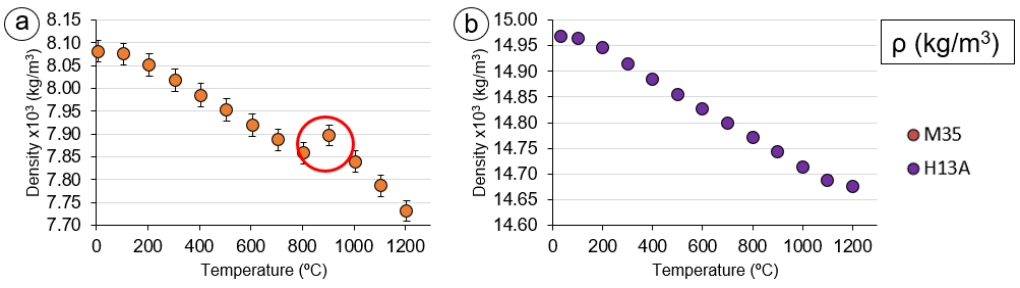

Figure 52. Tool materials' density variations versus temperature: a) M35-HSS b) H13A.

3.1.9 Specific heat (Cp)

The specific heat is the amount of heat per unit mass required to raise the temperature by one degree Celsius or Kelvin. This parameter is shortly named as Cp and the IS units are J/kgK. For the tests the samples have been also cut using the EDM machine (Ø10mm and h=3mm) and it had also had to be measured the exact Ø and height of the sample. These data were then input in the software before carrying out the measurements so that it could be possible to get correct results. In the Figure 53 it can be seen the C45R's sample and the shape given to it.

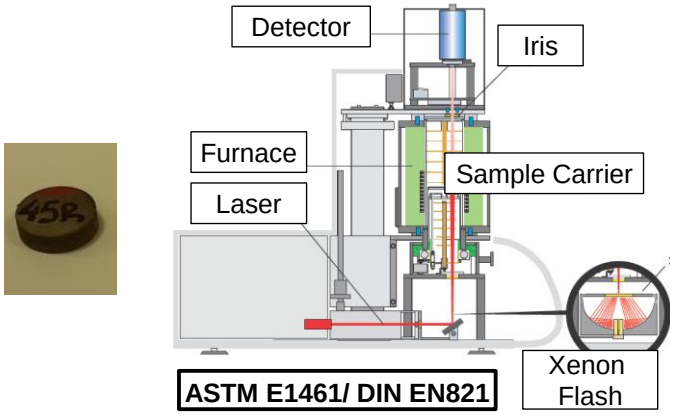

Figure 53. Specific Heat characterization sample (left) and the Laser Linseis LFA 1000 device (right).

FP steel's results

With the aim of obtaining all FP steel's specific heat values, they have been placed on the Linseis device. Then the measurement was performed three times per variant changing the specimen each time. Specific heat tests showed same absolute values and trends for all the grades. In a first term, the results have been split in grades in four different graphs (Figure 54) and as it can be seen there is an increase on their values from 400 to 800 J/kg·K with the increase of the temperature from 20 to 800ºC. Some measurements at 800ºC showed a discrepancy out of the previous trend due to limitations of the measurement equipment (these results will be kept aside). At temperatures lower than 600ºC measurements remain the same for the studied variants. Only when reaching temperatures between 600 and 800ºC some differences can be seen, but without any clear tendency between the grades and variants.

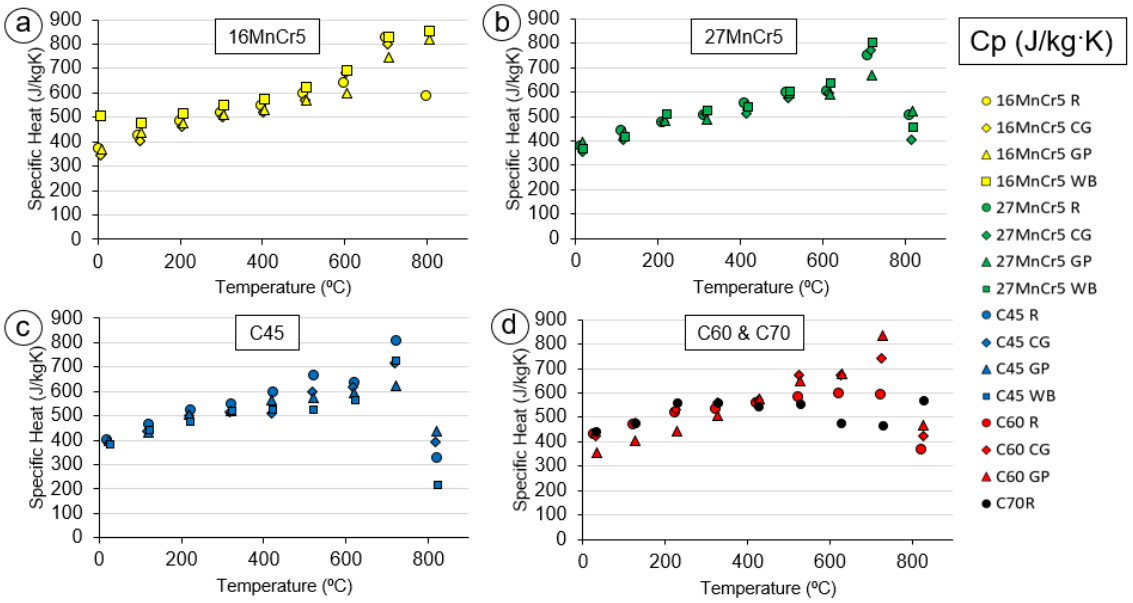

Figure 54. FP steel variant's specific heat versus temperature split in grades, a) 16MnCr5, b) 27MnCr5, c) C45 & d) C60 &C70

In a second term, the results have been plotted split in the different variants (Figure 54) so it can be seen any influence of the microstructure or composition feature. Focusing on the Standard (R) and the Coarse Grain (CG) variants it can be extracted a tendency when moving from 0ºC to 600ºC depending on the C content. It is seen that the lower is the C content the lower is the specific heat. This is something it can be also seen in the previous graphs (Figure 55) if we pay attention to the values of each grade at the same temperature. This can be linked with the fact that, separately, carbon's specific heat is higher than iron's specific heat.

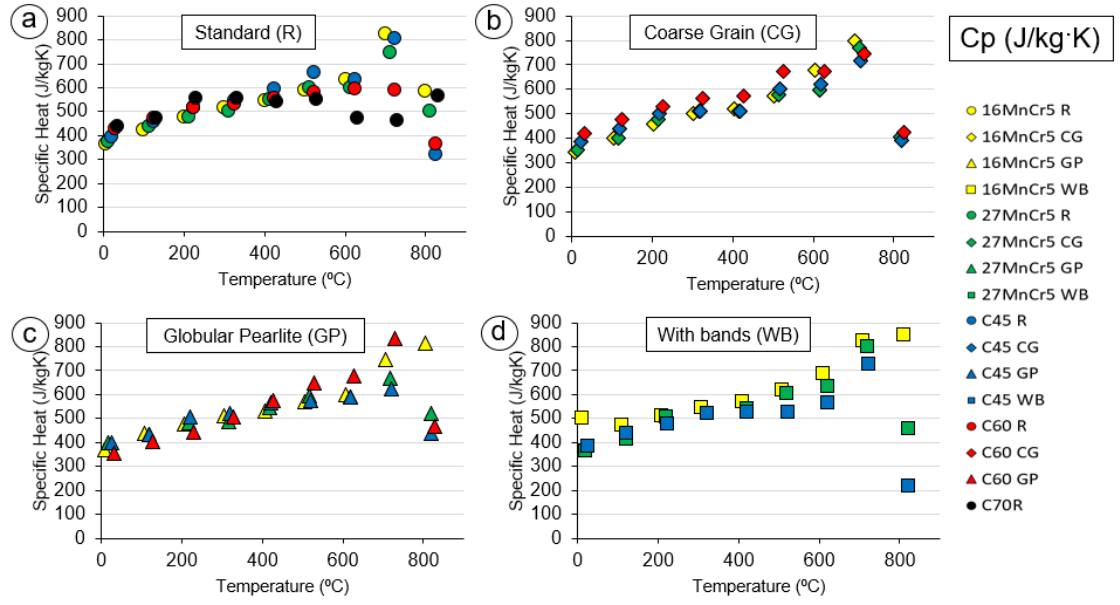

Figure 55. FP steel variant's specific heat versus temperature split in variants, a) Standard (R), b) Coarse Grain (CG), c) Globular Pearlitic (GP) & d) With Bands (WB)

Tool's results

As it had to be also implemented in the cutting models, the specific heat was also measured in the tool's materials versus the increment of the temperature. We have just two materials, so it is easy to see the differences between them. In this case, as the value differences are not that high (factor of two higher the HSS-M35 versus the WC-Co-H13A) than in the case of the density we have put the results in the same graph. As it can be seen in the Figure 56, the behaviour of the HSS-M35's points is like that obtained with the FP steels but in this case, the increase in the value as the temperature increases is not that high. On the contrary, if we focus our attention on the H13A we see that there is almost no variation remaining the specific heat value around 200J/kgK. It is quite curious that, after reaching 500ºC, the value starts to decrease until 6J/kgK at 800ºC what will drive to a very low conductivity in this tool material.

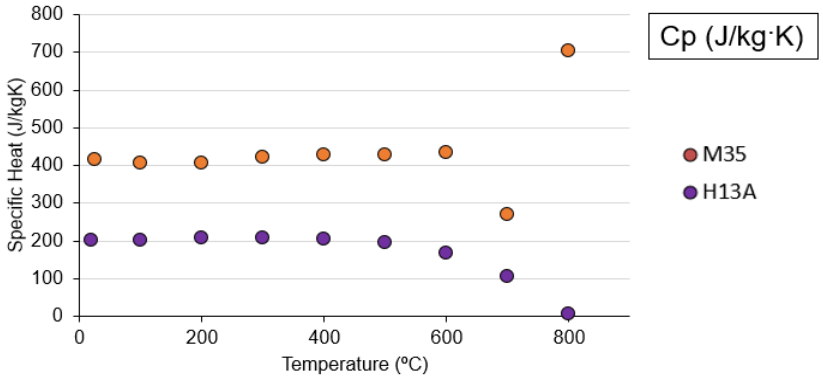

Figure 56. Tool's materials specific heat versus temperature

3.1.10 Diffusivity (α)

When talking about heat transfer, thermal diffusivity is related to the measurement of the rate of transfer of heat of a material from the hot side to the cold side. Its units in the IS are m^2/s and is usually denoted by "α". In the Figure 57 there can be seen the way the samples were manufactured (Ø4mm and h=3mm) and the device used to obtain the diffusivity in which the uncertainty is 5% at maximum.

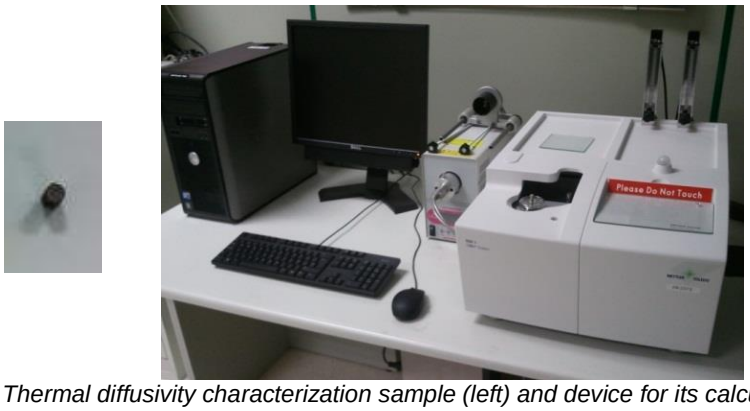

Figure 57. Thermal diffusivity characterization sample (left) and device for its calculation (right)

FP steel's results

With the increase of the temperatures, a decrease on the diffusivity values occurs for all the studied FP steels. Analysing the Figure 58, this tendency is found for the 16MnCr5 grade, but in this case, higher dispersion is found between the different material variants. In fact, it is the standard variant the one giving this strange result. Analysing in detail the results, WB and GP variants achieve the higher thermal diffusivity values except for the 16MnCr5 variant, where the maximum diffusivity is obtained on the R variant (to be explained from finer microstructure analysis). These range from 0.12 to 0.04 m^2/s except for the case of the 16CrMn5R grade that varies from 0.18 to 0.07 m^2/s. The 27MnCr5 grade is giving almost the same values for all its variants in all the temperature range. For the C45 the difference between its variants is around 30% at the lowest temperature decreasing up to 5% at 800ºC.

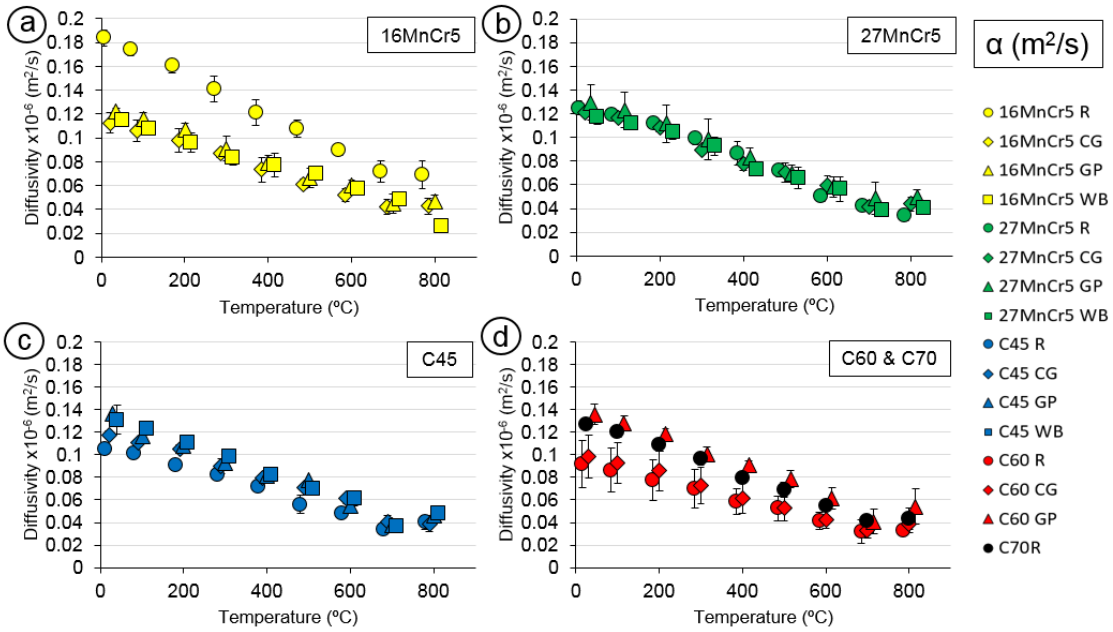

Figure 58. FP steel variant's diffusivity versus temperature split in grades, a) 16MnCr5, b) 27MnCr5, c) C45 & d) C60 &C70

In the Figure 59 the results have been plotted split in the different variants, focusing on the standard variant (Figure 59a), keeping aside the C70, the trend complies that the lower C content the higher is the diffusivity. For the rest of the variants there is no clear tendency regarding the C content or another feature related to the microstructure. In fact, for the GP and WB variants occurs the contrary of what we have seen in the R variant, that, the lower diffusivity values are obtained with the higher C content variants.

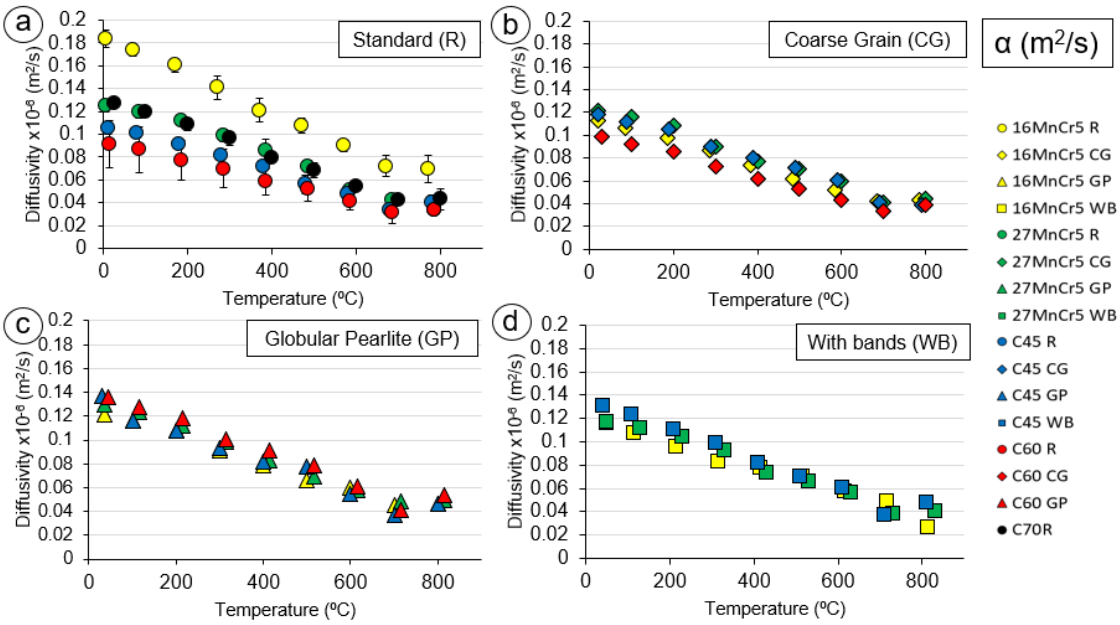

Figure 59. FP steel variant's diffusivity versus temperature split in variants, a) Standard (R), b) Coarse Grain (CG), c) Globular Pearlitic (GP) & d) With Bands (WB)

Tool's results

The diffusivity is not directly implemented in the models, but it is necessary to obtain the conductivity. This feature was also measured in the two tool materials versus the increment of the temperature. We have just two materials, so it is easy to see the differences between them. In this case as well, as the value differences are not that high it has been decided to put the results in the same graph. As it can be seen in the Figure 60, the behaviour of the HSS-M35 is stable and linear whatever the temperature is. For the H13A the values decrease the higher is the temperature going from 0.37m^2/s at room temperature to 0.16m^2/s at 800ºC.

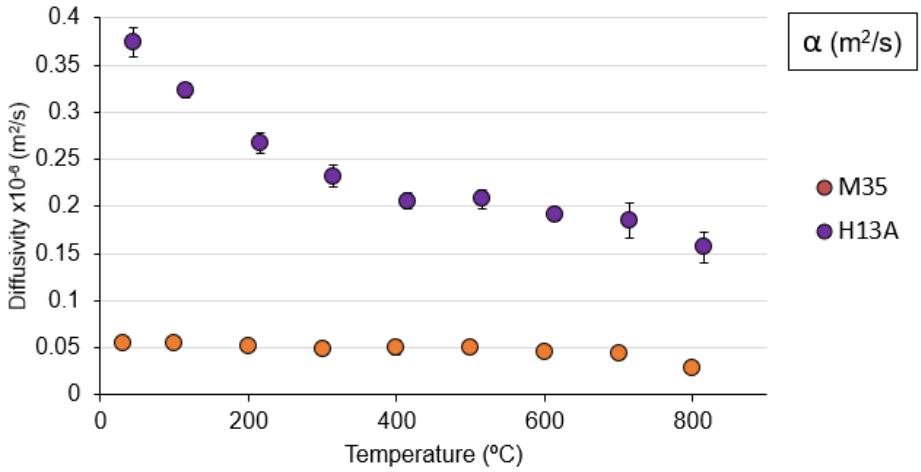

Figure 60. Tool materials' diffusivity variations versus temperature.

3.1.11 Conductivity (k)

Thermal conductivity is the property of the material that describes the ability to conduct heat. It can be physically defined as “the quantity of heat transmitted through a unit thickness of a material - in a direction normal to a surface of unit area - due to a unit temperature gradient under steady state conditions. The units of the thermal conductivity are W/(mK) in the SI system. This property has been obtained by multiplying the aforementioned three variables using the (Eq. 3.3.1).

FP steel’s results

As the results are concerned, the trends obtained for the conductivity are related to the previous variables have been already explained. In an overall view, conductivity results show a decrease with the increment of temperature for values ranging from 40 to 15 W/mK. Going more in deep through the results, this trend has been seen in all the studied grades except for the 16MnCr5 grade, whose conductivity remains in values between 25-40 W/mK for CG, GP and WB variants, and between 45-60 W/mK for the R variant. This behaviour is due to the variations achieved in the diffusivity measurements. Analysing the C60 grade, GP variant has achieved higher conductivity values in comparison with CG and R variant. For the C45 and 27CrMn5 grades, no clear tendency has been found between the variants.

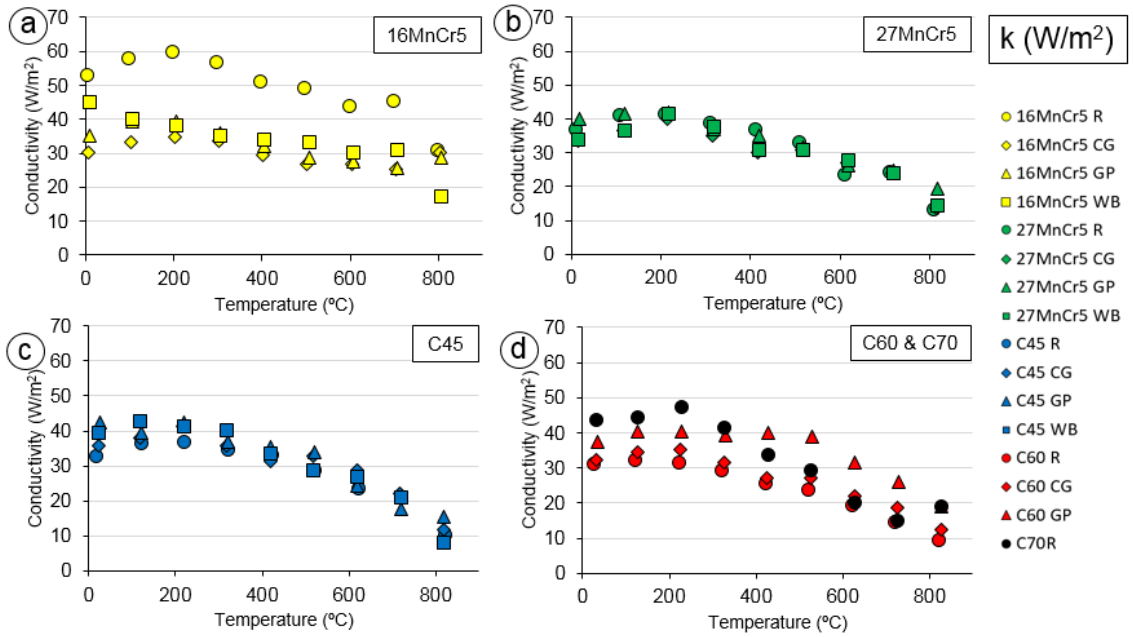

Figure 61. FP steel variant's diffusivity versus temperature split in grades, a) 16MnCr5, b) 27MnCr5, c) C45 & d) C60 &C70.

Now, splitting the results into the different variants there can be seen similar trends to the ones obtained with the calculation of the diffusivity. As previously commented,

scooping the standard variants it seems that the conductivity is related to the C content each variant has (again keeping aside the C70). The differences are quite high comparing to the 16MnCr5 where it can be seen that the diffusivity results are driving the differences obtained in the conductivity values. Now, paying attention on the CG and the GP variants it can be seen that the trends obtained at room temperature are similar but they are not related to the C content. Nevertheless, as the temperature increases the trends change being very dissimilar one from the other. For example, focusing on the GP grades at 500ºC we see that the trend is totally inverse to the one obtained with the standard variants. At this point, it can be seen that the higher is the C content the higher is the conductivity. At last, analysing the WB variant it is impossible to find a trend as in just two temperature rises (200ºC) the trend becomes the contrary it was obtained at room temperature.

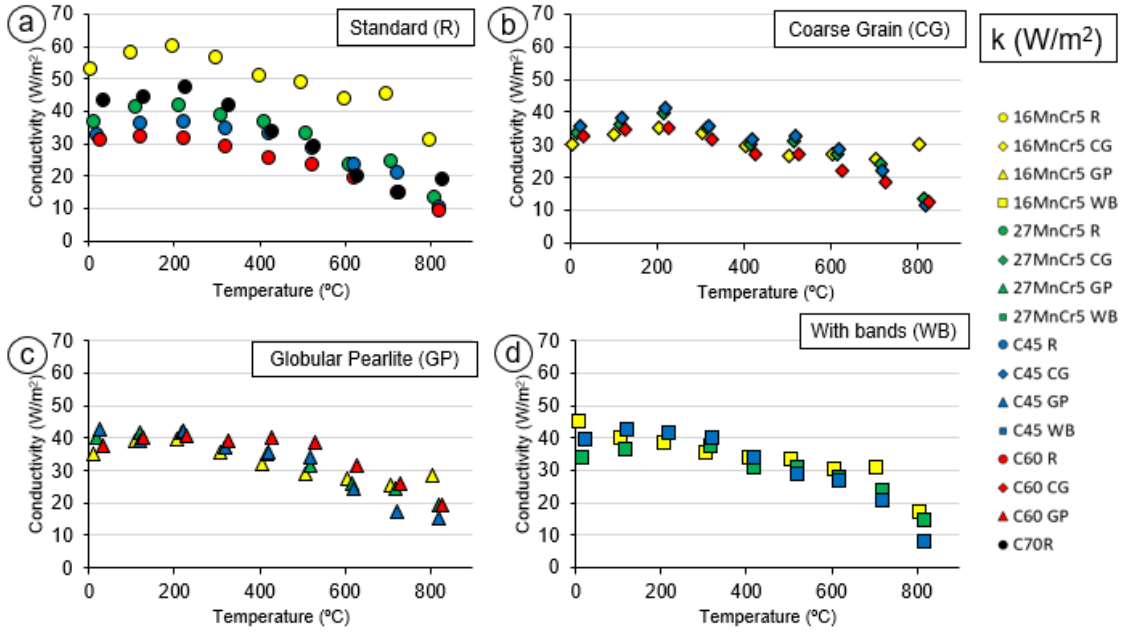

Figure 62. FP steel variant's specific heat versus temperature split in variants, a) Standard (R), b) Coarse Grain (CG), c) Globular Pearlitic (GP) & d) With Bands (WB)

Tool's results

Finally, analysing the conductivity of the material of the tools there can be seen the trends previously analysed as well as what we commented in the specific heat analysis. As it was previously commented, this feature was obtained starting from the other three variables and it was plotted versus the increment of the temperature. The low specific heat obtained at 800ºC in the H13A tool material lead its conductivity to be almost 0.

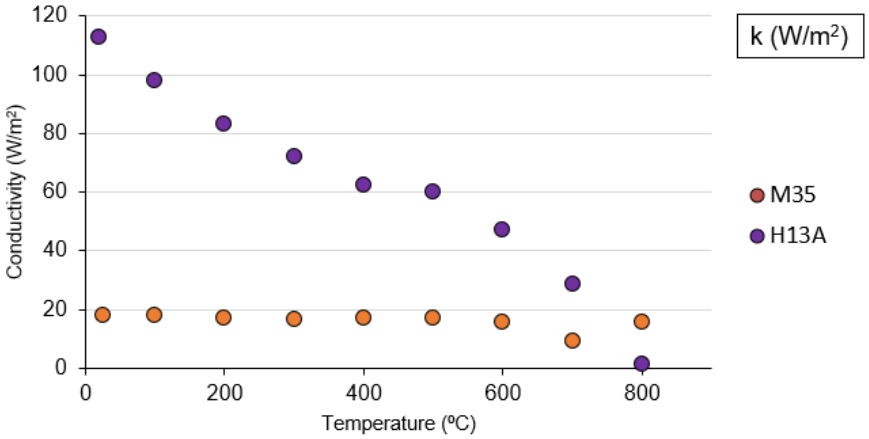

Figure 63. The conductivity variations of tool materials versus temperature.

Having just two materials it was easy to see the differences between them. In this case, the H13A values obtained at room temperature were almost six times the M35 values. However, increasing the temperature this difference became lower and at 800ºC the conductivity value of the H13A was lower than the M35 as it can be seen in the Figure 63. Although there was a decrease at 700ºC the behaviour of the HSS-M35 was stable and linear whatever the temperature was. For the H13A the values decrease the higher is the temperature going from 0.37m^2/s at room temperature to 0.16m^2/s at 800ºC.

3.1.12 Conclusions on the results

Conclusions on FP thermal analysis

Same trends of the characterized thermal properties have been found for all the grades and variants. Regarding the absolute values, the clearest differences between variants were achieved on the 16CrMn5 grade, where the standard (R) variant achieved the highest diffusivity (0.18 m^2/s) and thermal conductivity (60 W/m^2), doubling the values obtained with the C60 (0.9 m^2/s and 30 W/m^2 respectively). This is quite relevant as the uncertainty of the devices was 5% at maximum and the value of the 16MnCr5 is a 100% higher. There was not a clear cause to explain this. Focusing on the other grades, with the GP variant were obtained slightly higher density values in comparison with the reference grade in mostly all the grades. Regarding the diffusivity results, with the GP and WB variants were obtained the highest values for the studied grades. Regarding the resultant thermal conductivity, there were achieved noticeable differences between variants only in the 16MnCr5 and C60 grades, obtaining the highest values on the R (60 W/m^2) variant in the case of the first one, and the GP (40 W/m^2) variant for the second one.

Conclusions on tool materials thermal analysis

Thermal properties of tool materials presented high differences between high speed steel (M35) and tungsten-carbide (H13A). Density of carbide H13A doubled the one of the M35 with values of 15000 and 8000 kg/m^3 respectively. Thermal conductivity maintained constant along the analysed temperature for the M35 with a value of 17 W/m^2. In contrast the H13A decreased from 112 to 28 W/m^2 when increasing the temperature from 20 to 800°C. Diffusivity of H13A had also a decreasing tendency (0.37-0.16 m^2/s) while in the case of the M35 remained constant at 0.05 m^2/s. Specific heat of M35 doubled the one of H13A with a value of 425 and 206 J/kgK respectively. In contrast, Carbide-H13A presents high variations when increasing temperature. It is remarkable that thermal conductivity of the HSS is stablished around 20W/mK and the one of the Carbide H13A decreases from 120 to 30 W/mK when moving from room temperature to 800°C.

FP steel's flow stress

In this section the experimental procedure and resulting data used to identify a material constitutive model will be presented. The latter was developed bearing in mind not only the FP ratio of the steel but also the pearlite's interlamellar spacing and ferrite's grain size. The work was completely carried out in a joint work involving ASCO Industries, KIMAB and the University of Lorraine. Nevertheless, it is presented here as being part of the material characterization as this data will be implemented in the cutting model. The developed equations describing the experimental behaviour through the identification of the parameters driving that behaviour have been displayed in the annexes 10.1.1.

3.1.13 Methodology

For all the 16 steel variants an experimental plan was defined both at low and high strain rates. Each test was performed three times at the conditions shown in the Table 12.

The tensile test is up to date the most accurate test available when testing for material properties. It was also useful for the Young's modulus evaluation depending on temperature.

Tensile - compression tests were performed in strain control mode where the purpose was to establish the amount of kinematic hardening. The strain level is as high as possible to avoid buckling of test piece and still have relatively high strains.

Table 12. Design of experiments for the flow stress model development.

Compression	Tensile	Tensile – Comp.

	T(°C)	$\dot{\varepsilon}$ (s^{-1})	T(°C)	$\dot{\varepsilon}$ (s^{-1})	T(°C)	$\dot{\varepsilon}$ (s^{-1})
Low strain rate (ASCO)	20 / 500 / 680	0.5 / 5 / 50	20 / 500 / 680	5	20 / 500 / 680	5
High strain rate (KIMAB)	20 / 500 / 680	500 / 2000 / 5000	-	-	-	-

3.1.14 Characterisation at low strain rates

Testing device

All the steel grades variants were tested in compression conditions with Gleeble ® device (Figure 64) at the strain-rates of 0.5 s^{-1}, 5 s^{-1} and 50 s^{-1} and temperatures of 20°C, 500°C and 680°C. The extensometer inside the Gleeble was not totally free from rigidity effects that were more pronounced at 0.5 s^{-1} and 5 s^{-1}. Consequently, the slope of the elastic part presented for the different curves in this section were not representative of the Young Modulus of material. Therefore, by means of different formulas the strain had to be corrected to obtain the true stress. These corrections were not absolutely necessary for comparisons between variants (as they are tested in the same way), but they were essential for the good performance of the modelling task.

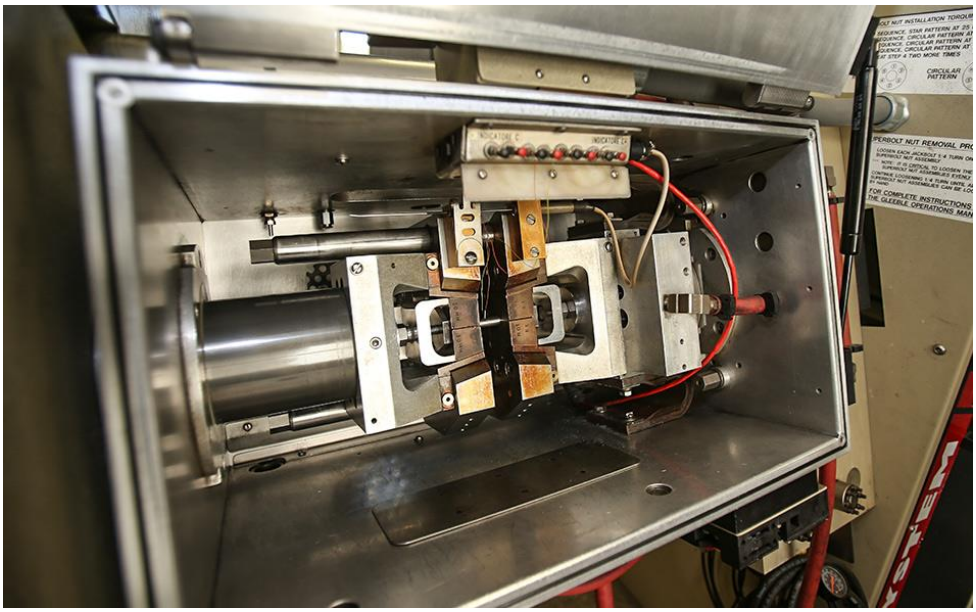

Figure 64. Gleeble 3800M machine used for the experimental strain stress tests at low strain.

The identification of the pearlitic behaviour with strain-rate and temperature dependency is the first step for the modelling task, which is described in the appendices. In the Figure 65 it can be seen one example of the obtained curves. This figure describes the complete behaviour of C70 steel in the considered temperature range and at low strain-rate (0.5 s^{-1} – 50 s^{-1}).

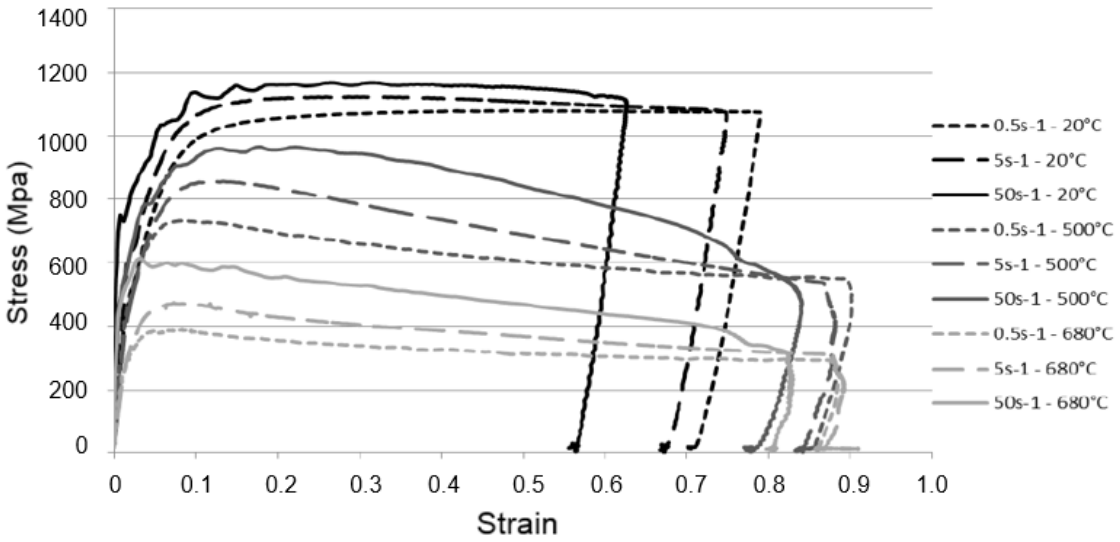

Figure 65. Complete description of the behaviour of C70 steel.

Behaviour of ferrite-pearlite grades considering strain-rate and temperature

Every variant was highly characterized both at low and high strain rates. In this section, results concerning low strain rates tests are presented. Considering the amount of data, it was chosen to highlight just for each grade (16MnCr5, 27MnCr5, C45 and C60), the influence of variants at a defined temperature and strain rate. The Figure 66 presents the differences for the C45 grade in its four variants. Instead of showing the results on the nine tested conditions only the most extreme ones are plotted (lowest T at lowest strain rate & highest T at highest strain rate).

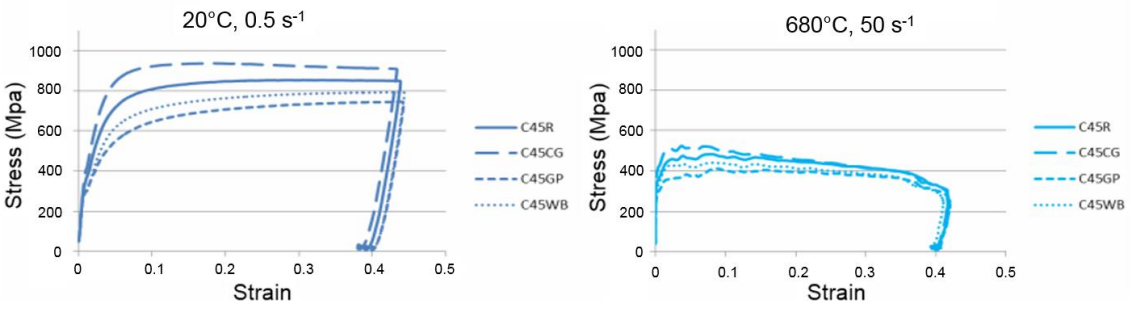

Figure 66. Behaviour curves for the C45 at the lowest strain rate and room temperature and highest strain rate and highest tested temperature.

Every grade shows positive strain-rate sensitivity in the considered strain-rate range, that is an increasing flow stress with increasing strain-rate. Evolution of flow stress with the temperature is typical from thermally activated behaviour with a decreasing of the flow stress by increasing the temperature. These curves are the experimental evidences that were compared to the model. The development of the model is shown in the appendices (10.1.1). In this subsection the formulas used to extract the modelled stress that will be implemented in the cutting simulations are detailed.

Analysing all the trends it was seen that for each grade the influence of variants was globally respected for each temperature and strain rate. To quantify this influence for each variant and make comparison between grades, there were selected the curves at 20°C and 0.5 s^{-1}.

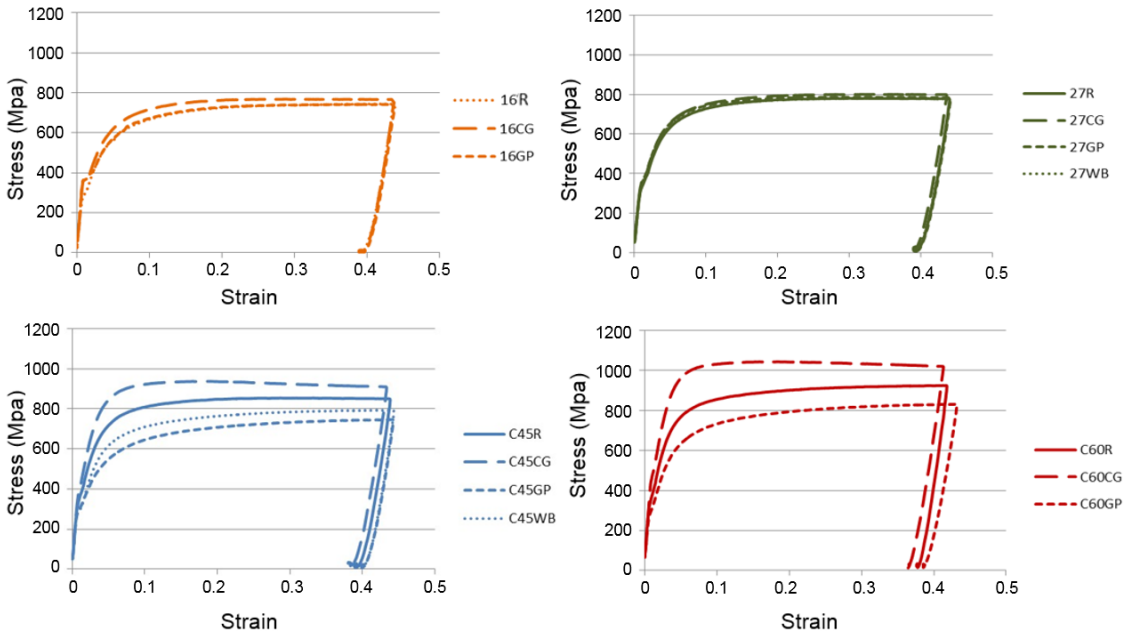

Figure 67. Comparison of the influence of variants for the different grades at 20°C, 0.5 s^{-1}.

Influence of variants on reference grades

It can be seen from Figure 67 that 16MnCr5 and 27MnCr5 grades do not show any important change in their behaviour considering the different variants. Both grades have a low and close pearlite content (check microstructure in section 3.1.5) and a very small variation of pearlite content between Reference, Coarse Grain, Globulized Pearlite and With more Bands variants. On the contrary, C45 and C60 grades with higher pearlite content show a more important influence of variants on the flow stress. Quantification of the influence of variants for each grade is given in Table 13. The values of the table are the ones obtained at room temperature (22°C) and $\dot{\varepsilon}$ = 0.5 s^{-1}. What is more, reference value has been taken arbitrarily at 0.2 strain since the order of the curve is kept constant whatever the strain is. The variation with respect to each variant is calculated from this reference value.

*Table 13. Summary of the impact of variant compared to reference grade strain (**ε** = 0.2).*

	Reference value (MPa)at 0.2 strain	Effect of variant (%)		
Grades/variants	R	CG	GP	WB
16MnCr5	773	- 4.46	- 12.52	+ 1.40
27MnCr5	812	- 6.56	+ 4.92	+ 5.14
C45	796	+ 7.12	- 11.80	+ 2.81
C60	872	+ 7.53	- 18.48	
C70	1056			

The Table 13 evidences that some variants have more pronounced influence on grades. As mentioned above, this effect seems highly dependent on the pearlite content, where higher differences have been found. The pearlite content influence on the flow stress is given in Figure 68.

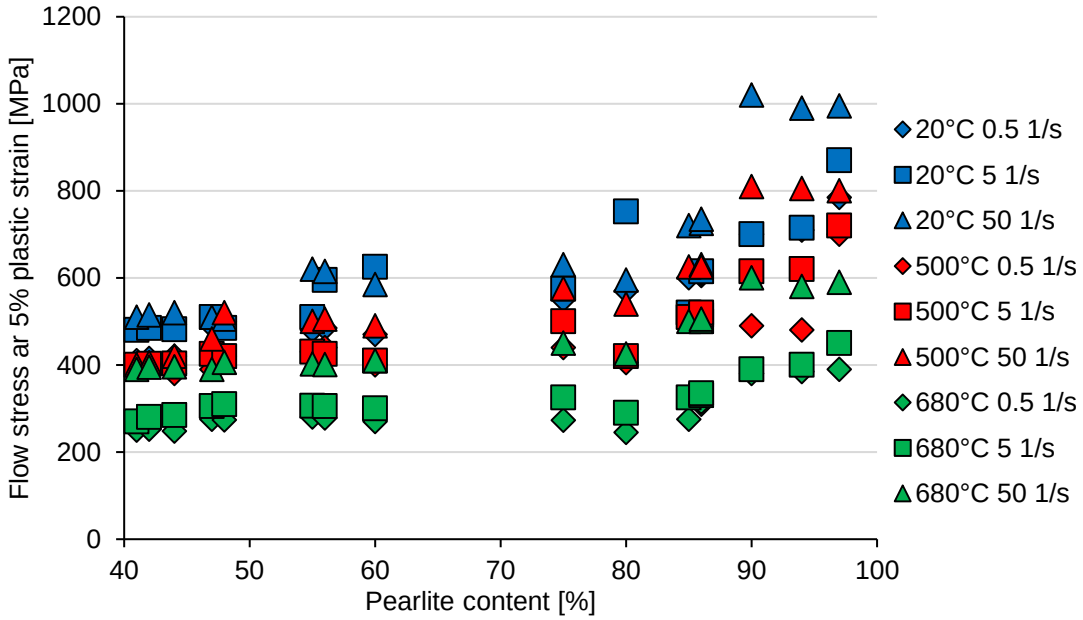

Figure 68. Evolution of flow stress as a function of pearlite content.

It can be clearly seen that the influence of pearlite content is less pronounced with the temperature increase. Strain-rate influence remains the same (higher strain-rate, higher flow stress) whatever is the pearlite content. These observations are of main importance for an accurate description of their behaviour in the model.

3.1.15 Characterisation at high strain rates

The strain rate and temperature dependent deformation behaviour of the steels was studied by the KIMAB research institute using the split Hopkinson pressure bar (SHPB) technique at high strain rates of 500 to 5000 s^{-1}. The method is based on propagation of longitudinal stress waves in long, elastic bars. A schematic illustration of the method is shown in Figure 69. The specimen of interest is placed between two bars, in this case high strength steel bars with 22 mm in diameter and 1200 mm in length. The steel bars have been carefully aligned with respect to each other. A 200 to 400 mm long striker bar of the same diameter and material is accelerated to a velocity of typically 2.5 to 40 m/s using pressurized air. When the striker impacts the end surface of the incident bar, a compressive stress wave is generated. This compressive stress wave propagates in the incident bar at the velocity of about 5800 m/s (in steel) until it reaches the interface with the specimen. At the interface, part of the stress wave is reflected back as a pulse of tension, while the remaining part is transmitted through the specimen to the transmitted bar. The three stress pulses, the incident, reflected, and transmitted, are recorded at the two strain gage stations (Figure 69). An example of the stress pulses generated in the incident and transmitted bars is also shown in the Figure 69. Stress, strain, and strain rate in the specimen were then calculated based on the recorded strain pulses as made by (Vuoristo 2004).

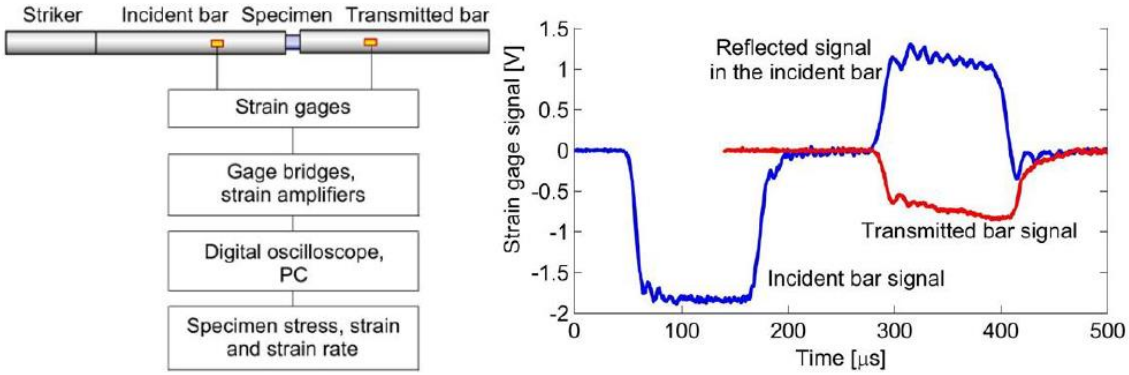

Figure 69.Split Hopkinson pressure bar (SHPB) system schema and strain gage signal (KIMAB).

The tests at elevated temperatures, 500 and 680 °C, were obtained using a computer controlled Split Hopkinson Pressure Bar (SHPB) testing system with a high temperature (HT) system. The system is based on fast pneumatic specimen and pressure bar manipulation devices, which enable heating up of the specimen only and limit the contact time of the hot specimen with cold pressure bars to 50-100 ms (Apostol et al. 2003).

To achieve the desired strain rates and strains in this study without compromising the quality of the test results, two different specimen dimensions were selected. In the high strain rate tests (2000 and 4500 s^{-1}), the specimens are 8 mm in diameter and 6 mm in

length whereas the length in the lower strain rate tests, 500 s^{-1}, is 8 mm. All the specimens were manufactured by EDM, cutting an 8 mm diameter blank of the 60 mm steel bars at half radius. These 8 mm bars were then precision machined to 6 or 8 mm discs.

Behaviour of ferrite-pearlite grades considering strain-rate and temperature

As it was done for low strain rate Gleeble tests, the influence of variants for each grade (16Mn, 27Mn, C45 and C60) is investigated for every temperature and strain rate. The behaviour evolution considering strain-rate and temperature were plot comparing the different variants in each case. For these curves, only the plastic part of the strain was considered. In the Figure 70, the four tested extremes obtained from the C45 can be seen.

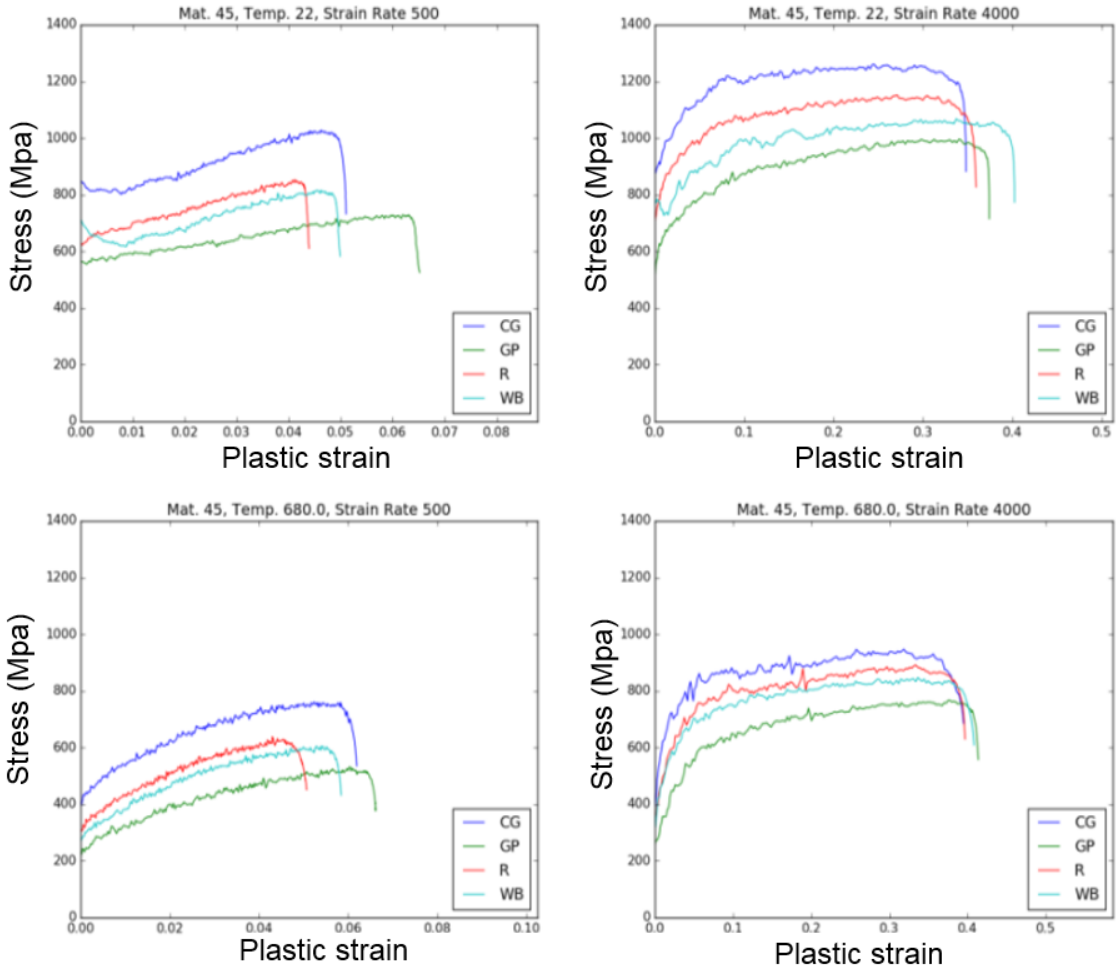

Figure 70. SHPB flow stress curves for C45 in its four extreme conditions T=22ºC-680ºC and ε=500 s^{-1} / 4000 s^{-1}.

It can be observed that for each grade the influence of variants is globally respected for each temperature and strain rate, except for some samples of 27MnCr5 (which should result from artefacts). As it was observed for low strain rates, the influence of variants is

not noticeable for 16MnCr5 and 27MnCr5. A quantification of variant influence on the flow curve response is presented in the next section.

Influence of variants on reference grades

Quantification of the influence of variants for each grade is given in the Table 4. Taking the stress of each of the reference variants it was calculated the impact of variant with respect to the result of reference. The values of the table are the ones obtained at room temperature (22°C) and $\dot{\varepsilon}$=4000 s^{-1}. Then in the first column of the table there are shown the stresses obtained for the reference variants and in the rest of the columns the variation with respect to it.

Table 14. Summary of the impact of variant compared to reference grade's stress at a given strain (ε = 0.2)

	Reference	Effect of variant (%)		
Grades/variants	R	CG	GP	WB
16MnCr5	1066	- 2.50%	- 6.81%	+ 1.02%
27MnCr5	1135	- 6.37%	+ 2.58%	+ 2.91%
C45	1145	+ 5.99%	- 4.09%	+ 2.55%
C60	1205	+ 8.37%	- 8.27%	
C70	1263			

The effect of variants in the stresses at 0.2 strain (Table 14) is similar to the one observed for low strain rates (Table 13). Nevertheless, this effect seems to be slightly reduced (around 5%) for higher strain rates. As mentioned above, this effect seemed to be highly dependent on the pearlite content. The influence of the pearlite content on the flow stress is given in Figure 71.

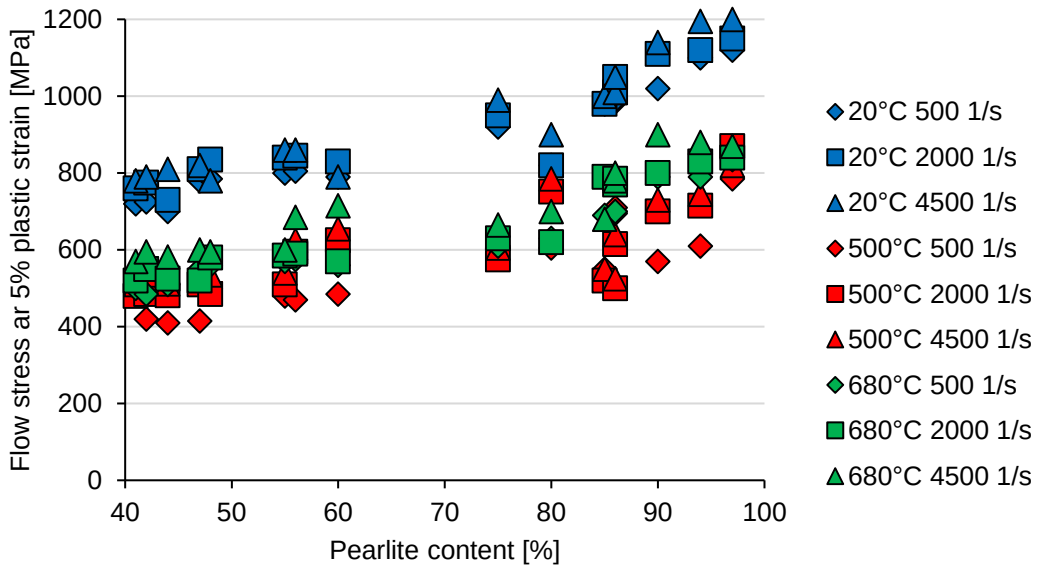

Figure 71. Pearlite content influence on flow stress at high strain rate tests.

3.1.16 Experimental and model comparison

In the previous sections, it has been shown that for an accurate modelling of a ferrite-pearlite steel, the necessary microstructural parameters are the pearlite/ferrite ratio, the interlamellar spacing of perlite and the ferritic grain size. The complete microstructure analysis presented in the section 3.1.5 gives all this information for the different grades. Therefore, the rheology behaviour of our ferrite-pearlite steels at room temperature can be modelled as shown in the annexes (10.1.1). Adjustments need to be done concerning the calculation of true interlamellar spacing from the apparent one measured in the section 3.1.5. Besides, the rigidity of the machine needs to be corrected to obtain the accurate material deformation curve. An example of the results obtained is given in Figure 72.

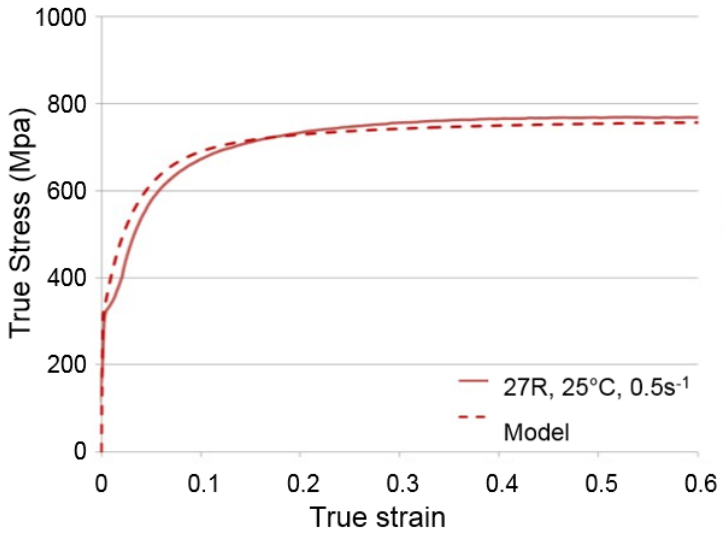

Figure 72. Comparison between the model and the experiment for 27MnCr5 R at room temperature.

This analysis has been done for C70 steel too and the comparison between experimental curve and the model curve is shown in Figure 73. At the beginning of the curve, there is little discrepancy with the accuracy of the elastic limit (given by the interlamellar spacing). As the strain increases from 0.1 up to 0.6, the experimental true stress is constantly around 100 Mpa higher than the model´s one.

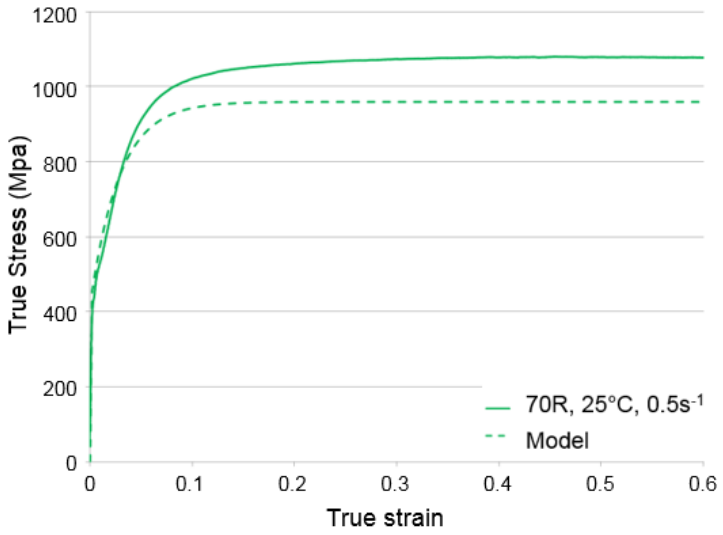

Figure 73. Comparison between the model and the experiment for C70 at room temperature.

3.1.17 Flow stress model

In the following subsection the formula describing the material behaviour is shown. Its development is widely explained in the appendix (10.1.1). So, the different variants (Reference, Coarse Grain, With Bands and Globular Pearlite) are only distinguished in the model by the description of ferrite, the pearlite and the apparition of the DSA (Dynamic Strain Ageing) effect. For the description of GP grades, the interlamellar spacing of the pearlite was taken into account. In order to allow a more appropriate description of the globular pearlite behaviour (cementite carbides in a ferritic matrix), a specific formulation *(Eq. 3.1)* was proposed:

$$\sigma^{pearlite\ G-static} = \left(\sigma_0 + \alpha M \mu \sqrt{b} \sqrt{\frac{1-\exp\left(-f_G M\left(\varepsilon_G^{pearlite}\right)\right)}{f d^{\alpha G}} + 8\left(\frac{F_m}{d_m}\right) \cdot \frac{1-\exp\left(-rM\left(\varepsilon_G^{pearlite}\right)\right)}{r}} + M\mu\sqrt{b}\left(\frac{F_m}{d_m}\right)\sqrt{\frac{1-\exp\left(-r'\left(M\varepsilon_G^{pearlite}\right)\right)}{r'}} + \theta^{IV} \cdot \varepsilon_G^{pearlite} \right) \cdot \frac{\mu(T)}{\mu^0} \qquad \textit{(Eq. 3.1)}$$

Where:

- $d^{\alpha G}$ is the ferritic grain size in globular pearlite.
- F_m is the fraction of cementite carbides.
- d_m is the size of cementite carbides.

- f_G is the dynamic recovery.
- r and r' are saturating parameter of isotropic and kinematic hardening, respectively

This equation is adapted from the formulation proposed for dual phase steels (ferrite steel with low fraction of hard martensite, which is assumed similar to the ferrite steel hardened by large granular carbides) (Allain 2012). The flow stress data were calculated based on this equation and then implemented in the numerical broaching model as tabular data.

3.1.18 Conclusions

The rheology of the different steel grades was studied via compression tests at different temperatures and strain rates. The investigation was focused on the influence of the microstructure on the flow curve for the considered range of temperatures and strain rates. The main results of this study are:

- The higher the pearlite percentage, the higher the flow stress.
- For the lower pearlite contain grade (27MnCr5 and 16MnCr5), the effect of variants is not noticeable. This tendency is independent from the temperature and the strain rate.
- For the higher pearlite contain grades (C45 and C60), CG variants tend to increase the flow stress. On the other hand, GP variants tend to decrease the flow stress. The presence of bands slightly decreases the flow stress of C45, being this tendency also independent from the temperature and the strain rate.

These characterizations were a key work for the cutting modelling performed in the chapter 5 of this research work. A huge amount of data emerged from the experimental characterizations. These data were treated to extract the most representative configuration of cutting conditions. Besides, the interesting feature of DSA was highlighted in the behaviour of all the steel grades. The subsequent modelling task was proved successful to capture the main tendencies of the experimental data considering the microstructure of the steel grades.

Conclusions

The analysis of sixteen ferritic-pearlitic steels was performed studying their microstructure parameters, performing the thermal characterization as well as developing a material behaviour model to be implemented in the cutting FEM.

From 5 different steel grades applying diverse heat treatments sixteen different variants were obtained, showing that same microstructure could lead to different ferrite content

percentages, hardness or grain sizes among other features e.g. 27MnCr5 R (40% ferrite) and 27MnCr5 CG (52% ferrite).

As the thermal characterization is concerned no influence of the microstructure was seen on the values but a correlation regarding the C content more visible in the R and CG variants.

A material behaviour model was developed with a good fitting towards the experimental tests performed both at high and low strain rates. It was seen that the flow stress was especially sensitive to the pearlite content. Furthermore, there was not seen almost any variability between the different variants of low C content grades. Besides this trend was found to be independent from temperature and strain rate.

Chapter 4

ANALYSIS OF THE FRICTION AND WEAR IN THE FP STEELS

4 ANALYSIS OF FRICTION AND WEAR IN FP STEELS

In this chapter, the tribological behaviour of the FP steels is analysed, i.e. the interaction between the material of the tools and the FP steels. Besides the friction coefficient, the wear occurring under certain sliding conditions as well as the friction under lubricated conditions is analysed.

Firstly, a state of the art will be presented to know what has been done until now, then it will be shown the setup and devices used so as to carry out these experiments. Secondly, the results will be displayed and discussed, finishing this chapter with the main conclusions.

Introduction

The machining performance appears to be highly dependent on the microstructural parameters (Klocke et al. 2009). During machining, the low deformability and greater hardness of pearlite cause, on the one hand, significant abrasive wear and high resultant forces (Doane 1988, Ebrahimi, Moshksar 2009). On the other hand, pearlite reduces the adhesion tendency and the formation of built-up edges of ferrite (Akasawa et al. 2004), promotes the formation of favourable chip forms, causes less burr formation on the work-piece and improves the surface quality (Akasawa et al. 2004, Ozcatalbas, Ercan 2003). Under a certain scale, the material clearly cannot be assumed as homogeneous and isotropic (Abouridouane et al. 2012, Mian et al. 2010). Hence, the reasons to study the tribology focused on the machining process in terms of microstructure are given until this point.

To date, it is still not clear how the heterogeneity may affect the tribological interaction between the cutting tool and these different microstructures.

With the aim of improving the fundamental understanding of the FP steel's frictional phenomena occurring at the tool–chip interface (Figure 74) ('secondary shear zone') and at the tool–work-piece interface ('rubbing zone') several researches have been carried out, that will be explained in the following subsections.

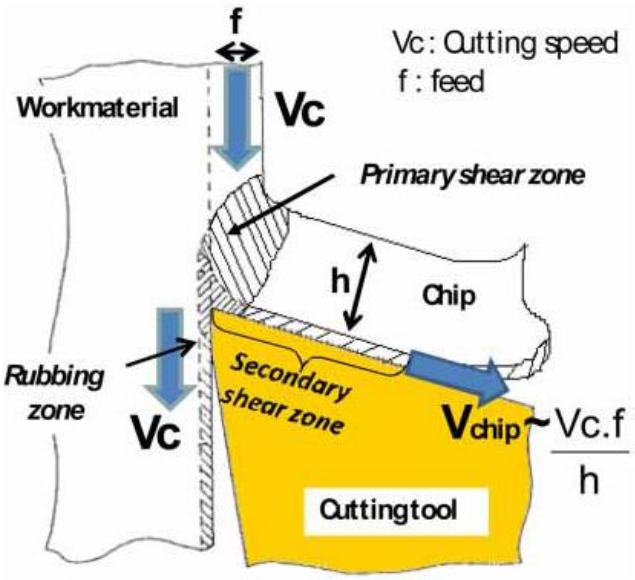

Figure 74. Tool-chip contact interface showing the primary and secondary shear zones (Rech et al. 2008).

4.1.1 Tribology approaches

Tribology is the science and engineering of interacting surfaces in relative motion. It includes the study and application of the principles of friction, lubrication and wear. Tribology is a branch of mechanical engineering and material's science.

In order to investigate experimentally the tribological phenomena at the tool–chip ('secondary shear zone') and the tool–workpiece interface ('rubbing zone') interfaces, scientists consider two approaches. The first approach consists in using the cutting process itself (M'Saoubi, Chandrasekaran 2005, P. Arrazola et al. 2008, Rech 2006, Grzesik, Nieslony 2004). The second one consists in using laboratory tests (Olsson et al. 1989, Hedenqvist, Olsson 1991, Hogmark et al. 1997).

Cutting process tests

Concerning the tribological based on cutting tests, (Albrecht 1960) already obtained friction values based on the formula (see Eq. 4.1.1) given by (Merchant 1945). The former obtained friction coefficients of around 0.19 on a 81b 45 steel at 244 m/min.

$$\mu = \frac{F_t + F_c \cdot \tan \alpha}{F_c - F_t \cdot \tan \alpha} \qquad \textit{(Eq. 3.1)}$$

Grzesik and Nieslony recorded it directly using orthogonal cutting (Grzesik, Nieslony 2004). Cutting forces obtained from a dynamometer were converted into the friction coefficient. They also measured contact areas, lengths and chip thickness after performing the essays. In the Figure 75 it can be seen the scheme of the tool–workpiece setup showing the input and outputs as well as the variables obtained after the process.

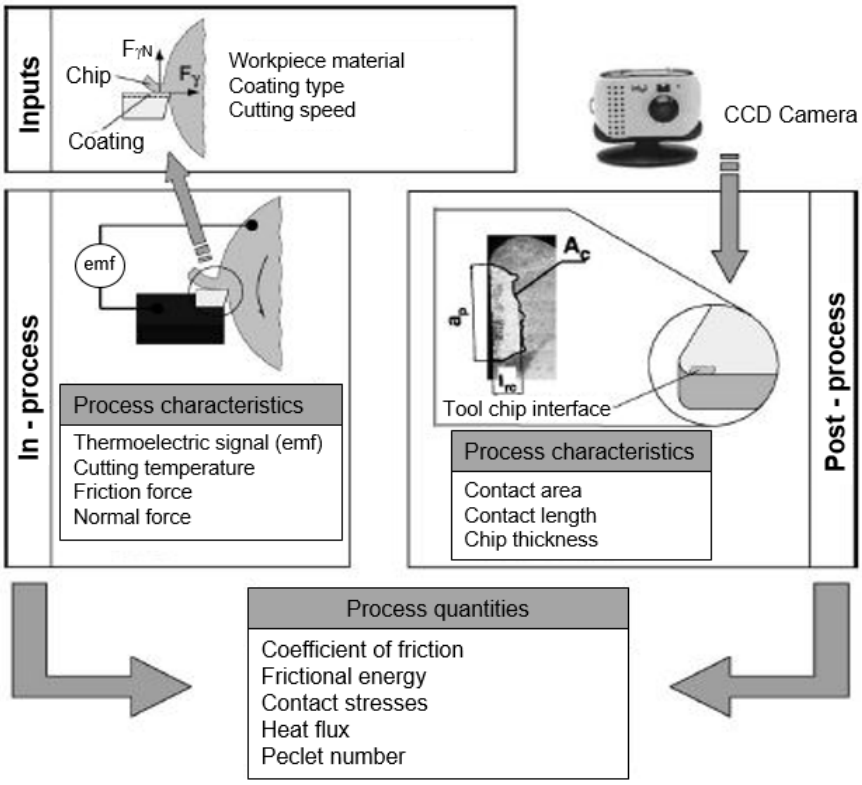

Figure 75. Experimental setup developed by (Grzesik, Nieslony 2004).

In addition, (Rech 2006) made an experimental research in an orthogonal cutting setup for a sole cutting condition (V_c=200m/min, a_p=3mm, feed=0.15mm/rev). He studied and compared experimentally the frictional behaviour and the wear of different coatings in a WC-Co substrate tool over a 27MnCr5 steel obtaining the values shown in Table 15.

Table 15. Friction coefficient (CoF) values obtained by (Rech 2006) using WC-Co over 27MnCr5 steel.

	Uncoated	TiN	TiAlN	TiAlN + MoS_2
CoF (μ)	0.82	0.80	0.80	0.78

Another work using a cutting process is the one carried out by (Franchi et al. 2016). Following an inverse method, they obtained data to be implemented in a finite element model of machining. In this way, they minimized the error between numerical results and experimental data related to the F_c, F_t and temperatures. For this purpose, a specific orthogonal cutting FE model, developed with AdvantEdge 2D and in parallel experimental tests in the radial feed direction were performed as it can be seen in Figure 76. Their methodology focused on both the identification of the Johnson-Cook (JC) coefficients (A, B, C, n and m) and on the calibration of a Coulomb friction model at the same time. Anyway, this kind of works are quite problematic as different coefficients may lead to obtain same results, so it can be said that this method it is not very trustworthy.

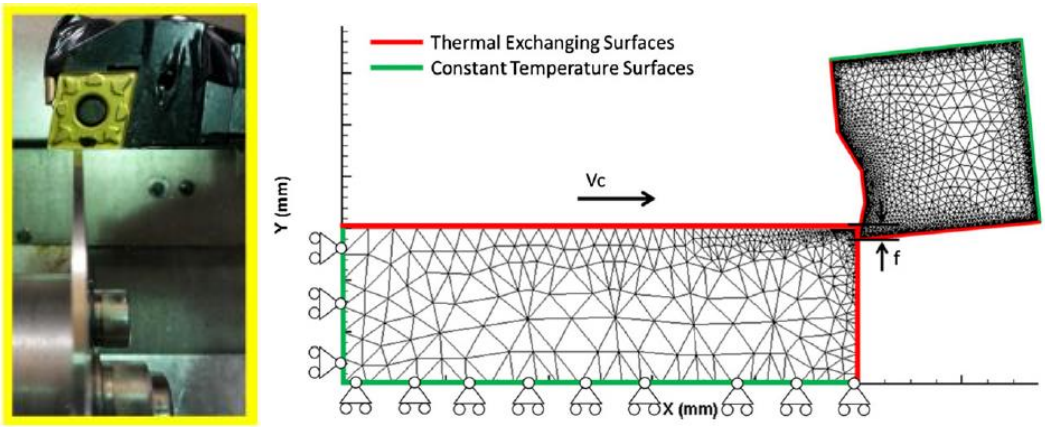

Figure 76. Right: Experimental set-up considering the radial feed direction and left: cutting FE model used by (Franchi et al. 2016).

Laboratory researches

This kind of investigation works are the most usual methods, which enable to master much more accurately the contact conditions and to modify these conditions as desired. There are two main advantages of doing laboratory tests compared to full-scale machining tests (Olsson et al. 1989):

(I) The simplified specimen geometry makes easier to manufacture specimens from experimental batches of new tool materials.

(II) In a realistic tool life test, tool performance is a function of both tool wear and edge chipping. By using a dedicated wear test, it should be possible to dissociate the contribution of each effect. In addition, two or more wear mechanisms are generally active simultaneously in metal cutting. By proper choice of laboratory testing conditions (work material, sliding speed, and normal force), it is possible to evaluate the wear resistance against each individual wear mechanism separately.

(Puls et al. 2012) developed a new experimental methodology to analyse the friction behaviour. They tested the C45 steel in normalised state using an orthogonal cutting setup but instead of cutting, roughing the workpiece against the flank face (Figure 77). They found that the increase and decrease of the forces were related to the increasing and decreasing deformed layer thickness within the feed. They did not only measure the friction coefficient versus the sliding speed but also the temperature above the contact zone. Analysing both, surprisingly, they did not find any influence of the temperature in the friction coefficient.

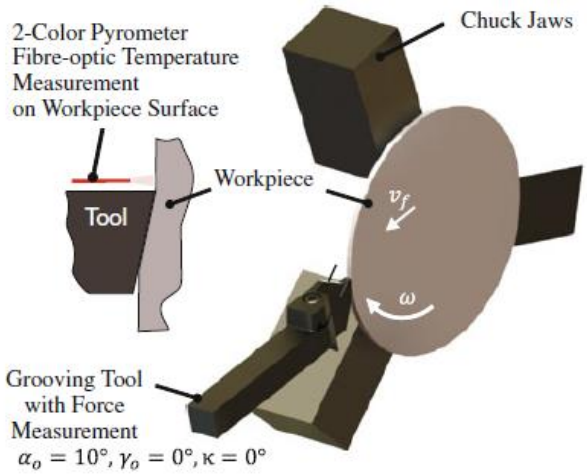

Figure 77. New experimental setup developed by (Puls et al. 2012).

The most widely known set-up is the pin-on-disc (POD) system. However, this method is called a closed tribo-system as the pin always rubs on the same track. In order to obtain reliable results of tool-chip-workpiece tribological phenomena an open tribo-system is needed (Olsson 1988). The open tribosystem is much more similar to a real cutting process because, generally, the tool encounters a new surface or at least a surface which has been previously machined.

The laboratory experimental studies can be split into two different types:

1. Closed tribometers: where the pin rubs on the same single track and the surface is not refreshed.
2. Open tribometers: in which the surface is renewed after the pin passes or the pin rubs always in a new surface.

- <u>Closed tribometers:</u>

The most common of the closed tribometers used is the so-called pin-on-disc system. In these devices, the pin rubs on the same surface after the first turn as it is explained by (Bahrudin et al. 2013). The experimental setup can be seen in the Figure 78 where the pin is hold in an arm and the load is applied with a dead weight pending with a wire. As its own name says, the track is done on a disc following in all the cases the same path.

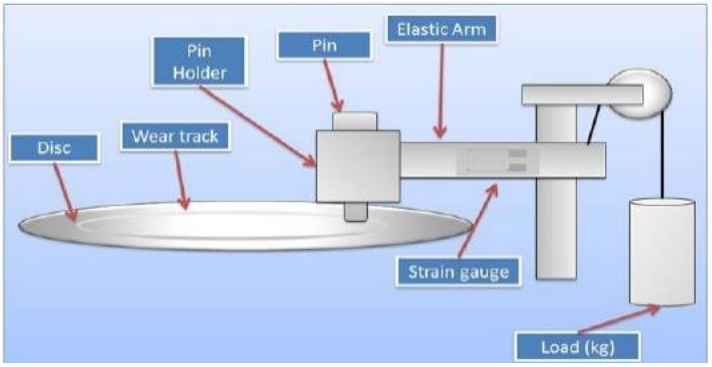

Figure 78. Pin on disc measure system used by (Bahrudin et al. 2013).

In this research there is made the frictional study on not specified materials, but it is highlighted that the addition of a lubricant significantly reduces the friction coefficient, something pointed by many researches, which is commonly accepted in the general literature.

Grzesik et al. designed a long sliding distance laboratory-testing device, employing a special equipment layout based on line type of contact between a cylindrical specimen (round insert) and a flat rotating disc as illustrated in Figure 79 (Grzesik et al. 2002). This tribometer can measure the friction force F_f and the linear wear of the coupling materials as a function of the sliding distance. This friction test were used to investigate the wear resistance of some cutting tool coatings under very high sliding speed (0.5–3 m/s) and high long test time (1200s). However, the contact pressure remains insufficient to simulate the contact conditions occurring at tool-chip-workpiece interfaces. Moreover, the pin rubs on a single track with a surface that is not refreshed. Sliding on a continuously work hardened layer is believed not to properly simulate the real machining process.

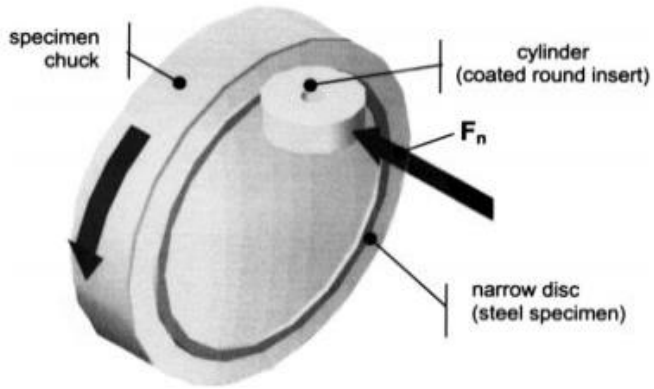

Figure 79. A scheme of the tribo-pair configuration used in the investigation performed by (Grzesik et al. 2002).

Conversely, Su et al. developed a wear system called SRV with a configuration consisted of a fixed lower specimen supporter and a replaceable upper specimen holder (Figure

80) (Su et al. 2004). The upper specimen is a cylindrical block, while the lower specimen is a coated disk. The cylinders used as upper specimens (counter bodies) in the SRV tester were AISI 1045 (C45) steel (Hv 295) cut off directly from round bars and then mechanically polished to a roughness of Ra=0.32µm. The uncoated lower specimens used as coating substrates were tungsten carbide (WC) containing 6 wt. % cobalt, so WC-Co. They performed and compared friction and wear tests highlighting the influence of the chromium coating in both.

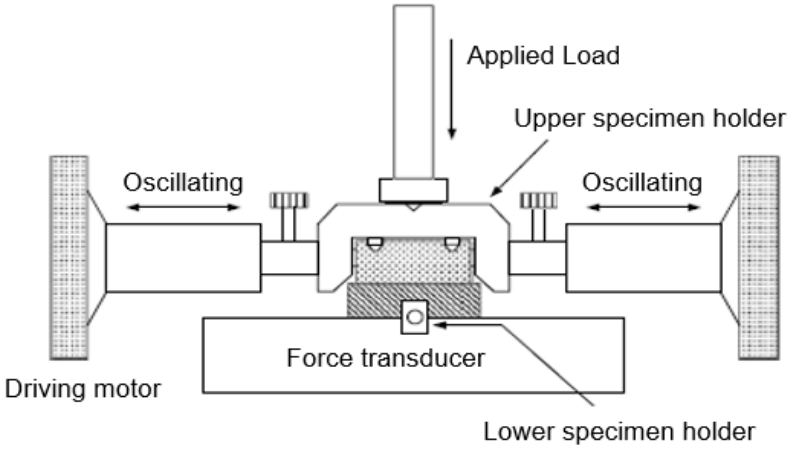

Figure 80. The SRV wear system developed by (Su et al. 2004).

There are more researches using the pin-on-disk devices (Abouei et al. 2007, Çetin 2011, Gündüz et al. 2008). Abouei et al. explained the friction, wear rate and wear coefficient of the steels with respect to microstructure, being one of them FP type. They reported a decrease in the friction coefficient for low applied forces and for high hardness. Nevertheless, the results cannot be comparable to the ones that are obtained in machining (2000 - 6000 N/mm^2) as the pressures they used are very low (0.55 - 1.19 N/mm^2).

Same problem happened to Çetin who performed tests with ferritic and pearlitic ductile iron, but they did not display the FP ratio data (Çetin 2011). What is more, in this case again low forces and speeds were applied being hard to link and compare these results to others obtained in turning conditions.

Another pin-on-disc study was made by Gündüz et al. performing tests with two different microalloyed medium carbon-forging steels with a FP microstructure (Gündüz et al. 2008). These two steels were heat treated in 3 different ways obtaining in this way 6 different microstructures regarding the FP% content and grain sizes (Table 16). Concerning the material used, this is the closest study to our research that has been found in the literature review. Anyway, they did not report any friction coefficient but wear rate as well as roughness in terms of each variant's hardness.

Table 16. Volume fraction of ferrite and pearlite and mean linear intercept grain sizes of as-received, sand and air-cooled samples (Gündüz et al. 2008).

Steels	Ferrite (%) $\pm \sigma$(St. dev.)	% Pearlite $\pm \sigma$(St. dev.)	Grain size (μm) $\pm \sigma$(St. dev.)
Steel-1, as-rec.	30 ± 2.0	70 ± 2.0	13 ± 0.4
Steel-1, sand	19 ± 1.7	81 ± 1.7	15 ± 0.5
Steel-1, air	21 ± 1.8	79 ± 1.8	12 ± 0.4
Steel-2, as-rec.	35 ± 2.1	65 ± 2.1	10 ± 0.3
Steel-2, sand	30 ± 2.0	70 ± 2.0	8 ± 0.3
Steel-2, air	33 ± 2.1	67 ± 2.1	6 ± 0.2

In short, many tribological studies using the pin-on-disc or similar closed tribometers have been seen through the literature review. This method cannot be used as reference to compare with results obtained in machining or use as inputs in models mainly due to two reasons:

a) The pin always rubs on the same track while in machining the tool always passes over a refreshed surface or, at least, over a machined surface.
b) The applied forces or pressures and sliding speeds are far from those obtained in any cutting operation ($2 \cdot 10^3$ higher).

- Open tribometers:

Open tribometers are characterised by a pin continuously sliding on a refreshed surface. In this way, different experimental setups have been developed over time.

One of the first approaches of the open-tribosystem was proposed by Olsson et al. (Olsson et al. 1989) in which the pin rubs on a refreshed surface in contact with the air (Figure 81). The basic idea is to obtain a contact situation where the tool material continuously slides against a fresh work material surface while maintaining the simplified test geometry of a standard wear test. The performance of the new test method has been evaluated for high-speed steel sliding against a quenched and tempered steel. In spite of getting reliable results, the contact pressure remains low (25.47 N/mm^2 as maximum), due to a lack of rigidity of the system and to a risk of chip formation in front of the pins.

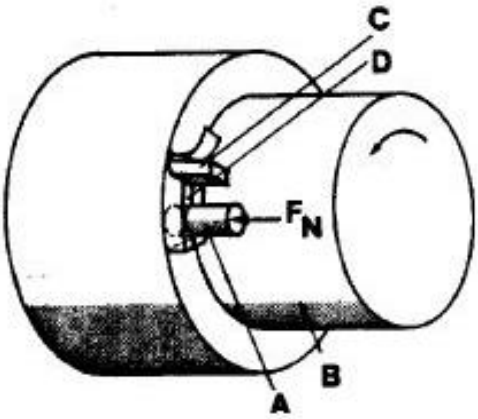

Figure 81. Schematic illustration of the modified pin-on-disc test geometry with test pin (A), workpiece (B), cutting tool (C) and argon gas inlet (D) (Olsson et al. 1989)

Olsson installed an argon gas inlet focusing it to the renewed surface Figure 81D. In this way they avoided to perform the tests on an oxidized surface keeping the surface free of oxygen. In these tests, they used two different grades of HSS pins (M2 and the M4) to be run on an AISI 4340 (40NiCrMo7). Anyway, in the tests carried out, they did not found high contribution of this in the results Figure 82.

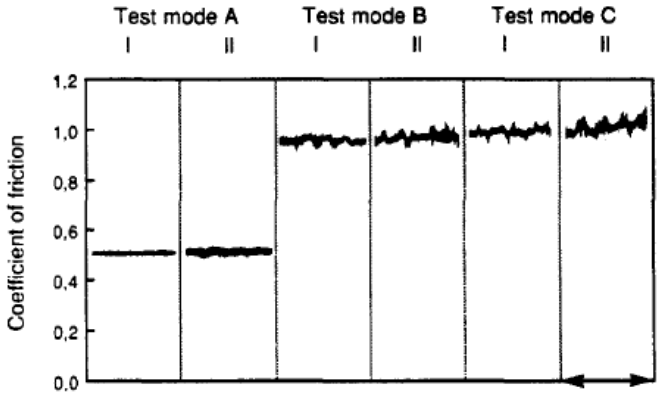

Figure 82. Test mode A: same surface roughing performing wear tests, Test mode B: new contact surface in air atmosphere & Test mode C: new contact surface in argon atmosphere. (Olsson et al. 1989)

In order to fix the problem of low contact pressure of the latter, Zemzemi et al. (Zemzemi et al. 2007) developed another tribometer inspired from the latter, as seen in the Figure 83, in which high contact pressures can be applied Zemzemi et al. 2007). However, in this new tribometer the set-up is very difficult to manage, and the manufacturing of tubes is very long and expensive. Moreover, the cutting tool interacts with the pin friction and as the cutting speed increases the surface temperature increases as well. Therefore, roughness is also modified disturbing this way the friction coefficient measurements.

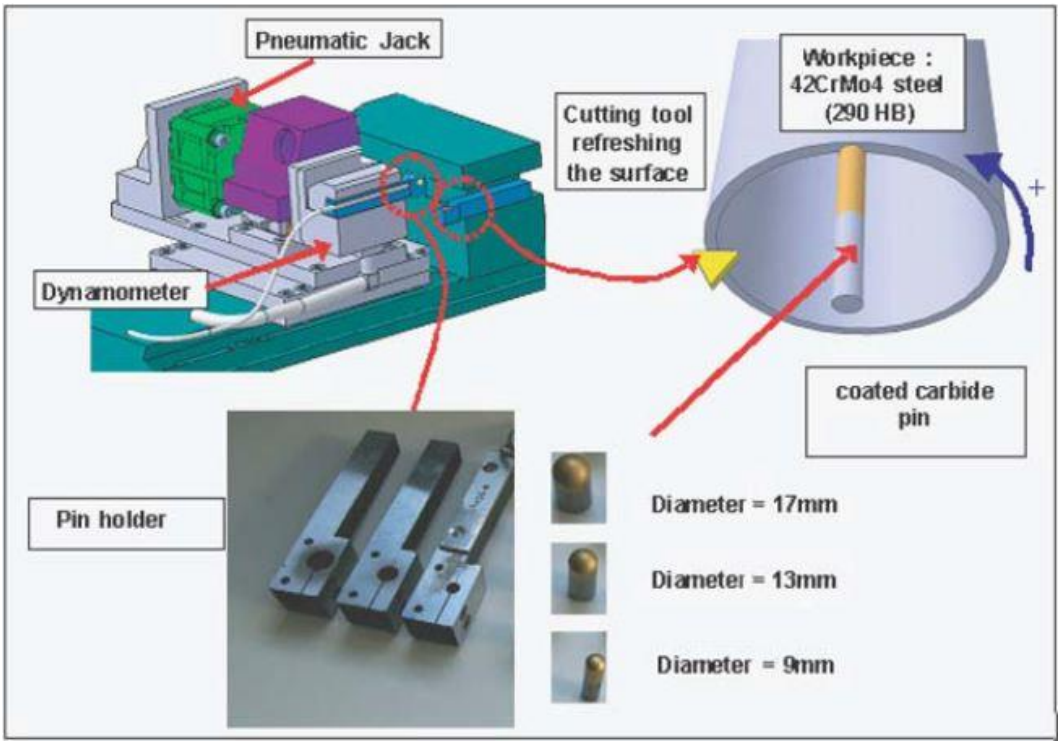

Figure 83. Illustration of the tribometer installed on a lathe (Zemzemi et al. 2007).

Smolenicki et al. developed a similar system to measure friction coefficients during orthogonal turning process on a lathe as shown in Figure 84 (Smolenicki et al. 2014). The tribometer consists of a spring preloaded tungsten carbide pin with a 3mm spherical tip mounted behind the cutting edge and rubbing on the freshly generated workpiece surface.

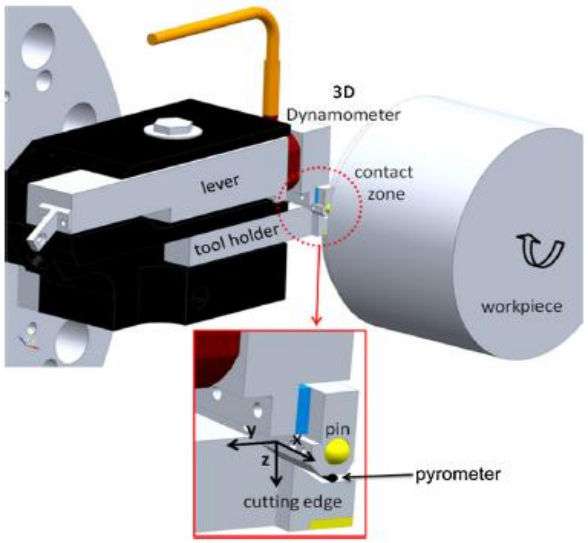

Figure 84. Orthogonal cutting system developed by (Smolenicki et al. 2014).

As the contact pressure was found to be low 25.47 (N/mm^2 as maximum), a new tribometer was developed by Hedenqvist and Olsson (Figure 85) (Hedenqvist, Olsson 1991). A pin, having a cylindrical geometry rubs on a refreshed surface in rotation. The

pin linear movement along the axial direction gives the helical movement while the bar is rotating. The application of conventional cylindrical bars facilitates tests preparation since such kind of bars can be easily provided by any steelmaker. Once the whole surface is used, surface regeneration can be made by a longitudinal turning operation. This system was not able to provide sufficient local pressures (about 15 MPa) compared with some GPa obtained in cutting to simulate the tribological phenomena exhibited during the machining process.

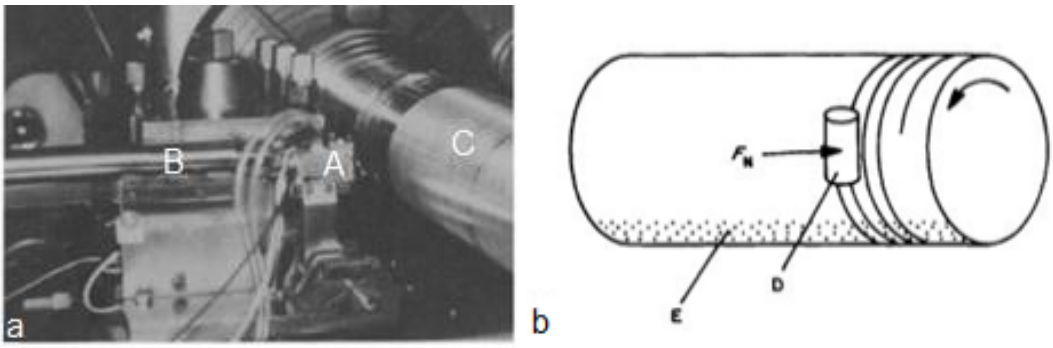

Figure 85. a) The pin-on-ring test set-up pin holder (A), loading mechanism (B) and counter material (C). (b) Schematic drawing of the test set-up, with test pin (D) and counter material (E) (Hedenqvist, Olsson 1991)

With the aim of avoiding the problems found in the previous setup by Zemzemi et al. (Zemzemi et al. 2007), a new tribometer was designed and shown for the first time (Rech et al. 2008) shown in the Figure 86 (Mondelin et al. 2011). Pins made by a similar material of the cutting tool and workpiece material is also similar to the cutting material were used in order to obtain reliable friction coefficients. Once the test is performed, the surface is refreshed by turning the bar. In order to reduce the potential influence of surface roughness, a good finishing operation is done by increasing speed and reducing the feed or by applying a belt finishing process.

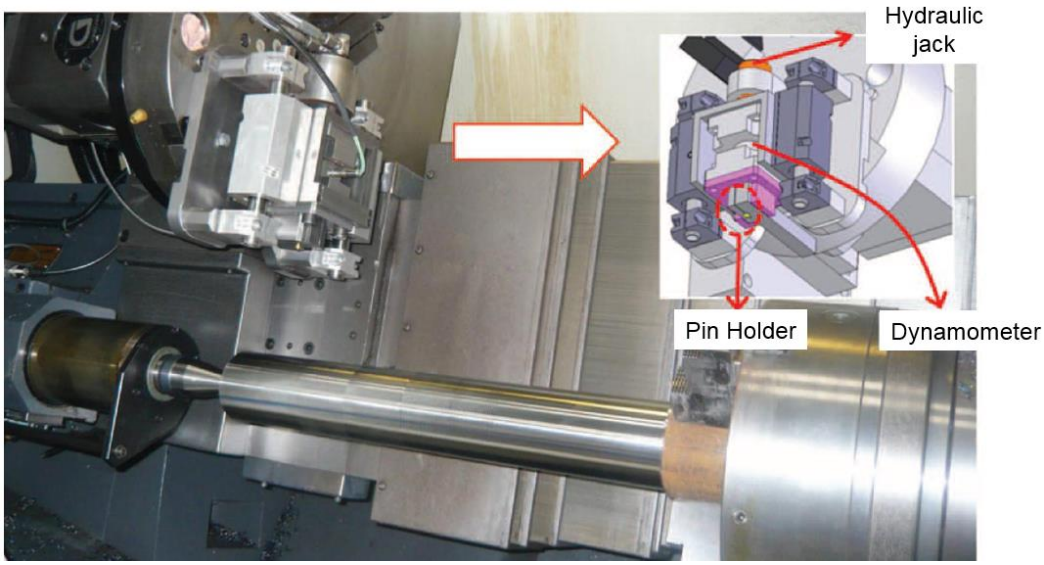

Figure 86. Open tribometer setup on a turning CN machine (Mondelin et al. 2011).

In the Table 17 the pros and cons of the tribology systems are shown and the setup in Figure 86 was decided to be used in the development of this research. It is assumed to be the most suitable as it gets the best approach to the cutting process due to these reasons:

- The pin always rubs on a new surface.
- The resulting contact pressures are close to those obtained in the real cutting processes.

Many of these researches have been focused on the study of the friction coefficient on the C45 steel (Ben Abdelali et al. 2011, Rech et al. 2009). The influence of inclusions was extensively studied (de Eguilaz et al. 2010) but until now nobody has analysed the influence of its microstructure.

At last, going across the researches with reference to FP steels, no study has yet clearly reported the exact contribution of ferrite/pearlite ratio, morphology of the pearlite, interlamellar spacing or even grain size on the tribology field. Hence, it is the reason to fulfil this research gap.

Table 17. Tribology studies summary table.

Tribo studies summary		
Cutting processes	Close tribometers	Open tribometer
(Rech 2006) (Grzesik, Nieslony 2004) (P. Arrazola et al. 2008) (Albrecht 1960)	(Gündüz et al. 2008) (Çetin 2011) (Abouei et al. 2007) (Su et al. 2004) (Grzesik et al. 2002) (Bahrudin et al. 2013)	(Olsson et al. 1989) (Hedenqvist, Olsson 1991) (Zemzemi et al. 2007) (Rech et al. 2008) (Rech et al. 2009) (de Eguilaz et al. 2010) (Ben Abdelali et al. 2011) (Puls et al. 2012) (Smolenicki et al. 2014)
Advantages		
- Real material/tool contact obtaining real friction coefficients.	- Possibility to perform long wear tests.	- The pin always rubs on a new surface. - The contact pressures are close to those obtained in the real cutting processes.
Disadvantages		
- Material, tool and time wasting tests.	- Far from the pressures obtained in machining processes.	- In contact with the air so the contact is done on a oxidized surface.

In the tribology history, many devices were designed trying to simulate the tool-workpiece contact occurring in machining. Although, some researches obtained the friction values directly from cutting tests, this was proved to be time and material consuming. On the other hand, the closed tribometers were proved also useless to simulate the machining contact. Finally, the open tribometers has suffered an evolution throughout the time up to the machine developed in the ENISE, which with its limitations is able to provide reliable friction data.

Tribological study setup

In this research laboratory tests were carried out as done by (Ben Abdelali et al. 2011) and (Rech et al. 2008). The setup was a special dedicated open tribometer used to study the macroscopic tribological behaviour of the steel variants.

Besides the influence of the sliding speed, the frictional behaviour was studied in terms of the following microstructural parameters:

- Ferrite/pearlite content (Ferrite percentage indeed as the pearlite is its complementary).
- Ferrite's grain size.
- Pearlite's interlamellar spacing.
- Hardness.

The tribometer was mounted on a CNC lathe (Figure 88a) and the friction at the cutting tool/machined material interface is estimated by the contact of a pin having a spherical geometry against a cylindrical bar (Figure 88 (c) and (d)). The pin was made of same grade as the cutting tool used in the target operation and the cylindrical bar was made of the same grade as the machined material (the above-mentioned FP steels). In order to eliminate the potential influence of surface roughness, pins were grounded and polished (Ra = 0.3 µm similar to a cutting tool). Anyway, before doing tests with them, they must be polished and cleaned (Figure 87) to remove any impurity adhered in the transport. Therefore, firstly, the pins were cleaned with acetone. Then the polishing process was carried out using diamond paste to eliminate possible flat surfaces in the spherical surface. Finally, they were cleaned again with acetone to eliminate any rest of oil that could affect to the test reliability.

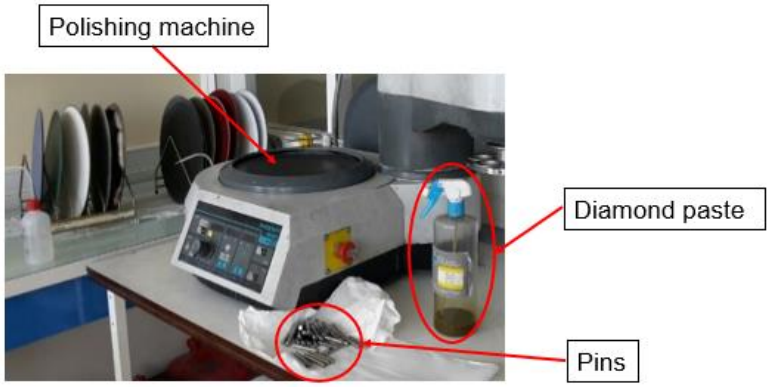

Figure 87. Polishing device and paste used to clean the pins.

After each friction test, a cutting tool refreshed the surface (Vc = 180m/min & f = 0.2 mm) ploughed by the pin, to remove the affected layer of workmaterial. Each friction test lasted at least 7 s so as to obtain a stationary situation. The pin-holder was fixed onto a

dynamometer (Figure 88 (e)) to provide the normal (F_n) and tangential (F_t) force (macroscopic forces). The desired normal force was assured with controllable hydraulic jack (Figure 88 (c)). The friction coefficient (i.e. macroscopic friction coefficient) is provided by the ratio of the two forces obtained with the piezoelectric sensor (Eq. 4.2):

$$\mu_{app}=\frac{F_t}{F_n} \qquad \textit{(Eq. 4.2)}$$

Apparent friction coefficient is used because it can slightly differ from the interfacial friction coefficient. These forces measured by the tribometer also include adhesion phenomena and plastic deformation.

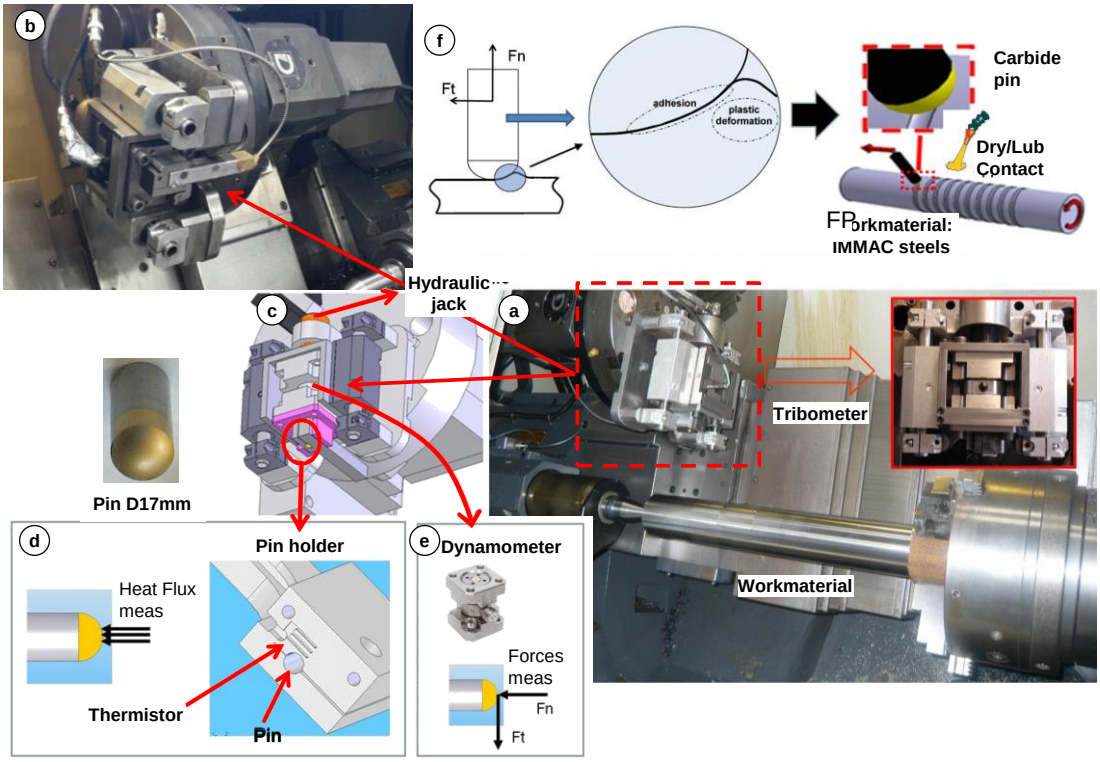

Figure 88. Detailed view of the setup: a) tribometer and workmaterial, b-c) view of the tribometer on the turret, d-e) existing instrumentation and f) close view on the sliding configuration.

4.1.2 Methodology

Two different studies were performed, on one side a fundamental study (0) using WC-Co pins and doing tests at 10, 100 & 300 m/min over a wide range of FP steels. On the other side, a broaching process focused study (0) i.e. performing the tests at lower speed so as to obtain friction coefficients that will be used to feed the numerical model. In this test campaign HSS M35 pins were used at 2, 20 & 60 m/min over the same batch of FP steels. This way friction coefficients were obtained over the whole bunch of FP steels but, although it was mounted, there was not used the thermistor to obtain the heat transmitted from the material to the tool.

Fundamental study's methodology

The first campaign (fundamental study) was focused on dry contact under turning conditions using coated carbide pins.

This campaign aimed at providing quantitative data to be input in numerical models but also to gain a fundamental understanding of how microstructural parameters can affect the tribological behaviour with a coated carbide pin. A wide range of sliding velocities was then selected to cover the mechanisms that could appear at high speeds but also at lower sliding velocities.

The following table (Table 18) summarizes the conditions employed in this campaign.

Table 18. Selected design of experiments for the fundamental study

Variables	Values
Contact force (N)	1000
Sliding speeds (rotation) (m/min)	10, 100 & 300
Lubrication	Dry
Pin (geometry Figure 88)	WC-Co (H13A) + TiN coated
Replicates per condition	3

It was seen through the literature that the selected three speeds (10, 100 and 300m/min) reported the main trend in terms of friction when using these carbon steels (Rech et al. 2013). Three conditions were enough to provide a reliable trend. Moreover, extending the objective of these tests, the selected speeds could be used to extrapolate the results to other cutting operations: 10 (speed related to broaching operation), 100 (speed related to drilling) & 300 (speed related to turning) m/min (Handbook 1990).

Three repetitions were performed for each sliding condition and sometimes one more leading to a total of 140 experiments. Based on some preliminary analyses showing no wear and sticking tendency, the same pin was used for the three tests at 10m/min. The tests at 100 and 300m/min were performed using one pin per test as the pins were clearly worn after one test or presented a too high adhesion.

Broaching focused methodology

As well as in the fundamental study, this campaign aimed at providing quantitative data to be implemented in the numerical models but also to gain a fundamental understanding

of how microstructural parameters can affect the tribological behaviour with a coated and uncoated HSS pin. The design of experiments is summarized in Table 19.

Table 19. Selected design of experiments for the broaching focused tribological study.

Variables	Values
Contact force (N)	1000
Sliding speeds (rotation) (m/min)	2 (linear), 20 & 60
Lubrication	Dry & Lubricated (just at 2m/min)
Pin (geometry Figure 88)	M35 HSS uncoated & TiN coated
Replicates per condition	3

After performing some preliminary tests at 300 and 1000 N (Figure 89), it was decided to perform the whole set of experiments only at 1000 N as no drastic difference were observed between these two normal loads. 1000 N also enables to perform the tests at a contact pressure of approximately between 1-2 GPa which is consistent with what is expected to occur at most of the tool-chip interface (Trent, Wright 2000).

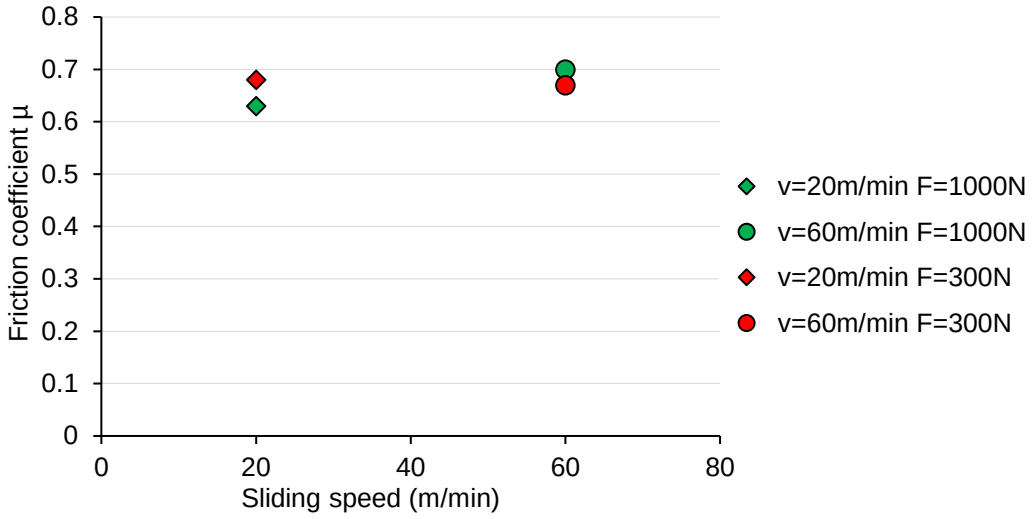

Figure 89. Friction versus speed in C45R material using HSS-M35 as tool material for the comparison of 300 N and 1000 N.

First, the essays were performed in dry conditions to amplify the possible differences between the variants and not to introduce, in this first step, a third body at the interface (Claudin et al. 2010). However, in a second bunch of tests, the use of the lubrication at 2m/min was implemented with the aim of getting its contribution to the frictional behaviour and to obtain the quantitative data so as to be implemented in the numerical models.

Broach teeth are most of the time TiN coated on the flank face and uncoated on the rake face (Figure 11 and Figure 90). Therefore, TiN coated (COA) but also uncoated (UNC) HSS pins have been used to clearly dissociate the contribution of the coating.

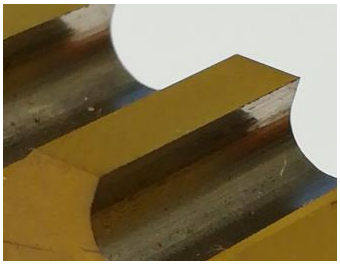

Figure 90. Broach tooth coated on the flank face and uncoated on the rake face.

Friction results in fundamental study

This part of the study was named as fundamental study since a big part of steel machining works is performed with carbide's tools (Handbook 1990).

The first section will be focused on the name given to the steel variants and the following one to the microstructural features each one of the steels has. In a third section, the contact zones and mechanisms occurring in the pins will be shown as well as the wear occurring at the highest speed (300m/min) as it is also considered an important part of the tribology.

4.1.3 Friction coefficient depending on sliding speed

In a first instance, the results were plotted versus the sliding speed. The colour and shape code was set as shown in (Table 5): yellow for the 16MnCr5, green for the 27MnCR5, blue for the C45, red for the C60 and black for the C70. The shape given to each of the variants was circle for the standard (R) i.e. as it is usually manufactured for the automotive industry), diamond shape for the Coarse Grain (CG) variant, triangle for the Globular Pearlitic (GP) and square for the With more Band (WB) variant.

There were not performed tests at 300 m/min with the C70 variant since the size of the bar that it was too small. Due to this, not only would not reach to steady stable state but there would appear chatter problems.

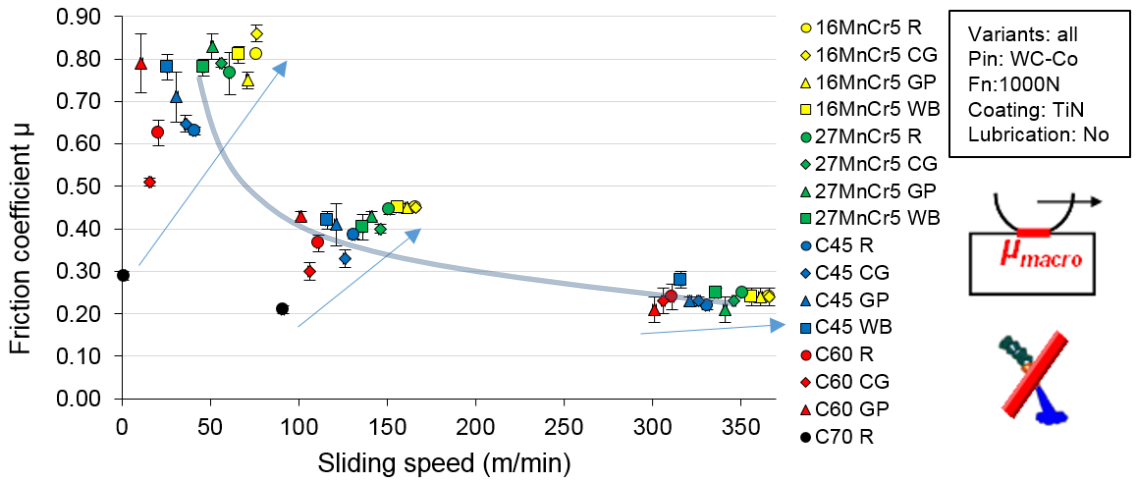

Figure 91. FP steel's friction coefficient versus sliding speed with carbide pins.

The Figure 91 clearly shows that the driving parameter in the friction coefficient's results is the sliding speed. Although there were differences among grades and variants, it could be seen that higher friction values were obtained for the lowest speed. For each sliding speed, there were differences between steels being quite huge (between 0.3 and 0.87) for the lowest (10 m/min). For the medium sliding speed (100 m/min) the differences were lower (between 0.2 and 0.45) and for the highest speed (300 m/min) the difference between the lowest and highest friction coefficient was 0.7 (0.21 the lowest and 0.28 the highest). Anyway, almost all the obtained values were 0.23 ± 0.2.

Friction coefficient versus sliding speed 'Reference' variant

Going through the differences between grades, if the attention is focused on the standard variant in the Figure 92, at the lowest speed, the lower the carbon content, the higher the friction coefficient is.

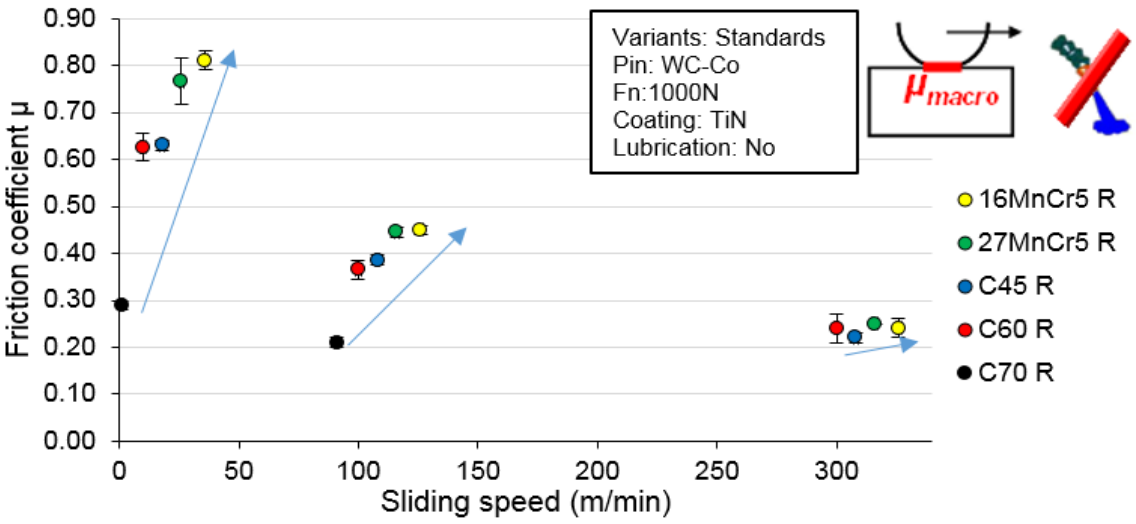

Figure 92. Standard FP steel's friction coefficient versus sliding speed.

For the medium speed, same behaviour was observed but for the highest speed there was not observed any change being all the values around 0.24.

Friction coefficient versus sliding speed 'Coarse Grain' variant

Checking the Figure 93, in which the coarse grain variants were plotted versus the sliding speed, it can be seen the same trend obtained with the standard variant steels but even more clearly and higher differences.

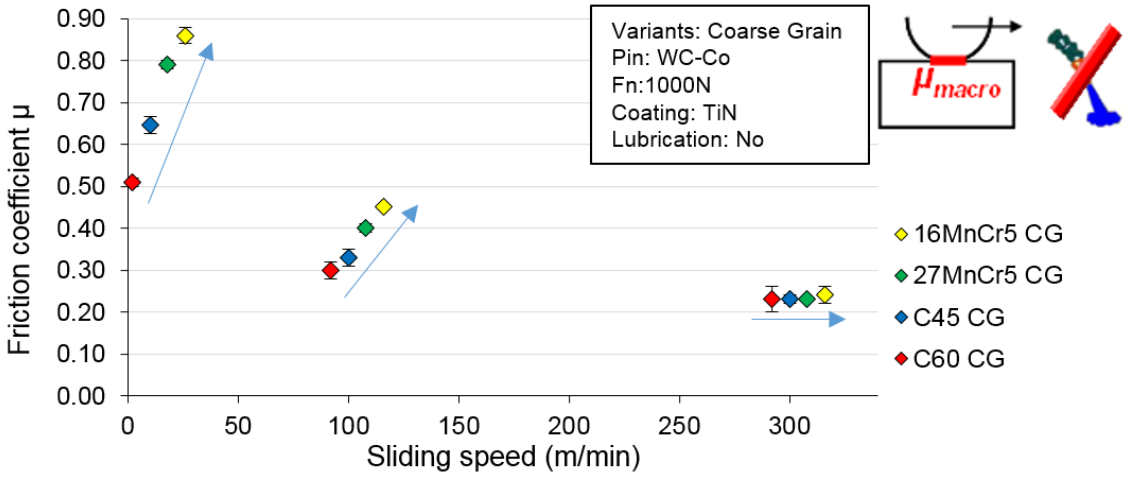

Figure 93. Coarse Grain FP steel's friction coefficient versus sliding speed.

For the highest speed, an equalization of the results occurs driving them to have the same value (0.23) being independent from any of their composition feature.

Friction coefficient versus sliding speed 'Globular pearlitic' variant

In the Figure 94, it could be seen that the trend previously seen completely disappeared for the lowest and medium speed. For the highest speed, the behaviour of the friction coefficient was the same whatever the steel is, with a value of 0.21 ± 0.1.

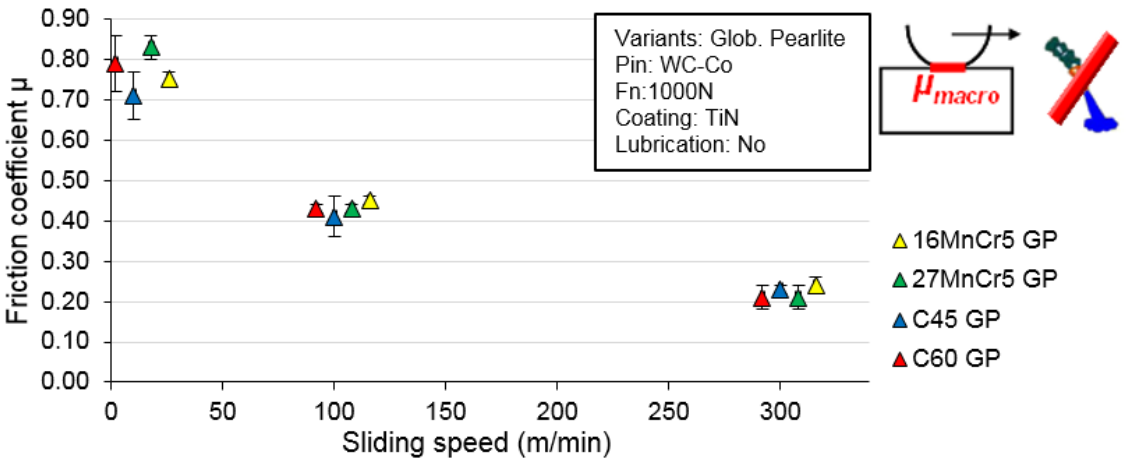

Figure 94. Globular Pearlitic FP steel's friction coefficient versus sliding speed.

Friction coefficient versus sliding speed 'With more Band' variant

When analysing the WB variant (Figure 95), it has to recalled that the C60 was not manufactured in this variant, so we have just three steels. Going through the friction coefficient trend, it can be seen, as in the previous one, that there are not consistent trends depending on any composition feature. Checking the values, they are around the same value in each speed regime, but the trends change completely from speed to speed as it increases.

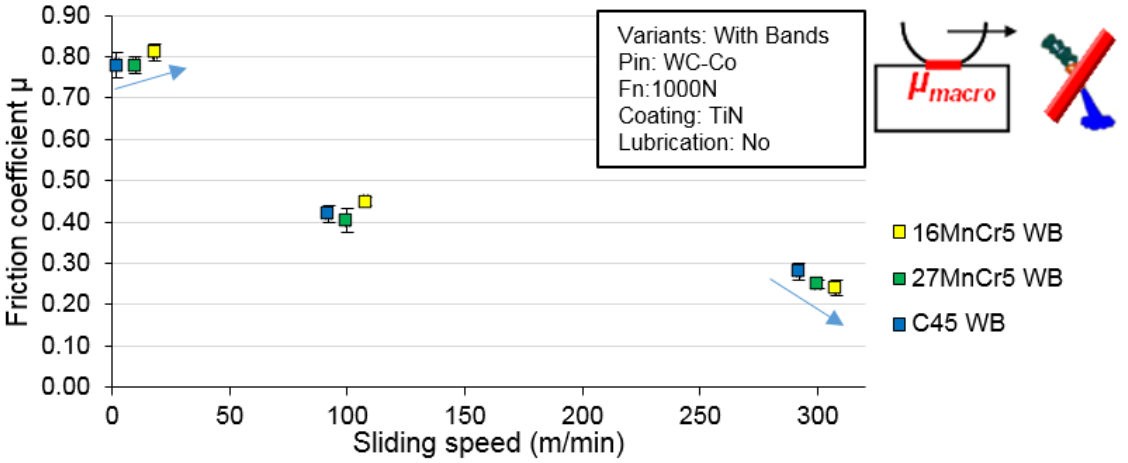

Figure 95. With more Band FP steel's friction coefficient versus sliding speed.

Summary of the fundamental study

Finally, there has been summarized all the results in a table checking the changes from variant to variant in each speed. The variations, taking as reference the standard (R) variant, will be represented with increments

- If the increment or decrease is lower than a 5% of the value of the standard variant it will be considered as if it were not any change representing it with a horizontal blue arrow.



- In the case the change is between 5% and 10% it will be represented with a tilted up or down arrow depending if it is increasing or decreasing.

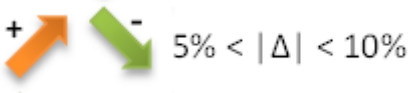

- For increments higher than 10% these changes will be represented with vertical arrows, red in case of being positive and green in case it is a decrease.

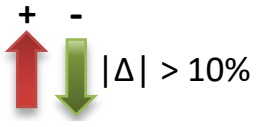

The summary of the comparison with the R steel variant can be seen in the Figure 96, in almost all the cases there were obtained lower or similar friction coefficients. Checking the steel's properties table (Table 11), it can be seen that in except of the 16MnCr5 steel the variants increment their hardness when changing from the standard to the Coarse Grain variant.

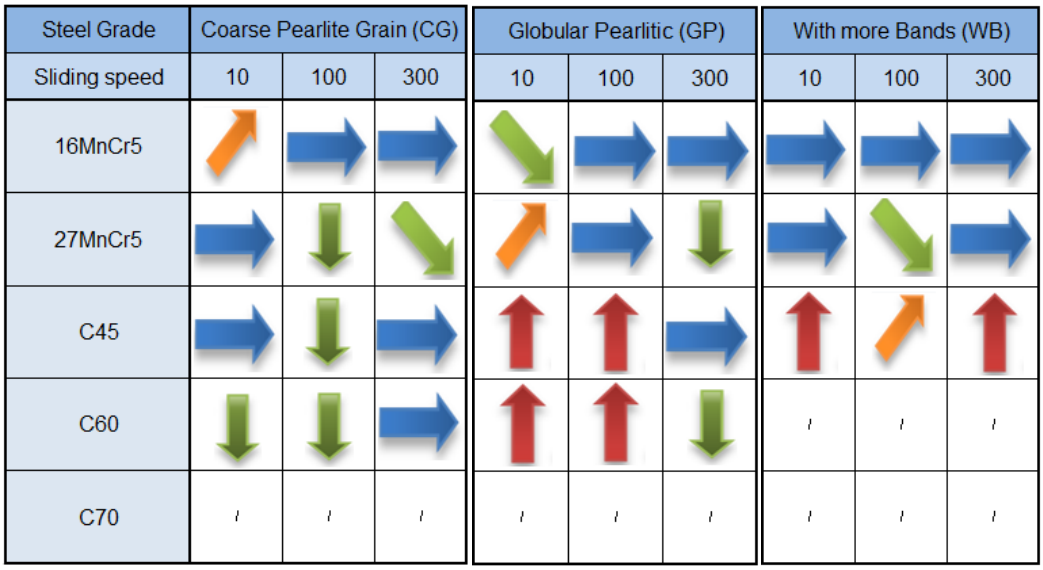

Figure 96. Friction coefficient comparison between reference and the modified variants.

When comparing the impact of a GP structure (Figure 96), very different trends can be observed but again it is linked with what we have commented above. The GP variants are softer than the standard ones leading the pin to a ploughing and sticking and sliding effect what increases its friction coefficient.

4.1.4 Friction coefficient versus microstructural parameters

As explained section 2, the previous results were plotted versus the microstructural parameters in order to clearly identify the main feature of the material controlling the tribological behaviour.

The same colour code was used in each of the following plots: the lowest sliding speed (10m/min) was graphed in green, the 100m/min tests in yellow and the highest speed (300m/min) in red.

Friction coefficient versus ferrite content

The first parameter to analyse is the ferrite-pearlite ratio. The Figure 97 summarises the friction coefficients obtained with the carbide pin versus the ferrite percentage of the 15 FP steel variants (all but the C70). Analysing the tendency over the low and medium speeds same pattern can be appreciated as the ferrite content increases. For the highest speed the friction stayed around the same value (0.23 ± 0.1).

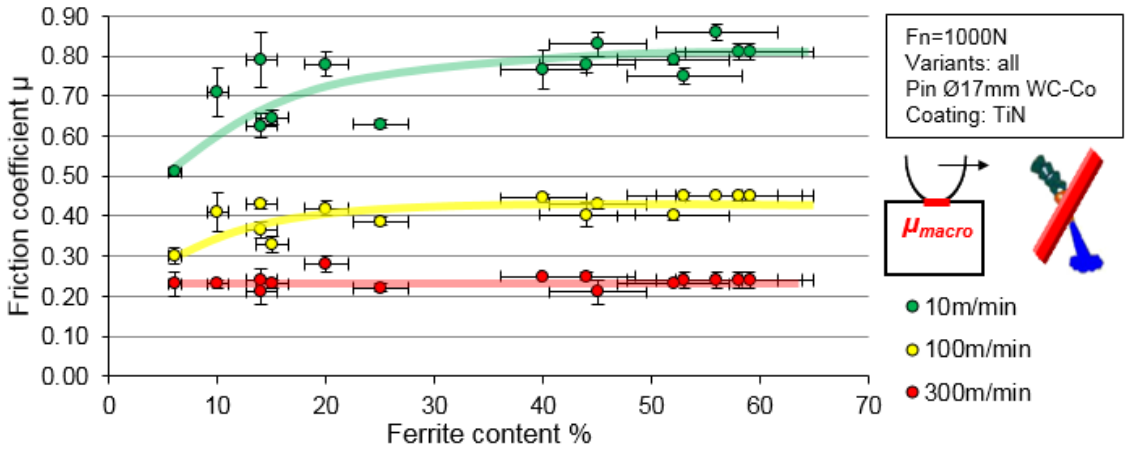

Figure 97. FP steel's friction coefficient versus ferrite content with carbide pins.

For the three speeds, much more remarkable for the lowest, as the ferrite content increases (from 10% to 30%) the friction value increases steadily, then as the ferrite content increases from 30% up to the 60% the friction value stabilizes around the same value for each of the speeds.

Friction coefficient versus Hardness

Hardness is also a parameter of interest, which it is not a microstructural feature but a characteristic obtained by the contribution of each of them.

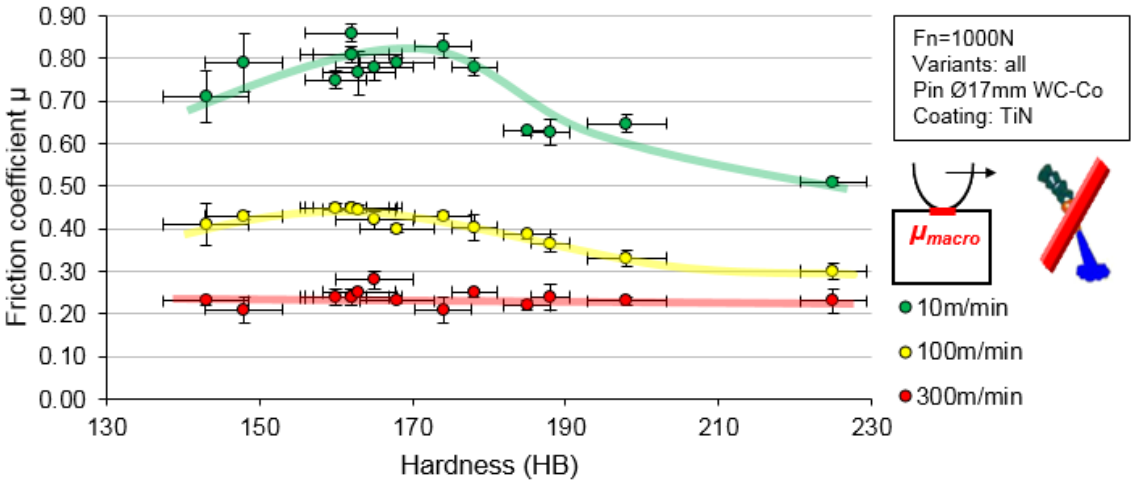

Figure 98. FP steel's friction coefficient versus hardness with carbide pins.

The results plotted in Figure 98 show different trends depending on the speed. For the lowest, three behaviours can be detected; with the softest variants, the friction values vary between 0.71 and 0.85. As the hardness increases the value stabilizes around 0.63 and the hardest steel (C60CG) provides a friction value of 0.51. For the medium speed, as the hardness increases a continuous decreasing trend appears varying from 0.41 to 0.3. Finally, as seen in the results versus the ferrite content, the highest speed made the

friction values to have low variability, so it can be said that for this speed the hardness had very low influence on the friction coefficient as all the values move around 0.24.

Friction coefficient versus the grain size of the ferrite

The friction results were also plotted versus the ferrite grain size of the ferrite. As it can be seen in the Figure 99 there is not any remarkable trend. Focusing the attention on the lowest speed, where the highest differences were found, for the same or similar grain size a wide range of friction coefficients was obtained.

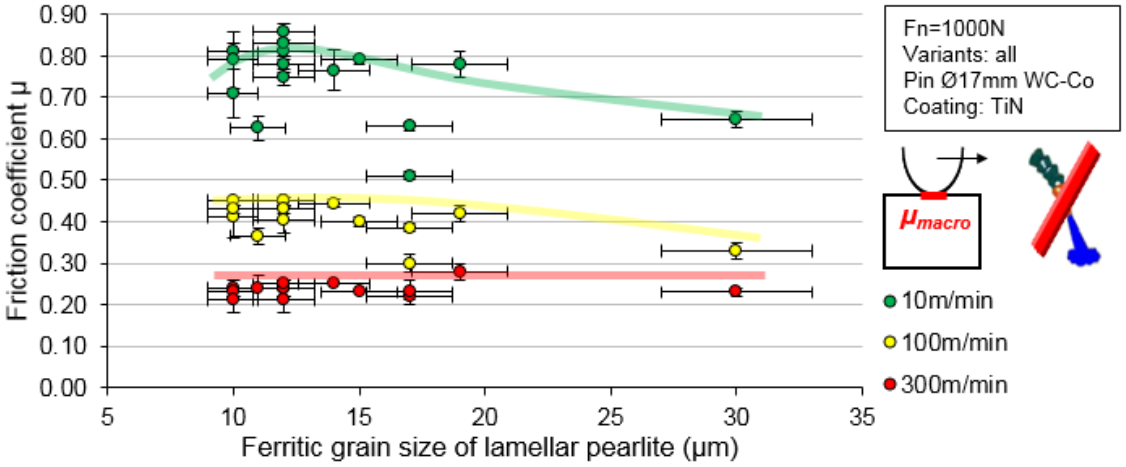

Figure 99. FP steel's friction coefficient versus the grain size of the ferrite.

For the medium speed, it is also hard to find a consistent trend and for the highest speed the friction coefficient does not change much in all the grain size range. After analysing the results, we can state that the grain size in this range (10µm-30µm) it is not a microstructural feature that affects the friction.

4.1.5 Contact mechanisms and pin's wear

In order to understand how the microstructure can affect the tribological behaviour, contact zone on the pins and contact tracks on the workmaterial have been analysed. Later, the analysis made of the wear is explained.

Overview of the contact zones and tracks

A selection of steel variants and speeds has been done to show the contact zones and tracks when performing the tribological tests. As it can be seen in the Figure 100, as expected, the higher is the speed the higher wear is observed on the pin's tip. Besides, analysing the friction results at 300m/min similar results were obtained, that is why this speed was the one selected so as to be analysed in terms of wear trying to make differences between variants.

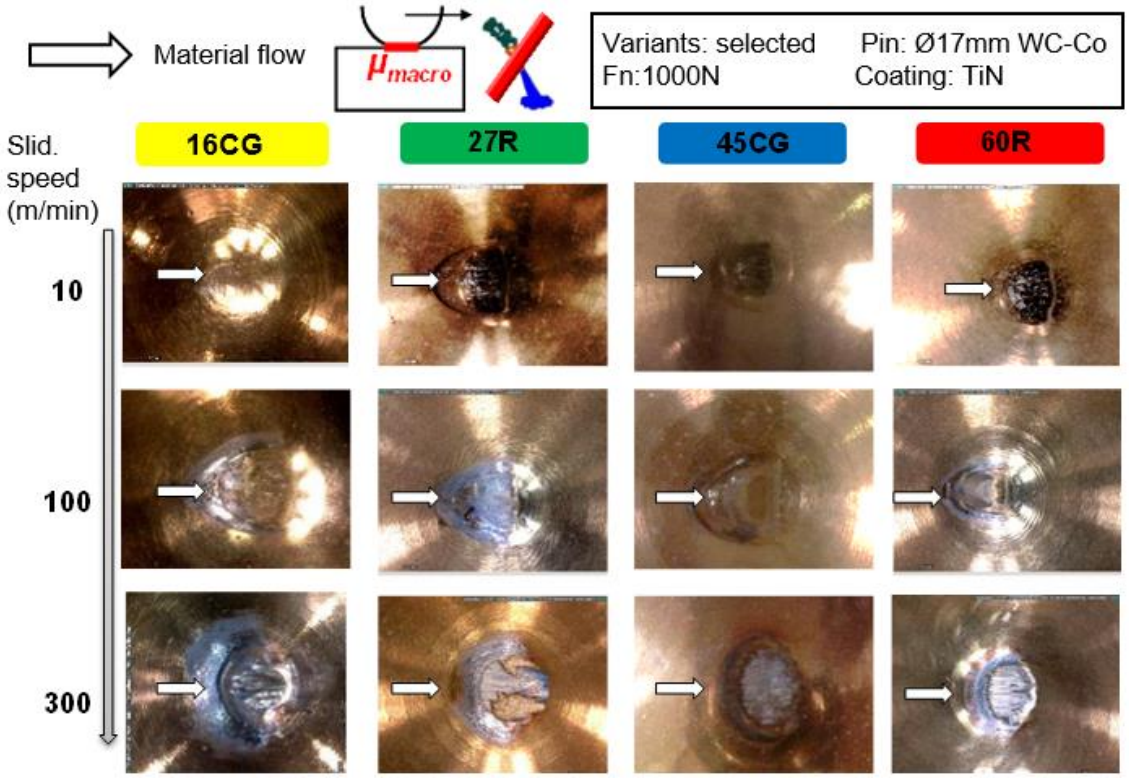

Figure 100. Examples of contact zones observed on the friction pins at different sliding velocities and for some variants – WC-Co+TiN pins.

Contact zone is seen to change when increasing the sliding velocity (Figure 100). Whereas no traces of wear were found at 10 m/min, there were rather obvious at 300 m/min. The morphology of the contact zone, for a given sliding velocity, is different from one variant to another showing the different tribological behaviours. Optical analyses did not provide much information about material transfer tendency as it can be difficult to dissociate material transfer from the steel bar and worn coating revealing the substrate below.

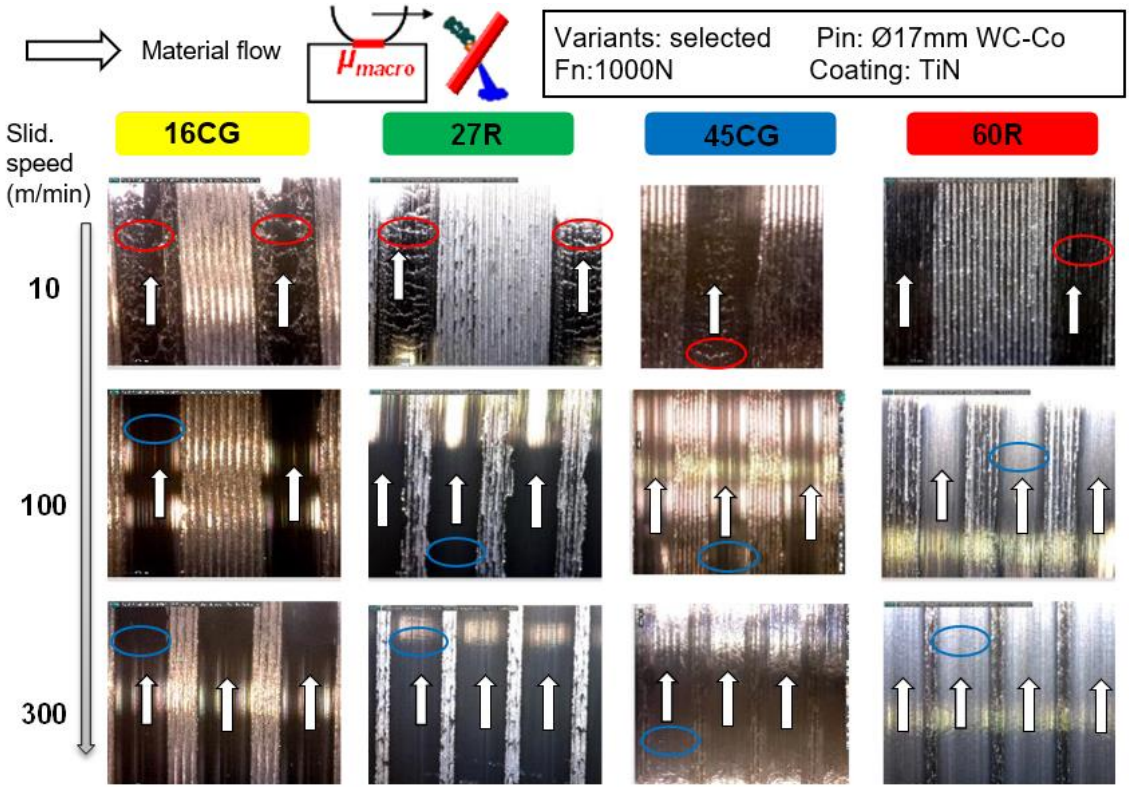

Figure 101. Examples of contact tracks observed on the workmaterial at different sliding velocities and for some selected variants – WC-Co+Tin pins.

Analysing the contact tracks (Figure 101) shows that low carbon variants lead to less stable frictional behaviours at low sliding velocities (stick-slip phenomenon). The topography of the contact tracks presents some wavelets marked in red in the images at 10 m/min in the Figure 101. Whereas increasing the carbon content (C45 and C60) or increasing the velocity limits or even erases the occurrence of this phenomenon.

Analyses of the contact mechanisms at 300 m/min

Transfer mechanisms were thoroughly analysed on the tests performed at 300 m/min using Energy Dispersive X-ray spectrometry (EDX). This sliding velocity is especially interesting as friction values are similar from one variant to another (around 0.22 ± 0.01) whereas the morphology of the contact areas is significantly different. This is a relevant condition to compare the variants in terms of adhesion tendency without including effects due to the contact geometry.

This analyse was carried out on 14 variants as there were not performed tests with the C70 at 300 m/min and due to delivery problems the 16MnCr5 WB was not received on time.

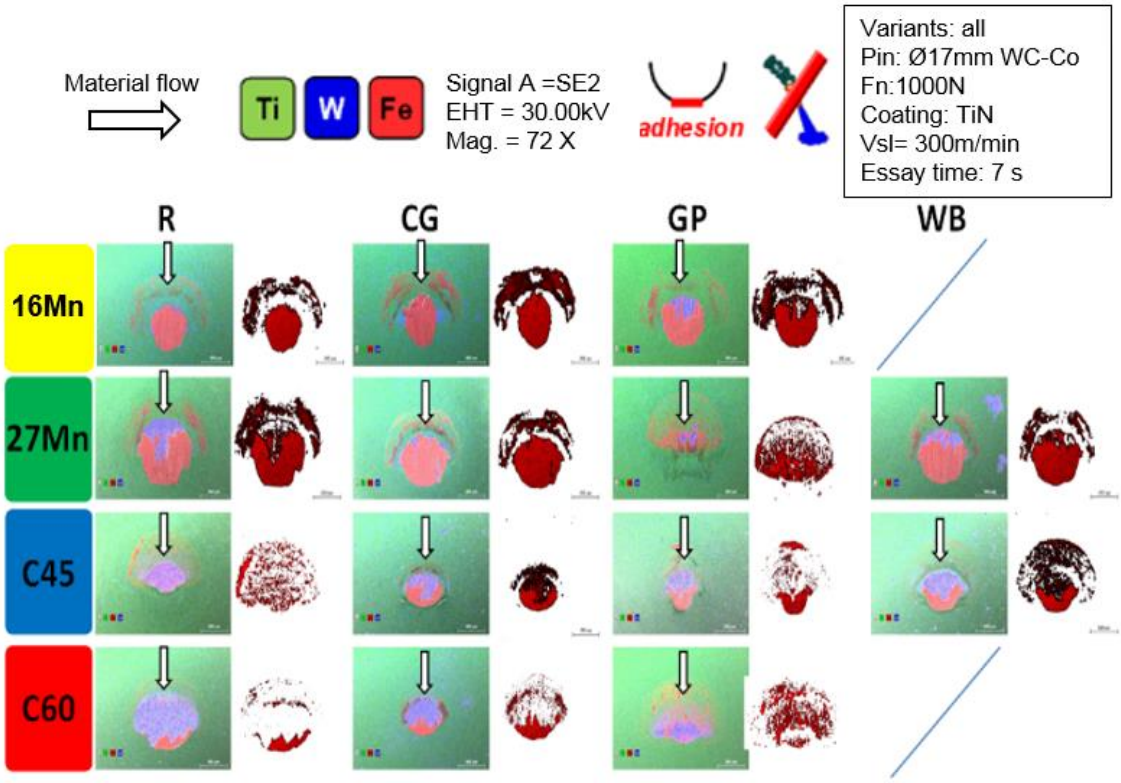

Figure 102. EDX analyses performed on the contact zone of the friction pins showing material transfer (iron in red) and wear of the coating (tungsten in blue). Extracted covered area based on image processing to assess material transfer tendency.

The EDX analysis shown above Figure 102 shows that both the size and morphology of the contact area depend on the carbon content and microstructure. From a general point of view, variants of the 16MnCr5 and 27MnCr5 exhibit a more intense material transfer than C45 and C60. In order to quantify this more precisely, EDX maps have been post-treated using an image processing technique to extract the covered area of the pin, shown next to the corresponding EDX map in Figure 102. Results are plotted in Figure 103 depending on the microstructural parameters.

Adhesion is often related to the hardness but as shown in Figure 103d very different material coverage on the pin tip can be seen for the same hardness e.g. C45WB and 27MnCr5 R. This proved that this was not the case under severe conditions and especially at extremely high sliding velocities. Keeping in mind one aspect of the thesis, results were plotted against some ferrite-pearlite microstructural parameters. Figure 103a and b prove instead that the adhesion tendency is mainly driven by the ferrite pearlite ratio.

4.1.6 Analysis of the wear tendency at 300 m/min

The selected sliding velocity of 300 m/min is also interesting as different worn areas can be seen (Figure 102) whereas friction was close from one variant to another. It is thus a

relevant condition to compare the variants in terms of wear tendency without including effects due to the contact geometry.

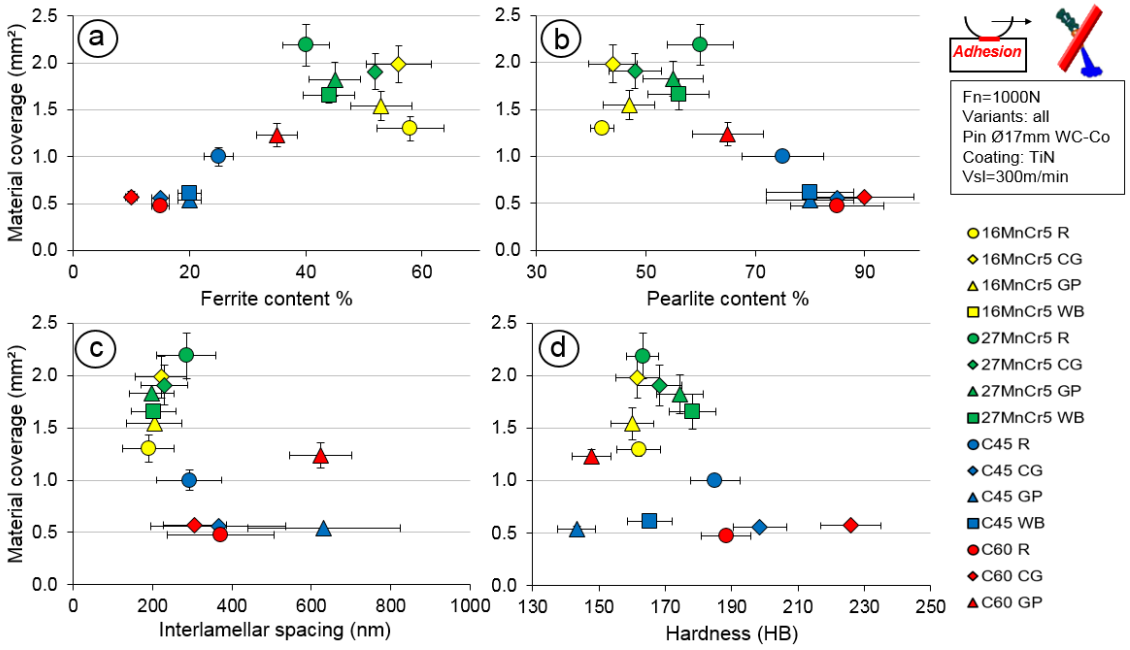

Figure 103. Evolution of material coverage on the pins with the microstructural parameters. a) Ferrite content, b) Pearlite content c) Interlamellar spacing and d) Hardness.

Different wear mechanisms were observed on the friction pins. Low carbon grades lead to an intense material transfer within the contact zone but also a severe delamination of the coating all around the entrance of the contact as Figure 104a and b shown. This has been observed on all the 16MnCr5 variants and on two 27MnCr5 variants. When increasing the carbon content, the dominant wear mode changed to abrasive wear. Abrasive grooves can be clearly seen in Figure 104d on the C60 variants whereas material transfer is found only at the back of the contact. The Table 20 summarizes the observed mechanisms.

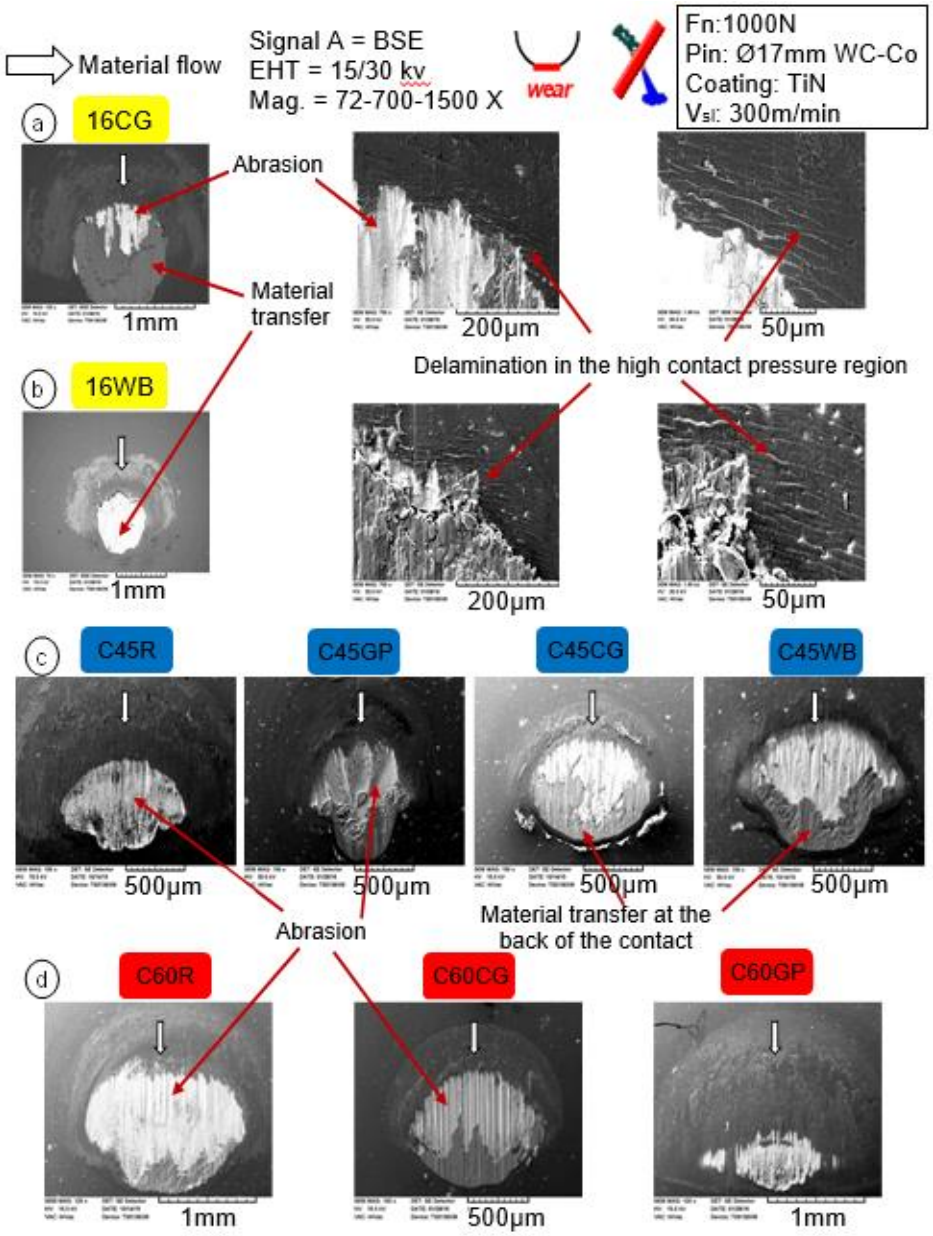

Figure 104. Wear mechanisms observed on some variants: a) 16MnCr5 Globular Pearlite (GP), b) 16MnCr5 banded structure (WB), c) C45 and d) C60.

However, it was not possible to differentiate qualitatively the variants as, despite some changes in the morphology of the contact zone, the main difference concerned the amount of wear on the friction pins. In order to dissociate them and provide a quantitative aspect, some image processing was applied on the SEM pictures to extract the worn area. It was assumed that material transfer was in fact hiding the worn part of the friction pin and the worn and/or covered part of the contact zone was considered as wear.

The previously showed figure (Figure 103) presents the results of this methodology and shows that GP variants tend to induce the lowest amount of wear on TiN coated carbide pins at high sliding velocity. The observed trends were displayed in the Table 20 and a wear ranking was also made shown in the Figure 106.

Table 20. Dominant wear mechanisms observed depending on the variant.

No delamination – Dominant abrasive wear
Not analysed
Delamination observed



F_n: 1000 N
Pin: ϕ17 mm WC-Co
Coating: TiN
V_{sl}: 300 m/min

Steel Grade	Standard	Pearlite Grain	Globular	Bands
16MnCr5	16R	16CG	16GP	16WB
27MnCr5	27R	27CG	27GP	27WB
C45	45R	45CG	45GP	45WB
C60	60R	60CG	60GP	-
C70	70R	-	-	-

Note: As the wear is concerned it was hard to conclude anything as this was only a draft based on a questionable assumption. Indeed, material transfer should be dissolved to really assess the actual worn part of the pin and this analysis would have to be repeated. Besides, no clear tendency could be extracted regarding the wear tendency based on microstructural considerations.

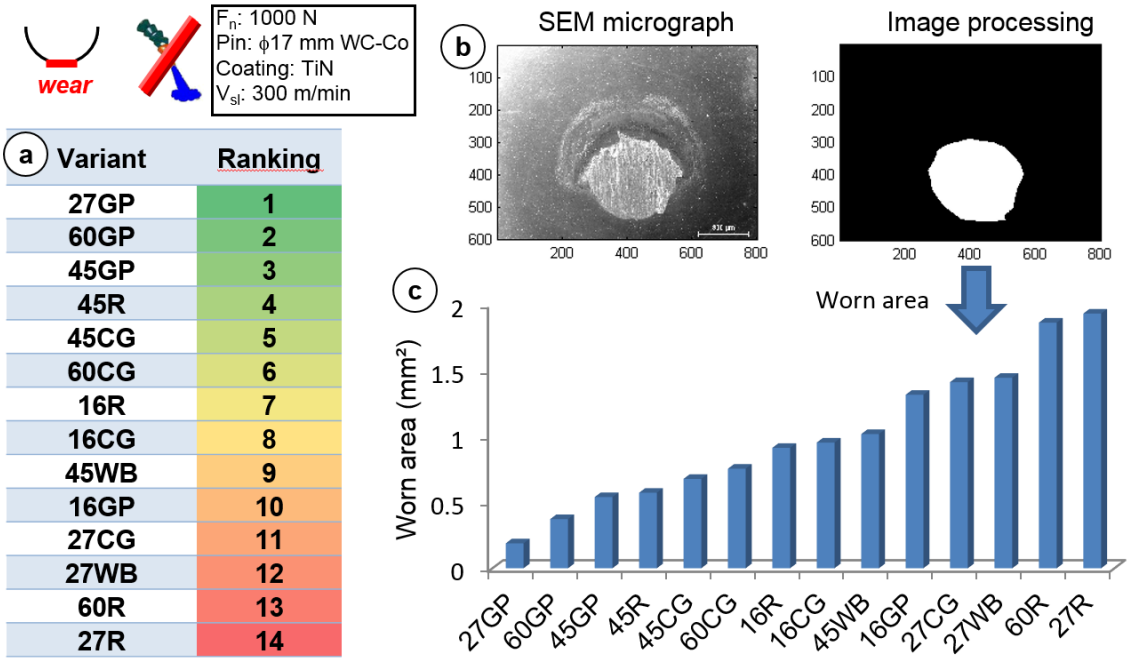

Figure 105. Wear tendency towards the different variants: a) wear ranking proposed b) image processing example to extract the worn area and c) worn area extracted for each variant (sorted from the less to the most worn).

4.1.7 Mechanical contact models

In this section, the objective is to identify contact models that can be implemented in any numerical model.

Results were thus plotted versus several material parameters (Figure 106). The large deviation observed on the interlamellar spacing did not enable to properly identify a friction model dependent on this parameter. The most relevant parameter appeared to be the sliding speed and the ferrite-pearlite ratio. Figure 106a and b show that a clear trend can be extracted, and that friction coefficient clearly increases when increasing the ferrite content. This effect is however limited when increasing the sliding velocity.

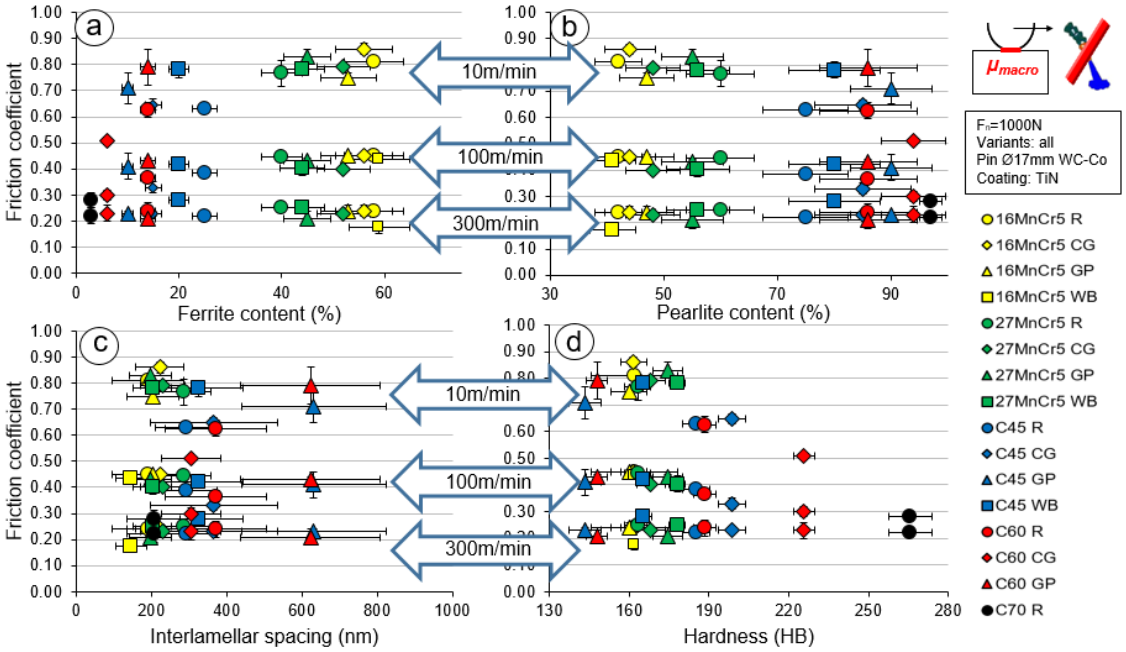

Figure 106. Friction coefficient plotted against ferrite-pearlite microstructural parameters: a) ferrite content, b) pearlite content, c) interlamellar spacing and d) macro hardness.

A fitting procedure already proposed in some early works (Courbon 2011) was developed. The proposed model ws then based on the obtained macroscopic friction coefficient results. Thus, there were obtained three different curves depending on the ferrite content, the static friction curve (μ_s), the kinematic friction curve (μ_k) and the decay of the values when increasing the speed (d_μ) i.e. how varies the friction coefficient when the sliding speed is increased but depending on the ferrite content.

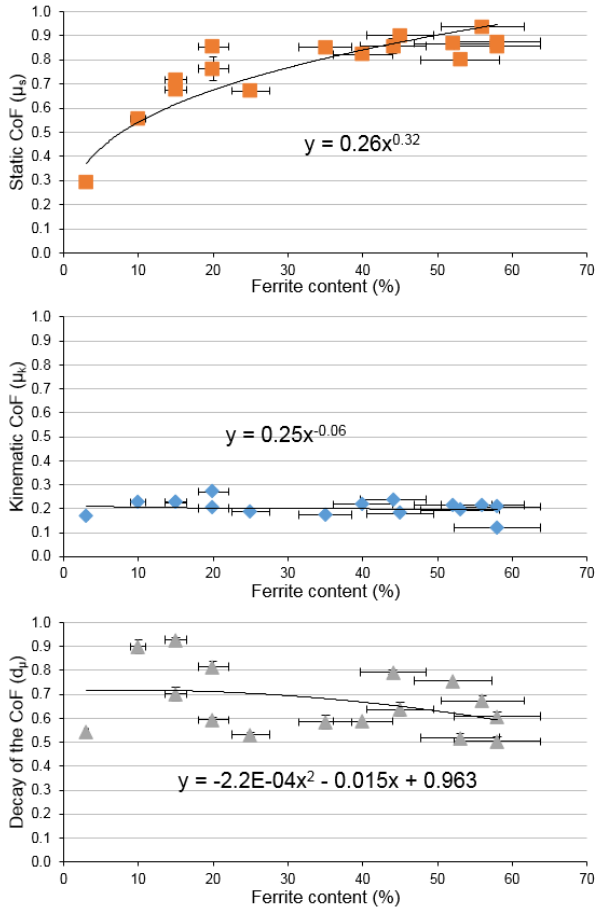

y =μ_s => static friction coefficient based on ferrite content

x = Ferrite %

y =μ_k => kinematic friction coefficient based on ferrite content

x = Ferrite %

y =d_μ => decay of the friction coefficient from μ_s to μ_k depending on the speed

x = Ferrite %

Figure 107. Frictional model curves depending on the steel's ferrite percentage.

This lead to the following equation relating the friction coefficient to the sliding velocity (V_{sl}) and ferrite content (%F):

$$\mu(V_{sl}) = \left(\mu_k + (\mu_s - \mu_k) \times exp\left(-d_\mu \|V_{sl}\|\right)\right) \times (1 + K(\|V_{sl}\|)) \quad \textit{(Eq. 4.2)}$$

$$\mu_s = 0{,}26 \times \%F^{0{,}32} \quad \textit{(Eq. 4.3.)}$$

$$\mu_k = 0{,}25 \times \%F^{-0{,}06} \quad \textit{(Eq. 4.4)}$$

$$d_\mu = -2.2 \cdot 10^{-0.4} \times \%F^2 - 0{,}015 \times \%F + 0{,}963 \quad \textit{(Eq. 4.5)}$$

Additional coefficients were identified considering the friction increase when changing the structure to a globular pearlite and the friction decrease when increasing the grain size.

$$K_{CG}(\|V_{sl}\|) = (-2 \cdot 10^{-5} \times \|V_{sl}\| - 5.8\ 10^{-3}) \times \%F + 7\ 10^{-4} \times \|V_{sl}\| - 0.239 \quad \textit{(Eq. 4.6)}$$

$$K_{GP}(\|V_{sl}\|) = (3 \cdot 10^{-5} \times \|V_{sl}\| - 7 \cdot 10^{-3}) \times \%F - 1.5 \cdot\ 10^{-3} \times \|V_{sl}\| + 0.355 \quad \textit{(Eq. 4.7)}$$

$$K_R(\|V_{sl}\|) = 0 \quad \textit{(Eq. 4.8)}$$

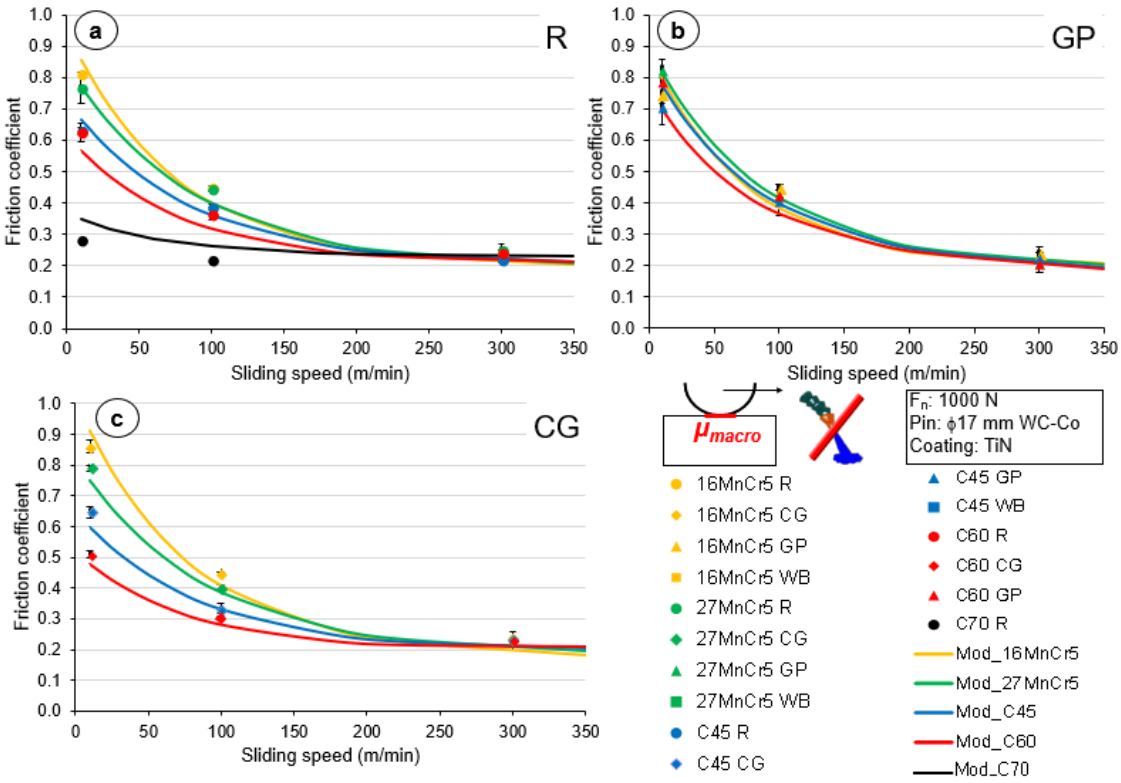

Figure 108. Comparison between the experimental data and the proposed models (continuous lines) in terms of friction coefficient for the standard variants are presented.

As it can be seen in the Figure 108 the curve for each grade does not fit exactly to the experimentally obtained values giving a maximum error of a 20% for the C70 variant at the lowest speed.

Tribological study focused on the broaching process

The second part of the tribological study is aimed to the broaching process that will be studied in the 4th and 5th chapter of this document. Briefly, broaching is a machining process where the operation is performed in one sole pass, usually with low feeds and high rake angles (Handbook 1990).

In this case, the selected working speed range is between 0 and 60m/min, 2m/min, 20m/min and 60m/min more precisely. The latter is considered as high-speed broaching (Schulze et al. 2012).

This part of the tribological study has been performed with pins made of M35 HSS the most common tool material used in broaching. Both uncoated and TiN coated pins have been used under dry and lubricated conditions.

4.1.8 Friction coefficient versus sliding speed

As done in the fundamental study, firstly the results were plotted versus the sliding speed.

Going through the results, the Figure 109 shows the friction coefficients obtained with the uncoated HSS-M35 pin versus the sliding speed (remind that the tests were performed in three speeds, the results were displayed in this way to be seen as clear as possible). Analysing the results, for the lower speed focusing on the standard steel variants there was obtained an increasing trend depending on the carbon content. It is curious that this trend was found as well for the Coarse Grain variant, but looking at the globular pearlitic and with more band variants it disappeared. As the sliding velocity increased, the standard deviation of the results was getting larger making hard to find any trend, showing a rather unstable tribological behaviour. This is mostly explained by the severe wear exhibited by the HSS pin at this high speed. On the contrary, it was quite surprising the behaviour of the 16MnCr5 tested at high speed that provided the lowest friction values of all the set of results disagreeing with what it was expected.

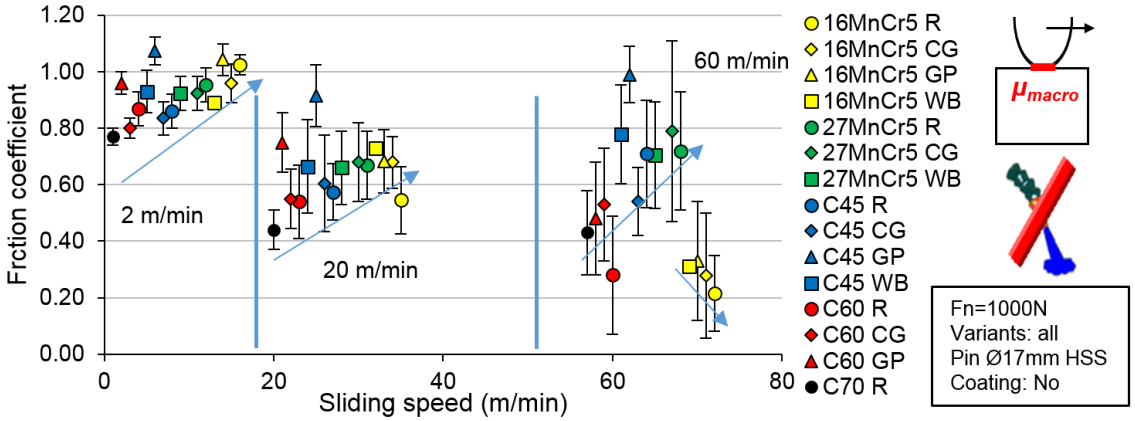

Figure 109. FP steel's friction coefficient versus sliding speed with uncoated HSS M35 pins.

On the other hand, in the Figure 110 the friction coefficients obtained with the TiN coated M35-HSS pin are presented.

In a rapid look to the results, there were three things drawing the attention that could be assigned to the coating. First, the results were quite lower comparing to the values performed with the uncoated pins which confirmed the well-known tribological effect of the TiN coating; second, in the three speed regimes almost all the variant's values moved around 0.5 ± 0.1 making in this case the friction coefficient independent from the speed. Finally but yet importantly, the coating reduced drastically the standard deviations making the results more stable.

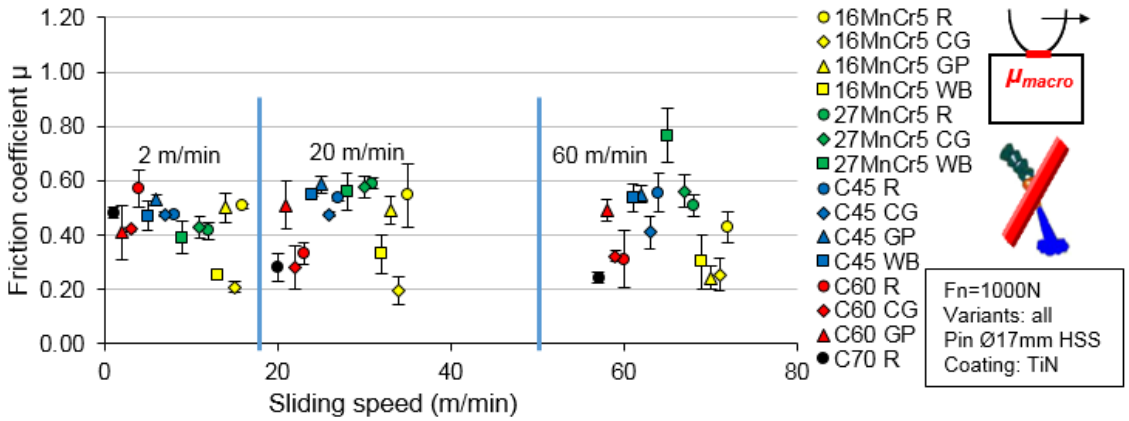

Figure 110. FP steel's friction coefficient versus sliding speed TiN coated HSS-M35 pins.

As it can be seen in the Figure 110 the low differences between the friction values, it was hard to find consistent trends. However, most of the variants increased their friction values changing from 2m/min to 20m/min and decreased when passed from 20 m/min to 60 m/min. There are cases such as the 27MnCr5 WB that increased its friction value increasing the speed or the C70 R that decreased its values increasing the speed.

4.1.9 Friction coefficient versus microstructural parameters

As explained in the section 2, the following results have been thus plotted in terms of the microstructural features.

Similar colour code was used, i.e. the lowest sliding speed (2m/min) was graphed in green, the 20m/min in yellow and the highest speed (60m/min) in red.

Friction coefficient versus ferrite content

Analysing the contribution of the ferrite content on the frictional coefficients with the uncoated M35-HSS in the Figure 111, two different behaviours can be differentiated depending on the ferrite percentage.

On the one hand, the low ferrite content steel variants (up to 30%) show very changing friction coefficients. From 40 ferrite percentage on, for the lowest speed the friction values stabilize around 0.98±0.1 and around 0.7±0.1 for the 20m/min tests.

On the contrary, for the highest speed, the highest ferrite content variants (the four 16MnCr5 steel variants) manifest very low friction coefficients (0.27±0.05).

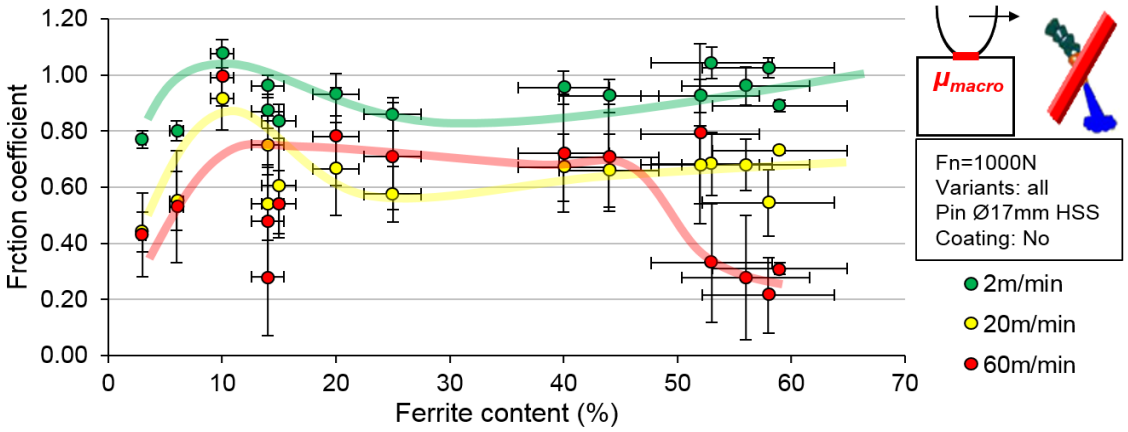

Figure 111. FP steel's friction coefficient versus ferrite content with uncoated HSS-M35 pins.

As it is shown in the results plotted versus the sliding speed, the use of coated pins takes within it some changes with respect to the results obtained with the uncoated pins. Although the drop of the values, the reduction of the standard deviation and the equalization of the results, there is still being a lack of trend and the friction values are very changing for low (3-15) and high (50-60) ferrite percentage steels.

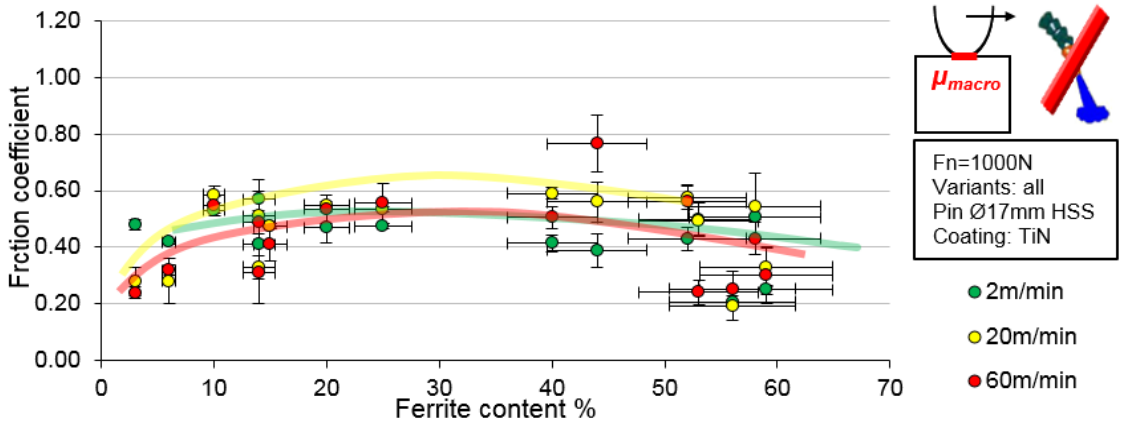

Figure 112. FP steel's friction coefficient versus ferrite content TiN coated HSS-M35 pins.

Friction coefficient versus hardness

The friction values versus the macro hardness of the 15 steel variants are presented in the Figure 113 when in contact with the uncoated M35-HSS tool. Analysing the tendency over the three speeds same decreasing pattern can be appreciated as the hardness increases. This trend can be related not only to the ploughing but also to the sticking/sliding effect happening during the tests that occurs more easily the softer is the material. What is more, there was not obtained a very clear trend at 60m/min where some variants around 162 HB gave back a wide range (between 0.2 and 0.8) of CoF values.

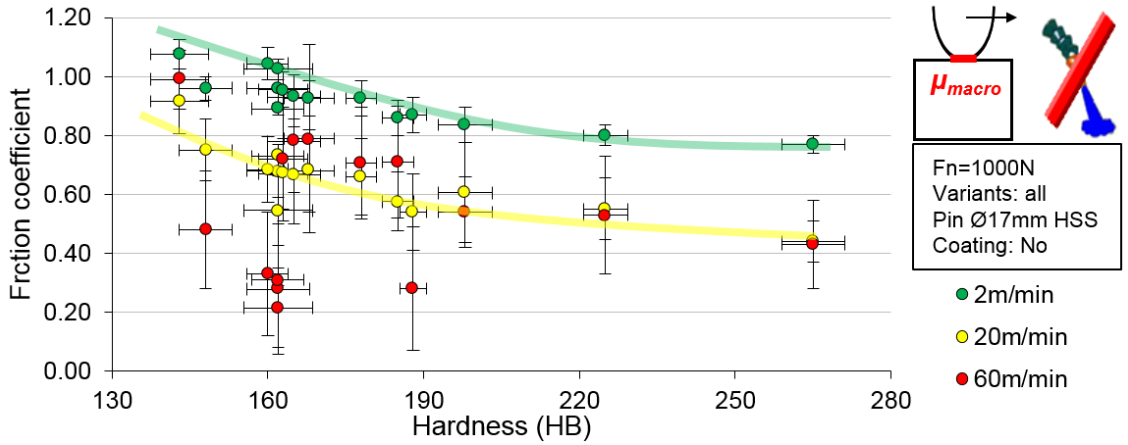

Figure 113. FP steel's friction coefficient versus hardness with uncoated HSS-M35 tools.

In the previous graph, some variants are out of the detected trend. These variants are the previously commented group of 16MnCR5 steels and two C60 variants, the standard (R) and the globular pearlitic (GP).

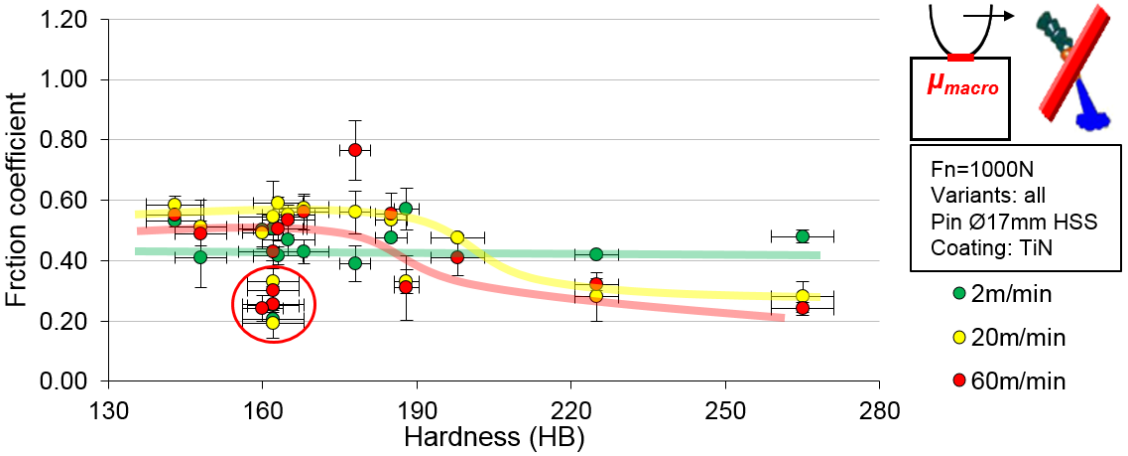

Figure 114. FP steel's friction coefficient versus hardness with TiN coated HSS-M35 tools.

In the same way, the tests performed with the coated HSS led to very dissimilar results compared to the uncoated ones. The clarity of the trend obtained in the Figure 113 was totally disappeared in the Figure 114. For the lowest speed, almost all the values were found between 0.4 and 0.5 not following any trend in terms of hardness. For the medium and high speed, keeping aside the group of 16MnCr5 (red circle), it seemed that followed the slightly decreasing trend as the hardness increases. Altogether, it draws the attention that in this case the friction values were independent from the speed as for each steel variant sometimes the higher value is obtained at the lowest speed, in another case at the medium speed and in few cases at the highest.

These two variants with the lowest hardness values are the before mentioned C45GP and C60GP variants, therefore it can be drawn that the hardness value is not directly

related to the steel's ferrite content, but other features take part in it such as the ferrite and pearlite grain size, the IS or the shape of the grains.

4.1.10 Friction coefficient under lubrication

With the aim of having an insight on the effect of lubrication, more tests were done at the lowest speed (2 m/min). For these tests, there was made a selection over the whole bunch of FP steels, taking all those providing highest differences in terms of friction coefficients. Subsequently, the data obtained from these tests would be also used for the numerical tests launched in the chapter 6. Three tests were performed per each variant and condition obtaining this way the mean value and the standard deviation.

In Figure 115 the previously obtained friction coefficients at the lowest speed were plotted with the uncoated pin and side by side the same tests but under lubrication. It is quite remarkable the effect of the straight oil that not only reduces the friction coefficient 900% but also makes impossible to make differences between the variants. The values obtained under lubrication vary between 0.12 and 0.15 with and an average standard deviation of 0.003 both with the uncoated and TiN coated pin.

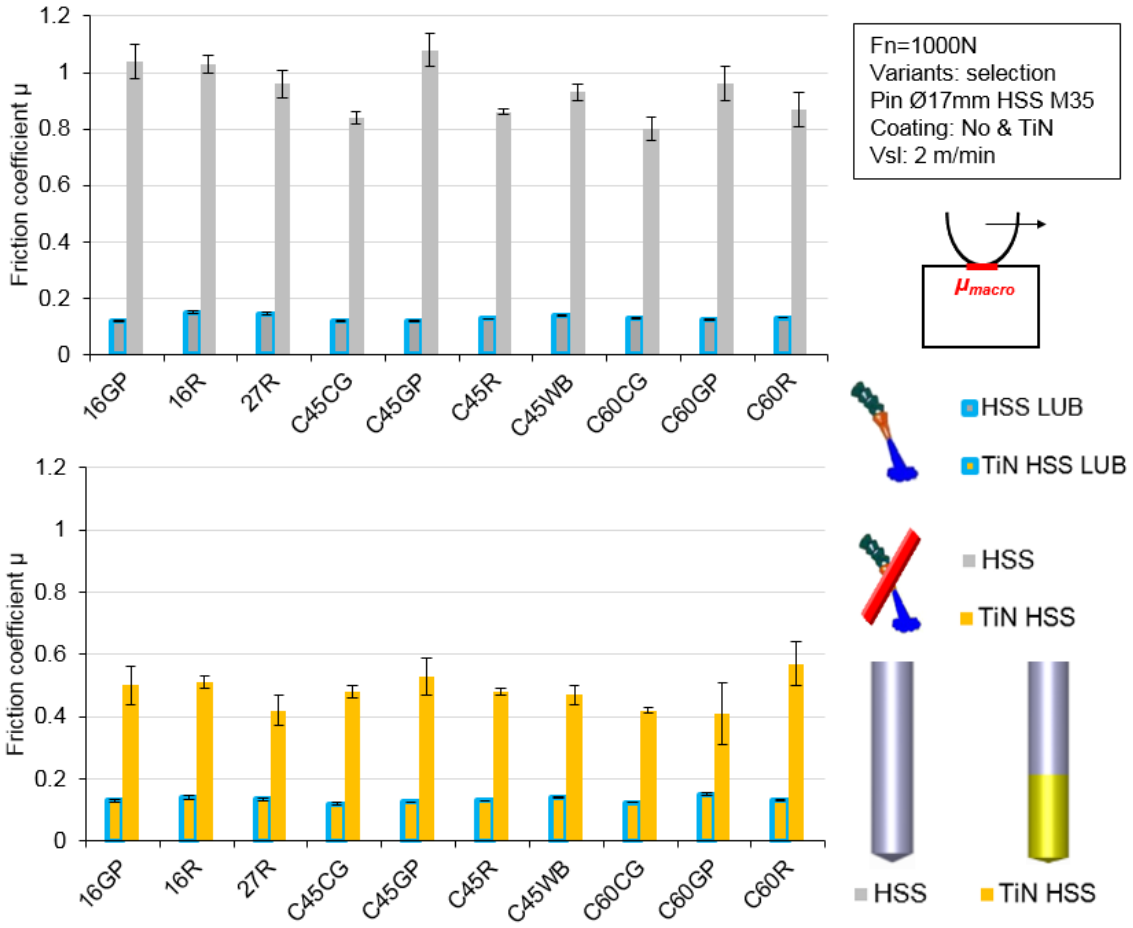

Figure 115. Effect of lubrication and comparison on coated and uncoated pins.

4.1.11 Mechanical contact models

As done in the fundamental tribology study, the goal was to identify the contact models with the aim of implementing them in any numerical model. As the tests were performed with two different kinds of pins, uncoated and TiN coated, two different contact models were proposed.

Results using uncoated HSS were thus plotted versus several microstructural parameters (Figure 116) as commented in the previous section, the large deviation observed on the interlamellar spacing did not enable to properly identify a friction model dependent on this parameter. In this case plotting the friction coefficients versus the FP ratio show that increasing from 0 to 30% ferrite the friction increases while from this point on in all the speed regimes the values stay around the same value. In the same line as the pearlite %, the higher is the hardness the friction coefficient decreases steadily.

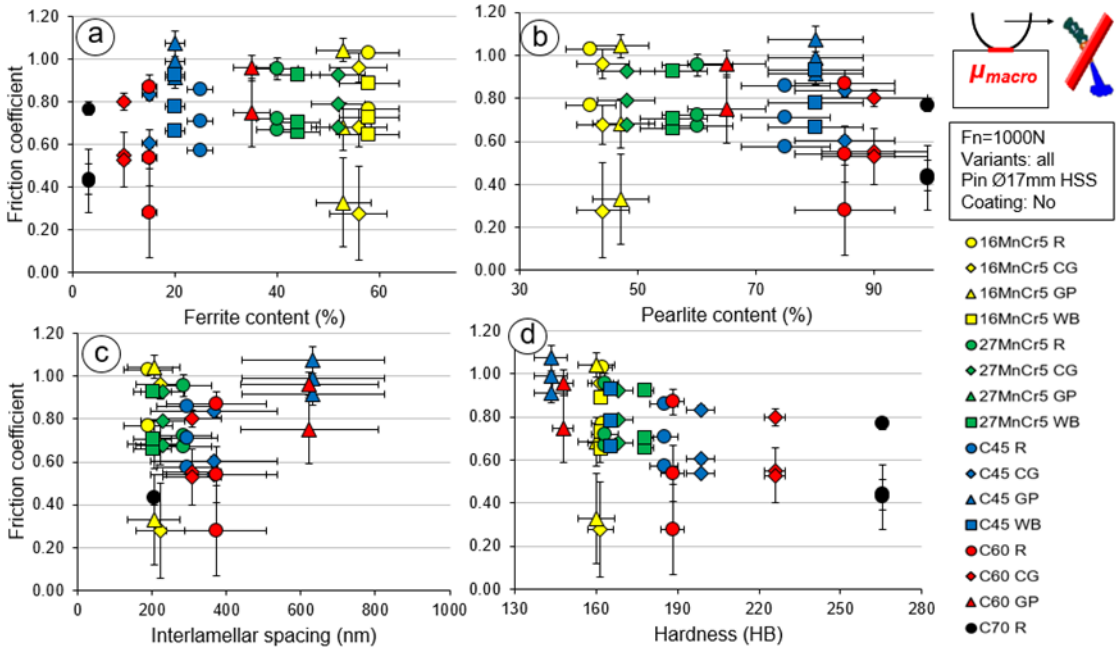

Figure 116. Friction coefficient plotted against ferrite-pearlite microstructural parameters using the uncoated HSS steel pin: a) ferrite content, b) pearlite content, c) interlamellar spacing and d) macro hardness.

As previously done in the fundamental study's Mechanical contact models section, a fitting procedure was developed based on the results obtained with the uncoated HSS-M35 steel. The proposed model is then based on the obtained macroscopic friction coefficient results. Thus, three different curves were obtained depending on the ferrite content. These three were the static friction curve (μ_s), the kinematic friction curve (μ_k) and the decay of the values when increasing the speed (d_μ) i.e. how varies the friction coefficient when the sliding speed is increased but depending on the ferrite content. In

the case of the decay, the low values obtained for the 16MnCr5 variant were kept aside as there were hugely out of the trend obtained with the rest of the variants.

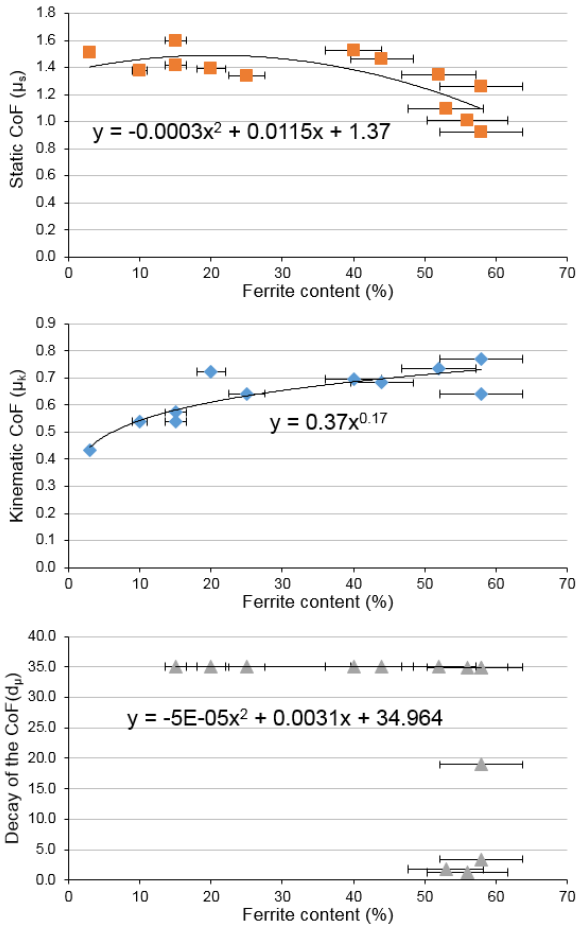

y =μ_s => static friction coefficient based on ferrite content

x = Ferrite %

y =μ_k => kinematic friction coefficient based on ferrite content

x = Ferrite %

y =d_μ => decay of the friction coefficient from μ_s to μ_k depending on the speed

x = Ferrite %

Figure 117. Frictional model curves depending on the steel's ferrite percentage.

This leads to the following equation relating the friction coefficient to the sliding velocity (V_{sl}) and ferrite content (% F):

$$\mu(V_{sl}) = \left(\mu_k + (\mu_s - \mu_k) \times exp\left(-d_\mu \|V_{sl}\|\right)\right) \quad \textit{(Eq. 4.2)}$$

$$\mu_k = 0{,}37 \times \%F^{0.17} \quad \textit{(Eq. 4.9)}$$

$$\mu_s = -3 \cdot 10^{-4} \times \%F^2 + 1.15 \cdot 10^{-2} + 1.37 \quad \textit{(Eq. 4.10)}$$

$$d_\mu = -5.10^{-5} \times \%F^2 + 0{,}0031 \times \%F + 34.964 \quad \textit{(Eq. 4.11)}$$

The model extracted from the model is shown in the Figure 118. This time the accuracy of the model was not that good as the previous developed one. This was due to the fact that the values do not vary that much in terms of speed and ferrite content making difficult to obtain a good model.

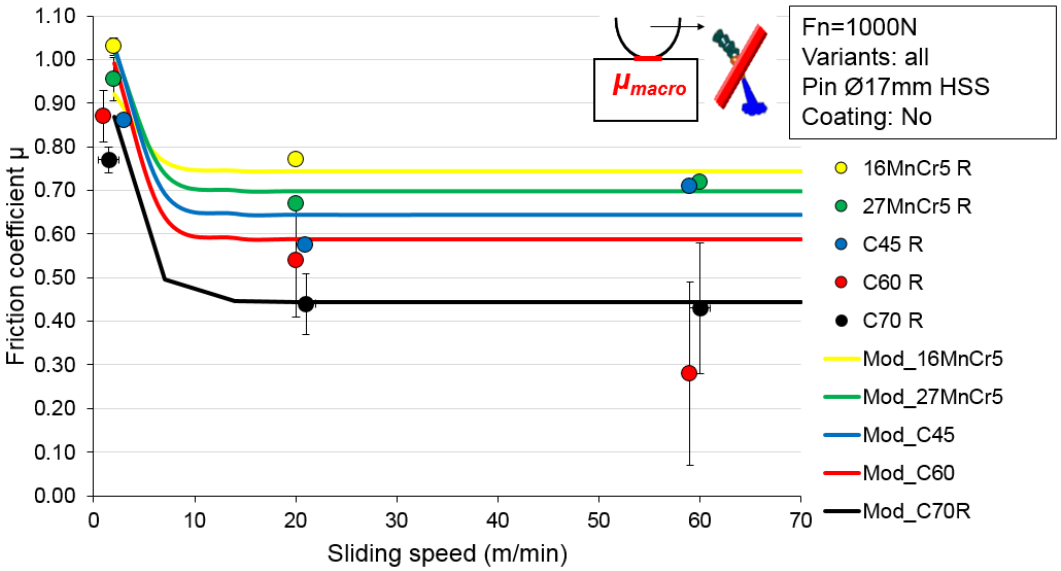

Figure 118. Comparison between the experimental data and the proposed models (continuous lines) in terms of friction coefficient for the standard variants are presented.

Conclusions

This chapter presented the friction coefficients obtained using TiN coated carbide (H13A) pins and TiN coated and uncoated HSS (M35) pins over a wide range of automotive FP steels. The open tribometer used is a specialised device for fast characterisation & identification of cutting tool-work material friction. These tests were carried out on a wide spectrum of ferritic-pearlitic steels and machining related cutting conditions. Large variations of friction coefficients have been highlighted depending on FP content and each steel's macrohardness.

The experimental results proved the interest of this tribometer to provide practical values for any kind of tool-work material pair. Based on these experimental results, the contribution of each of the analysed features was highlighted. Then, a rapid analytical post-treatment method was applied to identify friction models depending on sliding velocity.

4.1.12 Fundamental study's conclusions

The conclusions of the fundamental tribology study were based on the work done comparing the trends between the standard and the rest of the variants and the comparison made in terms of microstructural features. Firstly, it was seen in the standard (Figure 92) and coarse grain (Figure 93) graphs that the higher is the carbon content the lower is the friction coefficient. Analysing separately the variation of the different grades lead us to the Figure 96, which conclude on the main trends that were observed. Then,

the analysis was also made versus the microstructure of each of the steel variants. Therefore, following conclusions could be confirmed:

- Sliding velocity is an important parameter which drastically affects the tribological behaviour of the different variants (Figure 91);
- Differences in terms of friction coefficient are mostly found at low sliding velocities (Figure 91);
- Using a globular pearlite tends to increase the friction coefficient on the high carbon content variants at low and medium sliding speed (Figure 96);
- Using a coarse pearlite grain tends to reduce the friction coefficient and leads to higher wear for some variants (Figure 96);
- A banded structure (WB) seems to increase friction but to a lower extent (Figure 96);
- The ferrite is the most important microstructural parameter leading to higher friction coefficient the higher is the ferrite content, linked to this, increasing the pearlite content is leading to a lower friction coefficient (Figure 97);
- Contact mechanisms at lower speed might depend on the microstructural properties;
- Adhesion tendency seems to be dependent on the sliding velocity. On the other hand, wear mechanisms are mainly governed by the ferrite-pearlite ratio (Figure 103);
- A friction model depending on the sliding velocity and ferrite content was proposed based on WC-Co and FP steels contact (Figure 107).

4.1.13 Broaching focused tribology study's conclusions

As the investigated sliding speed range is narrower, the sliding velocity has a more limited effect on the tribological behaviour. The following conclusions can be drawn:

- The frictional behaviour is highly unstable when using uncoated HSS pins (Figure 109);
- The TiN significantly improve the tribological behaviour by reducing friction and making it more stable (Comparison of Figure 109 and Figure 110);
- Low deviation and differences in terms of friction coefficient are mostly found at the lowest sliding velocity of 2 m/min (Figure 109 and Figure 110);
- Using a globular pearlite or banded structures tends to increase the friction coefficient (Figure 109);
- The trend is not obvious as coarse grain and banded structures are concerned (Figure 109 and Figure 110);

- No clear differences were found when plotting the results versus the ferrite content both with the uncoated and the coated pin (Figure 111 and Figure 112);
- The increase of the steel's hardness lead to a reduction of the friction coefficient with the uncoated HSS pin at low and medium speed (Figure 113), this trend was not found with the coated pin (Figure 114).
- The use of a lubricant drastically reduces the friction level and completely erases the differences between the variants in terms of microstructural features and sliding speeds (Figure 115);
- A friction model depending on the sliding velocity and ferrite content has been proposed based on uncoated HSS pins and FP steels contact (Figure 118).

To sum up, the major aspects that have influence on friction are the sliding speed and ferrite content, bearing in mind that this is completely erased if there is use of lubrication.

Chapter 5

BROACHING TESTS

5 BROACHING TESTS

In this chapter, the experimental broaching campaigns undertaken at the LTDS in Saint-Etienne are displayed. Besides the machining forces and surface roughness measurements, a chip analysis was carried out focusing on the microstructure for each of the steel variants. The work done in this section can be clearly split into three parts. The first one presents a fundamental broaching study over the 16 FP variants with a wide range of cutting conditions. The second one is focused on a FP steel selection with a single cutting condition changing the tooth state regarding coating and lubrication. The third and last relies on broaching wear tests performed on three C45 variants in dry conditions.

Experimental Setup

Broaching is a complex process that can only be investigated via a “simplified” experimental set-up and easily instrumented. The device used for the broaching tests carried out in this PhD is a dedicated experimental set-up fitted on a PCI METEOR 3+1 axis machine. For the first and second campaigns the broaching process was performed in horizontal while the wear tests were performed with the set-up in vertical. It was used the movement of the carriage along with the movement of the spindle to reach cutting speeds up to 60 m/min. The set-up for the first two campaigns is shown in Figure 119:

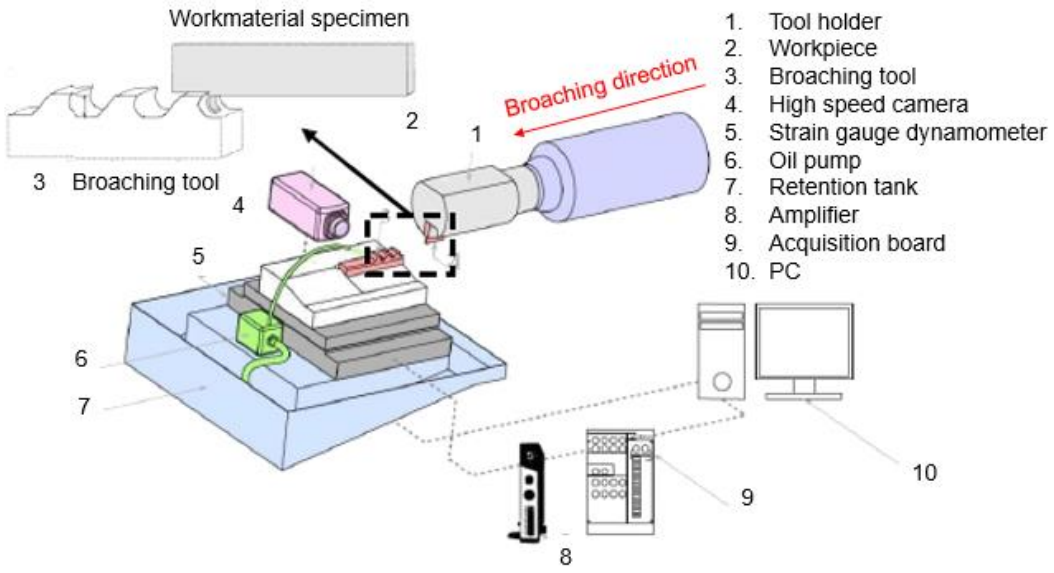

Figure 119. Scheme of the broaching system and devices used mounted on the CNC.

The broaching tool was simplified to a single row of teeth. A simple specimen was also manufactured from each variant and was considered as the workpiece. It was fitted on a specific holder in the spindle whereas the broaching tool was fixed onto the machine

table. A strain gauge dynamometer was used to record online the machining forces. With this configuration, it was also possible to set a camera that would focus on the phenomena occurring in the cutting zone. The setup overview (Figure 120) shows a detailed view of the set-up with the tool (a), specimen (b).

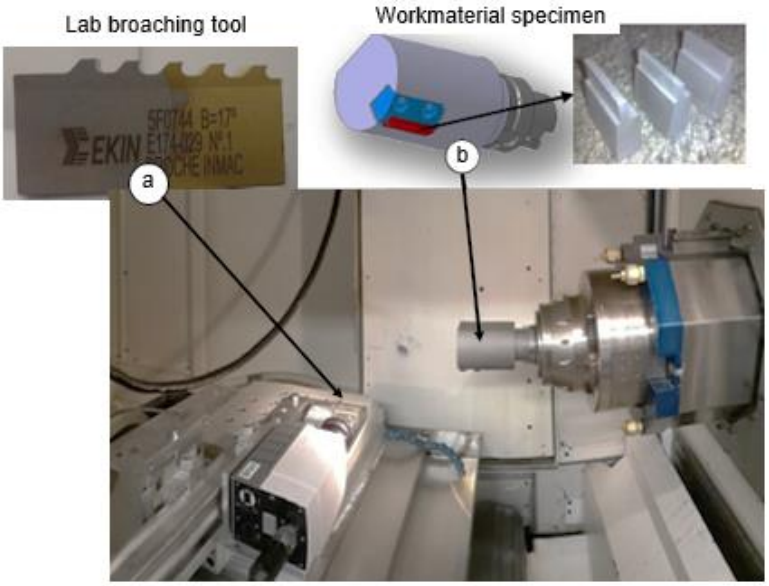

Figure 120. Overview of the experimental setup with a) the laboratory-broaching tool, b) the workpiece specimen.

After an extensive preliminary experimental campaign, the main limitation was, compared to the initial plan, that broaching with several teeth was not possible with the defined specimen geometry and expected cutting conditions. Even if the distance between the tool and the specimen was reduced to the maximum, it appeared that the spindle and corresponding sliding were not stiff enough to avoid a slight bending of the workmaterial specimen. The latter then, compared to the scale at which the material is removed, induced a fluctuating depth of cut, unstable cutting phenomena and a high deviation on the results. Therefore, it was finally decided to perform only single tooth broaching operation.

The three teeth types used were uncoated (UNC), fully coated (COA) and coated with the rake face resharpened (IND) (Figure 11). The rake angle (α) is 17°, the clearance angle (γ) 1° and the cutting-edge radius (r_β) is 12 µm on every broaching teeth used in the experiments. On the other hand, the workpieces were 30 mm long and 3 mm wide specimens specially manufactured to be held by the tool holder.

5.1.1 Methodology

Three different broaching campaigns were carried out being the first one a fundamental study using an uncoated M35 HSS tool on a wide range of cutting conditions, 2, 20 & 60

m/min cutting speed and 10, 25 & 40 µm rise per tooth (RPT hereinafter), over the whole bunch of FP steels without lubrication. Therefore, the 16 variants were investigated over 3 cutting speeds, 3 rises per tooth under dry conditions with an uncoated broaching tool and 5 repetitions were performed leading to a total of 720 runs.

The second campaign was carried out on one sole cutting condition (V=2m/min & RPT=40µm) over a selection among the sixteen FP steels we used at the beginning. Four different mini campaigns were carried out in which the differences were:

- The state of the tooth: uncoated (UNC), fully coated (COA) or manufactured in the industrial way (IND).
- The use or not of lubrication to perform the tests.

The third and last relied on broaching wear tests using the industrial tooth type in dry conditions on three C45 variants.

The aim in each of the campaign was to record the machining forces after each pass. Then, collect the chips generated and measure the roughness on the surface of the workpiece, both in the cutting and transversal directions.

In order to better understand the schedule of the tests the conditions were summarised in the following table (Table 21):

Table 21. Selected design of experiments for the fundamental study.

Campaign	Tooth	Lubrication	Cutting conditions		Steel	Goals of each
5.1.2 Fundamental	UNC	Dry	9	V_c = 2, 20 & 60 m/min RPT = 10, 25 & 40 µm	All	F and Ra study on a wide range of cutting conditions
5.1.3 Tooth state campaign	COA	Dry	1	V_c = 2 m/min RPT = 40 µm	Selected	Coating influence on F, Ra and λ_h
	UNC	Lubricated	1	V_c = 2 m/min RPT = 40 µm	Selected	Lubrication influence on F, Ra and λ_h
	COA	Lubricated	1	V_c = 2 m/min RPT = 40 µm	Selected	Coating and lubrication influence
	IND	Dry	1	V_c = 2 m/min RPT = 40 µm	Selected	Resharpening influence
5.1.4 Wear tests	IND	Dry	1	V_c = 20 m/min RPT = 40 µm	C45 R, CG and GP	Wear study

Results & Discussion

5.1.2 Fundamental broaching study

The first campaign was performed using an uncoated M35-HSS tooth and dry conditions under usual broaching conditions up to high speed broaching conditions. As done in the tribological investigation, first the cutting and feed forces were analysed versus cutting speed using the names given to each of the steel variants. This analysis was done comparing the results obtained in each of the variants to the reference variant and assessing the trends for each of the cutting conditions. In a second part the results were plotted versus the microstructural features of the steels so that the influence of the Ferrite/Pearlite ratio, the interlamellar space, the hardness or the grain size of the ferrite could be highlighted. For each cutting condition 5 repetitions were done to obtain the mean value and the standard deviation.

Table 22. Selected design of experiments for the broaching focused tribological study.

Variables	Conditions
Cutting speed (m/min)	2, 20 & 60
Rise per tooth (µm)	10, 25 & 40
Tool	M35 - HSS
Steels	All the FP steels
Lubrication	Dry
Coating	UNC
Replicates per condition	5

Cutting and feed forces versus cutting speed

In a first instance, the results were plotted versus the cutting speed following the same colour code presented in the fundamental tribological study section 4.1.3. Analysing the results in an overall way it can be first seen that the cutting speed and the RPT are the most influential parameters. Paying attention to the Figure 121, focusing first on the same RPT and changing the speed, it can be noted that increasing the speed the forces decreased. In the same way, focusing on the same speed and increasing the RPT, the forces increased around two times and, in some cases, up to three times. E.g. the cutting forces obtained on the 16MnCr5 at the lowest speed when broaching at 2 m/min and 10 µm RPT (143 N) comparing it with the same speed and 40 µm RPT (538 N).

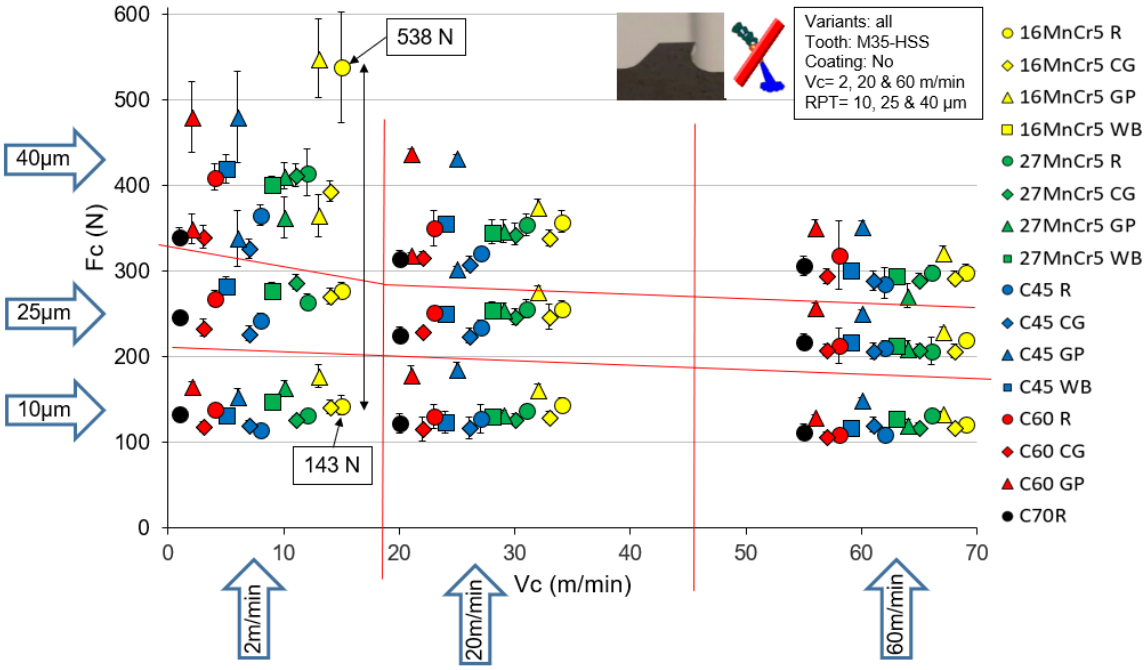

Figure 121. Cutting forces of all variants at all the nine cutting conditions in broaching.

In the Figure 122 the feed forces are plotted in the same way. As it can be seen, comparing both graphs, the cutting forces are two times higher than the feed forces but trends remain considerably the same.

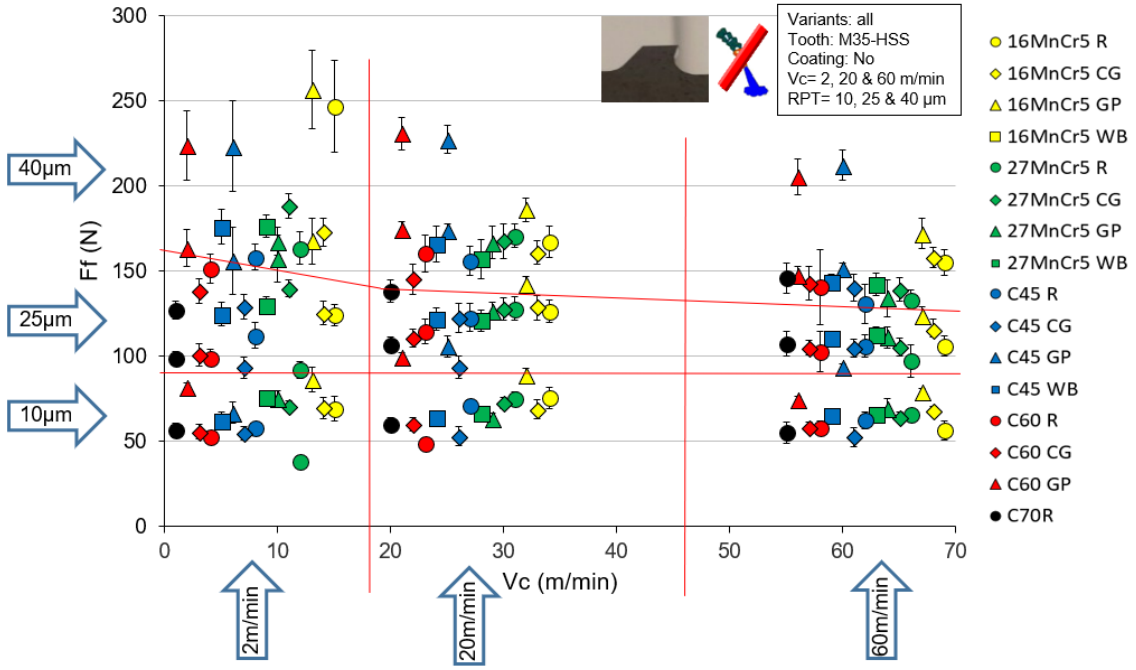

Figure 122. Penetration forces of all variants at all the nine cutting conditions in broaching.

Therefore, from this point on the displayed results will be only the cutting forces. For the analysis it was selected the 40µm RPT row since the differences between the steels were quite higher in comparison to those obtained with the other feeds.

- Broaching cutting forces versus cutting speed in 'Reference' variant:

Going through the Figure 123, it can be seen that all the variants comply with the premise that the higher is the speed the lower are the acquired forces. Nevertheless, as it was seen in the tribology work it is not seen the same trend in the three speeds which is in any case related to the carbon content. It can be also advised that for the lowest speed the differences between the results are quite high whereas for the medium speed, the differences are quite low. These differences are even negligible at the highest speed with cutting forces around 300N for every steel variant.

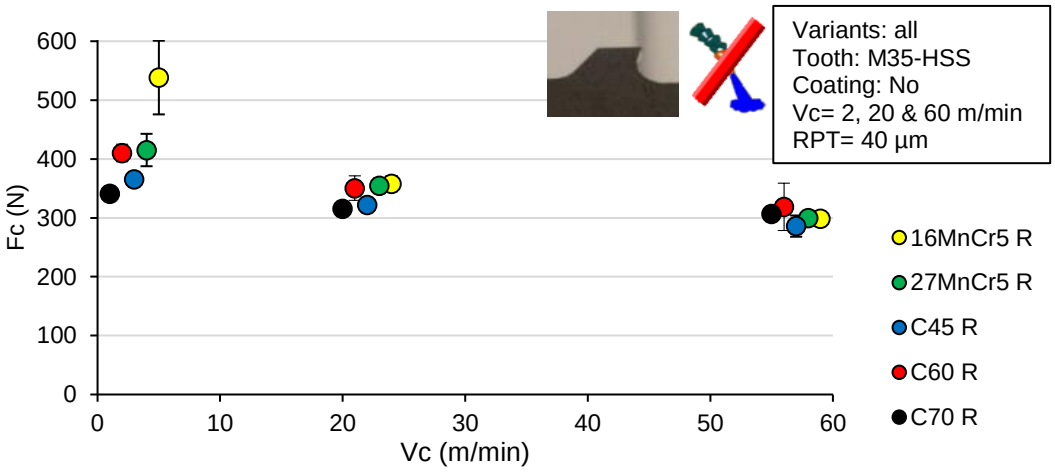

Figure 123. Cutting broaching forces versus cutting speed on standard FP steels.

- Broaching cutting forces versus sliding speed in 'Coarse Grain' variants:

Checking the Figure 124, it can be seen that the lower C content steels lead to higher forces at the lowest speed. The evolution is the same as seen before, being these differences lower for the tests performed at 20m/min and negligible for the essays carried out at 60m/min. The forces obtained at the lowest speed are in this case lower than those obtained with the standard variants. Conversely, at the medium and highest speeds similar values are obtained, around 350N the former and around 300N the latter.

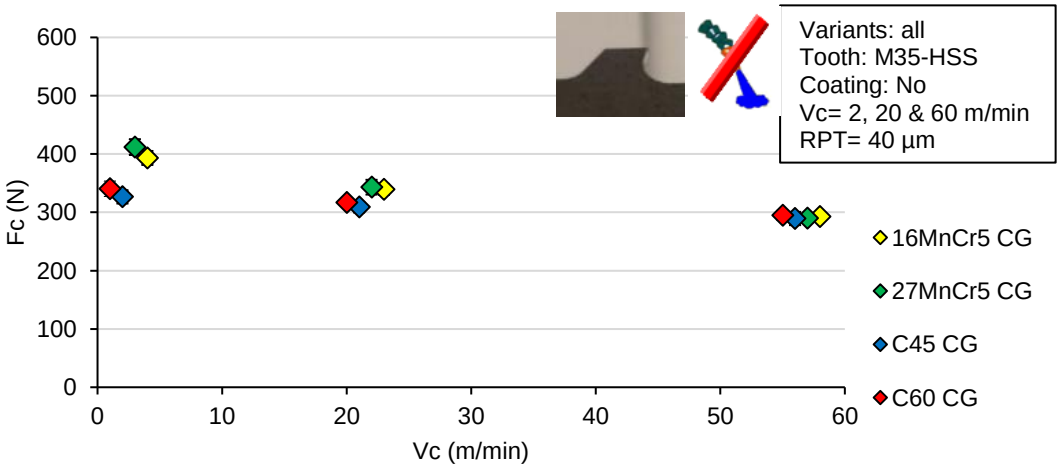

Figure 124. Cutting broaching forces versus sliding speed on Coarse Grain FP steels.

• Broaching cutting forces versus sliding speed 'Globular pearlitic' variant:

Except for the 16MnCr5 variant, the trend is very similar for the other variants as the speed increases. For the GP variants, conversely to that occurring in the previous cases the higher C content variants give in return higher cutting forces than the lower C content variants. This is also connected to the low hardness of these two steel variants (C45 and C60 GP). There is a difference of 20% for the 27MnCr5 steel grade below the C60 and the C45 GP. The 16MnCr5 variant is providing higher cutting forces at the lowest speed tests, in contrast, at medium and high-speed tests the forces are set between the C45 and the 27MnCr5 steels. In this way we cannot extract any trend related to the carbon content.

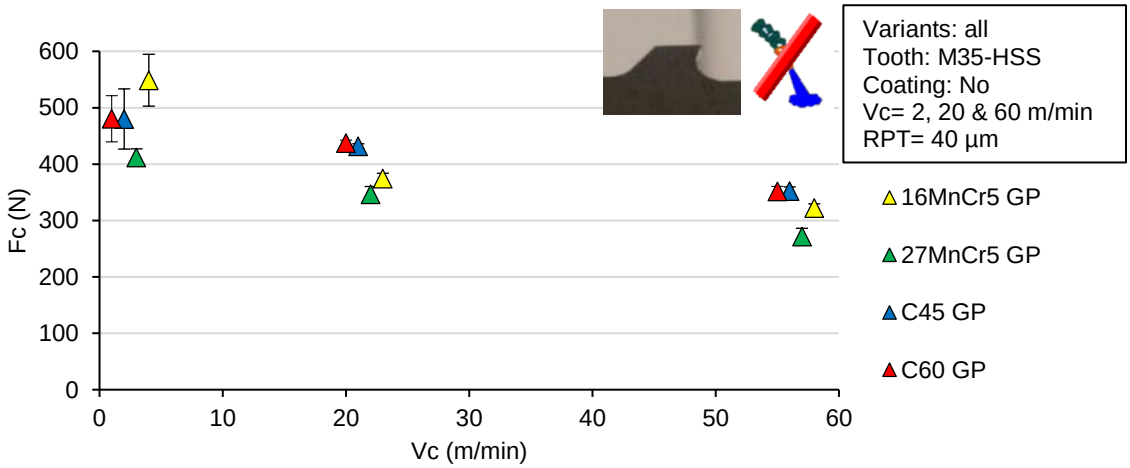

Figure 125. Cutting broaching forces versus sliding speed on Globular Pearlitic FP steels

• Summary of the fundamental study:

Finally, as done in the tribology part and following the same working way, all the results were summarized in a table checking the changes from variant to variant in each speed. The variations, taking as reference the standard (R) variant, were represented with increments as done in the chapter dedicated to tribology (Summary of the fundamental study).

Taking the standard variant as reference, the trends can be seen in the Figure 126. Comparing versus the CG variant, at the lowest speed in except for the 27MnCr5 in all the cases there were obtained much lower cutting forces. For the medium and highest speed the variation was negligible with respect to the 27MnCr5 and the C45 while the 16MnCr5 decreased at 20 m/min and varied a few at the highest speed. The C60 suffered a huge decrease at the medium speed and decreased a bit at 60 m/min.

Steel Grade	Coarse Pearlite Grain (CG)			Globular Pearlitic (GP)			With more Bands (WB)		
Cutting speed	2	20	60	2	20	60	2	20	60
16MnCr5	↓	↘	→	→	↗	↗	'	'	'
27MnCr5	→	→	→	→	→	↘	→	→	→
C45	↓	→	→	↑	↑	↑	↑	↑	↗
C60	↓	↓	↘	↑	↑	↑	'	'	'
C70	'	'	'	'	'	'	'	'	'

Figure 126. Cutting forces comparison between reference and variants.

Assessing the effect of a GP variant, different trends can be reported, for example the C45 and C60 variants show a high increase variation for all the speeds. Nevertheless, the 16MnCr5 and 27MnCr5 show similar results for the lowest speed whereas the former shows a slight increase for the medium and highest speed and the later shows similar results at medium speed and decreasing trend for the highest. Finally, checking the trends on the comparison towards the banded variants (WB), the only remarkable changes are seen for the C45 steel that the forces are hugely increased. The comparison with the forces obtained with the 27MnCr5 resulted in negligible changes.

Cutting and feed forces versus microstructural parameters

The cutting forces results were plotted in terms of the microstructural features as done in Chapter 3. The experimental design of experiments was set with 3 different cutting speeds and 3 different RPT giving an overall of nine cutting conditions. As it has been seen in the Figure 121, this occurs with the lower cutting speed (2 m/min) and the largest RPT (40 µm). In these cases, the green colour was given to the lower RPT or speed, the yellow to the medium one and the red colour to the highest, being in this way consistent as with the previously presented results.

- Broaching cutting forces versus ferrite content:

Going through the differences between forces in terms of ferrite content, keeping constant the speed and changing the RPT (Figure 127), we can see that, evidently, all the variants complied with the premise that the higher is the RPT the higher were the acquired forces. Besides, it can be also advised that for the lowest RPT the differences between the results were quite low whereas for the medium and highest RPT, the

differences were larger. Going through each of the cutting conditions, there was an increase in forces the higher was the ferrite content. What is more, the variability in forces was higher for the GP variants and the 16R.

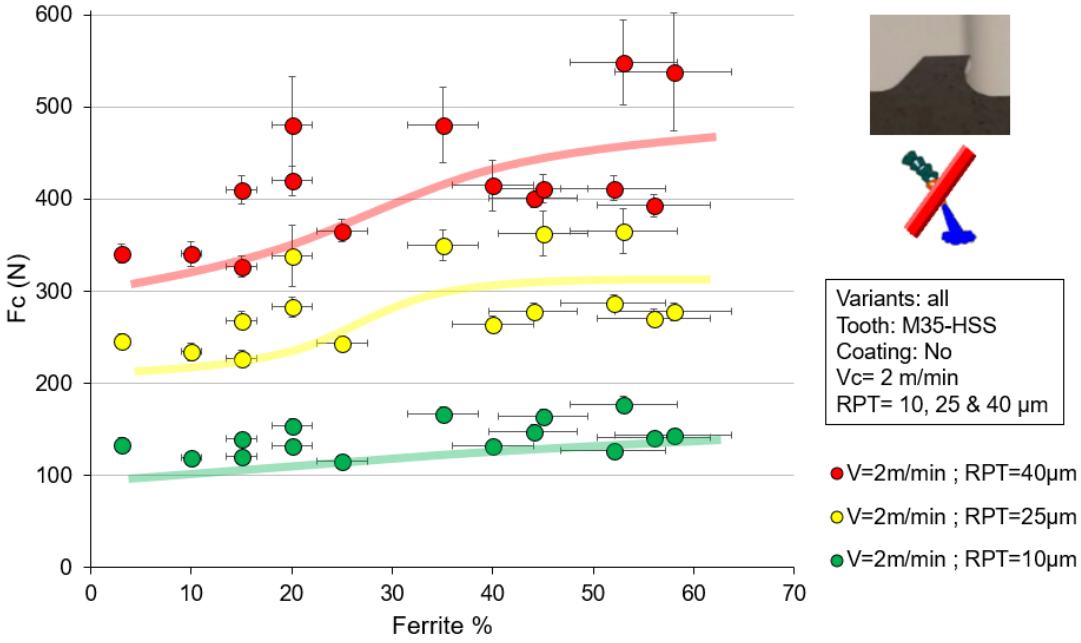

Figure 127. Broaching cutting forces versus ferrite content on FP steels changing RPT.

On the other hand, keeping constant the RPT and changing the speed (Figure 128), it can be seen that, for lower speeds, the acquired forces were higher. What is more, it can be also advised that for the low ferrite content variants the differences between the results is quite low. Going separately to each cutting conditions, there is a raise in forces the higher is the ferrite content. What is more, the variability in forces is higher for the higher ferrite content variants for the lower and medium speeds. For the highest speed there is almost no variability with the increase of the ferrite content.

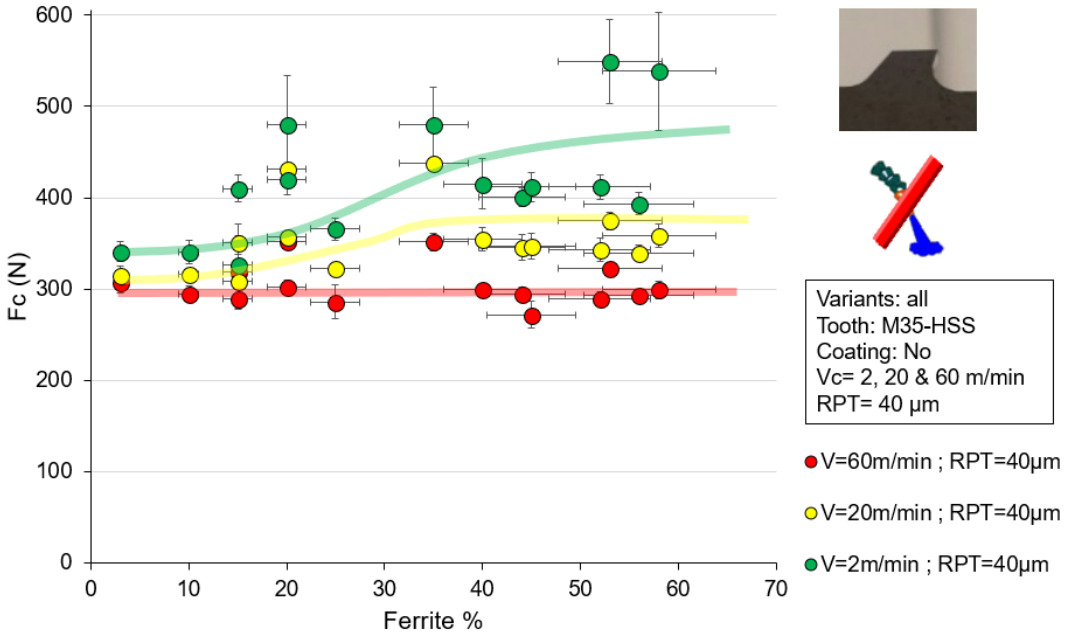

Figure 128. Broaching cutting forces versus ferrite content on FP steels changing speed.

- Broaching cutting forces versus interlamellar space (IS):

Cutting forces obtained in broaching versus the IS of the FP steels are plotted in the Figure 129. It was also seen that the higher the RPT, the larger the differences between the results were. Going through each of the cutting conditions, there is not a clear trend relating the cutting forces with the IS of the steels.

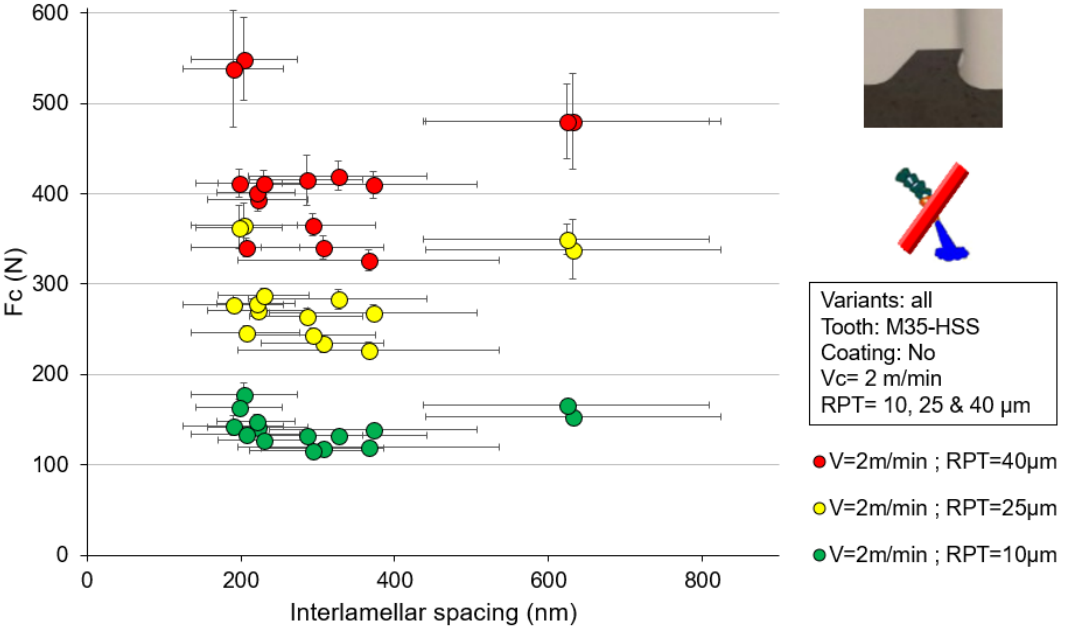

Figure 129. Cutting broaching forces versus IS changing RPT.

Note: The IS was proved to be of interest not only for the partners but also in the revision of the literature review. In this case, the standard deviation makes difficult to extract any conclusion on the results so from this point on this microstructural feature is kept aside.

- Broaching cutting forces versus hardness:

Analysing the cutting forces results in terms of hardness, it was first kept constant the speed changing the RPT (Figure 130). Besides, it can be also advised that for the lowest RPT the differences between the results is quite low whereas for the medium and highest RPT, the differences are larger. As the hardness increases the obtained forces become lower, with a variability also decreasing with the hardness and higher RPT conditions.

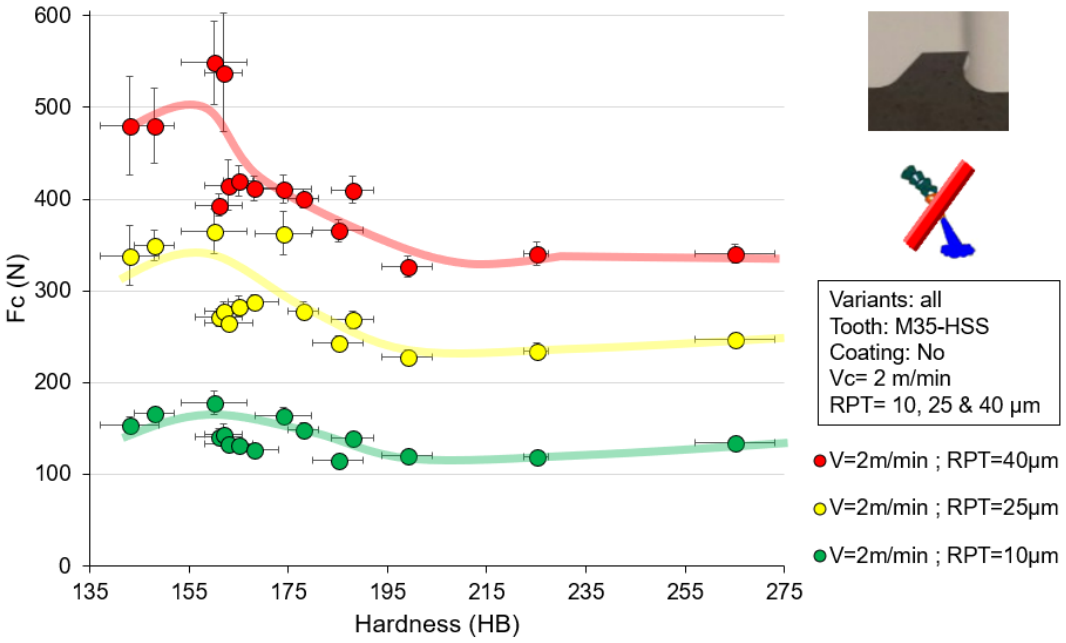

Figure 130. Cutting broaching forces versus hardness changing RPT.

Additionally, the results were plotted versus the hardness keeping constant the RPT and changing the speed (Figure 131). Firstly, it can be seen for lower speeds that the acquired forces are higher. It can be also advised the low variability of forces for the high speed that all the values are around 300 ± 25 N. Regarding the hardness, it has been easy to find a trend, it was surprising to see that the obtained forces are lower the higher is the hardness where the contrary effect was expected.

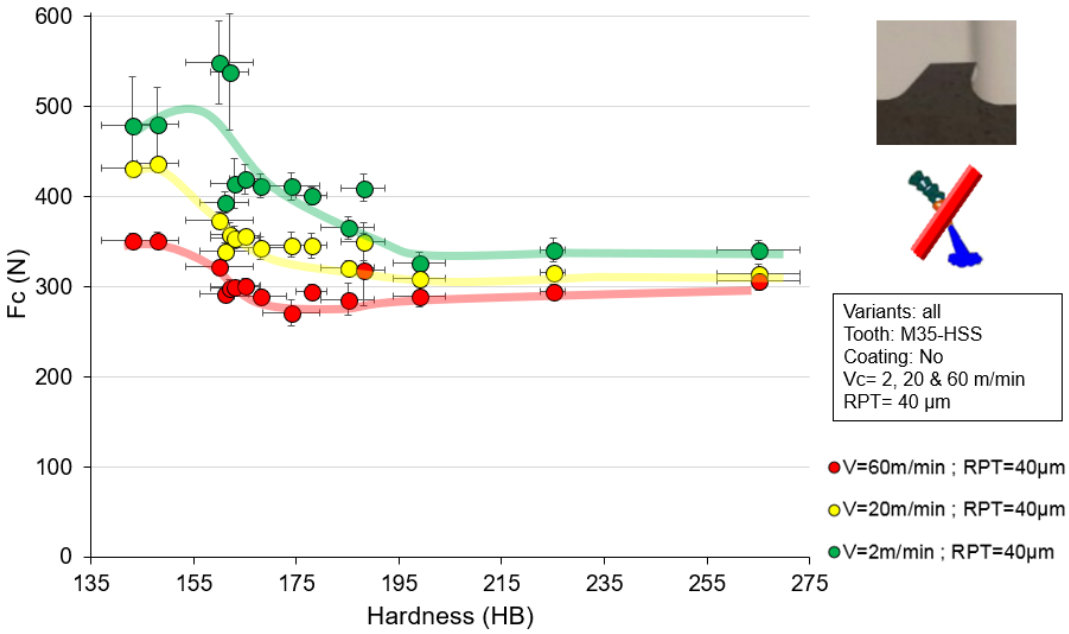

Figure 131. Cutting broaching forces versus IS changing speed keeping RPT constant.

- Broaching cutting forces versus ferrite grain size:

At last, the forces were plotted versus the grain size of the ferrite providing also interesting results (Figure 132). The grain sizes vary few microns (from 10 to 30µm), but consistent results could be seen with its increase. It was found that the larger the grain size the lower the cutting forces were. Checking the values, higher value variability was seen for the higher RPT tests. Furthermore, the trend was similar for any of the RPT tested.

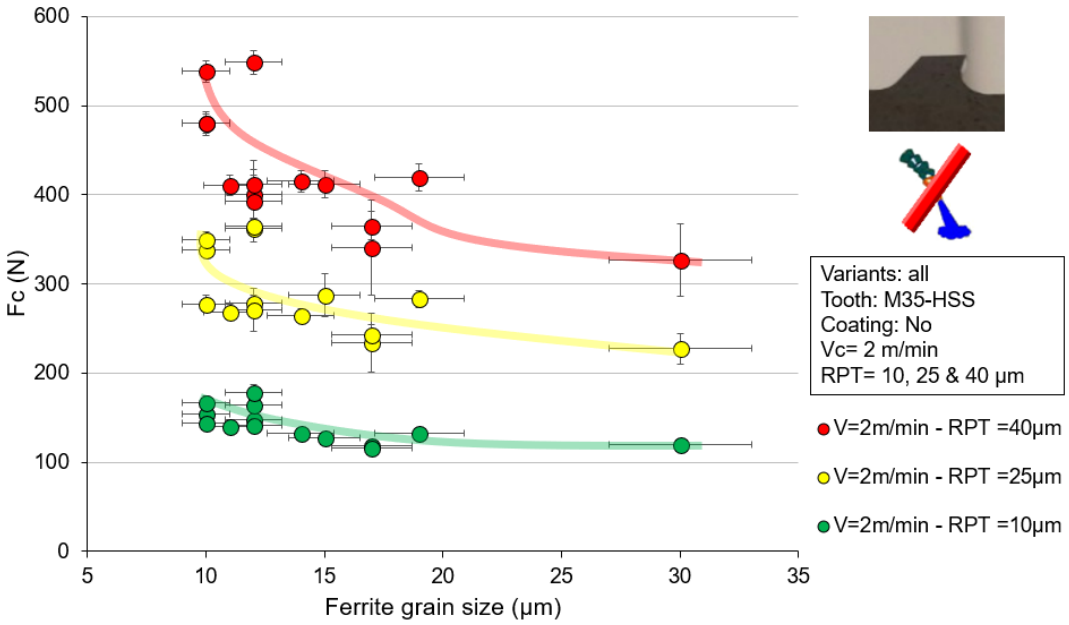

Figure 132. Cutting forces versus grain size keeping constant the speed and changing RPT.

On the other hand, in the Figure 133 the results were plotted keeping constant the RPT and varying the speed. It could be seen that for lower grain sizes and lower speeds the higher the forces were, whereas as the grain size increased the results tended to equalize. Focusing on the highest speed results, it could be seen that the highest and lowest forces were obtained for similar grain size (11 ± 2 µm).

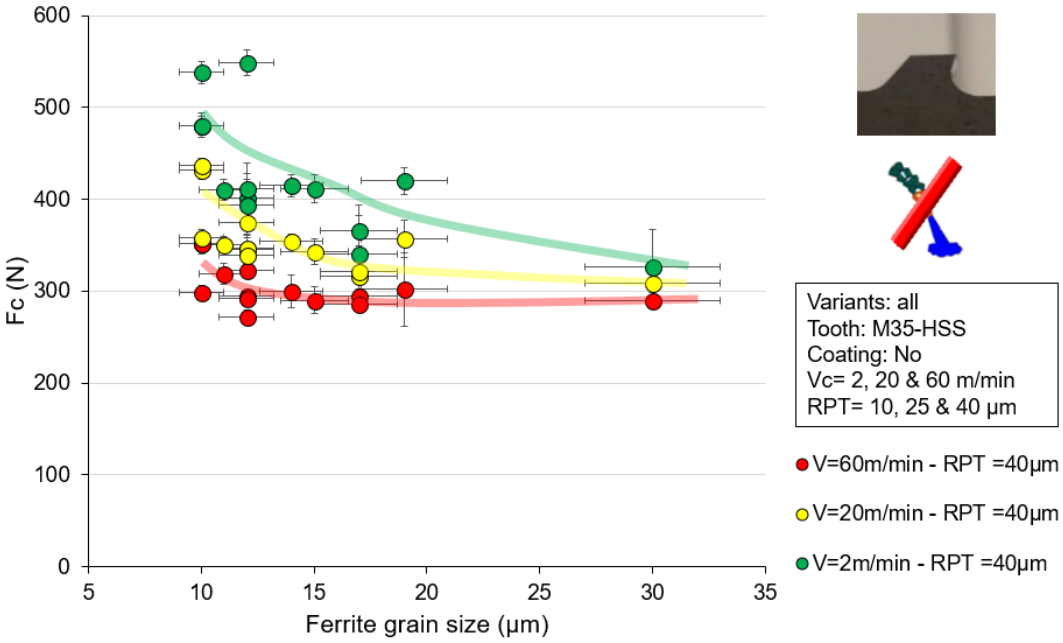

Figure 133. Cutting forces versus grain size keeping constant the speed and changing RPT.

Roughness versus cutting speed

This section deals with the roughness obtained in the fundamental broaching campaign i.e. in nine different cutting conditions over the whole bunch of FP steels. The aim was to give an overall view of the roughness behaviour when changing the speed or the RPT. In this case, the lines dividing the results obtained at different progressions was not easy to make but the highest roughness are obtained at the highest speed. Ra (Figure 135) and Rz (Figure 136) roughness were obtained measuring it three times in the cutting direction in a randomly selected area around the centre of the workpiece (Figure 134).

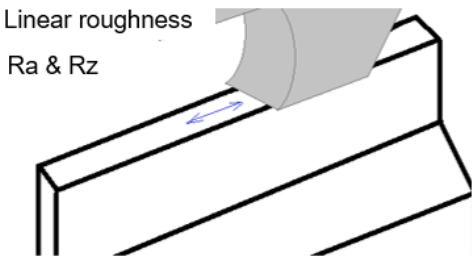

Figure 134. Scheme of the roughness measurements zone and direction.

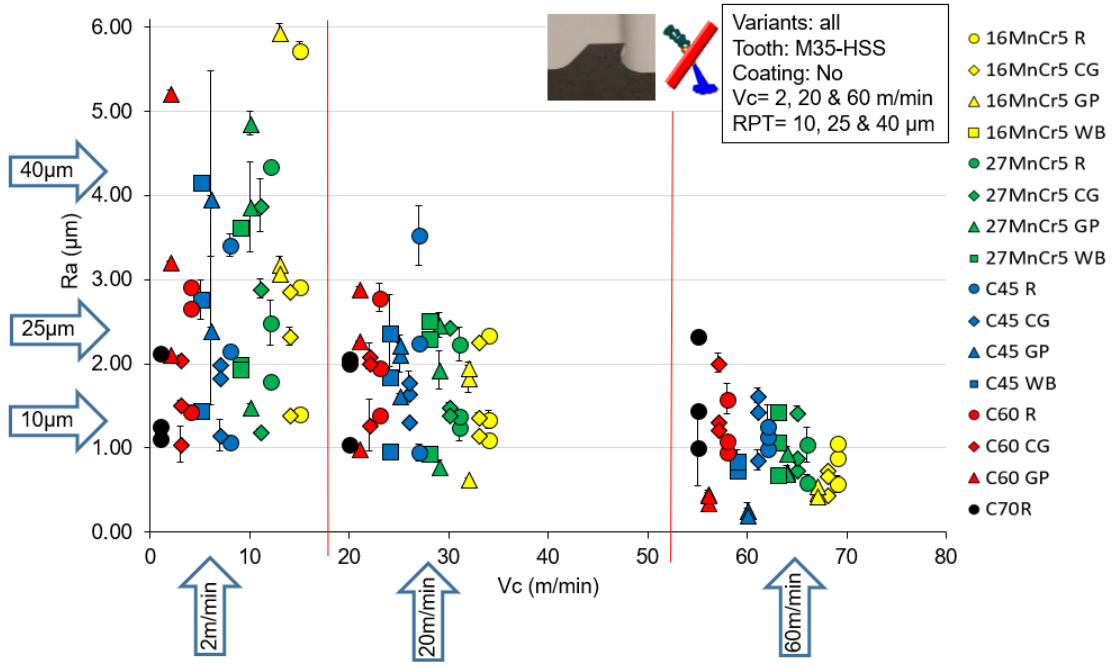

Figure 135. Ra roughness obtained in the fundamental broaching campaign.

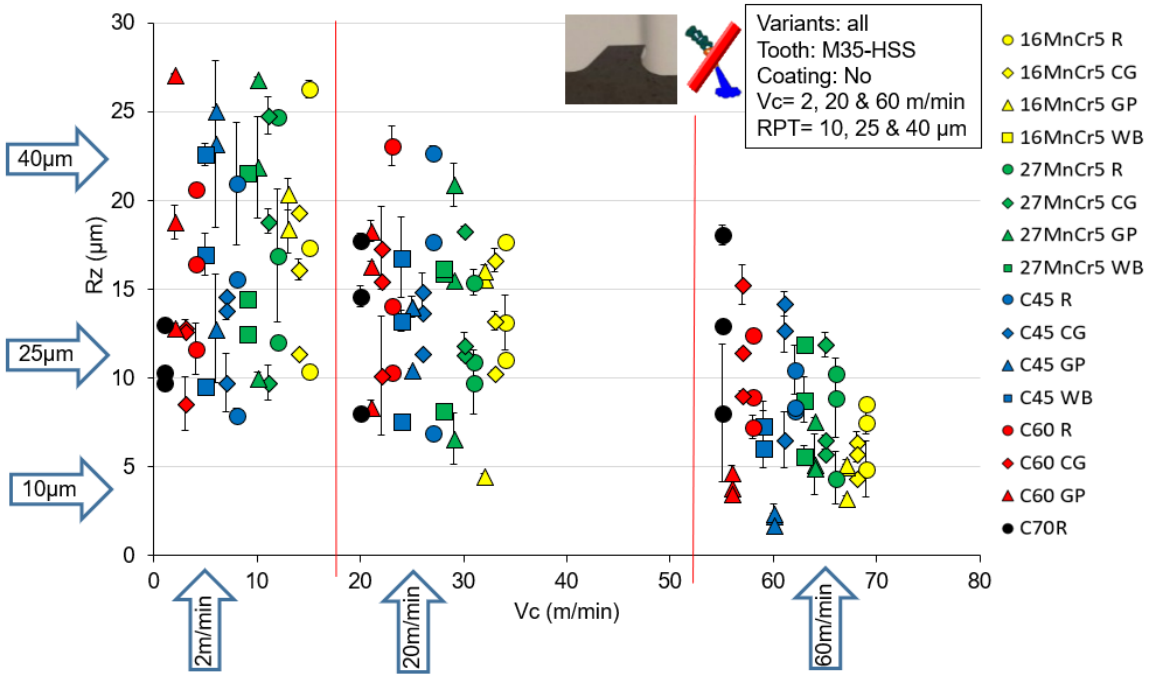

Figure 136. Rz roughness obtained in the fundamental broaching campaign.

Roughness analysis in terms of microstructure features

The roughnesses obtained (linear to the cutting direction) after the tests were plotted in terms of the microstructural features as done with the fundamental and broaching focused study of the tribology. From this point on there were only displayed the Ra results keeping aside the Rz as although the values differed quite much, it was seen that the trends were similar in both. As in the case of forces, the higher roughness values were

obtained with the lower speed (2 m/min) and the largest RPT (40 µm). In these cases, the same colour code was applied; green colour for the lower RPT or cutting speed, the yellow for the medium one and the red colour to the highest.

• Roughness versus ferrite content:

In the Figure 137, the roughnesses were plotted in terms of ferrite content keeping constant the speed and changing the RPT. In this graph, it can be seen that, for the medium and highest RPT as the ferrite content increased the roughness increased. On the contrary, for the lowest RPT the best roughness values were obtained. This trend varied increasing (from around 1.1 µm to 2 µm) and decreasing again as the ferrite content increased. Therefore, it can be said that for the lowest speed the shift of the ferrite content did not affect to the roughness.

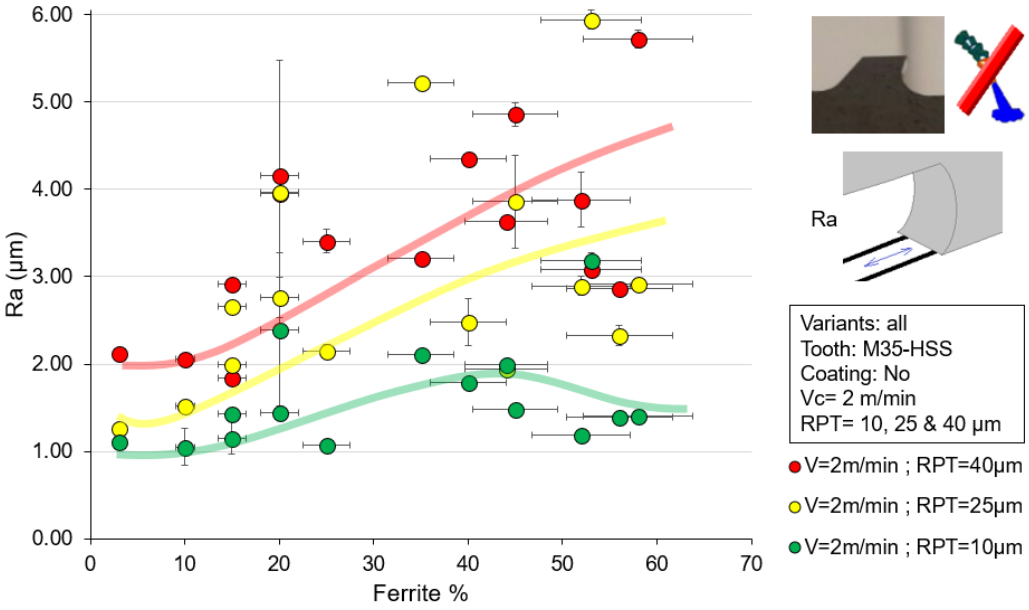

Figure 137. Ra roughness versus ferrite content on FP steels changing RPT.

On the other hand, keeping constant the RPT and changing the speed (Figure 138) three different trends can be seen. All the three essays provided around 2 µm roughness for the lowest ferrite content variant (C70). From this point on, the experiments performed at the lowest speed provided a great variety of roughness values moving between 2.9 and 5.7 µm. The tests performed at medium speed, as the ferrite content increased, the roughness values kept around 2.4 µm except for three variants. For the high speed tests, as the ferrite content increased from 3% to 25% the roughness decreased steadily and from 30% ferrite on, the values moved around 0.5 and 1 µm with very low deviation. Surprisingly, the negative effect of the ferrite content disappeared with the increase of the cutting speed.

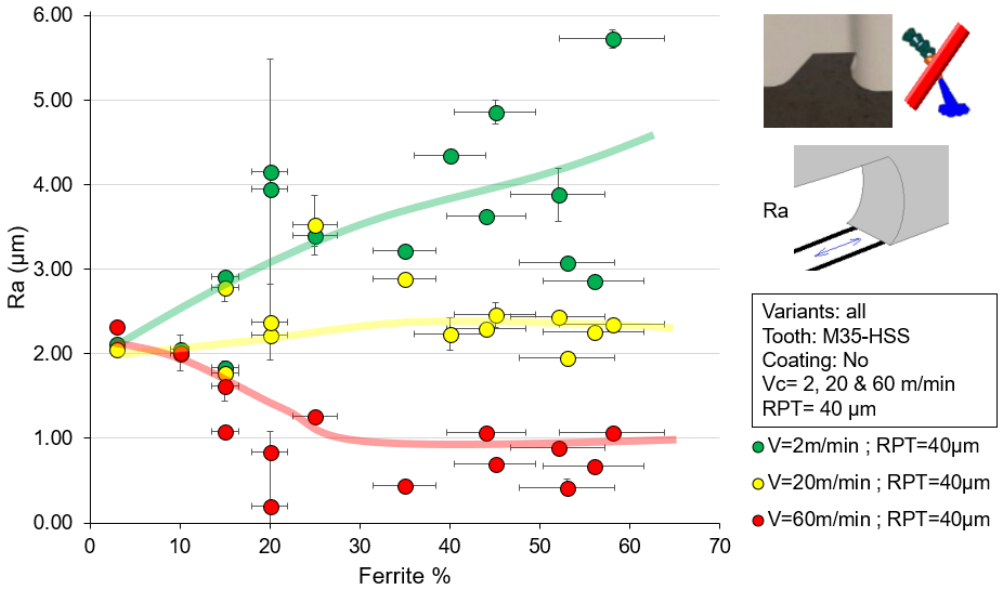

Figure 138. Ra roughness versus ferrite content on FP steels changing speed.

- <u>Roughness versus hardness:</u>

Analysing now the roughness in terms of hardness, the results keeping constant the speed and changing the RPT are plotted in Figure 132. Analysing this graph, the same trend can be observed with the three different RPT: the larger was the hardness the lower was the roughness, this decrease is steeper when increasing the RPT.

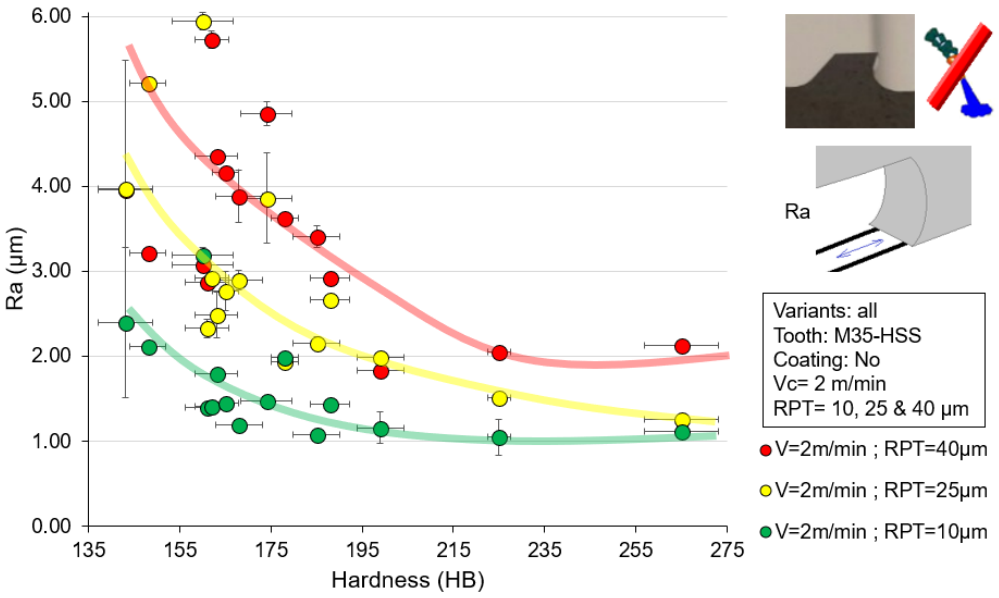

Figure 139. Ra roughness versus hardness changing RPT.

Additionally, the results were plotted versus the hardness keeping constant the RPT and changing the speed (Figure 140). For the medium speed, it can be also advised that for almost all the steels the roughness varied very few (between 2 and 3 µm). For the

highest speed a clear trend appeared, showing that as the hardness increased the roughness increased from 0.03 µm up to 2.3 µm on the hardest steel.

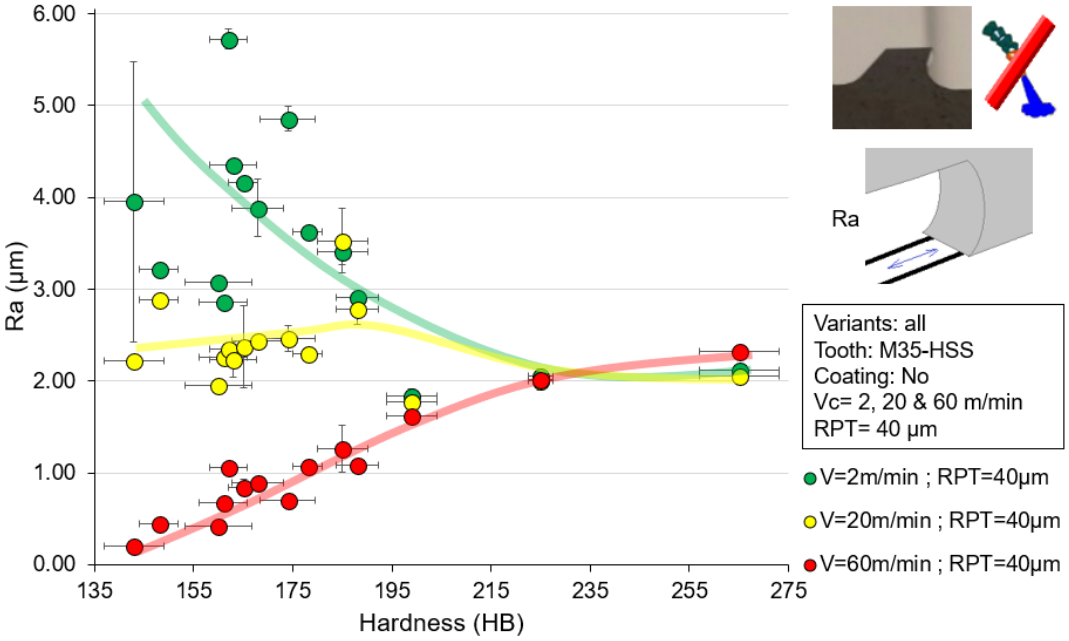

Figure 140. Ra roughness versus hardness changing speed keeping RPT constant.

Analysing the two previous graphs, it can be pointed out that with the increase of the hardness, the Ra was reduced except for high cutting speeds where low hardness values improved the roughness.

- Ra roughness versus ferrite grain size:

At last, the roughness was plotted versus the grain size of the ferrite providing also interesting results (Figure 141). The obtained trends were quite similar to those obtained with the hardness. The grain sizes vary few microns (from 10 to 30µm), but there were obtained consistent results with its increase. It was found that with higher grain size the obtained roughness values were lower. In overall, higher roughness values were obtained for higher RPT but the variability in results was quite higher compared to the tests performed at lower RPT. So, for some cases the roughness values obtained with the medium RPT were higher. For the highest grain size variant the obtained results are equal for the high and medium RPT and similar to that obtained at the lowest.

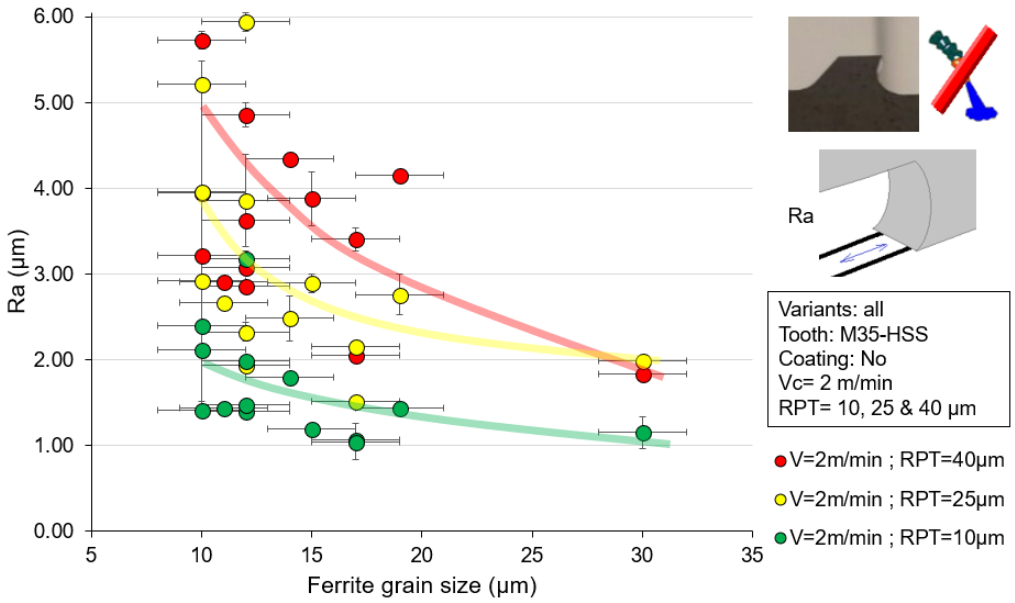

Figure 141. Ra roughness versus grain size keeping constant the speed and changing RPT.

On the other hand, in the Figure 142 the results were plotted versus the grain size keeping constant the RPT and varying the speed. In this graph, it can be seen that for lower grain sizes was found the highest variety in roughness for any cutting condition. For the lowest and medium speeds, the roughness decreased as the grain size increased. As the ferrite grain size increased, the Ra reduced except for high cutting speeds where low grain size values improved the roughness.

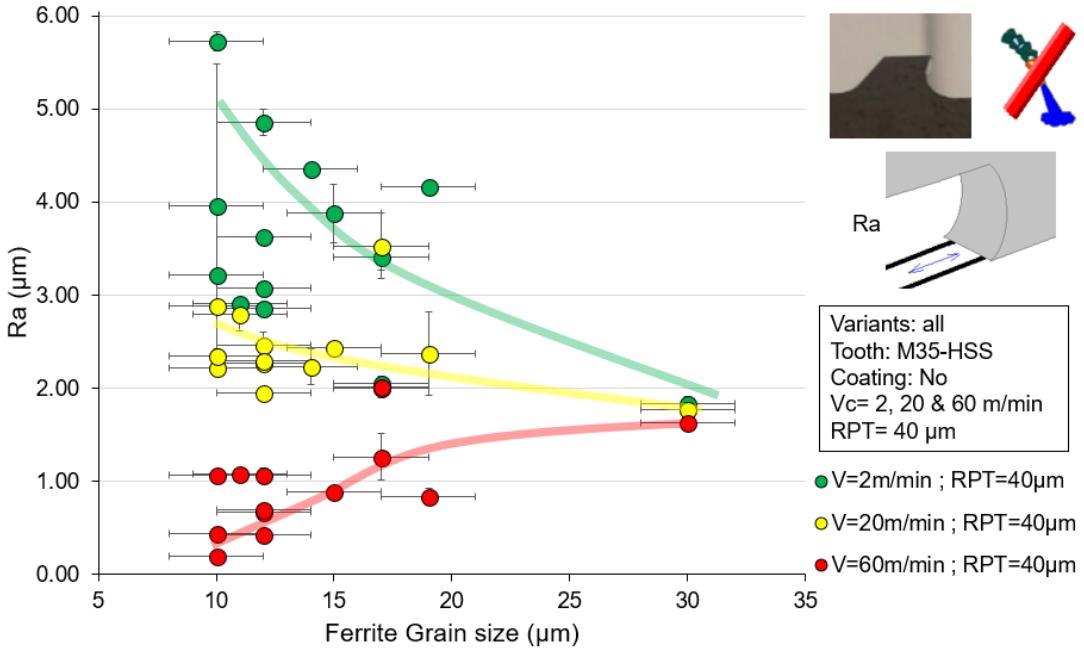

Figure 142. Ra roughness versus grain size keeping constant the speed and changing RPT.

5.1.3 Tooth state campaign

After performing the first broaching campaign over all the FP steels it was seen that the main differences in terms of forces and roughnesses were found at the lowest speed and highest rise per tooth (V=2m/min & 40µm). In this second campaign, the goals were to assess the influence of the coating and the lubrication on the previously studied broaching outputs. So, four additional campaigns were prepared, in this case working with the same speed and RPT but with two different ways of coating the tool (fully coated and coated with the rake face resharpened) and in dry or under lubricated conditions. When displaying the results, the following abbreviations were employed: UNC for the uncoated tooth, COA for the fully coated tooth and IND for the coated tooth with the rake face resharpened (Figure 11). Based on the results obtained in the first campaign linked to the tribology results it was also made a selection among the steels shown in the Table 23. The most interesting, i.e. those providing the most different results in terms of forces, roughness as well as tribological behaviour were selected.

Table 23. Steel selection for the focused campaign.

Steel grades	**Microstructure status**			
	Standard (Reference)	Coarse pearlite Grain	Globular Pearlite	More Banded
16MnCr5	16R	16CG	16GP	16WB
27MnCr5	27R	27CG	27GP	27WB
C45	45R	45CG	45GP	45WB
C60	60R	60CG	60GP	-
C70	70R	-	-	-

Cutting and feed forces

As done in the previous section, the recorded feed forces results were quite similar in trends to the cutting forces, so only the latter were displayed. Anyway, the reader will be able to find the results of the feed forces in the appendices.

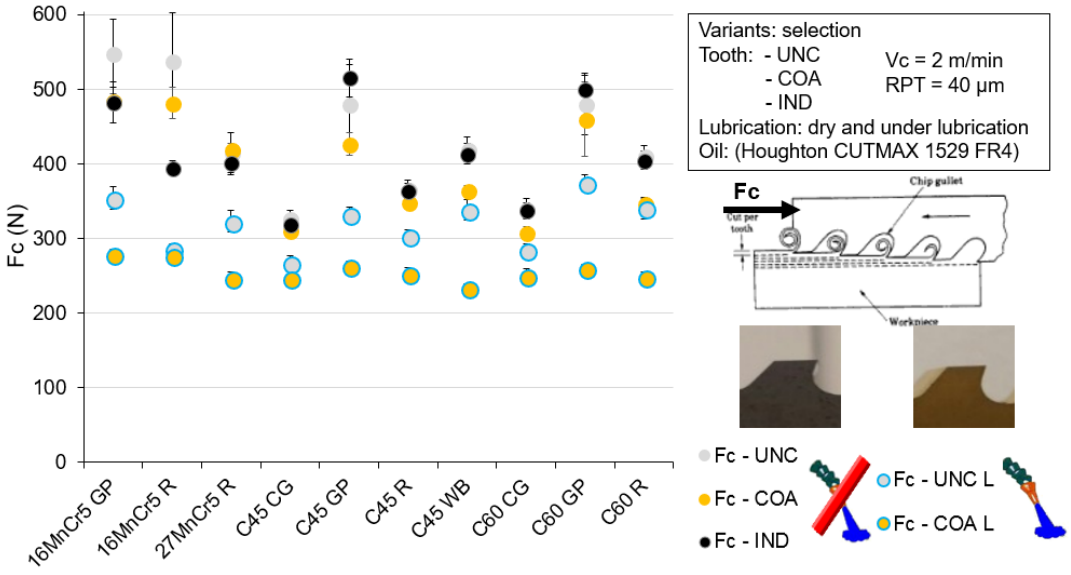

Figure 143. Cutting forces in one sole cutting condition over different tooth state and lubrication.

Figure 143 shows the clear influence of the lubricant and the influence of the coating. When analysing the results in terms of microstructural features, the results were split showing the influence of lubrication and separately the influence of the coating in dry.

Cutting forces versus microstructural parameters

The cutting forces results obtained in the tooth state campaign were also plotted in terms of the microstructural features as done in the fundamental broaching campaign.

- Broaching cutting forces versus ferrite content:

The tests carried out under lubrication (Figure 144a) showed an increasing trend but less steep. Besides, comparing the uncoated and the coated tooth tests under lubrication it was also advised that the tests performed with the uncoated tooth provided higher forces for each variant (up to 130 N more). Comparing the tests performed in dry conditions similar trends were perceived in the Figure 144b, although there were little differences between them there was a clear increasing tendency the higher was the ferrite percentage. In general, it can be said that the forces acquired with the any coating type in the tooth in dry conditions increased as the ferrite content increased.

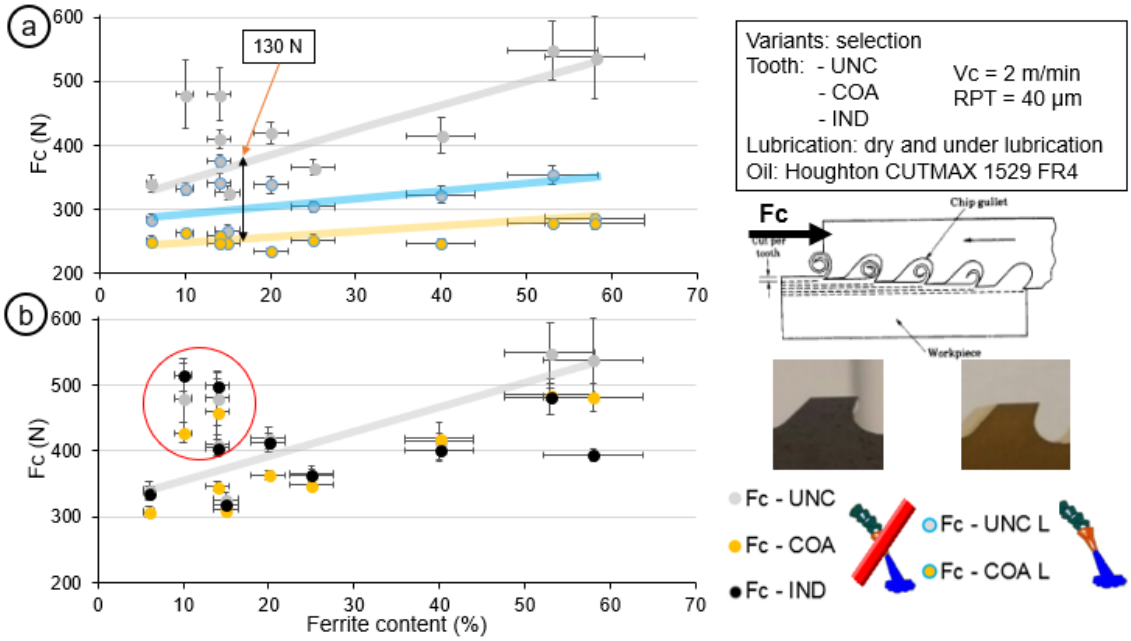

Figure 144. Material selection campaign broaching cutting forces versus ferrite content.

- <u>Broaching cutting forces versus hardness:</u>

Analysing the cutting forces results in terms of hardness (Figure 145), it was seen that the acquired forces turned lower the higher was the hardness. Besides, it can be also observed that the lubrication tended to limit the effect of the hardness (Figure 145a) and that the combination with a TiN coating drastically reduced the forces. The tests performed in dry conditions provided similar decreasing trend with the hardness increase (Figure 145b).

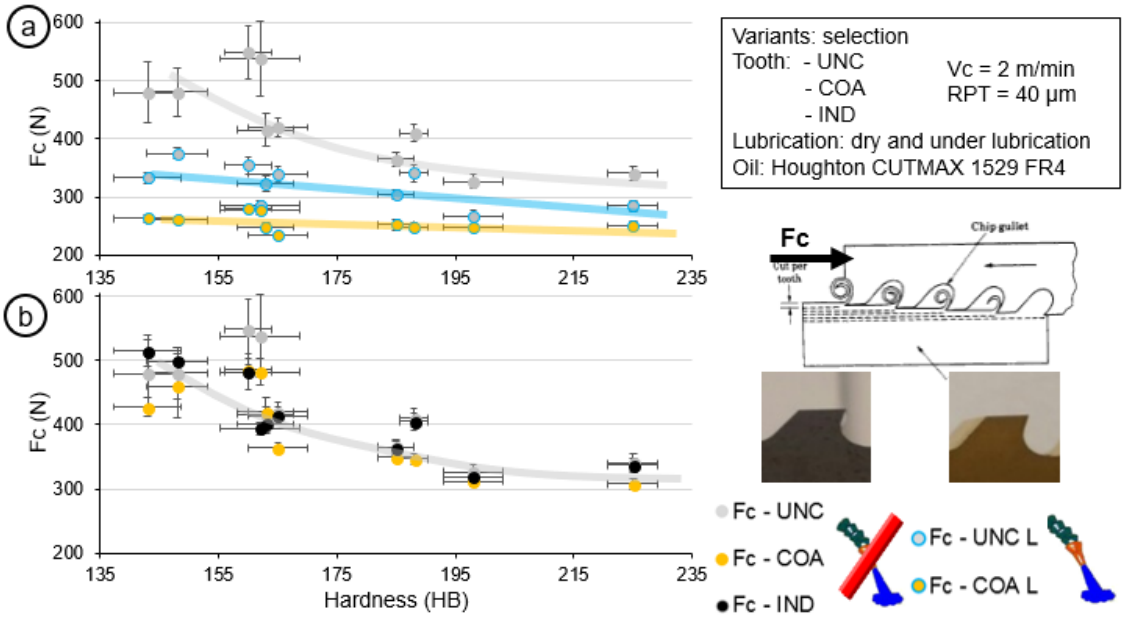

Figure 145. Cutting forces obtained in the selection campaign versus hardness.

The trend found on the cutting forces versus ferrite grain size were consistent results with its increase being very similar to those obtained versus hardness, so they were moved to the appendices.

Roughness analysis

The roughness obtained (linear to the cutting direction) are shown in the Figure 146. This time were only displayed the Ra results keeping aside the Rz as although the values differed quite much, it was seen that the trends were similar in both. In this figure, it can be seen that the higher values were obtained with the lower speed (2 m/min) and the largest RPT (40 µm).

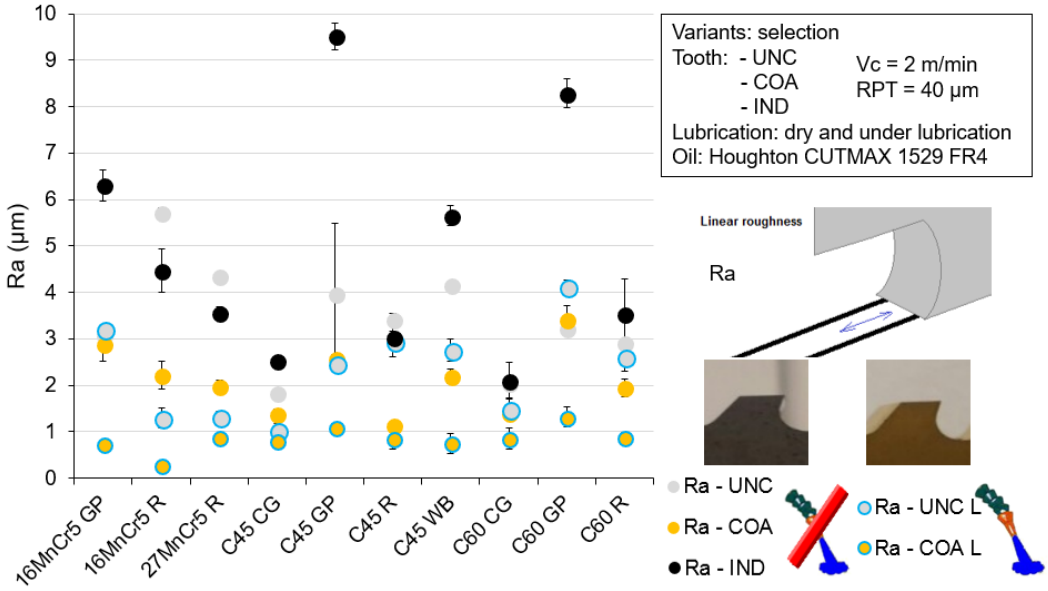

Figure 146. Ra roughness obtained in the material selection campaign.

Roughness in terms of microstructural features

The Ra roughnesses obtained (linear to the cutting direction) after the tests were plotted in terms of the microstructural features as previously done.

- Ra roughness versus ferrite content:

On the tests performed under lubrication (Figure 147a) for the uncoated tooth the trend was increasing up to 35 ferrite percentage, from that point on the obtained Ra values did not follow this trend. On the contrary, the values obtained with the coated tooth under lubrication provided almost the same value (Ra = 1 µm) whichever was the ferrite content. Hence, it cannot be clearly said that the lubrication tended to equalize the results but it can be stated that the combination of coating and lubrication did. In the Figure 147b, the three tests performed in dry conditions were compared where a great variation of roughness can be perceived for the tests performed with the industrial tooth. For the

tests performed with the coated tooth the trend was similar to that obtained with the uncoated tooth but in this case the tendency was less steep.

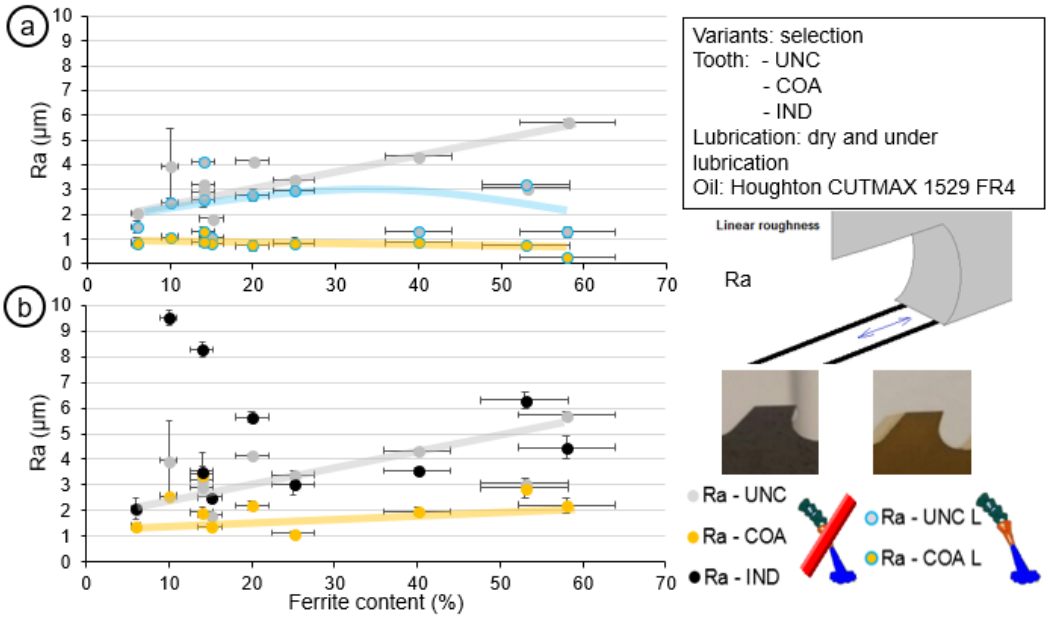

Figure 147. Material selection campaign Ra roughness versus ferrite content.

- <u>Ra roughness versus macrohardness:</u>

It can be seen in Figure 148a that for the coated tooth tests under lubrication, the roughness was independent from de hardness as it varied very few. For the rest of the tests decreasing trends were obtained with the increasing hardness. Analysing the Figure 148b, the tests performed with the industrial tooth in dry conditions provided a constant decreasing trend the higher was the hardness. The rest of the tests put up similar decreasing trends but less steep.

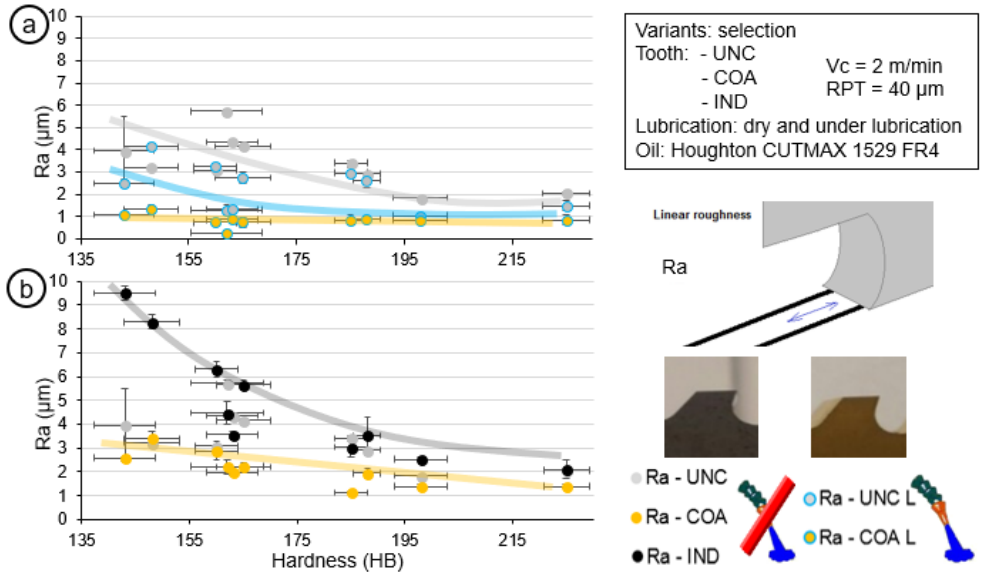

Figure 148. Material selection campaign Ra roughness versus hardness.

When plotting the Ra roughness versus ferrite grain size it was found that the obtained trends were quite similar to those obtained with the hardness. The graph can be found in the annexes for readers with further interest on this.

Chip analysis

The chips were studied measuring the chip compression ratio. This can be done in two ways, measuring the length of the chip or the width after machining. The latter is the most used method as usually there is not known the uncut length of the sample.

$$t_1 * l_1 = t_2 * l_2,$$

Being t_1 and l_1 the uncut chip thickness and length; and, t_2 and l_2 the after cut chip thickness and length. Therefore, we are estimating the λ_h (chip compression ratio) dividing l_1 and l_2.

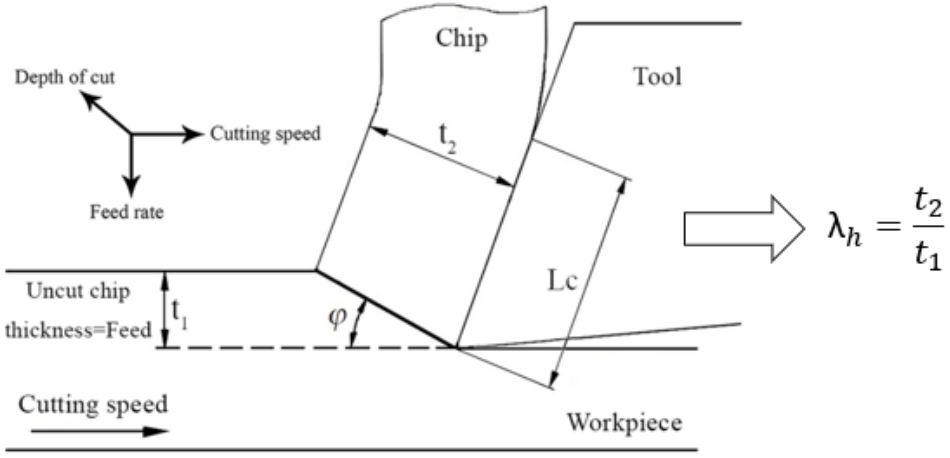

Figure 149. Scheme of the cutting focused on the tool tip.

After measuring all the lengths with the use of the Leica microscope, these results were plotted versus the microstructure of each steel, obtaining a wide variety of trends in terms of the different features.

- Chip compression ratio (λ_h) versus ferrite content:

Going through the differences between chip compression ratios, there were firstly plotted in terms of ferrite content (Figure 150). In both graphs, we can see that, as the ferrite content increased the λ_h increased meaning that the chip got thicker. The influence of the lubrication is clearly seen on the graph upper in the Figure 150, leading to almost no differences even for the tests performed with the fully coated or uncoated tooth. In the Figure 150 are showed the tests performed in dry, where the industrial tooth type exhibited a similar behaviour. However, the coating did not lead to a λ_h reduction as it increased with the ferrite content increase.

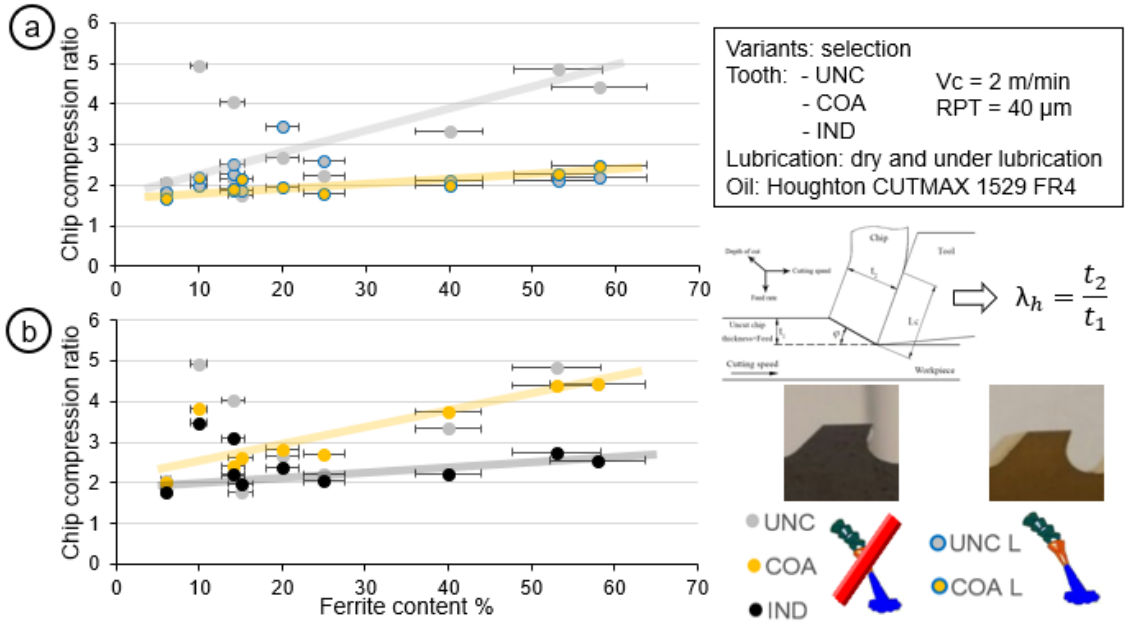

Figure 150. Material selection campaign chip compression ratio versus ferrite content.

- Chip compression ratio (λ_h) versus hardness:

Analysing now the (λ_h) in terms of hardness, it can be seen in both graphs of the Figure 151 a decreasing trend of the λ_h when increasing the hardness. Analysing separately both graphs, as it was previously seen, the lubrication limited the influence of the hardness (Figure 151a). The different coating analysis provided similar trends, being decreasing for the three tests and less steep for the tests performed with the industrial tooth (Figure 151b). It can be also seen that the hardest steel led to almost the same λ_h value whichever the tooth state was even in dry or lubrication.

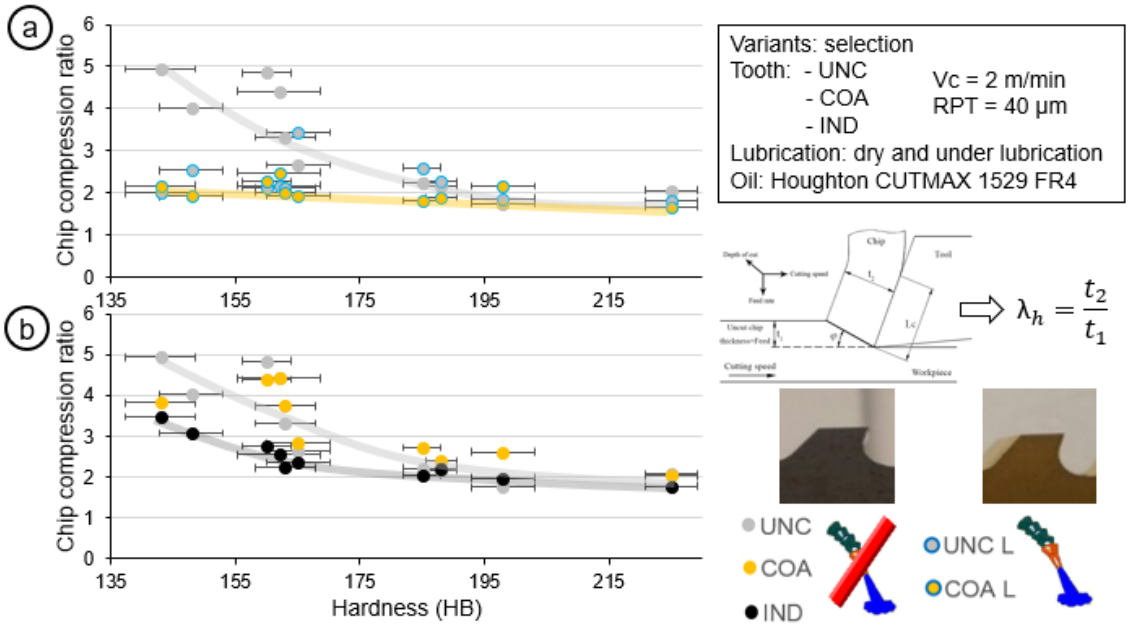

Figure 151. Material selection campaign chip compression ratio versus hardness.

The λ_h measurements were also plotted versus the grain size of the ferrite providing similar results to those obtained versus the hardness so the figure was moved to the appendices (0).

Microstructure of the chips

Within the tooth state broaching campaign chips were carefully collected during the experiments, embedded in resin, polished, etched and thoroughly analysed. The objective was to observe the deformed microstructure and measure the average chip thickness so as to obtain the already shown ship compression ratio.

As it can be seen in the micrographs of the Figure 152, the microstructure was found to be highly deformed with, even under lubricated conditions, an intense shear occurring at the tool-chip interface. If a pseudo serration could be observed on the standard R, a more pronounced one was visible on the globular pearlite GP ones. This serration could be related to the amplified sticking behaviour characterising these type of microstructure as seen in the chapter 4 concerning the tribology in the tool-material contact. An innovative finding was that GP variants behave almost as a purely ferritic material as the ferritic matrix is deformed whereas the pearlite globules only move within this matrix.

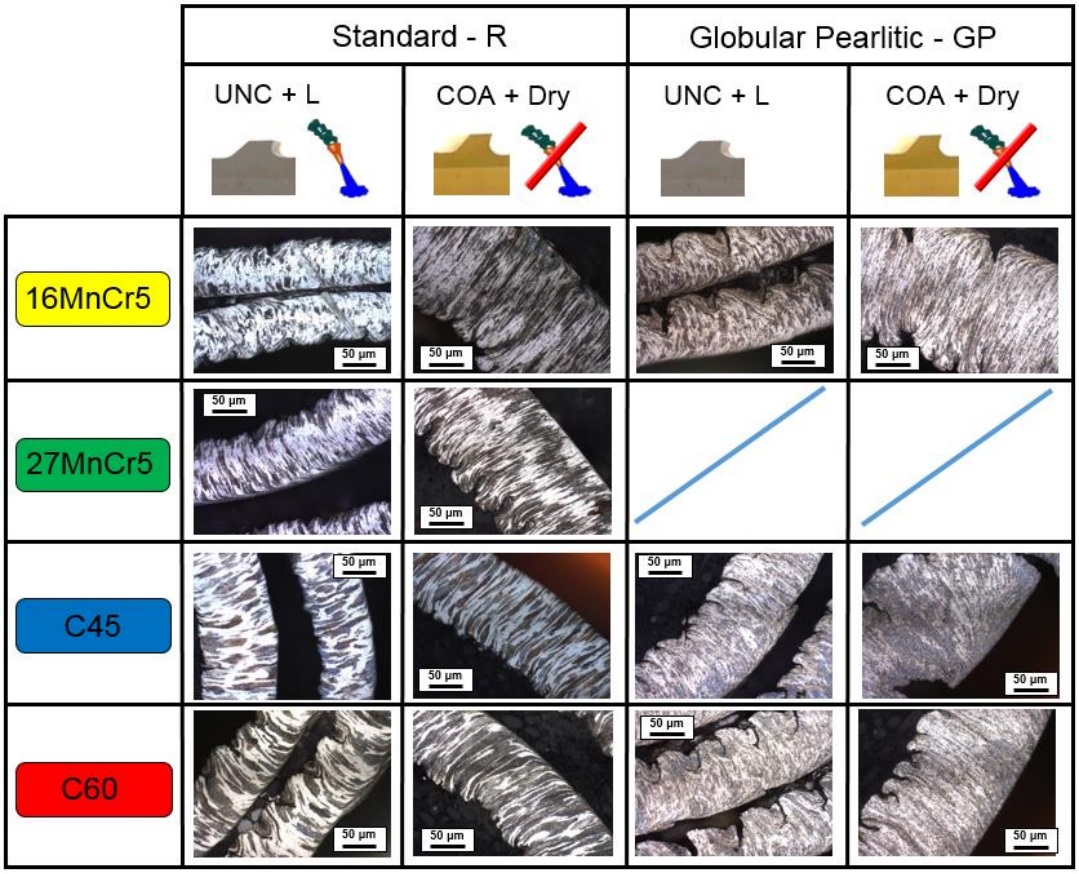

Figure 152. Examples of chip micrographs showing the deformed microstructure (a)

Chip compression ratio and more precisely the average chip thickness is an interesting output parameter providing an image of the average chip sliding speed over the tool (mass flow conservation): thicker chips correspond to a slower chip meaning that larger friction can be expected. On the contrary, thinner ones are generated when the chip can easily slide over the tool meaning lower friction at the tool-chip interface. The latter were found in those tests run under lubrication that can be seen in the “UNC + L” columns of the Figure 152. Using a lubricant reduced the chip thickness which became constant around 100µm whatever the ferrite content was. This was again in good agreement with the data from the tribology chapter (4) as the friction coefficient under lubricated conditions was close to 0.12 for all the investigated variants.

5.1.4 Wear tests in broaching

With the aim of having a picture of the wear generated by the steels on the broach, tool life tests were run. As there were supposed to be long and, therefore, time consuming tests, there were selected just the three C45 steel variants. This way it could be analysed the same composition in three different microstructural variants, so it could clearly be obtained the wear just in terms of microstructural features.

Methodology

For these tests, completely new teeth were used for each material so it could be assessed the wear correctly. It was decided to use the industrial tooth to make them more consistent compared to the final potential application. In this case, the setup was updated to improve the stiffness, then, cutting was thus performed in a vertical direction (Figure 153).



Figure 153. Broaching setup vertically mounted showing the wear tests sample and sued tooth.

One of the drawbacks was that the machine could not reach 60 m/min speed any more due to working length reduction. This way, the most severe cutting conditions already used in a previous campaign were V_c=20 m/min and RPT=40 µm. Although the broaching process in the industry is performed under lubrication these tool life tests were performed in dry conditions in order to amplify the wear behaviour and reduce time required for this campaign.

Table 24. Tool life tests cutting conditions.

Variables	Conditions
Cutting speed (m/min)	20
Rise per tooth (µm)	40
Steels	C45: R =>30 m, CG =>75 m & GP =>15 m
Lubrication	Dry
Coating	IND: Industrial type tooth (flank face coated & rake face resharpened)
Broached distance	Tool life tests (checking every 5 m)

Thus, the main idea was to start broaching and stop each meter machining length, acquiring forces, measuring the roughness on the surface of the workpiece and checking the evolution of the wear. The wear checking relied on removing each stop the tool from the machine, taking it to the Alicona profilometer. Once in the Alicona, the workpiece had to be correctly positioned focusing on the cutting edge (Figure 156) with the precise lens and light adjustment so as to take an accurate photo of the edge. Finally, after taking the photo, the measurement process was carried out based on the previously obtained photo analysing the profile of the cutting edge (Figure 157).

Results

As commented before, besides quantitatively obtaining the wear, the evolutions of machining forces and roughness were also recorded. The first selected steel was the standard C45 (R) which was broached up to 30 m (600 passes over the workpiece). There was not seen any significant change in forces (Figure 154) nor in roughnesses (Figure 155). The following selected steel was the C45 GP, the softest one among all the bunch of steels indeed. With this steel there were machined just 10m not obtaining significant results. There was obtained a decrease in forces when passing from the first force acquisition at the first pass to the second force acquisition after machining 5 meters (Figure 154). After analysing the images taken with the alicona it was thought that could

be related to the burr generated in the resharpening process in the broach manufacturing (Figure 11). Concerning the roughness obtained with this material there was an increase in value and in deviation the longest is the machined distance (from 0 to 10 m).

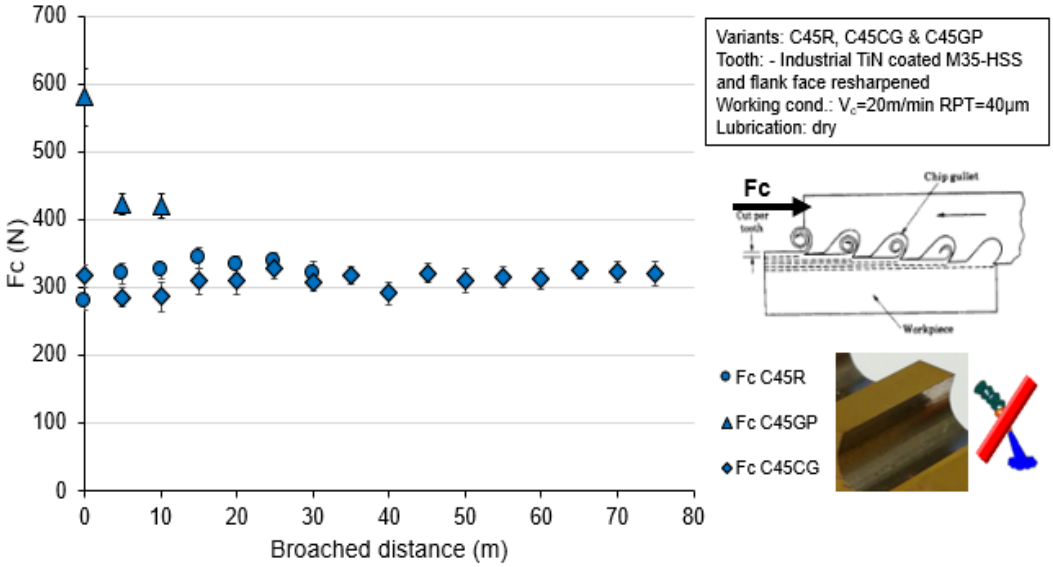

Figure 154. Cutting forces evolution while broaching C45 steel variants.

Finally, it was taken the toughest material among the four C45 variants, the Coarse Grain in fact. It was decided to run the tests stopping each 5 meters until the wear apparition or the end of the sample, surprisingly the latter happened first. It was expected to obtain some kind of wear but it did not emerge. The roughness measurements were stopped after machining 30 m as no changes were observed as the part was being broached. Summarizing the results, it was not expected to see anything different to what it was obtained up to that point.

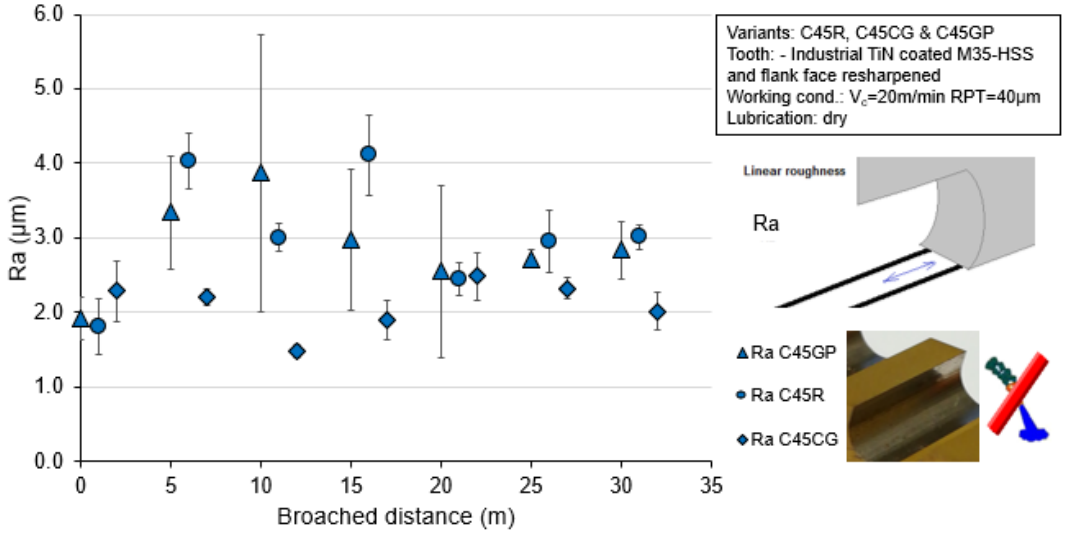

Figure 155. Ra roughness evolution while broaching C45 steel variants.

After checking the pictures obtained in the alicona microscope it was not seen any relevant change from image to image (Figure 157). In each image it can be seen the flank face below (uncoated) and the clearance face above (coated). In some cases, adhesion effect could be advised on the edge of the tool (e.g. after machining 70 m) but any trace of wear.

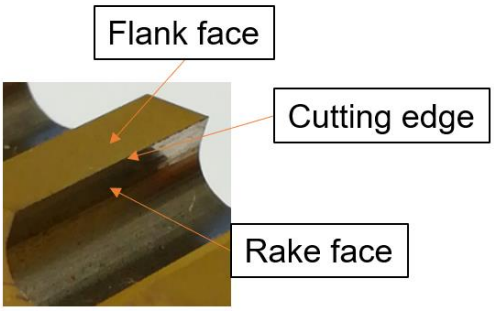

Figure 156. Zone of the tooth photographed.

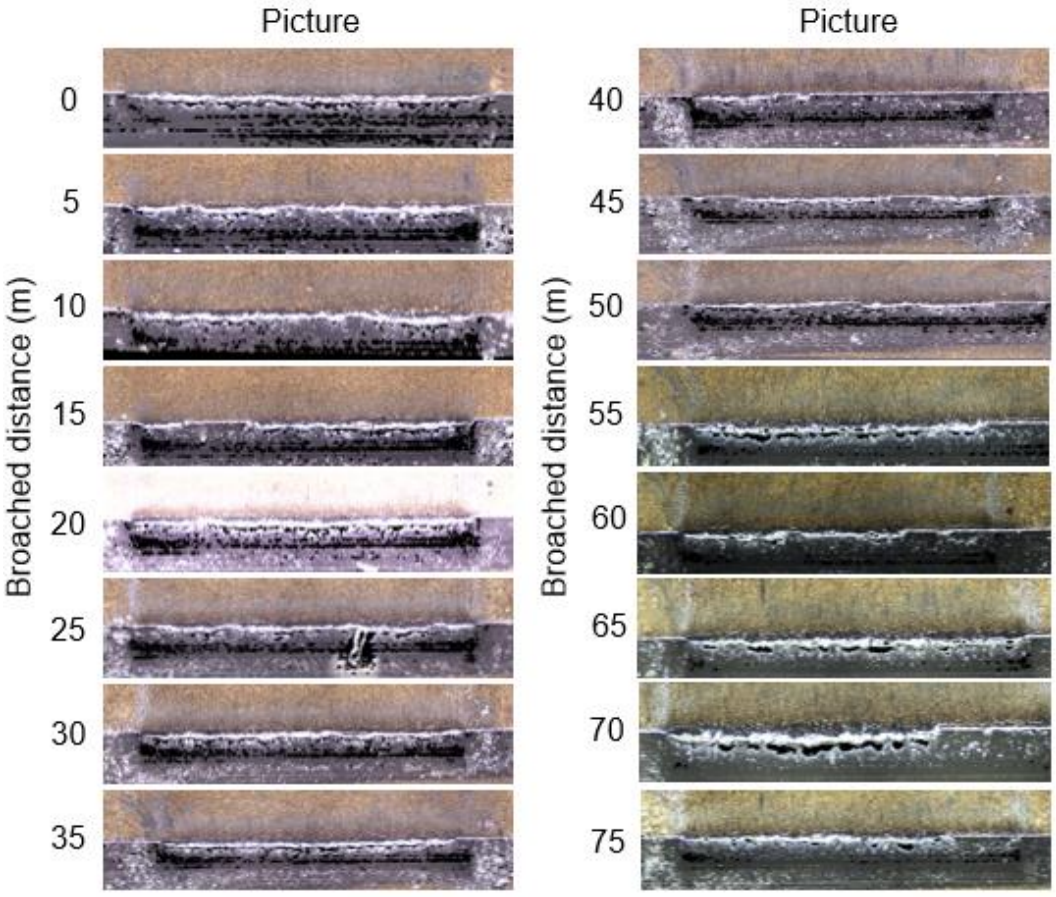

Figure 157. Evolution of the tool edge state after broaching each 5 meters.

Conclusions

After performing these wear tests there was not obtained any remarkable results. As it could be seen, there was no change in forces neither in roughness related to the machined meters quantity. Besides, analysing the photographs of the tool edge it could not be seen anything.

For the future, longer life tests linked to more severe cutting conditions could lead to wear. This form of performing the tests showed that the tool lasted more than expected, being a surprise for the tool manufacturer.

5.1.5 Broaching outputs versus friction coefficient

In this subsection, a correlation was proposed comparing the data obtained from the broaching tests with the friction coefficients obtained in the fundamental study chapter 0.

Forces comparison

- Fc & μ comparison versus ferrite content:

The first parameter to analyse was the ferrite-pearlite ratio. From one side, the friction values versus the ferrite percentage in the fifteen different variants can be seen in the Figure 158b. Analysing the tendency over the three speeds, the same pattern can be appreciated as the ferrite content increases. For the three speeds, as the ferrite content increased (from 10% to 30%) the friction value increased steadily, then as the ferrite content approached to the 50% the friction value stabilized around the same value for each of the speeds although the high ferrite contents provided low values at the highest speed.

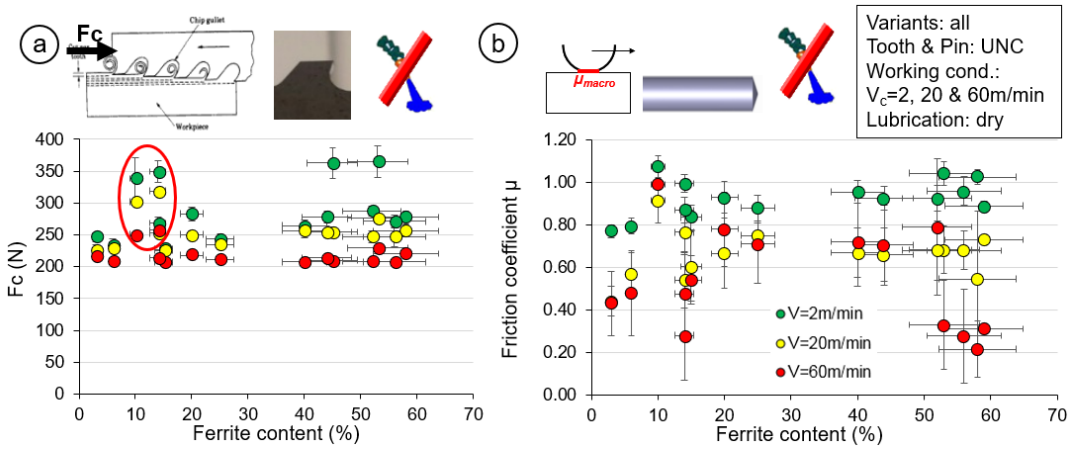

Figure 158. Cutting forces and friction coefficient comparison versus ferrite content.

In the Figure 158a cutting forces obtained from the broaching tests versus the ferrite content of the steels are displayed. At the lowest speed similar increasing CoF trend could be seen as the ferrite content rised from 10 to 30% and then stabilized from 40 to 60% . For the medium and high speed no real tendency could be appreciated. In these tests, two variants outstood over the rest of steels, the C45GP (10% ferrite) and C60GP (15% ferrite), resulting to the larger cutting forces (circled in red). At the lowest speed two high ferrite content variants provided high forces (16R & 16GP) not being that clear in tribology.

- Fc & μ comparison versus hardness:

The second parameter to analyse was the macrohardness. The friction values versus the hardness of the 15 different variants can be found in the Figure 159b. Analysing the tendency over the three speeds same decreasing pattern could be appreciated as the hardness increased with some variants out of the trend around 160HB. This trend could be related to the sticking/sliding effect happening during the tests that occurred more easily in softer materials.

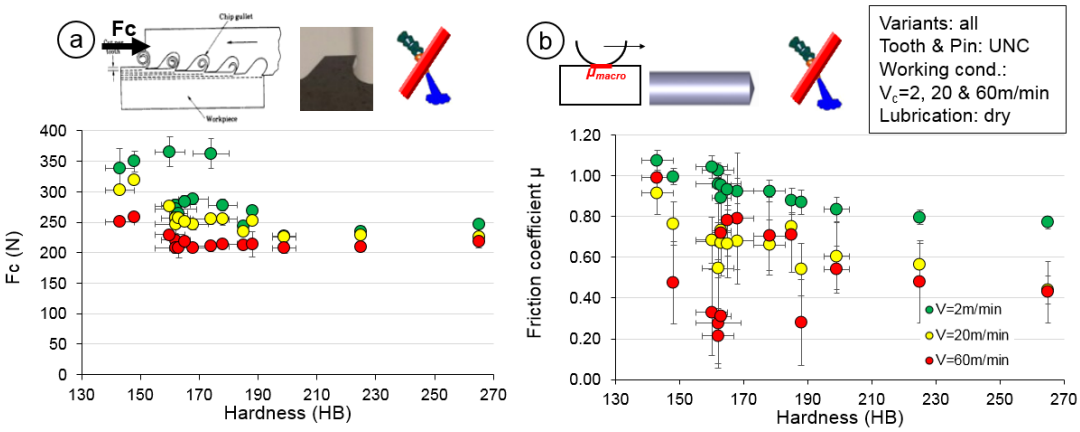

Figure 159. Cutting forces and friction coefficient comparison versus hardness.

In the Figure 159a cutting forces obtained from the broaching tests versus the hardness of the steels can be found. For the low and medium speeds similar decreasing trend could be seen as the hardness raised but for the highest speed almost all the values varied between 200 and 250 N. It could be also noted that passing from 140HB to 160HB the forces fell a 30% for the three speeds. This two variants with the lowest hardness values are the before mentioned C45GP and C60GP variants. Therefore, it could be drawn that the hardness value is not directly related to the ferrite content of the steel but other features take part in it.

When comparing forces and CoF versus the grain size of the ferrite, similar trends and behaviours were found (shown in the appendices subsection Friction coefficient and forces comparison in the page 256). As done in the previous chapters, the analysis versus interlamellar spacing was kept aside due to the large standard deviation observed on this parameter.

Roughness comparison

- Ra & µ comparison versus ferrite content:

Figure 160b shows that a similar tendency can be appreciated over the three speeds as far as the friction coefficient is concerned: as the ferrite content increases (from 10% to 30%), the friction value increased steadily and reaches a threshold for each of the speeds for a ferrite content larger than 35%. It could also be noticed that the macroscopic friction coefficient generally decreased as the sliding speed increased.

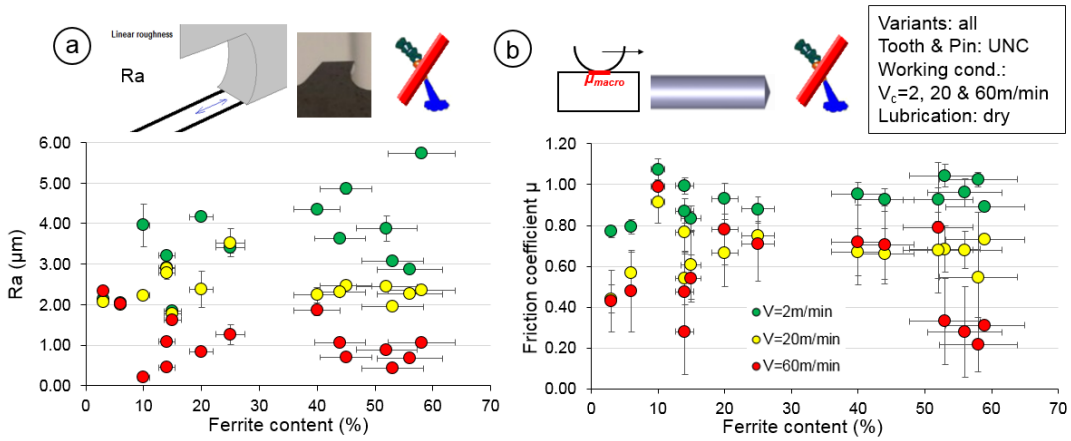

Figure 160. Ra roughness and friction coefficient comparison versus ferrite content.

Concerning the Ra roughness obtained from the broaching tests (Figure 160b), a different evolution can be observed for the three investigated cutting speeds. At the lowest speed, similar increasing trend can be seen as the ferrite content rises from 10 to 30% and then reaching a threshold around Ra = 4 µm from 35 to 50%. For the medium and high cutting speed, no clear effect of the ferrite content can be highlighted with a Ra values close to 2 µm at 20 m/min and 1 µm at 60 m/min were recorded. For the latter, a slight decreasing trend could be extrapolated but would require more tests or repetitions. However, it can be seen that the higher the ferrite content, the larger the differences between the selected cutting speeds in terms of Ra roughness.

This first analysis showed that at low cutting speeds, a correlation with the tribological behaviour seemed to be in reasonable agreement. Higher friction coefficient at tool-workpiece interface could lead to higher ploughing component, larger sticking phenomena and the occurrence of a built-up edge (BUE) affecting the surface roughness. At higher cutting speeds, the tribological behaviour of the steels with the ferrite content did not seem to be the only parameter governing the performance of the process. Even if the cutting speeds could still be considered as low compared to some other processes such as turning, thermal effects with HSS tools could be expected to take place and could start a thermal softening of the workmaterial in the primary shear zone.

- Ra & μ comparison versus hardness:

The friction values versus the hardness of the 9 different variants can be found in Figure 161b. Analysing the tendency over the three speeds, the same decreasing pattern could be appreciated as the hardness increases. This trend can be related to the sticking/sliding effect happening during the tests that occurs more easily the harder is the material (limited ploughing and sticking component).

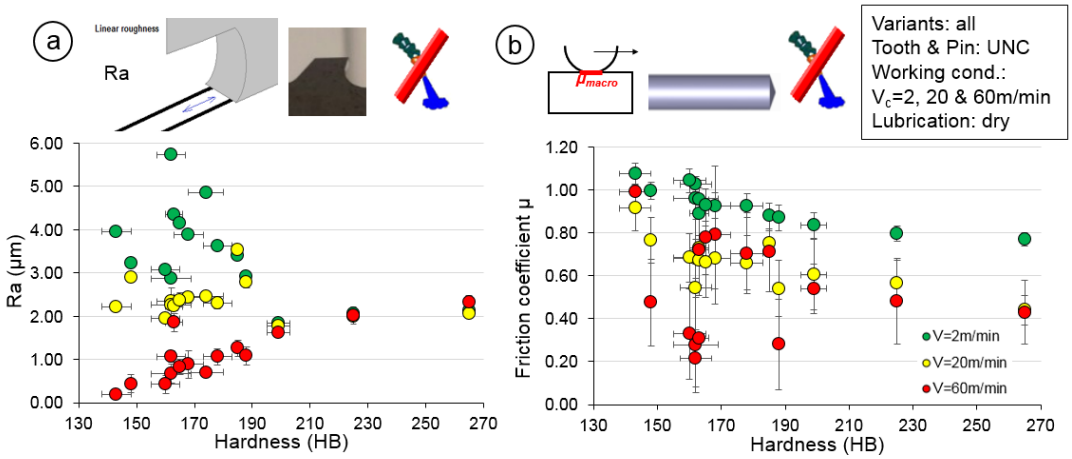

Figure 161. Ra roughness and friction coefficient comparison versus hardness.

In Figure 161a, large differences in terms of Ra roughness can be observed on the broaching tests comparing the different cutting speeds. For the lowest one, Ra decreased as the hardness increased. This could be due to the BUE effect occurring at lower hardness of the steels and correlates again well with the tribological tests in Figure 161b. At 20 m/min, the values stay stable around 2 μm but appears to slightly decrease with the hardness. At the highest speed, as the hardness increased, Ra roughness linearly increased which is in total contradiction with the observed tribological behaviour. If chatter effect could be expected at high speed, it was not clearly recorded with the available instrumentation. More advanced methods such as high-speed imaging, or further post-analysis of the machining forces (dynamic components) could confirm this statement.

Therefore, it can be drawn that the hardness value is related to the friction value but it is not directly related to the surface roughness of the steel after broaching. Comparing these results with those presented in the previous section shows that the FP ratio is not the only parameter defining the macro hardness that can affect the machining performance of FP steels in broaching. It has to be reminded that the 15 selected variants exhibited other different microstructural properties than only the FP ratio: larger grain size, pearlite morphology and phase distribution (banded structure). These properties were studied not seeing any correlation, however, this study thus showed that further

investigations on these parameters have to be carried out to clearly extract the key properties of a FP microstructure under such conditions.

Chip compression comparison

- Chip compression ratio & µ comparison versus ferrite content:

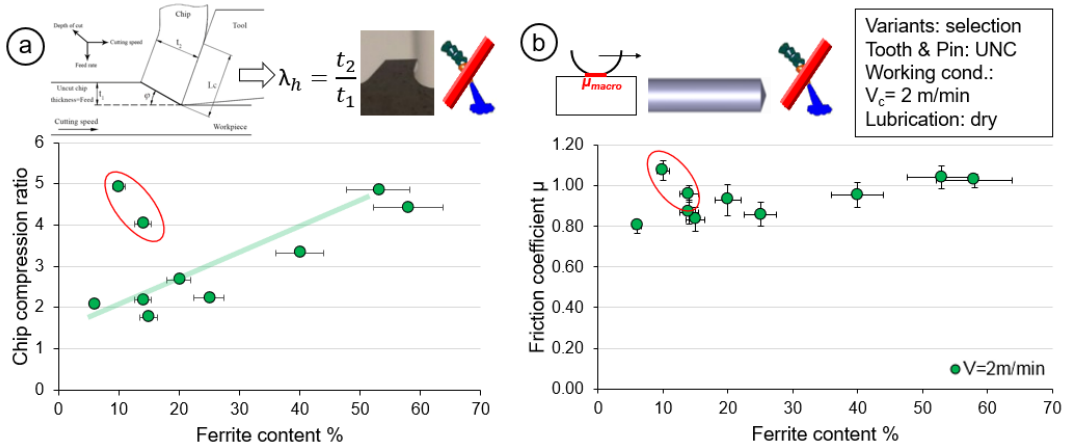

Figure 162. Chip compression ratio and friction coefficient versus ferrite content.

This comparison was only done at 2 m/min speed as the chip study was carried out in the tooth state study. Thus, increasing the ferrite content the chip thickness increased under dry conditions (Figure 162a) and the same increasing trend was seen in the Figure 162b concerning the friction coefficient. The two runs exhibiting a thicker chip between 10 and 20% of ferrite correspond to the C45 GP and C60 GP variants. This was also shown in the 5.1.3 section in the Microstructure of the chips subsection. This was in good correlation with the findings obtained in the tribology work showing that friction during the tribotests increased with the ferrite content and when changing from R (standard) to GP variants.

- Ra & µ comparison versus hardness:

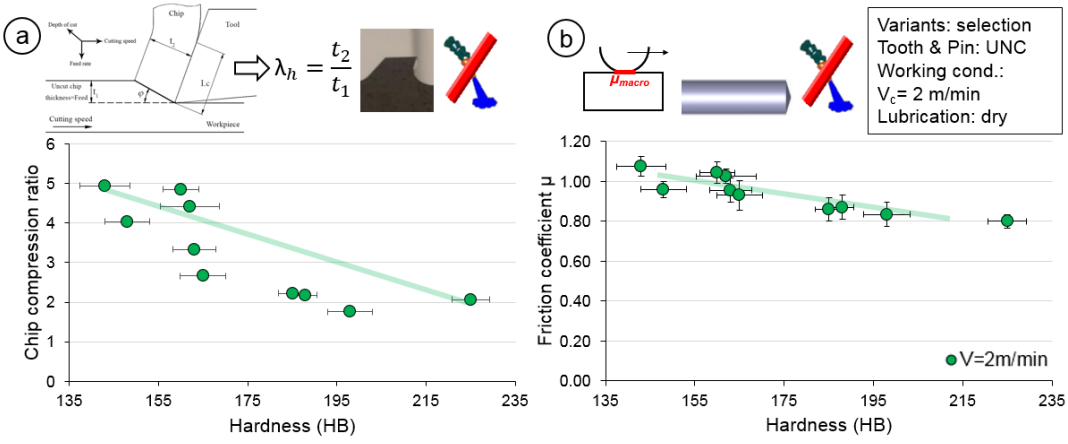

Figure 163. Chip compression ratio and friction coefficient versus hardness.

In the case of the hardness, the harder is the steel the chip thickness increases under dry conditions (Figure 163a) and the same increasing trend is seen in the Figure 163b concerning the friction coefficient. The two runs exhibiting a thicker chip between 10 and 20% of ferrite correspond to the 45 and 60 GP variants. This was also shown in the 5.1.3 section in the Microstructure of the chips subsection. This was in good correlation with the findings obtained in the tribology work showing that friction during the tribotests increased with the ferrite content and when changing to the GP variants.

Conclusions

This chapter presented a machining work performed on an experimental broaching setup fitted on a PCI METEOR 3+1 axis machine. The setup based on a single tooth operation provided consistent machining forces and in-situ chip formation. The tests were carried out on the previously presented automotive FP steels at industrial related cutting conditions. Large variations of cutting forces and roughness as well as chip analysis were highlighted depending on FP content, interlamellar spacing, macro hardness and ferrite's grain size. In a first part, the forces and roughness obtained with an uncoated HSS (M35) tool over the wide range of FP steel variants were presented. Then, doing a selection among the whole bunch of steels more tests were carried out using one sole cutting condition. These tests were performed in dry or under lubrication and with the tooth fully coated or just coated on the flank face.

5.1.6 Fundamental FP steels broaching campaign

The conclusions of the fundamental broaching campaign study will be based on the work done comparing the obtained forces and roughness in all the variants. There were highlighted the most significant conclusions:

- Largest differences between the microstructures were observed at the lowest cutting speed (Vc = 2 m/min) and largest rise per tooth (RPT = 40 µm) (Figure 121);
- The increment is a clear parameter affecting the machining forces (Figure 121);
- Overall the variations in terms of forces are quite higher on the C45 and C60 variants (Figure 126);
- Comparing to the reference variant, using a coarse pearlite grain tends to reduce the cutting forces and improves the roughness (Figure 126, Figure 135);
- The globular pearlite tends to increase the cutting forces and worsen the surface roughness (Figure 126, Figure 135);

- No clear trends were found with the ‘with banded’ structure, which sometimes provided totally different trends for different materials (Figure 126);
- The increase of the ferrite content was proved to affect to the increase of the cutting forces, at low and medium speeds and RPT (Figure 127, Figure 128);
- The increase of hardness and the ferrite’s grain size lead to a decrease on the obtained cutting forces (Figure 130, Figure 131, Figure 132, Figure 133).
- The speed was proved to be the variable affecting the most to the roughness (Figure 135);
- The increase of the ferrite content worsened the roughness at 2 m/min being more noticeable for high RPT but, surprisingly, at the highest speed (60m/min) an improving trend was found (Figure 138).
- The roughness versus hardness and ferrite’s grain size lead to different results depending on the speed. For the lowest speed, increasing the hardness the roughness had an improving trend whereas for the highest speed was totally contrary (Figure 140).

5.1.7 Tooth state campaign

The material selection campaign was performed at one sole cutting condition assessing the influence of the lubrication and the coating. The following conclusions were drawn:

- Under dry conditions, the benefit from the coating can be only visible with the material presenting the largest ferrite content (Figure 144, Figure 147);
- The use of a lubricant drastically reduces the cutting forces and reduces the differences between the variants in terms of microstructural features (Figure 146);
- Combining a fully coated tool to a lubricant led to the most interesting performance in terms of forces and roughness (Figure 146);
- Increasing the ferrite content, using GP variants, or using dry conditions increase the chip thickness, i.e. the friction at the tool chip interface (Figure 150, Figure 152);
- The use of lubricant drastically reduced the chip thickness even more so if the tooth was coated (Figure 152).

Chapter 6

FEM SIMULATIONS IN BROACHING

6 FEM SIMULATIONS IN BROACHING

In this chapter, the numerical analysis of broaching as well as the comparison with the experimental data is presented. This numerical investigation was similar to the tooth state broaching campaign, i.e. the simulations were launched in one sole cutting condition but comparing different ways of coating and the influence of the lubrication.

After a brief introduction of broaching modelling, the finite element model was described as well as the methodology to carry out the different simulations. Then the results were described and discussed. Finally, the conclusions extracted from the results and the comparisons were presented assessing the suitability of the model to predict the broaching outputs.

Introduction

Modelling of machining processes enables predicting the influence of input cutting parameters on output variables such as (i) fundamental variables and (ii) industrial relevant outcomes. Fundamental variables are forces, temperatures, strains, strain rates, stresses, and pressures. Furthermore, the industrial relevant outcomes include tool life, surface roughness, surface integrity, distortion, stability and burrs (P. Arrazola et al. 2013).

In order to predict the abovementioned outputs (Figure 164 outputs Stage I & II), different modelling approaches can be employed. For years, analytical and empirical models were the most commonly used. Recently, numerical and artificial intelligence (AI) based methods are gaining relevance with the increase in computing power. The reason for this is the capability of computers to deal with complex problems such as tool–chip contact and material nonlinearities. In this work it is used a numerical type model, so the literature review was focused on this type of models.

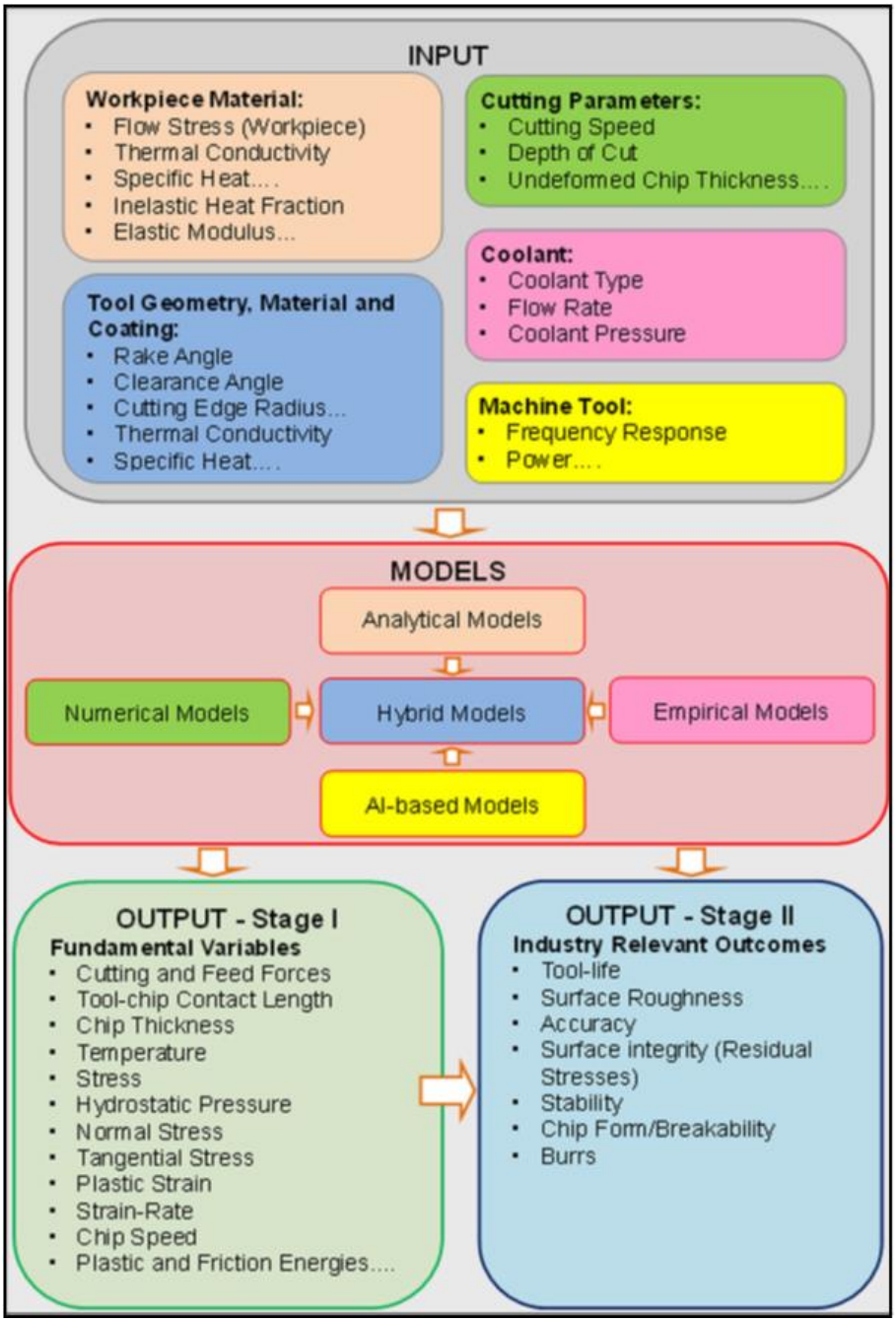

Figure 164. Two-stage modelling approach adopted for machining processes (P. Arrazola et al. 2013).

Computational/Numerical modelling in machining

There are two primary mathematical formulations of continuum-based FEM: Lagrangian and Eulerian. The lagrangian mesh deforms in time with the material while the eulerian mesh allows the flow of the material. In both analyses, either implicit or explicit time integration techniques can be utilized. A major disadvantage of the Eulerian formulation is the assumption of a steady-state mesh configuration. Thus, many researchers have adopted the computationally intensive Lagrangian approach. Schermann et al. utilized the Lagrangian technique to study the interaction between cutting process and the dynamic behaviour of the machine tool (Schermann et al. 2006).

The Arbitrary Lagrangian–Eulerian (ALE) technique combines the unique features of Lagrangian and Eulerian formulations. The ALE adopts an explicit solution technique for fast convergence (P. J. Arrazola 2010, Movahhedy et al. 2000, Ozel et al. 2011). Arrazola and Özel compared the ALE and explicit FE simulation techniques for the orthogonal cutting process (Figure 165) (P. J. Arrazola 2010). While the ALE technique with Eulerian boundaries requires a predefined chip geometry assumption, chip formation is free of any geometrical assumption in ALE with Lagrangian boundary conditions. They also showed that these two similar approaches result in different chip formation.

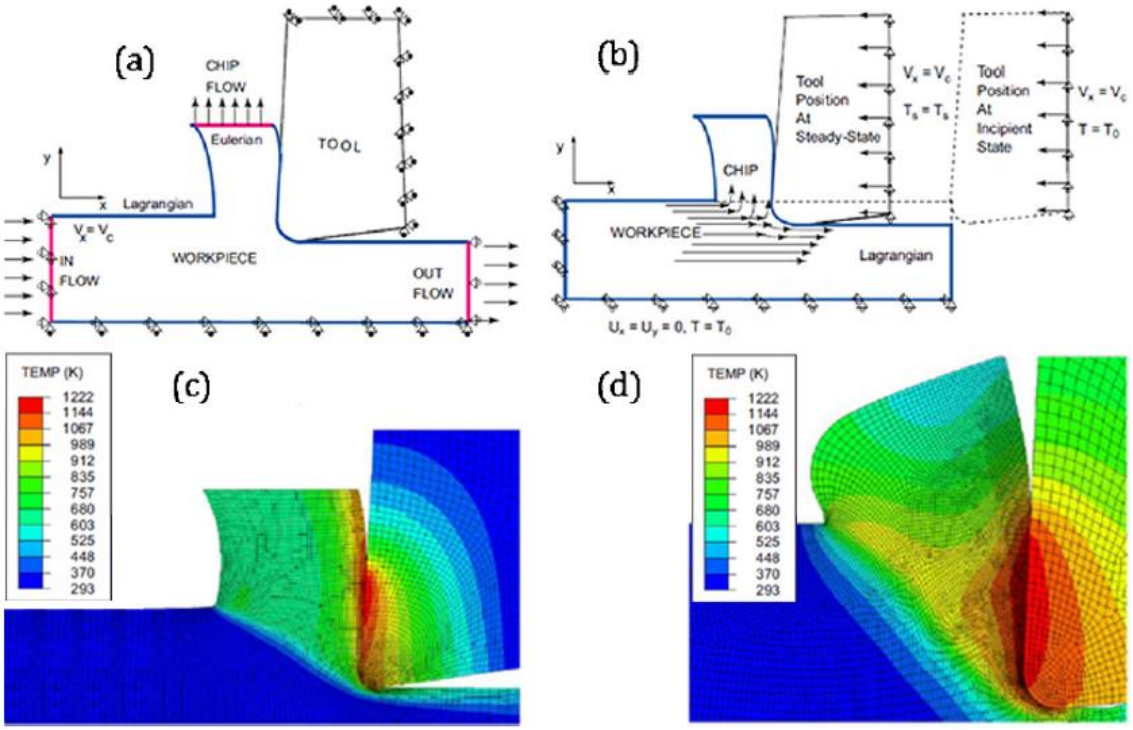

Figure 165. FEM models for ALE formulation with (a) Eulerian and Lagrangian boundary conditions, and (b) pure Lagrangian boundary conditions, and the predicted temperature fields, respectively ((c) and (d) (P. J. Arrazola 2010)

Broaching process modelling

In the same way as the discussed experimental devices, different approaches to model a process can be foreseen depending on the phenomenon to highlight.

In the case of broaching, it is common to find analytical methods of prediction, particularly adapted to the cutting edges, and requiring little computing resources. It can be mentioned the work of (Gilormini et al. 1984) for the comparison of simulated cutting forces with experimental outputs, or those of Schroeter et al. (Schroeter et al. 2007) or Sutherland et al. (Sutherland et al. 1997). The formulation of analytical models (e.g. cutting forces) may allow a macroscopic study of the overall operation of a tool. (Mandrile 2014), for example, show the correlation between premature wear of broach teeth and an experimental test that is superior to analytical forces.

However, if the focus has to be on the physical mechanisms involved in the tool/material interface, the use of computation codes based on finite element methods is today unavoidable. To represent an elementary machining operation, several modelling methods are commonly employed. The Lagrangian formulation consists on representing the fixed material within a predefined mesh and moving a tool on the elements of the piece to be machined. To represent the separation of the material, the piece can be divided into three zones; a solid, a chip and an intermediate zone at which the elements can be removed when a boundary condition is reached, allowing the formation of the chip.

This method developed by Mabrouki et al. makes it possible to represent in a good way the formation of the chip and its eventual segmentation (Mabrouki et al. 2008). Kong et al. implemented a method of this type on the Abaqus Explicit in 2D software to represent a broaching operation (Figure 166) (Kong et al. 2011).

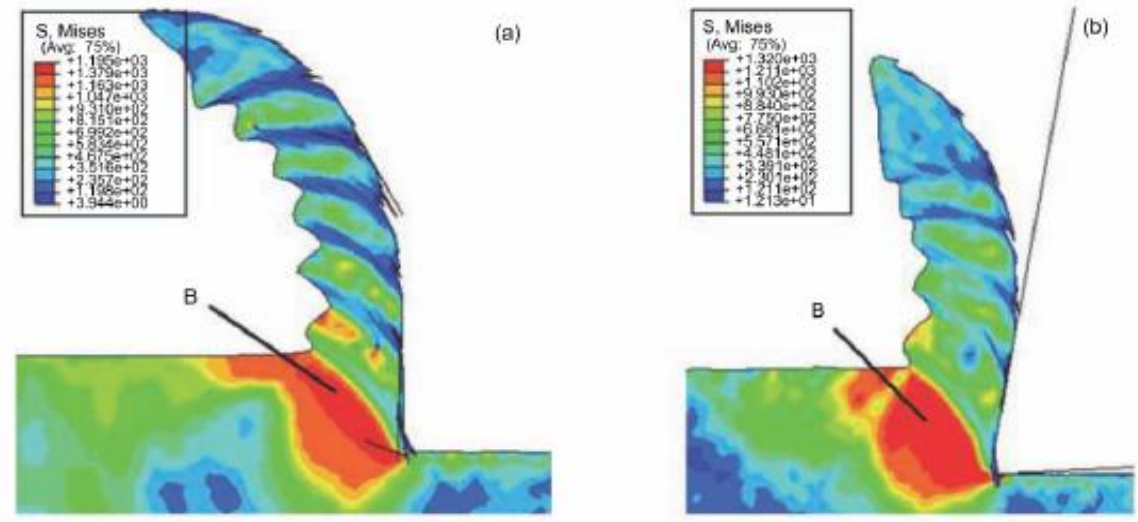

Figure 166. Lagrangian simulation of the broaching operation carried out by (Kong et al. 2011).

Another strategy for simulating the broaching operation also based on lagrangian modelling has been developed by Schulze et al. (Schulze et al. 2011). In this case, it is no longer necessary to divide the piece into three zones as the separation of the material is allowed by a remeshing algorithm. Compared to the lagrangian method previously commented, this strategy allows a better contact representation at the level of the cutting edge, but also requires much longer computation time. This generally results in a shorter chip generation, nevertheless chip removing process cannot be represented by this method.

In this study, Schulze et al. coupled this remeshing algorithm to a strategy of reimporting fields, to consider the influence of previous teeth, especially on residual stresses. Zanger et al. used the same strategy of reimporting and remeshing to represent the work of a

single tooth over a longer distance, forming this way a more representational chip (Zanger et al. 2014).

Mabrouki presented also a work based on lagrangian modelling. This model consists of a deformable workpiece and a rigid cutting tool with both solids, meshed using 4-node plane strain thermally coupled quadrilateral elements (CPE4RT). The main drawback of this approach is that it requires a separation criterion such as a damage initiation and evolution for the elements deletion in the passage zone to form the chip. The data in this region is therefore lost and its size must be carefully selected to limit these effects (Mabrouki et al. 2017).

Other methods of cutting simulation are commonly used to study processes such as orthogonal cutting which is really close to the broaching process. For example, the ALE simulations (Arbitrary Lagrangian/Eulerian), the material to be machined is then assimilated to a fluid able to circulate through a mesh which can itself be deformed itself (Figure 167).

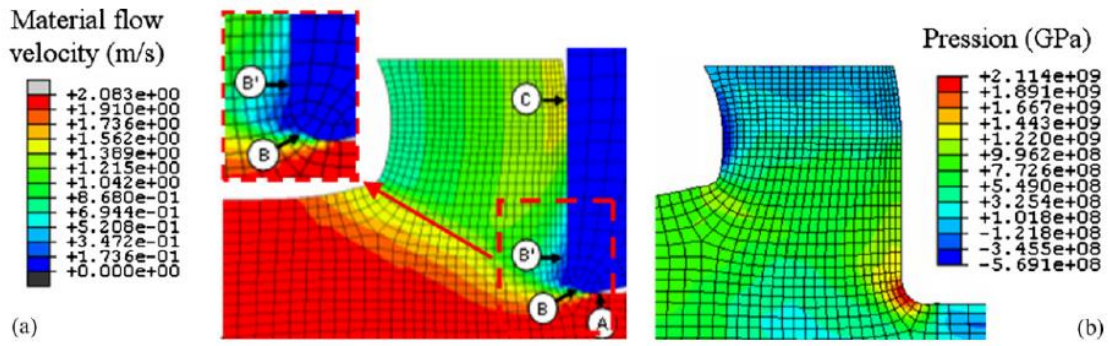

Figure 167. Orthogonal cutting numerical simulation (ALE) by Bonnet et al. (Bonnet et al. 2008)

This method, used by Bonnet et al. to simulate turning, is adapted to the representation of the tool/material interface. If the required computation time is reduced, only the chip root can be represented (Bonnet et al. 2008).

Fabre et al. developed an original Lagrangian model that enabled to simulate long cutting time by means of an iterative procedure. Cutting forces, temperatures evolutions and chip morphology obtained with this model were compared with results obtained from experimental tests and ALE simulations (Fabre et al. 2017).

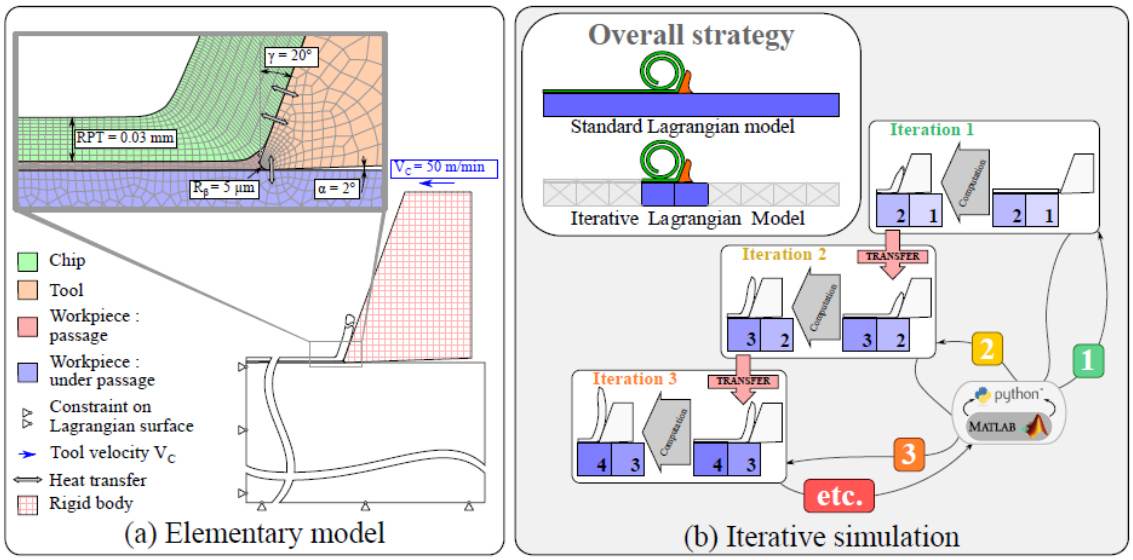

Figure 168. (a) the elementary Lagrangian model and (b) the Iterative Lagrangian Model (ILaM) (Fabre et al. 2017).

Another simulation method of the cutting is presented by Xi et al., this time not based on finite elements but on the SPH (Smoothed Particle Hydrodynamics) method (Xi et al. 2014). The material is then discretized into elementary particles that makes it possible to overcome the common distortion problems appearing during the use of the previously mentioned simulation methods. In addition, the use of damage criteria is not necessary, unlike some Lagrangian formulations. This method also makes it possible to represent the segmentation of the chip as presented in Figure 169.

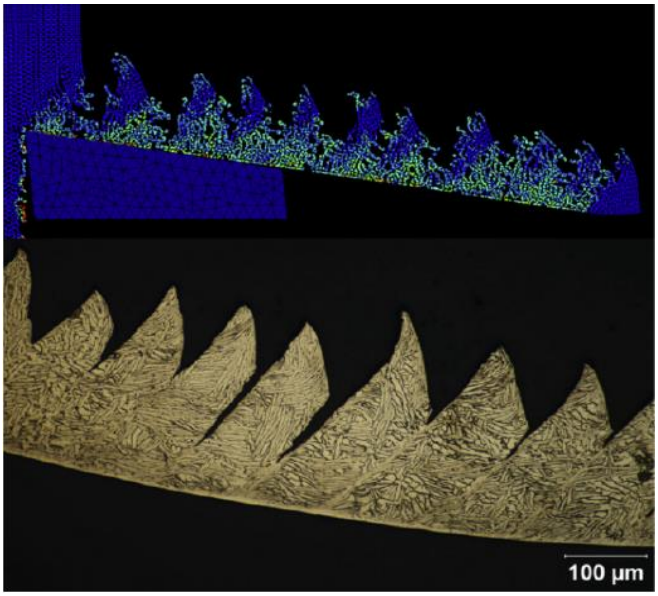

Figure 169. SPH simulation of an orthogonal machining process (Xi et al. 2014).

Like the previously mentioned ALE method, this strategy has not yet been used to represent a broaching operation.

Numerical tests

6.1.1 Model development

The developed cutting model based on the ALE approach was inspired by some previous works (Courbon et al. 2013, P. J. Arrazola 2010, Ducobu et al. 2011).

General description

The model (Figure 170) consists of a deformable workpiece and a solid rigid tool (fully constrained allowing a thermal calculation). The shape given to the tool was the same as the teeth used in the experimental tests i.e. rake angle = 17º, clearance angle = 1º and r_β = 12 µm. The Eulerian surfaces were defined constraining the mesh (in red in the Figure 170) to allow the flow of the material. The rest of the surfaces were defined as lagrangian allowing the mesh deformation.

Predefined fields and boundary conditions

In this Eulerian-based ALE model, Eulerian boundaries, such as input and output surfaces, have to be defined to permit the flow of the workpiece material. The inflow takes place on the left with the prescribed cutting speed set at the nodes and input temperature of 20 °C, whereas the outflow is made possible through the upper chip and end-right surfaces of the workpiece, as specified in Fig. 170. Thermal conduction within the solids is possible but heat exchange with the surrounding environment, i.e. convection and radiation, has been considered as negligible. The nodes at the bottom of the workpiece are fixed vertically via a symmetry condition whereas the tool is completely embedded. Regarding the cutting conditions, the uncut chip thickness was predefined at 40 µm and the cutting speed (material entry speed) was set to 2 m/min.

Mesh

The two solids were meshed with quadrilateral elements in plane strain, coupled temperature-displacement and reduced integration (CPE4RT). On the workpiece, the mesh was refined around the zones of primary and secondary shear zones in order to compute at best the strong gradients of deformation. The size of the elements in these areas was reduced to about 3 to 4 µm. The rest of the mesh covering the points far from the cutting zone is also formed by quadrilateral CPE4RT elements but with a larger size (12 µm). The simulated machining time was fixed in 18 ms.

Contact model

A master-slave penalty contact method is used to model the interaction between the workpiece and the broaching tool.

With the aim of simulating the contact behaviour occurring in the SSZ (Secondary Shear Zone), the data from the tribological campaign shown in the chapter 4 were implemented in this numerical model. The frictional behaviour of the interface was modelled according to the contact models generated in Section 4.1.11 and was thus dependent on the local sliding velocity and some microstructural parameters. For each steel variant, the friction values were thus specifically implemented as tabular data versus the local sliding speed. From the thermal point of view, the interface is also simulated at a macroscopic scale. Solids were thermally connected by a thermal contact resistance which represents the perturbation induced by the asperities of each surface. This resistance can be seen as the capability of the interface to conduct heat between the two bodies in contact. During the tool-workpiece interaction, the frictional heat generated at the interface was distributed on each contact surface. According to the low cutting speed employed and to the fact that both solids were made of steels, the partition of the frictional heat has been kept constant: 50 percent of the frictional heat transmitted to the workmaterial against 50 percent into the cutting tool (Grzesik, Nieslony 2003, Rech et al. 2013). The thermal contact resistance has been fixed to 10^{-4} m^2K/W, as it provided the most consistent results in terms of heat fluxes in a previous study conducted on a C45 (Courbon et al. 2013).

Material properties

The implemented flow stress data of the FP steels was already detailed in section 0, using for each variant the appropriate constitutive equation, i.e. with the consistent microstructural parameters. These data were calculated based on the equation shown in the subsection (3.1.17) and then implemented in the numerical broaching model as tabular data. The implemented thermal data results were also shown and explained in the subsection 0 concerning the FP steels thermal characterization. This data helped to better predict heat flow and temperature distribution, in one hand, for the chip and workpiece, and on the other hand, in the cutting tool.

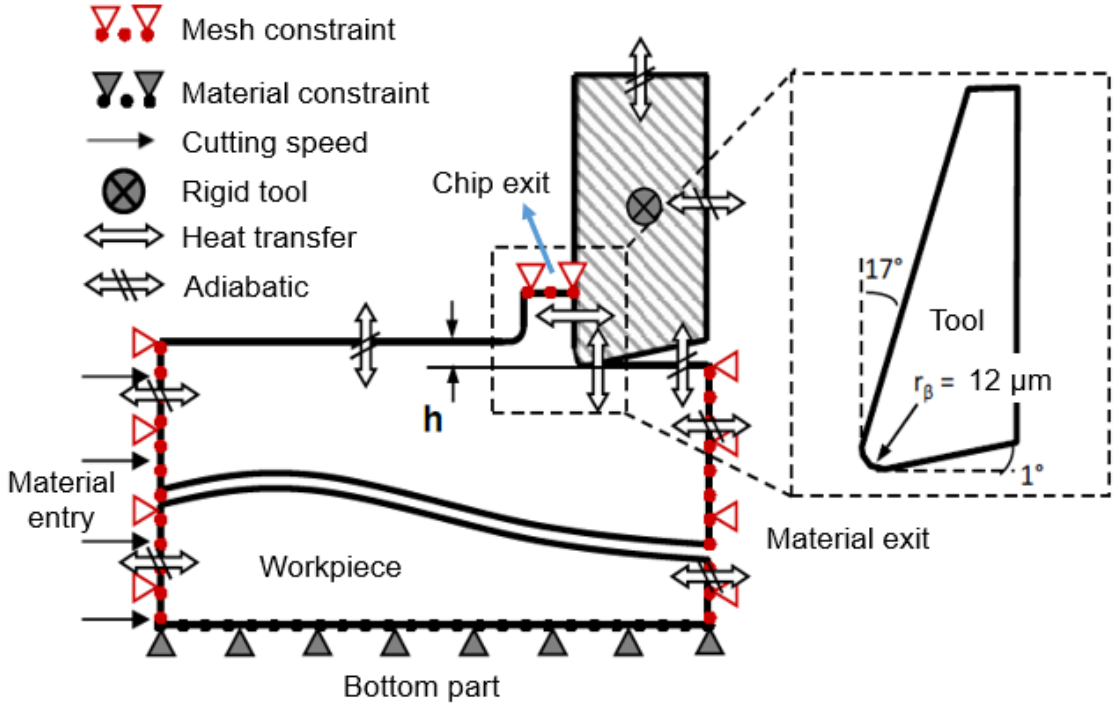

Figure 170. Boundary conditions of the last developed 2D ALE broaching model.

The present model developed at ENISE showed the following advantages:

- It enabled a more physical material separation around the tool cutting edge without using a damage criterion which would be impossible to properly identify in this PhD.
- Friction, thermal and flow stress data could be consistently implemented without excessive mesh distortion and numerical tricks.

6.1.2 Methodology

The variables and materials selected for the modelling of the broaching are displayed in Table 25. The comparison was done with the experimental results obtained in the selected broaching campaign.

The results obtained from the model were displayed in terms of forces and chip compression ratio. From the experimental tests it was impossible to obtain the contact length with enough resolution to be a reliable output. From the numerical point of view, it was of course not possible to predict the roughness left on the workpiece.

Table 25. Cutting conditions selected for the modelling part.

Variables	Conditions
Cutting speed (m/min)	2 & 20
Rise per tooth (µm)	40
Tool	HSS (M35)
Steels	Selection
Lubrication	Dry & under lubrication
Coating	Uncoated & fully coated

Remark: in the modelling part, three different results were just obtained, uncoated and coated in dry conditions and those performed under lubrication. This occurred because the data obtained under lubrication in tribology lead to the same results whether the tooth was coated or uncoated. Therefore, the tests launched in numerical simulations are UNC and COA in dry as well as the under lubrication tests gathered in one and named as UNC & COA L.

Results and comparison with the experiments

Cutting and feed forces

The Figure 171 summarised the experimental cutting forces plotted side by side with the cutting forces obtained from the numerical model. It was noticeable the huge difference that could be seen when focusing on each grade and condition. Feed forces graphs can be seen in the Figure 171c and d, where the obtained results were very different in terms of scale and trends. Besides, the huge influence of the implemented friction data under lubrication can be also noted, which is especially greater on the feed force than on the cutting force. This was expected as friction takes part mainly in the tool-chip contact in the secondary shear zone (Figure 74).

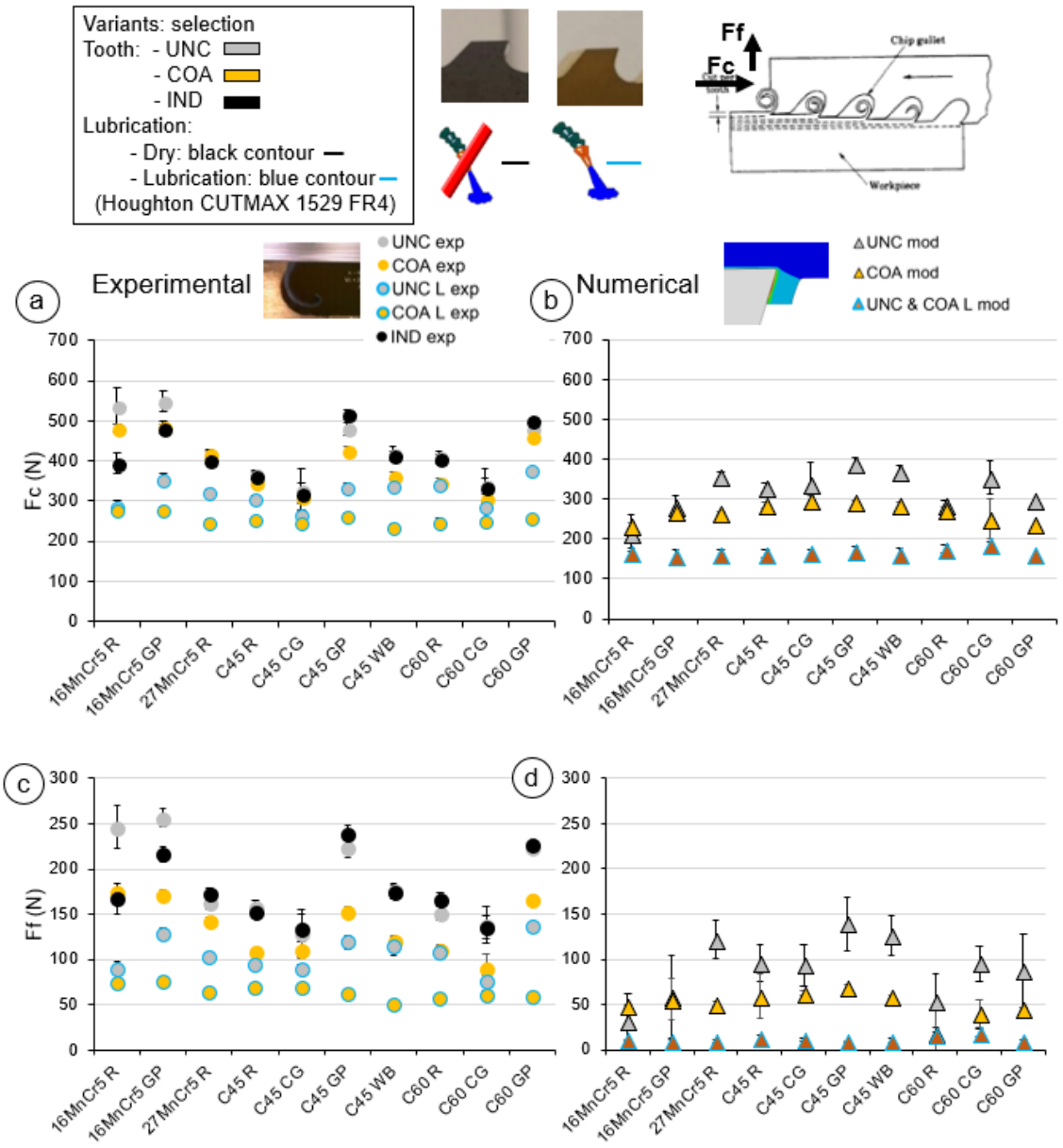

Figure 171. Experimental cutting and feed forces comparison with modelling forces.

- <u>Cutting forces versus ferrite content:</u>

At first sight, it can be observed in the Figure 172 that the predictions were not so close neither in terms nor in trends. Going first with the uncoated tooth in dry condition results (Figure 172a) at low ferrite content were quite similar for some variants but for the high ferrite content variants (16MnCr5 R & GP) the results were totally the opposite. For the coated tooth in dry conditions (Figure 172b), while the experimentally recorded forces increased with the ferrite content, the modelling did not show this trend with all the simulated values around 250-300 N whichever was the ferrite content. As occurring in the uncoated tests at low ferrite content the approach was quite good obtaining for some variants a low error (30%). In the comparison of the tests performed under lubrication (Figure 172c), the oil tended to equalize the results as it was seen before in the selected

broaching campaign 5.1.3. Besides, the forces obtained with the uncoated tool were higher than those obtained with the coated one and both higher than the modelling results.

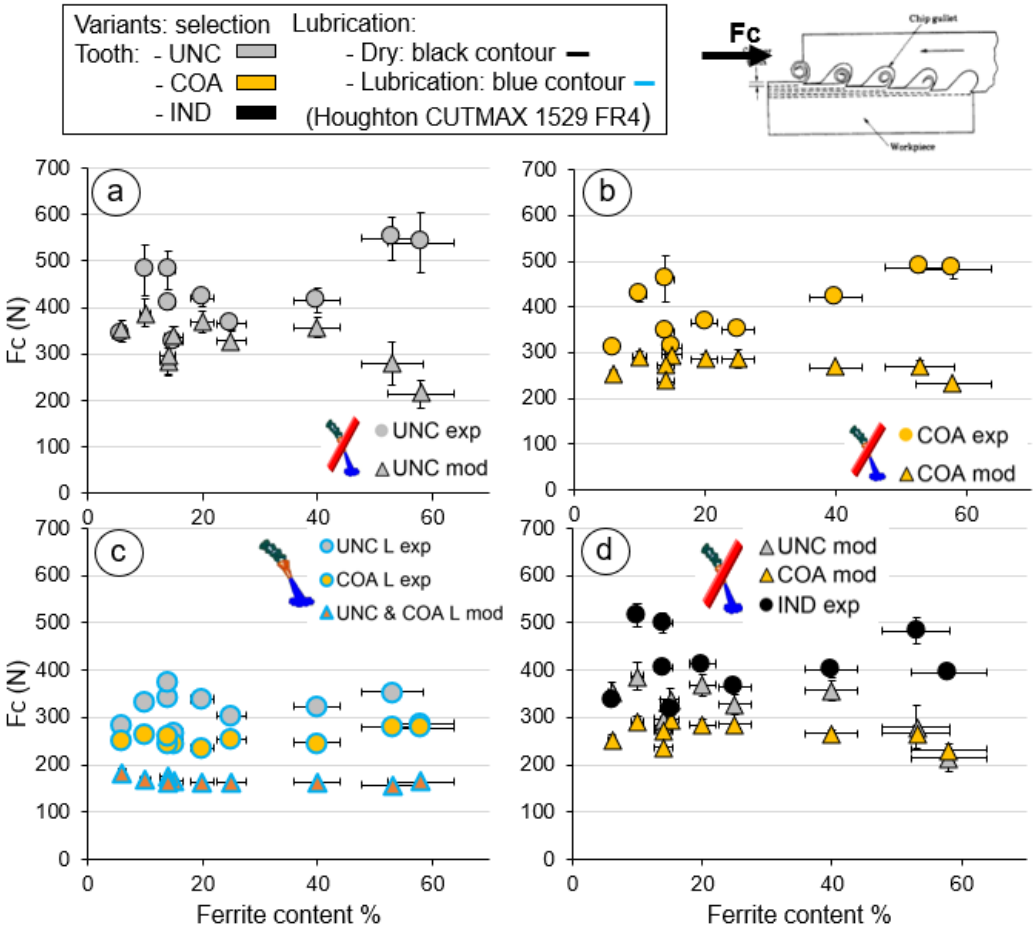

Figure 172. Experimental and numerical cutting forces obtained at different teeth state and lubrication versus ferrite content.

At last, in the Figure 172d there were displayed the results comparing the industrial tooth in dry versus the modelling of the forces obtained with the coated and the uncoated tooth in dry conditions. For the low ferrite content variants similar behaviours in values and trends were obtained for the uncoated modelled and experimental forces obtained with the industrial tooth. However, the forces obtained with the coated tooth from modelling did not show any similarity with the forces obtained with the industrial type tooth.

Chip compression ratio

The chip compression ratios were also plotted in terms of microstructure not only to compare them but also to asses if the model is able to predict the after-cut chip widening. In the Figure 173 the experimental chip compression ratios plotted side by side with the chip compression ratios obtained from the numerical model could be analysed. Again, there was a huge difference when focusing on each grade and condition. Furthermore,

it seemed that the modelling was not able to dissociate this output as its variability was really low and there were almost no differences between different variants and grades.

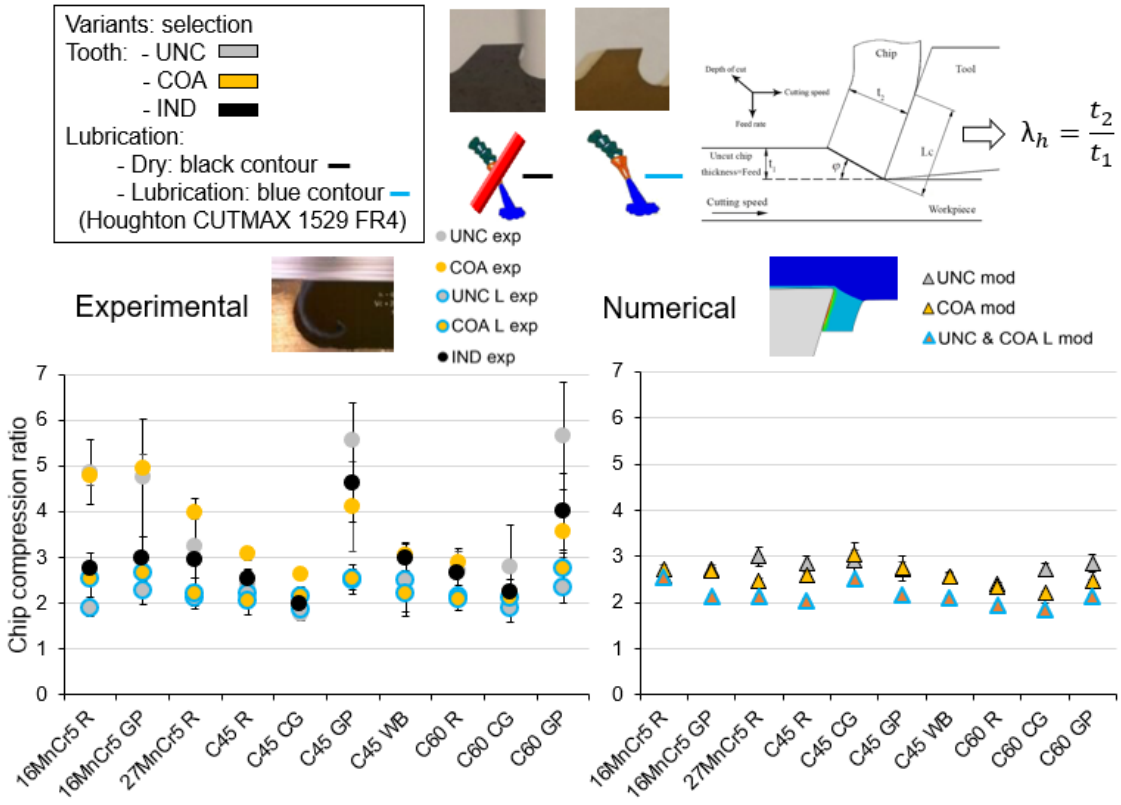

Figure 173. Experimental chip compression ratios comparison with numerical chip compression ratios.

- <u>Chip compression ratio versus ferrite content:</u>

In Figure 174 it can be seen that the results were dissimilar in terms and trends. Besides, all the values obtained with the numerical results were almost the same and had low variability. Going first with the uncoated tooth in dry condition results, at low ferrite content the results were quite similar for all except two variants (C45GP & C60GP). For the high ferrite content variants (16MnCr5 R & GP) the results were again totally contradictory. For the coated tooth in dry conditions (Figure 174b), while the experimentally obtained chip compression ratios increased with the ferrite content, the modelling did not show this trend leading all the values to be between 2 and 3 whichever the ferrite content was. Very similar chip widths were obtained under lubrication as it was seen before in the tooth state campaign 5.1.3. All the results obtained under lubrication were quite similar obtaining a good accuracy with the modelling although the variability of these results was quite low, moving between 2 and 3 for all the ferrite content range. At last, the results comparing the industrial tooth in dry versus the chip compression ratios obtained with the coated and the uncoated tooth in dry conditions are reported in

Figure 174d. In except of the two variants which provided the most different results (C45GP & C60GP) the rest of the variants showed a similar behaviour.

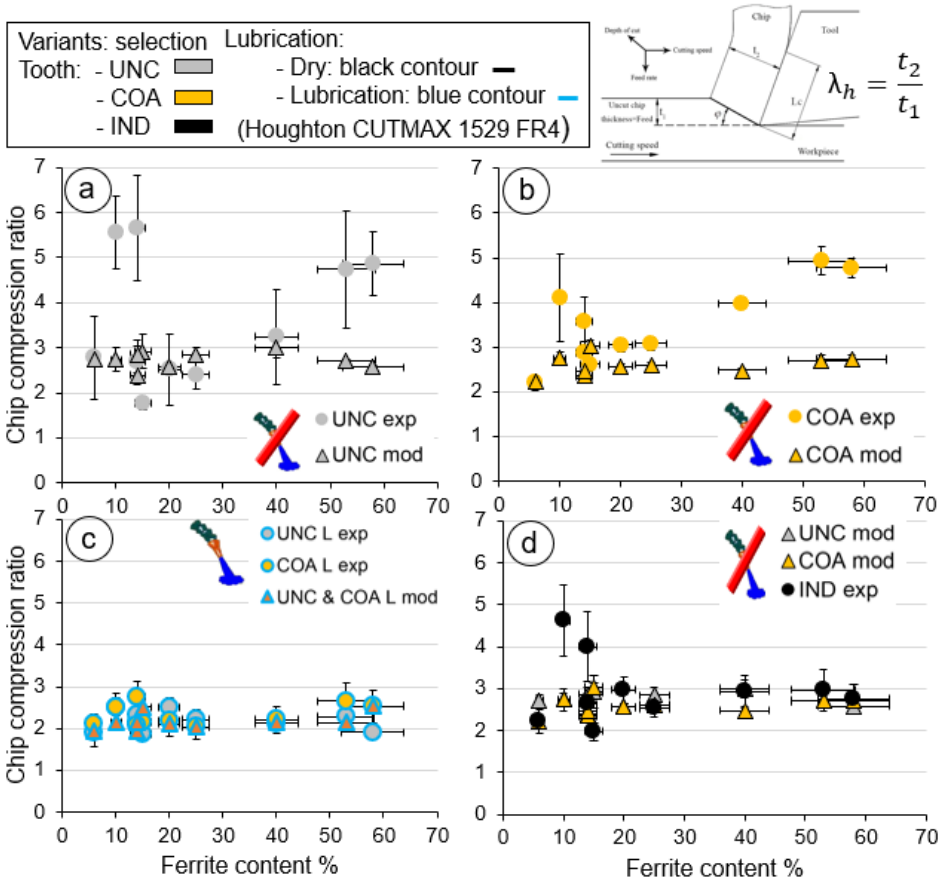

Figure 174. Experimental and numerical chip compression ratios obtained at different tooth state and lubrication versus ferrite content.

At this point, it could be said that the developed model was not able to predict the after-cut chip thickness so the results were not plotted in terms of any other microstructural feature. The results obtained on the FEM and the comparison with the experimental outputs, led to a scientific discussion developed in the following subsection.

Scientific discussion

The previous subsection dealing with the cutting simulations and subsequent comparison with the experimental data, showed some inaccuracies leading to the discussion presented in the following lines.

6.1.3 Temperature gap in rheology 20-500

In the broaching experiments, temperatures were not recorded during the broaching process but it was a variable that could be assessed thanks to the numerical simulations. In these simulations, it was seen that the temperature on the workpiece did not exceed 115°C in any material (Figure 175).

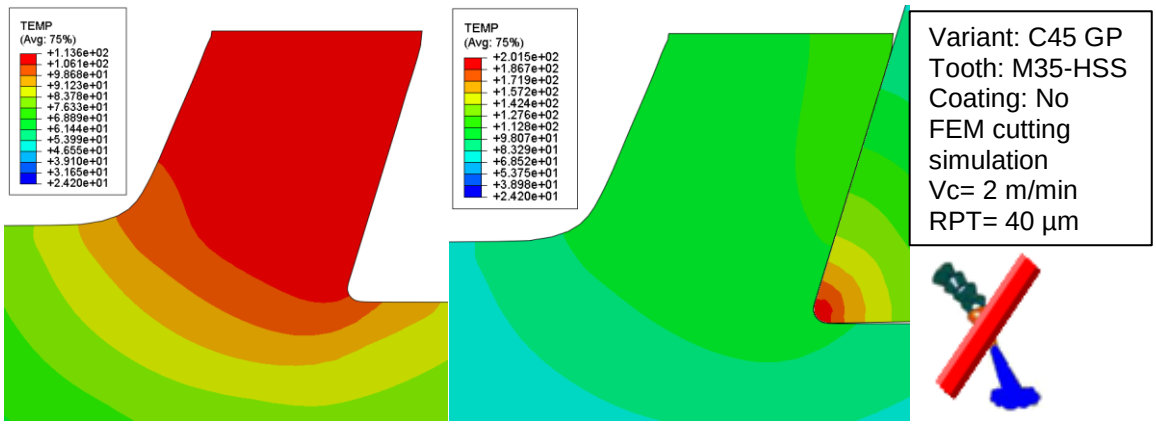

Figure 175. Temperature fields computed with the ALE model: on the left without the tool on the right with the tool (C45GP with the Uncoated tooth in dry conditions at 2 m/min and 40 µm).

As it was seen in the subsection 0 dealing with the development of the flow stress model, all the experimental tests at low and high strain rates were performed under three different temperatures (20°C, 500°C & 680°C). Therefore, the model was developed based on an information gap of 480°C and resulted in a flow stress extrapolated based on these three points only.

Then, further simulations were launched without considering the temperature influence on the strain-stress relation. These tests were launched in the same cutting conditions as in the previous subsection (2 m/min and 40 µm) and with the uncoated tooth in dry conditions.

The previously obtained results as well as the new ones were plotted side by side with the experimental ones in terms of the names given to the steel variants (Figure 176). As it can be seen, the outputs simulated with the new flow stress input provided results closer to the experimental ones in most of the cases. Taking a look on the CG variants it can be seen that the new simulation is giving even larger forces than previously simulated. As the worst approach is concerned (16 R and 16 GP), the results were improved but to a lower extent, not leading to a satisfactory agreement. The best approaches were obtained with the 27MnCr5 R and the C45 variants minimizing the error for example in the case of the C45GP from a 19% to a 7%.

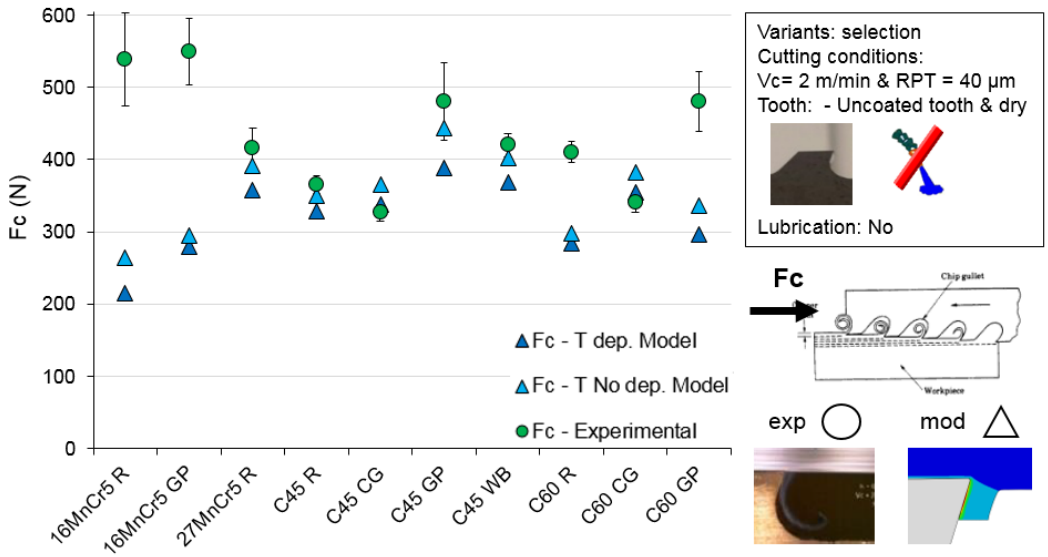

Figure 176. Temperature gap assessment in model results comparing versus the experimental cutting forces.

6.1.4 Model consistency assessment

With the aim of checking the consistency of the numerical results, additional broaching simulations were launched at the wear tests cutting conditions i.e. V_c=20 m/min and RPT= 40 µm (Figure 177). The objective was to assess if the viscosity, i.e. strain rate dependency of the flow stress, was an important factor which could explain why the results/trends deviate when increasing the cutting speed.

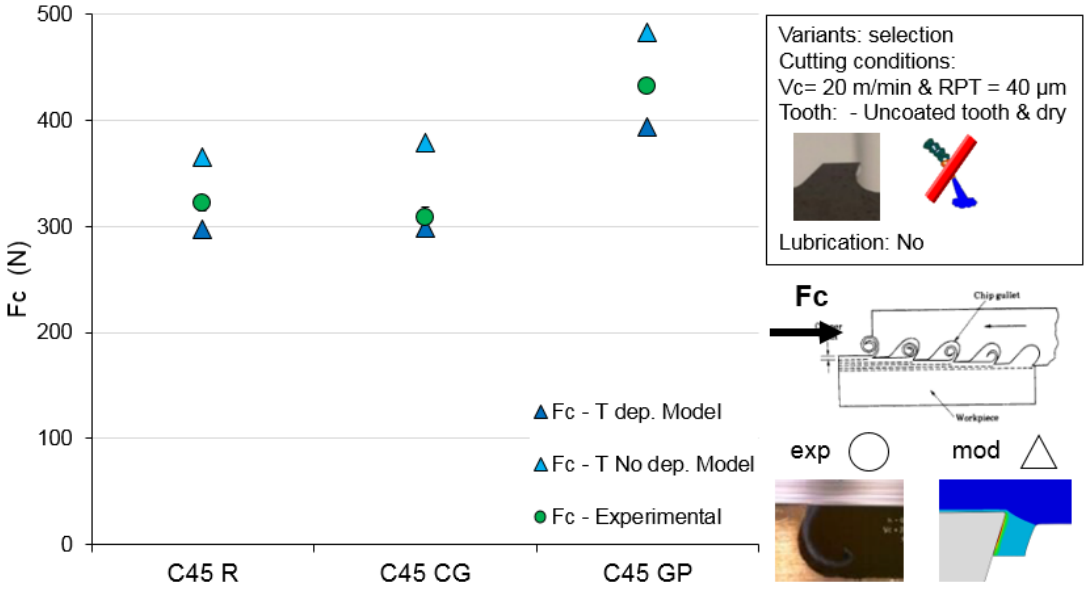

Figure 177. Numerical and experimental forces comparison at 20 m/min assessing the viscosity and the influence of the temperature dependency on the flow stress.

These simulations showed that the reached temperatures in these cutting conditions were around 350°C. That is why considering the temperature dependency in the material

behaviour model seemed to be in a better agreement with the obtained experimental results. Therefore, these results reinforce the fact that more rheological experiments should be performed between 20°C and 560°C in order to properly consider the temperature dependency at low to medium temperatures when developing the flow stress model.

6.1.5 Dry / lubricated contact

For the discussion in this subsection it was recalled the analysis performed in the comparison between the experimental and the modelling tests. It is important to remind that, at the time of preparing the simulations, the only changing input data between the dry and under lubrication is the tribology data. Checking the results obtained, it was seen that the numerical results obtained with the dry uncoated and coated teeth compared to the experimental tests performed with the same teeth under lubrication led to similar outputs in terms of cutting forces. Furthermore, the simulations launched under lubrication lead to a low force results and great difference comparing to the experimental ones (Figure 178).

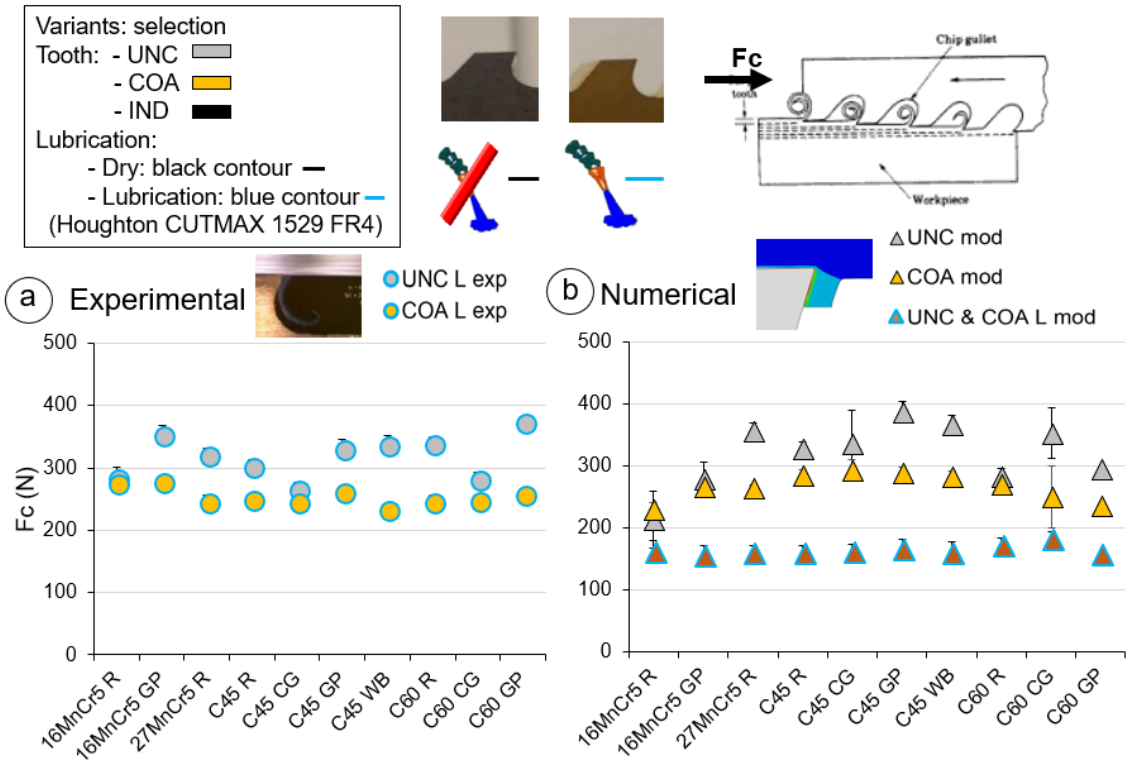

Figure 178. Cutting forces comparison experimental under lubrication versus numerical in dry conditions.

This would tend to show that the influence of the lubrication on the tribology tests was overestimated. i.e. in tribology the oil might remain longer in the contact whereas it did not remain on the cutting edge during the whole cutting but only at the beginning of the tests. Besides, the lubricant might not be able to penetrate the tool-chip contact zone as

it was doing on the tool-material contact on the tribology tests. This might be due to the shape and type of the contact zones leading to difficulties in the lubricant spreading in the case of the cutting. Namely, one part of the tool-chip contact area might be lubricated while the other part of the contact area was in fact dry.

From this comparison could be envisaged an improvement on the cutting simulation, for example, for the under lubrication tests implementing a friction law not exactly based on the results obtained on the tribometer but a mix between the tests in dry and with lubrication.

6.1.6 Material microstructure

The last but not least question under discussion were the differences between the material microstructure available for the experimental tests and the generated material flow stress model. When generating the flow stress model, the most important microstructural features such as the FP ratio and the grain size were considered. However, all these data was being used to develop a material behaviour model that would be implemented in a Finite Element. In this context, the heterogeneity of the material would turn in homogenous in the simulated material. Nevertheless, the reality was different, checking the microstructure of the material, it was seen that the FP steel not only had two clearly differentiated phases but also the microstructure was different depending on the depth of the bar (Figure 38). What is more, according to the low rise per tooth (RPT) existing in broaching, one cannot neglect the fact that the material was being cut at the scale of the grain size (Figure 179). Thus, it is even more difficult to consider the workmaterial as homogeneous.

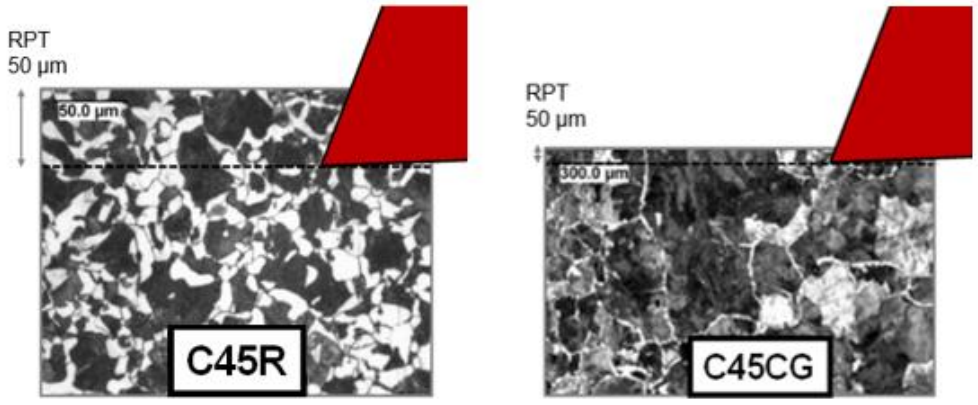

Figure 179. Illustration of the scale effects to consider when cutting a) a standard C45R and b) a coarse grain C45CG with a RPT of 50µm.

Conclusions

The developed ALE model was proved to run simulations successfully implementing the tribological, the rheological as well as the thermal data. Large discrepancies were obtained comparing the numerical results with the experimental ones not only in amplitude but also in terms of trends. The best fitting trends were obtained from the UNC & dry tests, however, for the high ferrite content variants, the trends are totally contrary (16R &16GP).

As it was seen in the experimental tests, in the simulations also the lubrication tended to equalize the values of the cutting forces. Besides, the feed forces obtained in lubricated models are very low, so it could be said that the implemented tribological data was being overestimated or that the contact in the experiments was not fully wet during the whole cutting. In all cases, the forces obtained from the models were lower than experimental.

From the chip analysis, it was difficult to find consistent trends as the model showed very similar results on the whole ferrite content range. It was seen that all the measures were very low nearby to the lubricated essays results. As previously commented, the influence of the tribology was being overestimated or at least how the lubricant was affecting the rubbing zone.

A specific subsection was developed discussing the facts that led to the discrepancies mentioned above. The main conclusions extracted from this were, on the one hand, the necessity of a better accurate flow stress model, gaining a better understanding of the local contact phenomena under lubrication. On the other hand, the development of an heterogeneous cutting model in which the ferrite and pearlite phases could be implemented separately with each ones features on each one of them.

Chapter 7

CONCLUSIONS AND FUTURE LINES

7 CONCLUSIONS AND FUTURE LINES

The influence of microstructure of the ferritic pearlitic steels was studied and analysed on the mechanical characterization, tribological behaviour and broaching operation outputs leading to a wide range of results. The problem to solve came from the fact that a single FP steel composition could lead to different microstructures depending on the steel manufacturing process.

Based on the whole work and research throughout this PhD, the main contributions can be summarised as:

Material characterization

- The thermal properties of the FP steels depend on the carbon content as seen on the standard and coarse grain variants. This trend was not seen on the GP and the WB variants. Dependence on the microstructure was not noticed.
- A material behaviour model was successfully developed on the FP steels microstructure being proved useful to be implemented in the cutting FEM.

Friction identification

- Carbide pin:

- It was observed that there is an increase of friction coefficient when ferrite content increases. On the tests performed at the lowest sliding speed (10 m/min) with the carbide pin the CoF increased from 0.5 to 0.8 varying the ferrite content from 6 to 60 percent. This trend was not that appreciable at higher speeds.
- It was also observed that the friction effect decreased when the hardness or grain size increased. It was found that increasing the hardness 65 HB (from 160 HB to 225 HB) the CoF was reduced in 40 percent.
- Adhesion tendency seems to be dependent on the sliding velocity, while wear mechanisms are mainly governed by the FP ratio. This way, it could be assessed which were the FP steel variants leading to highest wear on the pin at 300 m/min, the C60 R and 27MnCr5 R.

- High Speed Steel pin:

- In the whole range of ferrite percentage low variability in values was observed for the lowest and medium sliding speed (2 m/min and 20 m/min) however, there was a slight increasing trend: from 0.8 to 1 at the lowest sliding speed and from 0.44 to 0.7 at the medium sliding speed. For the highest speed (60 m/min), however, a trend could hardly be obtained as the variability of CoF was very high.
- A decreasing trend was found plotting the results against the hardness at the medium and lowest tested speeds (2 m/min and 20 m/min). At the highest speed it could be

seen a similar decreasing trend but some of the values gave back very dissimilar friction coefficients.

- The TiN coating was proved to remove the trends obtained with the uncoated pin. This fact made it impossible to extract any trend to develop a mechanical contact model.
- Almost the same value for all the FP tested steels (0.13 ± 0.2) on the very few tests launched under lubrication. The reduction of the CoF comparing to the experimental tests launched in dry conditions with the uncoated and coated pins were on the range of 80-90 % and 40-50 % respectively.

Broaching experimental results

- It was also proved that the broaching outputs obtained from the FP steels machining are linked to the FP steel microstructure. These results were in the same line of the tribological results, leading to larger forces for the higher ferrite content variants and lower for those that were harder or with lower ferrite grain size.
- Regarding the roughness, generally, worse results were obtained for lower cutting speeds and higher RPT. In the fundamental study the roughness provided dissimilar results depending on the speed. At the lowest speed the ferrite increase worsened the roughness obtaining the opposite trend for the highest speed.
- The obtained chip compression ratio was proved to be directly related to the ferrite and inversely to the hardness i.e. the higher the ferrite content the thicker the chip and the harder the steel the thinner the chip. This was also proved to be correlated with the recorded forces as the higher ones were linked to the higher chip thicknesses.
- On the wear tests performed on the C45 variants in dry conditions, surprisingly, there were no significant results obtained in terms of wear after broaching 75 m.

Numerical Modelling of broaching

- Although the results obtained from the numerical model were not that accurate compared to the experimental outputs, they worked with all the implemented data obtained in this PhD and they were used as a numerical tool to explain the results. The results especially supported the discussion pointing out that they did not seem to be properly considered and that there are potential improvements to be made.

The following points could be mentioned when it comes to perspectives:

- Steels manufacturing seems to be one way of improvement obtaining better differentiated steel variants for each grade concerning the grain size or interlamellar space on the pearlite grain.
- The material flow stress model development could also be more accurate conducting more rheological experiments between 20°C and 500°C.
- Regarding the tribological part, although the values obtained seemed to be qualitatively consistent, comparing the lubricated configurations showed that numerical simulations and experimental data are not in agreement in the same way as the dry tests are. Therefore, a better understanding of the phenomena occurring under lubrication is definitely needed.
- As far as the broaching tests are concerned, using imaging could be proposed to in-situ capture the chip formation process and observe chip curvature and tool-chip contact length. Local temperatures occurring in the tool-chip interface could be recorded by using an infrared camera. At last, measuring the strain and strain rates on the first and second shear zones would lead to a better understanding of what is happening in the chip generation process. These outputs would be later used to be compared with the results obtained from the FEM leading to a great improvement of the cutting model development.
- Regarding the modelling, the implementation of the material feature on the model should be improved. One way could be to model the workmaterial at the grain size level, making it heterogeneous and implementing to each grain its own mechanical properties to each grain based on the ferrite or pearlite features.

Chapter 8

ORIGINAL CONTRIBUTIONS

8 ORIGINAL CONTRIBUTIONS

Published articles

Conferences

I.M. Arrieta, C. Courbon, F. Cabanettes, J. Rech, P.-J. Arrazola (2016) Effet de la microstructure d'un acier ferrito-perlitique sur son comportement tribologique sous conditions extremes – 28th French-speaking International Tribology congress, April 27-29, Saint-Etienne, France

I.M. Arrieta, C. Courbon, F. Cabanettes, P.-J. Arrazola, J. Rech (2016) Experimental study of machinability in broaching of ferritic-pearlitic steels – Proceedings of the 13th High Speed Machining Conference (HSM 2016), October 4-5, Metz, France.

I.M. Arrieta, C. Courbon, F. Cabanettes, P.-J. Arrazola, J. Rech (2017) Influence of the ferritic-pearlitic steel microstructure on surface roughness in broaching of automotive steels – Accepted for presentation at the 20th International ESAFORM Conference on Material Forming – ESAFORM 2017, April 26-28, Dublin, Ireland.

T. Mabrouki, C. Courbon, D. Fabre, I.M. Arrieta, P.-J. Arrazola, J. Rech (2017) Influence of Microstructure on Chip Formation when Broaching Ferritic-Pearlitic Steels - Accepted for presentation at the 16th CIRP Conference on Modelling of Machining Operations (CIRP CMMO), June 15-16, Cluny, France.

CHAPTER 9

BIBLIOGRPAHIC REFERENCES

9 BIBLIOGRAPHIC REFERENCES

ABOUEI, V., SAGHAFIAN, H. and KHEIRANDISH, S., 2007. Effect of Microstructure on the Oxidative Wear Behavior of Plain Carbon Steel. *Wear*, vol. 262, no. 9, pp. 1225-1231.

ABOURIDOUANE, M., KLOCKE, F., LUNG, D. and ADAMS, O., 2012. Size Effects in Micro Drilling Ferritic-Pearlitic Carbon Steels. *Procedia CIRP*, vol. 3, pp. 91-96.

AKASAWA, T., FUKUDA, I., NAKAMURA, K. and TANAKA, T., 2004. Effect of Microstructure and Hardness on the Machinability of Medium-Carbon Chrome-Molybdenum Steel. *Journal of Materials Processing Technology*, vol. 153, pp. 48-53.

ALBRECHT, P., 1960. New Developments in the Theory of the Metal-Cutting Process: Part I. the Ploughing Process in Metal Cutting. *Journal of Engineering for Industry*, vol. 82, no. 4, pp. 348-357.

ALLAIN, S., 2012. HDR Report.

ALLAIN, S. and BOUAZIZ, O., 2008. Microstructure Based Modeling for the Mechanical Behavior of Ferrite–pearlite Steels Suitable to Capture Isotropic and Kinematic Hardening. *Materials Science and Engineering: A*, vol. 496, no. 1-2, pp. 329-336.

ALLAIN, S., BOUAZIZ, O. and LEMOINE, X., 2009. A Viscoplastic Behavior Law for Ferritic Steels at Low Homologous Temperature. *Revue De Métallurgie–International Journal of Metallurgy*, vol. 106, no. 2, pp. 80-89.

APOSTOL, M., VUORISTO, T.and KUOKKALA, V., 2003. *High Temperature High Strain Rate Testing with a Compressive SHPB.* EDP sciences.

ARRAZOLA, P.J., 2010. Investigations on the Effects of Friction Modeling in Finite Element Simulation of Machining. *International Journal of Mechanical Sciences*, vol. 52, no. 1, pp. 31-42.

ARRAZOLA, P., et al, 2013. Recent Advances in Modelling of Metal Machining Processes. *CIRP Annals*, vol. 62, no. 2, pp. 695-718.

ARRAZOLA, P., UGARTE, D. and DOMINGUEZ, X., 2008. A New Approach for the Friction Identification during Machining through the use of Finite Element Modeling. *International Journal of Machine Tools and Manufacture*, vol. 48, no. 2, pp. 173-183.

ASTAKHOV, V.P. and XIAO, X., 2008. A Methodology for Practical Cutting Force Evaluation Based on the Energy Spent in the Cutting System. *Machining Science and Technology*, vol. 12, no. 3, pp. 325-347.

AXINTE, D., et al, 2005. Broaching of Ti-6-4–Detection of Workpiece Surface Anomalies on Dovetail Slots through Process Monitoring. *CIRP Annals-Manufacturing Technology*, vol. 54, no. 1, pp. 87-90.

AXINTE, D., 2007. An Experimental Analysis of Damped Coupled Vibrations in Broaching. *International Journal of Machine Tools and Manufacture*, vol. 47, no. 14, pp. 2182-2188.

BAHRUDIN, M.S., ABDULLAH, S.F.and KHAN, M.R.B., 2013. *Friction Measurement System using Load Cell for Tribotronic System on Pin-on-Disc (POD) Tribometer.* IOP Publishing.

BEJNOUD, F., ZANGER, F. and SCHULZE, V., 2015. Component Distortion due to a Broaching Process. *Applied Mechanics & Materials*, vol. 794.

BELLAIS, C., 1997. Outils Coupants: Brochage*. Techniques De L'Ingénieur.Génie Mécanique*, no. B7087, pp. B7087. 1-B7087. 19.

BEN ABDELALI, H., et al, 2011. Identification of a Friction Model at the Tool-Chip-Workpiece Interface in Dry Machining of a AISI 1045 Steel with a TiN Coated Carbide Tool*. Journal of Tribology*, vol. 133, no. 4, pp. 042201.

BERGSTRÖM, Y., 1970. A Dislocation Model for the Stress-Strain Behaviour of Polycrystalline A-Fe with Special Emphasis on the Variation of the Densities of Mobile and Immobile Dislocations*. Materials Science and Engineering*, vol. 5, no. 4, pp. 193-200.

BONNET, C., VALIORGUE, F., RECH, J. and HAMDI, H., 2008. Improvement of the Numerical Modeling in Orthogonal Dry Cutting of an AISI 316L Stainless Steel by the Introduction of a New Friction Model*. CIRP Journal of Manufacturing Science and Technology*, vol. 1, no. 2, pp. 114-118.

BUI-VAN, A., ALLAIN, S., LEMOINE, X. and BOUAZIZ, O., 2009. An Improved Physically Based Behaviour Law for Ferritic Steels and its Application to Crash Modelling*. International Journal of Material Forming*, vol. 2, no. 1, pp. 527.

BYERS, J., 2006. Metalworking Fluids, CRC.

CALLISTER, W.D. and RETHWISCH, D.G., 2011. *Materials Science and Engineering.* John Wiley & Sons NY.

ÇETIN, M., 2011. Pin-on-Disc Characterization of Brass/Ferritic and Pearlitic Ductile Iron Rubbing Pair*. High Temperature Materials and Processes*, vol. 30, no. 1-2, pp. 87-98.

CLAUDIN, C., MONDELIN, A., RECH, J. and FROMENTIN, G., 2010. Effects of a Straight Oil on Friction at the Tool–workmaterial Interface in Machining*. International Journal of Machine Tools and Manufacture*, vol. 50, no. 8, pp. 681-688.

CLAYTON, P. and DANKS, D., 1990. Effect of Interlamellar Spacing on the Wear Resistance of Eutectoid Steels Under Rolling-Sliding Conditions*. Wear*, vol. 135, no. 2, pp. 369-389.

COURBON, C., 2011. *Vers Une Modelisation Physique De La Coupe Des Aciers Speciaux: Integration Du Comportement Metallurgique Et Des Phenomenes Tribologiques Et Thermiques Aux Interfaces*.

COURBON, C., et al, 2013. On the Existence of a Thermal Contact Resistance at the Tool-Chip Interface in Dry Cutting of AISI 1045: Formation Mechanisms and Influence on the Cutting Process*. Applied Thermal Engineering*, vol. 50, no. 1, pp. 1311-1325.

CUBBERLY, W.H., 1989. *Tool and Manufacturing Engineers Handbook Desk Edition.* Society of Manufacturing Engineers.

DE EGUILAZ, E.R., RECH, J. and ARRAZOLA, P., 2010. Characterization of Friction Coefficient and Heat Partition Coefficient between an AISI4140 Steel and a TiN-Coated Carbide–influence of (Ca, Mn, S) Steel's Inclusions. *Proceedings of the Institution of Mechanical Engineers, Part J: Journal of Engineering Tribology*, vol. 224, no. 10, pp. 1115-1127.

DEGARMO, E.P., BLACK, J.T., KOHSER, R.A. and KLAMECKI, B.E., 1997. *Materials and Process in Manufacturing.* Prentice Hall.

DOANE, D.V., 1988. Softening High Hardenability Steels for Machining and Cold Forming. *Journal of Heat Treating*, vol. 6, no. 2, pp. 97-109.

DUAN, C. and ZHANG, L., 2012. Adiabatic Shear Banding in AISI 1045 Steel during High Speed Machining: Mechanisms of Microstructural Evolution. *Materials Science and Engineering: A*, vol. 532, pp. 111-119.

DUCOBU, F., RIVIÈRE-LORPHÈVRE, E. and FILIPPI, E., 2016. Material Constitutive Model and Chip Separation Criterion Influence on the Modeling of Ti6Al4V Machining with Experimental Validation in Strictly Orthogonal Cutting Condition. *International Journal of Mechanical Sciences*, vol. 107, pp. 136-149.

DUCOBU, F., RIVIÈRE-LORPHÈVRE, E. and FILIPPI, E., 2011. *A Lagrangian FEM Model to Produce Saw-Toothed Macro-Chip and to Study the Depth of Cut Influence on its Formation in Orthogonal Cutting of Ti6Al4V.* Trans Tech Publ.

EBRAHIMI, A. and MOSHKSAR, M., 2009. Evaluation of Machinability in Turning of Microalloyed and Quenched-Tempered Steels: Tool Wear, Statistical Analysis, Chip Morphology. *Journal of Materials Processing Technology*, vol. 209, no. 2, pp. 910-921.

ESTRIN, Y., 1996. Dislocation-Density-Related Constitutive Modeling. *Unified Constitutive Laws of Plastic Deformation*, vol. 1, pp. 69-106.

EYRAUD, C., 1954. Appareil Danalyse Enthalpique Differentielle. *Comptes Rendus Hebdomadaires Des Seances De L Academie Des Sciences*, vol. 238, no. 14, pp. 1511-1512.

FABRE, D., BONNET, C., RECH, J. and MABROUKI, T., 2017. Innovative Lagrangian Model of Broaching to Reduce CPU Time. *Procedia CIRP*, vol. 58, pp. 19-24.

FABRE, D., BONNET, C., RECH, J. and MABROUKI, T., 2016. Optimization of Surface Roughness in Broaching. *CIRP Journal of Manufacturing Science and Technology*.

FABRE, D., 2016. *Mécanismes De Coupe Induits Par Le Brochage D'un Acier Inoxydable Ferrito-Martensitique*.

FORST, O., 1973. Hints on Broaching Handbook.

FRANCHI, R., DEL PRETE, A. and UMBRELLO, D., 2016. Inverse Analysis Procedure to Determine Flow Stress and Friction Data for Finite Element Modeling of Machining. *International Journal of Material Forming*, pp. 1-11.

GHOSH, G. and OLSON, G., 2002. The Isotropic Shear Modulus of Multicomponent Fe-Base Solid Solutions. *Acta Materialia*, vol. 50, no. 10, pp. 2655-2675.

GILORMINI, P., et al, 1984. A Comparative Analysis of Three Machining Processes: Broaching, Tapping and Slotting. *CIRP Annals-Manufacturing Technology*, vol. 33, no. 1, pp. 19-22.

GRIGULL, U., 1984. Newton's Temperature Scale and the Law of Cooling. *Heat and Mass Transfer*, vol. 18, no. 4, pp. 195-199.

GRZESIK, W. and NIESLONY, P., 2004. Prediction of Friction and Heat Flow in Machining Incorporating Thermophysical Properties of the Coating–chip Interface. *Wear*, vol. 256, no. 1, pp. 108-117.

GRZESIK, W. and NIESLONY, P., 2003. A Computational Approach to Evaluate Temperature and Heat Partition in Machining with Multilayer Coated Tools. *International Journal of Machine Tools and Manufacture*, vol. 43, no. 13, pp. 1311-1317.

GRZESIK, W., ZALISZ, Z. and NIESLONY, P., 2002. Friction and Wear Testing of Multilayer Coatings on Carbide Substrates for Dry Machining Applications. *Surface and Coatings Technology*, vol. 155, no. 1, pp. 37-45.

GÜNDÜZ, S., KAÇAR, R. and SOYKAN, H.Ş, 2008. Wear Behaviour of Forging Steels with Different Microstructure during Dry Sliding. *Tribology International*, vol. 41, no. 5, pp. 348-355.

HANDBOOK, A., 1990. Properties and Selection: Irons, Steels, and High Performance Alloys. *ASM International*, vol. 1, pp. 140-194.

HEDENQVIST, P. and OLSSON, M., 1991. Sliding Wear Testing of Coated Cutting Tool Materials. *Tribology International*, vol. 24, no. 3, pp. 143-150.

HOGMARK, S., HEDENQVIST, P. and JACOBSON, S., 1997. Tribological Properties of Thin Hard Coatings: Demands and Evaluation. *Surface and Coatings Technology*, vol. 90, no. 3, pp. 247-257.

HÖHNE, G., HEMMINGER, W.F. and FLAMMERSHEIM, H., 2013. *Differential Scanning Calorimetry.* Springer Science & Business Media.

HUNT, L., 1964. The Early History of the Thermocouple. *Platinum Metals Review*, vol. 8, no. 1, pp. 23-28.

KAYSER, F. and PATTERSON, J., 1998. Sir William Chandler Roberts-Austen—His Role in the Development of Binary Diagrams and Modern Physical Metallurgy. *Journal of Phase Equilibria*, vol. 19, no. 1, pp. 11-18.

KISHAWY, H.A., HOSSEINI, A., MOETAKEF-IMANI, B. and ASTAKHOV, V.P., 2012. An Energy Based Analysis of Broaching Operation: Cutting Forces and Resultant Surface Integrity. *CIRP Annals-Manufacturing Technology*, vol. 61, no. 1, pp. 107-110.

KLOCKE, F., GIERLINGS, S., BROCKMANN, M. and VESELOVAC, D., 2014. Force-Based Temperature Modeling for Surface Integrity Prediction in Broaching Nickel-Based Alloys. *Procedia CIRP*, vol. 13, pp. 314-319.

KLOCKE, F., GIERLINGS, S., BROCKMANN, M. and VESELOVAC, D., 2011. Influence of Temperature on Surface Integrity for Typical Machining Processes in Aero Engine Manufacture. *Procedia Engineering*, vol. 19, pp. 203-208.

KLOCKE, F., GERSCHWILER, K. and ABOURIDOUANE, M., 2009. Size Effects of Micro Drilling in Steel. *Production Engineering*, vol. 3, no. 1, pp. 69-72.
KLOCKE, F. and KUCHLE, A., 2011. Processes with Rotational Primary Movement. *Manufacturing Processes 1*, pp. 383-444.

KOMANDURI, R. and HOU, Z.B., 2001a. Thermal Modeling of the Metal Cutting process—Part II: Temperature Rise Distribution due to Frictional Heat Source at the Tool–chip Interface. *International Journal of Mechanical Sciences*, vol. 43, no. 1, pp. 57-88.

KOMANDURI, R. and HOU, Z.B., 2001b. Thermal Modeling of the Metal Cutting process—Part III: Temperature Rise Distribution due to the Combined Effects of Shear Plane Heat Source and the Tool–chip Interface Frictional Heat Source. *International Journal of Mechanical Sciences*, vol. 43, no. 1, pp. 89-107.

KOMANDURI, R. and HOU, Z.B., 2000. Thermal Modeling of the Metal Cutting Process: Part I—temperature Rise Distribution due to Shear Plane Heat Source. *International Journal of Mechanical Sciences*, vol. 42, no. 9, pp. 1715-1752.

KONG, X., LI, B., JIN, Z. and GENG, W., 2011. Broaching Performance of Superalloy GH4169 Based on FEM. *Journal of Materials Science & Technology*, vol. 27, no. 12, pp. 1178-1184.

KULJANIC, E., 1975. Cutting Force and Surface Roughness in Broaching. *Ann.CIRP*, vol. 24, no. 1, pp. 77-82.

LAPOINTE, F.J., 1920. *Cutter-Bar and Bushing Therefor*.

LAPOINTE, F.J., 1914. *Cutter-Bar and Bushing Therefor.*

LE CALVEZ, C., et al, 2003. Gains Achieved by using New Generations of Plastic Injection Mold Steels. *CIRP Annals-Manufacturing Technology*, vol. 52, no. 1, pp. 69-72.

LOIZOU, J., TIAN, W., ROBERTSON, J. and CAMELIO, J., 2015. Automated Wear Characterization for Broaching Tools Based on Machine Vision Systems. *Journal of Manufacturing Systems*, vol. 37, no. 2, pp. 558-563.

MABROUKI, T., et al, 2017. Influence of Microstructure on Chip Formation when Broaching Ferritic-Pearlitic Steels. *Procedia CIRP*, vol. 58, pp. 43-48.

MABROUKI, T., GIRARDIN, F., ASAD, M. and RIGAL, J., 2008. Numerical and Experimental Study of Dry Cutting for an Aeronautic Aluminium Alloy (A2024-T351). *International Journal of Machine Tools and Manufacture*, vol. 48, no. 11, pp. 1187-1197.

MAKAROV, V., TOKAREV, D. and TYKTAMISHEV, V., 2008. High Speed Broaching of Hard Machining Materials. *International Journal of Material Forming*, vol. 1, no. 1, pp. 547-550.

MALEKIAN, M., MOSTOFA, M., PARK, S. and JUN, M., 2012. Modeling of Minimum Uncut Chip Thickness in Micro Machining of Aluminum. *Journal of Materials Processing Technology*, vol. 212, no. 3, pp. 553-559.

MANDRILE, S., 2014. Development of an in-House Cutting Forces Simulation for Fir Tree Broaching Process. *Mandrile, S., Dessein, G., Denape, J., Larroche, G. C., Vernault, C. and Paris, J.Y*, vol. 15, no. n°1/2, pp. 18 DOI 10.1504/IJMMM.2014.059185.

MASSEGLIA, M., 2009. Http://Mla.Masseglia.Free.Fr/Index.Htm*. Http://Mla.Masseglia.Free.Fr/Index.Htm*.

MECKING, H. and KOCKS, U., 1981. Kinetics of Flow and Strain-Hardening*. Acta Metallurgica*, vol. 29, no. 11, pp. 1865-1875.

MEIER, H., NINOMIYA, K., DORNFELD, D. and SCHULZE, V., 2014. Hard Broaching of Case Hardened SAE 5120*. Procedia CIRP*, vol. 14, pp. 60-65.

MENCZEL, J.D. and PRIME, R.B., 2014. *Thermal Analysis of Polymers: Fundamentals and Applications.* John Wiley & Sons.

MERCHANT, M.E., 1945. Mechanics of the Metal Cutting Process. II. Plasticity Conditions in Orthogonal Cutting*. Journal of Applied Physics*, vol. 16, no. 6, pp. 318-324.
MIAN, A.J., DRIVER, N. and MATIVENGA, P.T., 2010. A Comparative Study of Material Phase Effects on Micro-Machinability of Multiphase Materials*. The International Journal of Advanced Manufacturing Technology*, vol. 50, no. 1-4, pp. 163-174.

MO, S.P., AXINTE, D.A., HYDE, T.H. and GINDY, N.N.Z., 2005. An Example of Selection of the Cutting Conditions in Broaching of Heat-Resistant Alloys Based on Cutting Forces, Surface Roughness and Tool Wear*. Journal of Materials Processing Technology*, 3/30, vol. 160, no. 3, pp. 382-389 ISSN 0924-0136.

MONDELIN, A., CLAUDIN, C., RECH, J. and DUMONT, F., 2011. Effects of Lubrication Mode on Friction and Heat Partition Coefficients at the Tool–work Material Interface in Machining*. Tribology Transactions*, vol. 54, no. 2, pp. 247-255.

MOVAHHEDY, M., GADALA, M. and ALTINTAS, Y., 2000. Simulation of Chip Formation in Orthogonal Metal Cutting Process: An ALE Finite Element Approach*. Machining Science and Technology*, vol. 4, no. 1, pp. 15-42.

M'SAOUBI, R. and CHANDRASEKARAN, H., 2005. Innovative Methods for the Investigation of Tool-Chip Adhesion and Layer Formation during Machining*. CIRP Annals-Manufacturing Technology*, vol. 54, no. 1, pp. 59-62.

NEMAT-NASSER, S. and GUO, W., 2003. Thermomechanical Response of DH-36 Structural Steel Over a Wide Range of Strain Rates and Temperatures*. Mechanics of Materials*, vol. 35, no. 11, pp. 1023-1047.

OLSSON, M., SÖDERBERG, S., JACOBSON, S. and HOGMARK, S., 1989. Simulation of Cutting Tool Wear by a Modified Pin-on-Disc Test*. International Journal of Machine Tools and Manufacture*, vol. 29, no. 3, pp. 377-390.

OZCATALBAS, Y. and ERCAN, F., 2003. The Effects of Heat Treatment on the Machinability of Mild Steels*. Journal of Materials Processing Technology*, vol. 136, no. 1, pp. 227-238.

OZEL, T., LLANOS, I., SORIANO, J. and ARRAZOLA, P., 2011. 3D Finite Element Modelling of Chip Formation Process for Machining Inconel 718: Comparison of FE Software Predictions*. Machining Science and Technology*, vol. 15, no. 1, pp. 21-46.

ÖZLÜ, E., et al, 2010. Simulation of Broaching Operations for Tool Design Optimization.

PULS, H., KLOCKE, F. and LUNG, D., 2012. A New Experimental Methodology to Analyse the Friction Behaviour at the Tool-Chip Interface in Metal Cutting*. Production Engineering*, vol. 6, no. 4-5, pp. 349-354.

RECH, J., 2006. A Multiview Approach to the Tribological Characterisation of Cutting Tool Coatings for Steels in High-Speed Dry Turning*. International Journal of Machining and Machinability of Materials*, vol. 1, no. 1, pp. 27-44.

RECH, J., et al, 2013. Characterisation of Friction and Heat Partition Coefficients at the Tool-Work Material Interface in Cutting*. CIRP Annals-Manufacturing Technology*, vol. 62, no. 1, pp. 79-82.

RECH, J., CLAUDIN, C. and D'ERAMO, E., 2009. Identification of a Friction model—Application to the Context of Dry Cutting of an AISI 1045 Annealed Steel with a TiN-Coated Carbide Tool*. Tribology International*, vol. 42, no. 5, pp. 738-744.

RECH, J., CLAUDIN, C., GRZESIK, W. and ZALISZ, Z., 2008. Characterization of the Friction Properties of various Coatings at the Tool—chip—workpiece Interfaces in Dry Machining of AISI 4140 Steel*. Proceedings of the Institution of Mechanical Engineers, Part J: Journal of Engineering Tribology*, vol. 222, no. 4, pp. 617-627.

ROBERTS-AUSTEN, W.C., 1899. Fifth Report* to the Alloys Research Committee: Steel*. Proceedings of the Institution of Mechanical Engineers*, vol. 56, no. 1, pp. 35-102.

Sandvik Coromant (Firm)., 1994. *Modern Metal Cutting: A Practical Handbook.* Sandvik Coromant.

SCHERMANN, T., MARSOLEK, J., SCHMIDT, C. and FLEISCHER, J., 2006. Aspects of the Simulation of a Cutting Process with ABAQUS/Explicit including the Interaction between the Cutting Process and the Dynamic behaviour of the Machine Tool.

SCHROETER, R., BASTOS, C. and CRICHIGNO FILHO, J., 2007. Simulation of the Main Cutting Force in Crankshaft Turn Broaching*. International Journal of Machine Tools and Manufacture*, vol. 47, no. 12, pp. 1884-1892.

SCHULZE, V., ZANGER, F., KRAUSSE, M. and BOEV, N., 2013. Simulation Approach for the Prediction of Surface Deviations Caused by Process-Machine-Interaction during Broaching*. Procedia CIRP*, vol. 8, pp. 252-257.

SCHULZE, V., BOEV, N. and ZANGER, F., 2012. Simulation of Metal Cutting Process with Variable Cutting Thickness during Broaching*. Procedia CIRP*, vol. 1, pp. 437-442.

SCHULZE, V., MEIER, H., STRAUSS, T. and GIBMEIER, J., 2012. High Speed Broaching of Case Hardening Steel SAE 5120*. Procedia CIRP*, vol. 1, pp. 431-436.

SCHULZE, V., OSTERRIED, J., MEIER, H.and ZANGER, F., 2011. *Simulation of Multiple Chip Formation when Broaching SAE 5120 Low Alloy Steel.* Trans Tech Publ.

ŠESTÁK, J., 2011. Some Historical Features Focused Back to the Process of European Education Revealing some Important Scientists, Roots of Thermal Analysis and the Origin of Glass Research*. Some Thermodynamic, Structural and Behavioural Aspects of Materials Accentuating Non-Crystalline States.OPS-ZCU Pilsen*, pp. 29-58.

ŠESTÁK, J., HUBÍK, P. and MAREŠ, J.J., 2011. Historical roots and development of thermal analysis and calorimetry. In: Glassy, amorphous and nano-crystalline

materialsSpringer. *Historical Roots and Development of Thermal Analysis and Calorimetry*, pp. 347-370.

SHI, D. and GINDY, N.N., 2007. Tool Wear Predictive Model Based on Least Squares Support Vector Machines. *Mechanical Systems and Signal Processing*, vol. 21, no. 4, pp. 1799-1814.

SIMONEAU, A., NG, E. and ELBESTAWI, M., 2006. Chip Formation during Microscale Cutting of a Medium Carbon Steel. *International Journal of Machine Tools and Manufacture*, vol. 46, no. 5, pp. 467-481.

SMOLENICKI, D., et al, 2014. In-Process Measurement of Friction Coefficient in Orthogonal Cutting. *CIRP Annals-Manufacturing Technology*, vol. 63, no. 1, pp. 97-100.

STEPHENS, A.P., 1873. *Improvement in Broaching Machines.* United States Patents Office ed., United States Patents Office.

SU, Y., et al, 2004. Tribological Characteristics and Cutting Performance of Cr X% C-Coated Carbide Tools. *Journal of Materials Processing Technology*, vol. 153, pp. 699-706.

SUTHERLAND, J., SALISBURY, E. and HOGE, F., 1997. A Model for the Cutting Force System in the Gear Broaching Process. *International Journal of Machine Tools and Manufacture*, vol. 37, no. 10, pp. 1409-1421.

TRENT, E.M. and WRIGHT, P.K., 2000. *Metal Cutting.* Butterworth-Heinemann.

VOGTEL, P., et al, 2013. Modelling of Process Forces in Broaching Inconel 718. *Procedia CIRP*, vol. 8, pp. 409-414.

VUORISTO, T., 2004. *Effect of Strain Rate on the Deformation Behavior of Dual Phase Steels and Particle Reinforced Polymer Composites.* Tampere University of Technology.

WENDLANDT, W., 1964. Thermal Methods of Analysis Wiley Int.

WEULE, H., et al, 2005. Structural Optimization of Machine Tools Under Consideration of their Static and Dynamic Behaviour within the Workspace. *Production Engineering XII*, vol. 2, pp. 201-204.

WOO, W. and LEE, C., 2015. A Study of the Machining Characteristics of AISI 1045 Steel and Inconel 718 with a Cylindrical Shape in Laser-Assisted Milling. *Applied Thermal Engineering*, vol. 91, pp. 33-42.
XI, Y., BERMINGHAM, M., WANG, G. and DARGUSCH, M., 2014. SPH/FE Modeling of Cutting Force and Chip Formation during Thermally Assisted Machining of Ti6Al4V Alloy. *Computational Materials Science*, vol. 84, pp. 188-197.

YEN, Y., SÖHNER, J., LILLY, B. and ALTAN, T., 2004. Estimation of Tool Wear in Orthogonal Cutting using the Finite Element Analysis. *Journal of Materials Processing Technology*, vol. 146, no. 1, pp. 82-91.

ZANGER, F., BOEV, N. and SCHULZE, V., 2014. Surface Quality After Broaching with Variable Cutting Thickness. *Procedia CIRP*, vol. 13, pp. 114-119.

ZEMZEMI, F., et al, 2007. Development of a Friction Model for the Tool-Chip-Workpiece Interfaces during Dry Machining of AISI4142 Steel with TiN Coated Carbide Cutting

Tools*. International Journal of Machining and Machinability of Materials*, vol. 2, no. 3-4, pp. 361-377.

Chapter 10

APPENDICES

10 APPENDICES

In this section it is shown the work performed during the development of the PhD that due to its importance or exceeded information it is displayed as attachments.

Material Characterization

10.1.1 Identification of the parameters of the model

In this section it is shown the way the ASCOmetal steel company extracted the parameters to generate the flow stress model presented in the section 0. The goal of the modelling task was to consider the microstructural parameters that differentiate grades and variants to accurately model the machining performance. This would be obtained thanks to a good modelling of both rheology and tribology effects implemented in the material behaviour model. To reach this target, the rheology of the five steel grades chosen would be modelled using a mesoscopic physical-based model proposed by (Allain, Bouaziz 2008). This model allowed a good description of ferrite-pearlite behaviour at room temperature, thanks to the application of an original homogenization law described in the next section. The detailed behaviour of each phase and the development are described in the following sections.

Appearance of the DSA (Dynamic Strain Ageing)

Before going with the explanation of the model development it has to be necessarily explained the appearance of the DSA effect. From the huge amount of experimental data that was obtained, the temperature dependence of the high strain rate tests was particularly striking. Classically, the flow stress decreases with increasing temperature, as it can be seen in Annex figure 1 for C45, at low strain-rate. At high strain-rate (Annex figure 1(right) and Annex figure 2), a bell shaped flow stress–temperature curve appears with a flow stress which first decreases as temperature increases until a peak value is reached, and then the flow stress increases with further increase of temperature. This feature is characteristic of the Dynamic Strain Ageing (DSA).

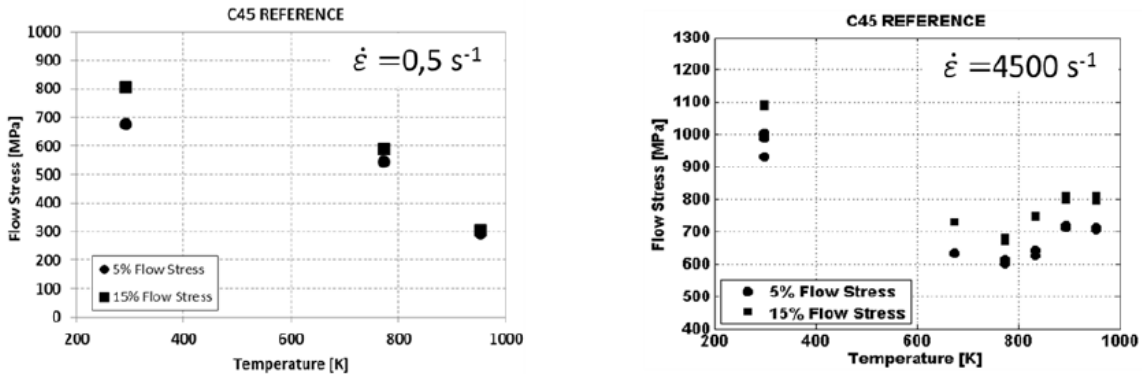

Annex figure 1. Experimental data of C45 R: evolution of the flow stress with temperature at low strain-rate (left) and high strain-rate (right).

The same feature was observed for all steel grades and variants, independently of their ferrite/pearlite ratio. For this reason, only two examples were presented in Annex figure 2. It should be noted that additional compression tests were conducted at temperatures between 500°C and 680°C for 27MnCr5 and C45 grades (Annex figure 2 (e) and (f)) to highlight this phenomenon. The results show that for the grade 27MnCr5, the peak temperature of DSA appears to be above the highest testing temperature of 680 °C whereas for the grade C45 (specially variant C45CG), the peak temperature is lower, between 620 and 680 °C.

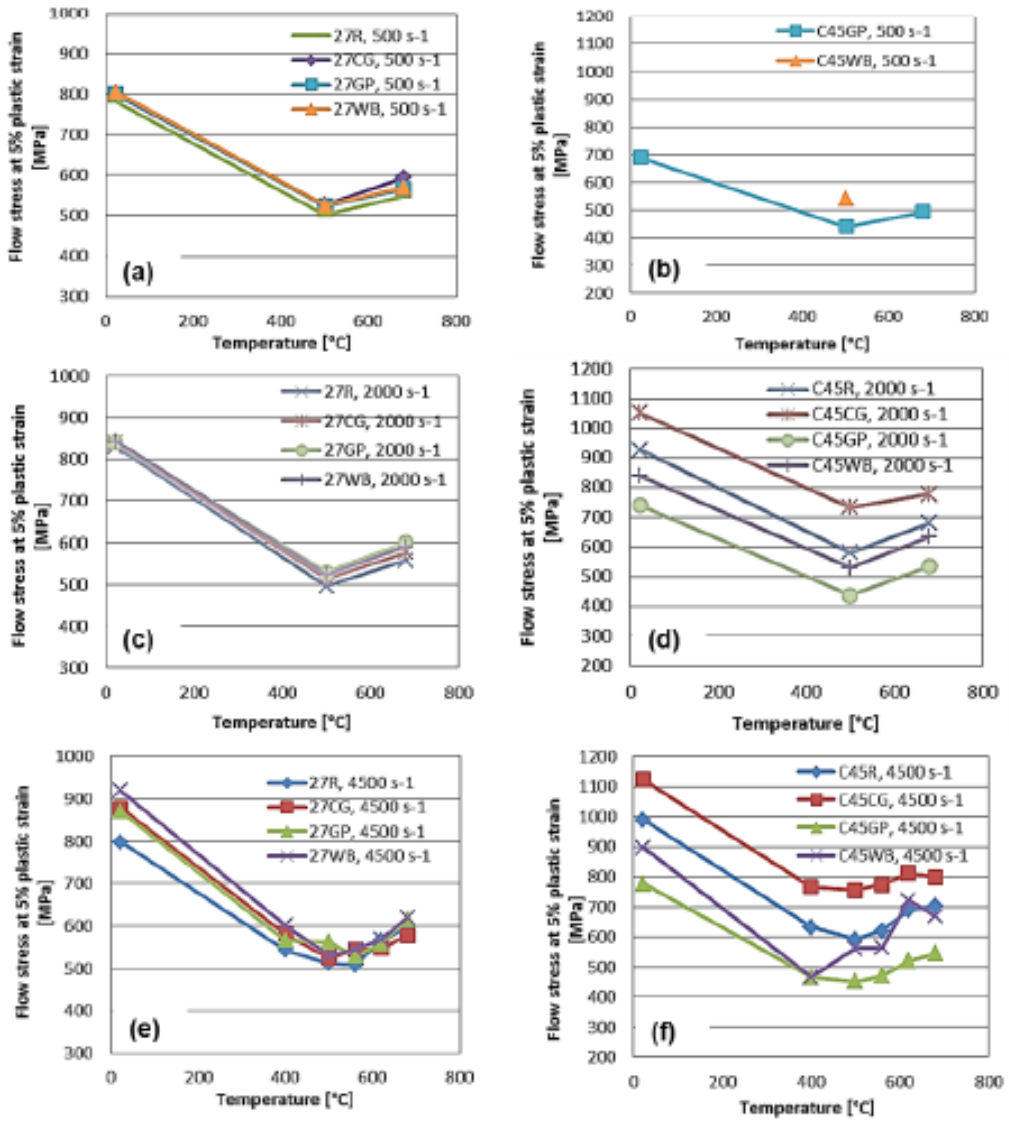

Annex figure 2. Temperature dependence of the low pearlitic steel 27MnCr5 ((a), (c), (e)) and of the higher pearlitic steel C45 ((b), (d), (f)) tested at different strain-rates using the Split Hopkinson pressure bars method (SHPB). Data for 5 % plastic strain.

- Origin of DSA:

DSA occurs due to recurrent pinning of dislocations while arrested at obstacles during their motion that results in plastic straining (Nemat-Nasser, Guo 2003). This phenomenon is attributed to the additional resistance of dislocation motion produced by the mobility of solute atoms (*e.g.*, C and N for steels) that can diffuse to dislocations above a certain temperature while the dislocations are waiting at their short range barriers. As the solutes catch up with moving dislocations and pin them down, the flow stress increases. By increasing strain rates, higher temperatures are required to drive the solute atoms to dislocations at sufficient speeds. Thus, the plastic deformation behaviour and DSA are dependent on both temperature and strain rate as the example in Annex figure 3 shows. The results in the figure illustrate that the peak point of the flow

stress versus temperature curve is shifted to higher temperatures by increasing strain rate. It was thus not visible at low strain-rate in the compression experiments since it should appear at temperatures around 200-300°C (i.e. not for the initial tested conditions: 20°C, 500°C and 680°C).

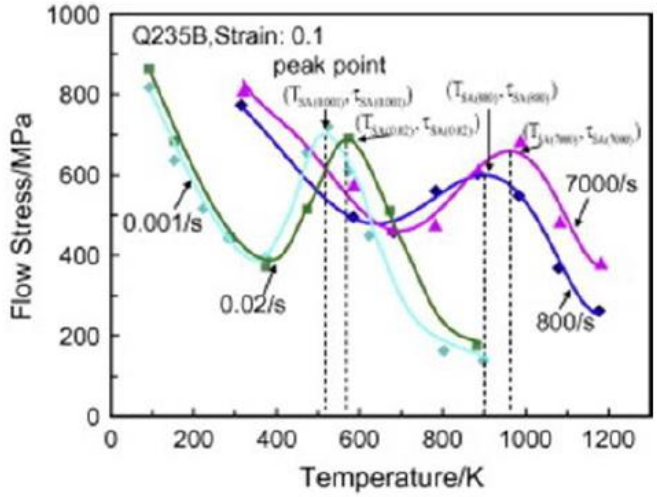

Annex figure 3. Example on temperature and strain rate dependence of dynamic strain ageing (DSA).

- <u>Manifestation of DSA at low strain-rate:</u>

To verify the manifestation of DSA in the whole temperature range, additional tensile tests were performed at a low strain-rate of about 0.7 s^{-1} at temperatures between 20°C and 500°C. The tensile tests were carried out in a servo-hydraulic materials testing machine and the high temperatures were obtained using induction heating. These tests were carried out for 16GP variant and for C70, the lowest and highest pearlitic steel grade, respectively (Annex figure 4). The presence of DSA is thus confirmed at low strain-rate, and it is supposed to appear in other steel grades since their behaviour at high strain-rate was similar.

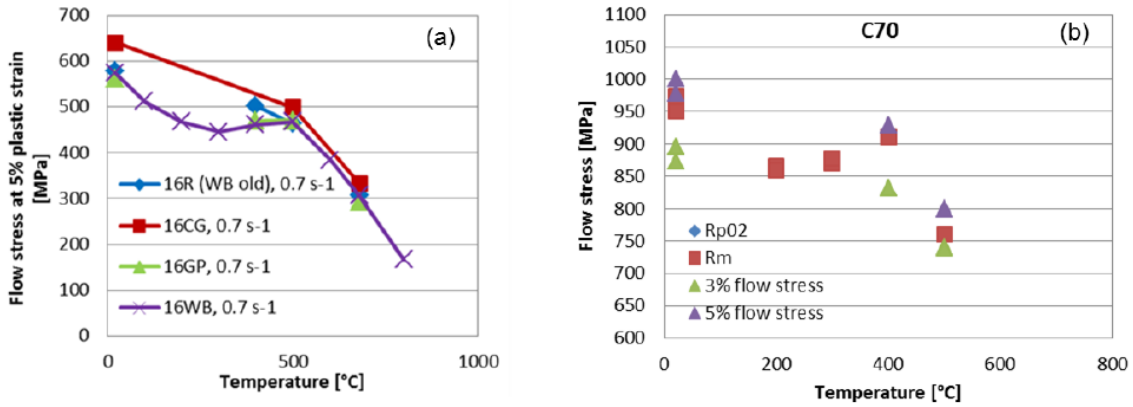

Annex figure 4. Tensile tests results at 0.7 s^{-1} at various temperatures for 16MnCr5 (left) and C70 (right). The flow stress value is taken at 15% plastic strain for 16MnCr5. For C70, different plastic strain level are considered; Rm and Rp02 refer to Ultimate tensile strength and Yield strength respectively; these values have been taken instead of a given plastic strain because of an extensometry problem.

Philosophy of the model

The rheological model is a microstructure-based behaviour law with more empirical contributions (especially to account for the dynamic strain ageing mechanisms). The macroscopic behaviour is deduced from a homogenisation law knowing the behaviour of each constituting phase (1):

$$\sigma = F \cdot \sigma^{pearlite-dynamic} + (1 - F) \cdot \sigma^{ferrite-dynamic} \quad (1)$$

Where:

- σ is the flow stress of the ferrite-pearlite steel.
- *F* is the pearlitic phase volume fraction.
- $\sigma^{pearlite\text{-}dynamyc}$ is the flow stress of the pearlitic phase with dependence on temperature and strain-rate.
- $\sigma^{ferrite\text{-}dynamyc}$ is the flow stress of the ferritic phase with dependence on temperature and strain-rate.

The dynamic behaviours for each phase are given by the same formulae based on the work of (Allain et al. 2009, Bui-Van et al. 2009) initially developped for 100% ferritic steels. It is given by equation (2) with the addition of the term DSA when compared in comparison to the original formulation:

$$\sigma^{dynamic} = \left(\sigma_0 \cdot \frac{\mu(T)}{\mu^0}\right) + \frac{\sigma^*}{2} + \frac{1}{2}\sqrt{(\sigma^*)^2 + 4\left(\sigma^{static} - \left(\sigma_0 \cdot \frac{\mu(T)}{\mu^0}\right)\right)^2} + DSA \quad (2)$$

Where:

- σ_0 is the lattice friction at RT (Room temperature).
- $\mu(T)$ is the shear modulus, normalized by its value μ^0 at RT; the evolution of μ(T) with temperature is taken from the literature (Ghosh, Olson 2002).
- σ* is the effective stress necessary for dislocations to overcome local obstacles (thermally active mechanism).
- σ^{static} is the long-range internal stress that hinders dislocation glide (structural hardening
- DSA is the contribution of Dynamic Strain Ageing (DSA)

The differentiation between pearlitic and ferritic phase is made through the term σ^{static} whose formulation is different for both phases.

The effective stress to overcome local obstacles derives from the most general formulation based on the Orowan's relation and is given by equation (3):

$$\sigma^* = \left[\frac{k_B T}{V^* b^3} \cdot asinh\left(\frac{\dot{\varepsilon}}{2M\rho_m \nu_{Debye} b^2 exp\left(-\frac{\Delta G_0}{k_B T}\right)}\right)\right] \quad (3)$$

Where:

- k_b is the Boltzmann constant.
- T is the temperature.
- V^* is the activation volume (different values are necessary for pearlite and ferrite).
- b is the Burgers vector.
- $\dot{\varepsilon}$ is the strain-rate: $\dot{\varepsilon}^{pearlite}$ or $\dot{\varepsilon}^{ferrite}$.
- ρ_m is the density of the mobile dislocations.
- ν_{Debye} is the Debye frequency.
- *M* is the mean Taylor factor.
- ΔG_0 is the activation energy (different values are necessary for pearlite and ferrite).

Description of the ferritic phase:

The evolution of the flow stress of the ferritic phase is based on the forest hardening model proposed by (Mecking, Kocks 1981, Estrin 1996, Bergström 1970) (4):

$$\sigma^{ferrite-static} = \sigma_0 \cdot \frac{\mu(T)}{\mu^0} + X^{ferrite} + \alpha M \mu(T) b \sqrt{\rho^{ferrite}} \quad (4)$$

Where:

- $X^{ferrite}$ is the kinematical hardening of the ferrite which increase with the density of geometrically necessary dislocations.
- α is a constant related to the forest dislocations hardening.
- $\rho^{pearlite}$ is the statistically stored dislocation density in ferrite.

The variable $X^{ferrite}$ is related to the key parameter *d* that is the ferritic grain size.

Development made for the pearlitic phase:

The description of the behaviour of lamellar pearlite is more empirical (Allain, Bouaziz 2008). The initial flow stress for pearlite is controlled by the key parameter s, which is the interlamellar spacing of lamellar pearlite, and by plastic work-hardening, considered here as isotropic. It is given by the following equation (5):

$$\sigma^{pearlite-static} = \left(\sigma_0 + \frac{M\mu(T)b}{s.10^{-9}} + \left(\frac{K}{g} \cdot \left(1 - exp\left(\frac{\varepsilon^{pearlite}.g}{2}\right)\right)\right) + \theta^{IV}.\varepsilon^{pearlite}\right) \cdot \frac{\mu(T)}{\mu^0} \quad (5)$$

Where:

- s is the interlamellar spacing of pearlite.
- K is an empirical constant hardening parameter.
- g is an empirical hardening parameter which depends on the temperature.
- θ^{IV} is the stage IV, saturating, of work-hardening.

The experimental determination of the interlamellar spacing of the different steel grades was a time- consuming and key task for the validation of the model with the experimental data. It is important to mention that the uncertainties in microstructure measurements were a possible source of discrepancies between simulation and experimental results that should be considered carefully in the analysis.

Description of the Dynamic Strain Ageing (DSA):

The DSA contributions have been determined using an empirical approach adjusted on experimental results observed for each steel grade at high strain-rate and confirmed at low strain-rate, as shown in Annex figure 1, Annex figure 2 and Annex figure 4.

Physically, as it was explained before, the DSA is caused by the interaction of the jerky mobile dislocations and the diffused solute atoms. The nature of the interactions is still under debate and many physical models emerged in the literature. Even if it cannot be said if the DSA will have an impact at the scale of cutting tests (cutting force for example), it is proposed here (6) a phenomenological description of the DSA contribution, inspired from literature (Wang 2005) and calibrated on experimental observations:

$$DSA^{pearlite} = \sigma^{max} \cdot exp\left(-\left(\frac{\left(T-\left(T_C + cste \cdot (log(\dot{\varepsilon}^{pearlite}) + 5)\right)\right)^2}{\Delta T^2}\right)\right) \quad (6)$$

Where:

- σ^{max} is the maximum stress for DSA.
- T_C is the temperature of DSA peak at low strain-rate.
- $Cste$ is a constant (evolution of T/speed of DSA peak).
- ΔT is the temperature range for DSA.

These parameters have been calibrated for almost 100% pearlitic steel (C70). The temperature-strain-rate dependent behaviour of our steel grades can thus be captured by equation (2) which combine equation (3) (description of the classical decrease of flow stress with increasing temperature when DSA does not occur) with the DSA contribution

(equation (6)). The resulting variation of the flow stress as a function of strain rate and temperature is plotted in Annex figure 5.

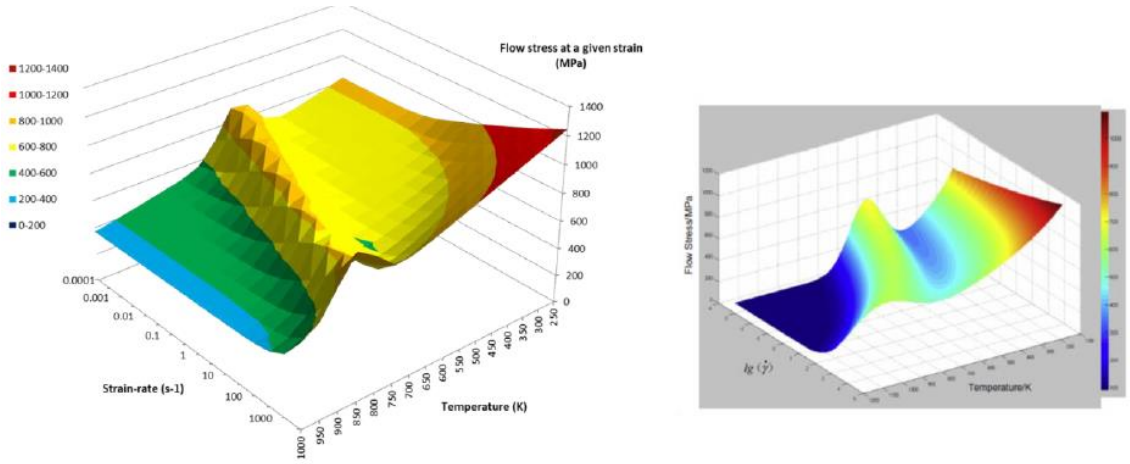

Annex figure 5. Representation of the variation of flow stress with strain rate and temperature; left: simulation results for C70; right: simulation results from literature (Wang 2005).

The presence of DSA is also guessed for 100% ferritic steels but cannot be highlighted based on our experimental data. Consequently the corresponding parameters for the ferritic phase are adjusted on the C60R ferrite/pearlite grade, with the fitted parameters deduced from the C70 fully pearlitic steel.

Analysis of the friction in the FP steels

In this section will be displayed the results in graphs to better understand each section's summary results but which have not been introduced in the text in order not to be too tough.

10.1.2 Tribology

Tribological work focused on the broaching process

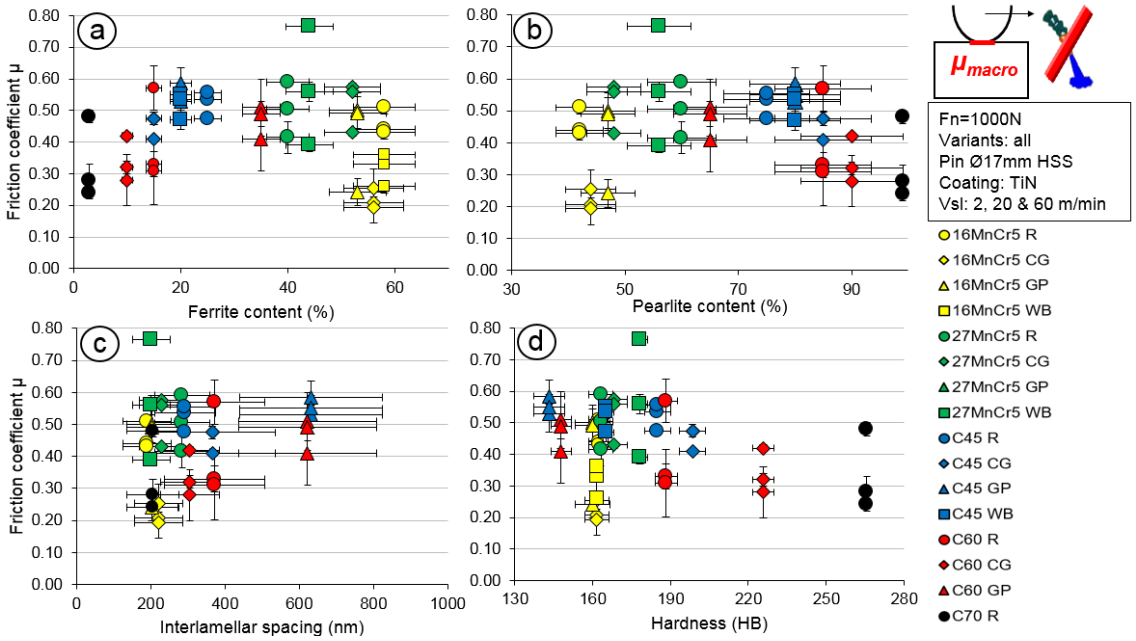

Annex figure 6. Friction coefficient plotted against ferrite-pearlite microstructural parameters using the TiN coated HSS steel pin: a) ferrite content, b) pearlite content, c) interlamellar spacing d) hardness.

Broaching tests

In this section are displayed the results that were not included in the document but are still interesting for the reader if wanted further information. The results appearing here are basically feed forces and Rz roughness graphs. It was already commented in the document both are similar to cutting forces and Ra respectively.

Fundamental broaching study

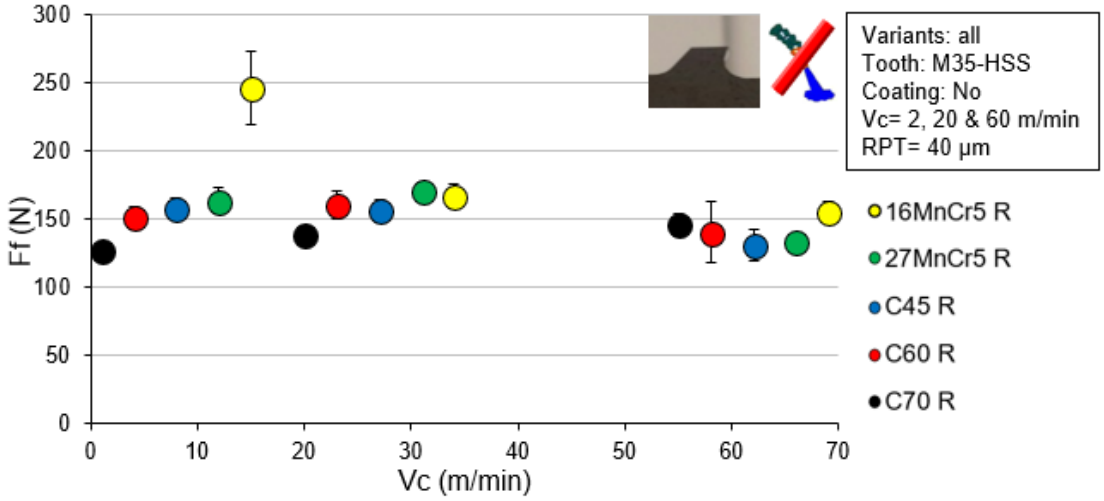

Annex figure 7. Broaching feed forces versus cutting speed on standard FP steels.

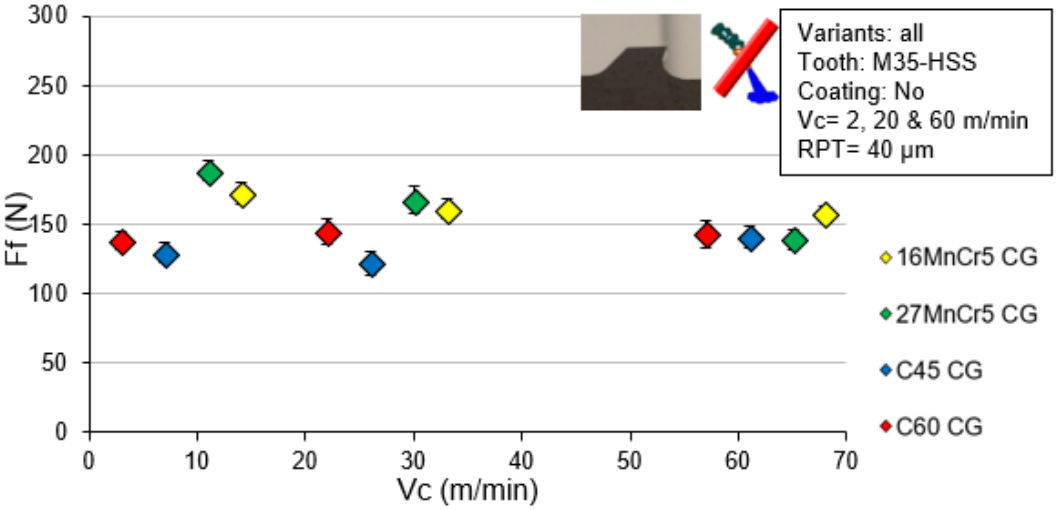

Annex figure 8. Broaching feed forces versus cutting speed on coarse grain FP steels

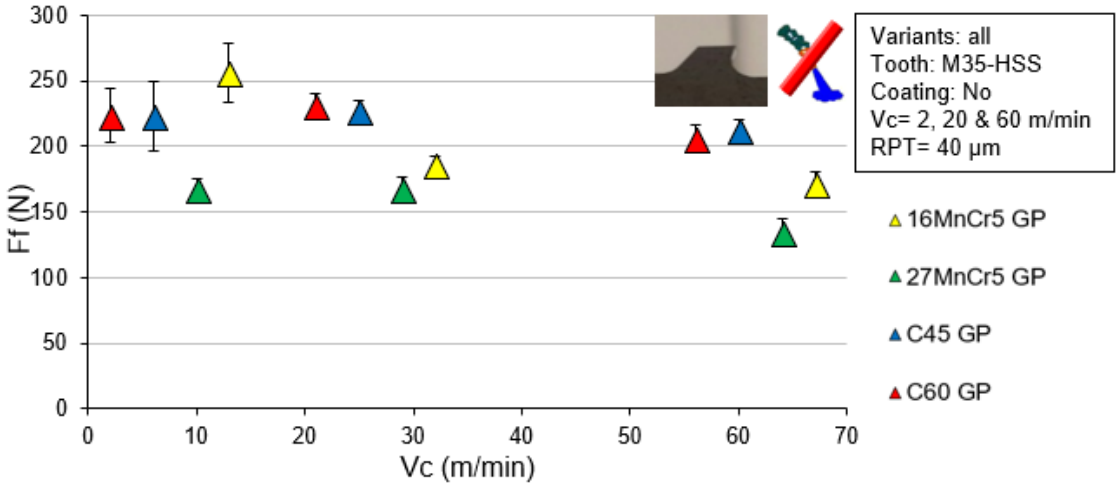

Annex figure 9. Broaching feed forces versus cutting speed on globular pearlitic FP steels.

Tooth state broaching campaign

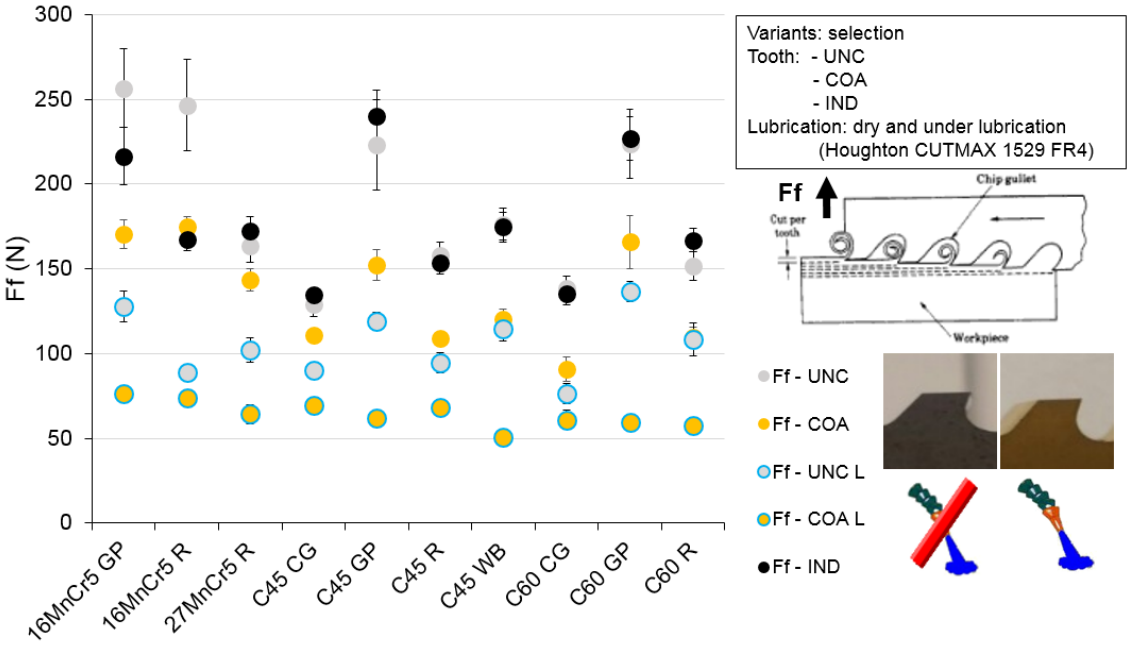

Annex figure 10. Feed forces obtained in the tooth state broaching campaign.

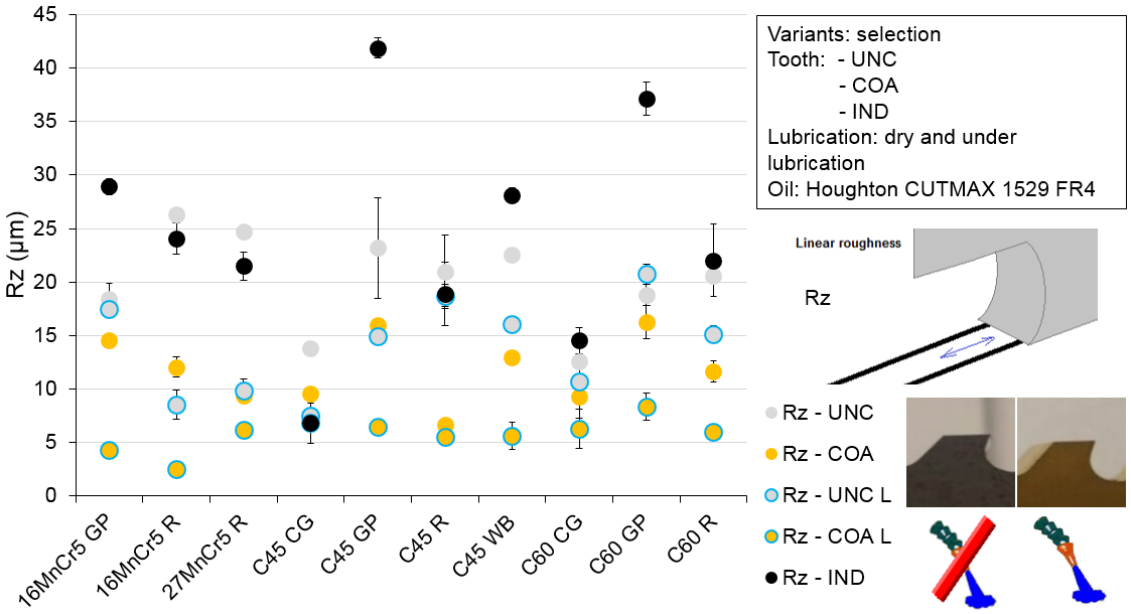

Annex figure 11. Rz roughness obtained in the tooth state broaching campaign.

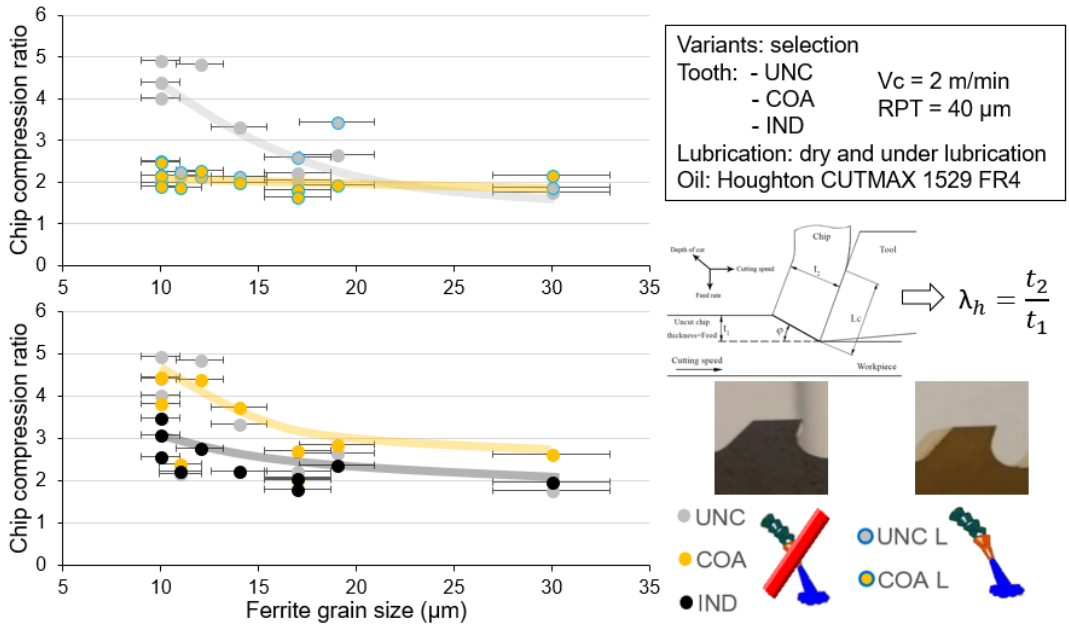

Annex figure 12. Chip compression ratio analysis versus the grain size of the ferrite.

Wear tests campaign

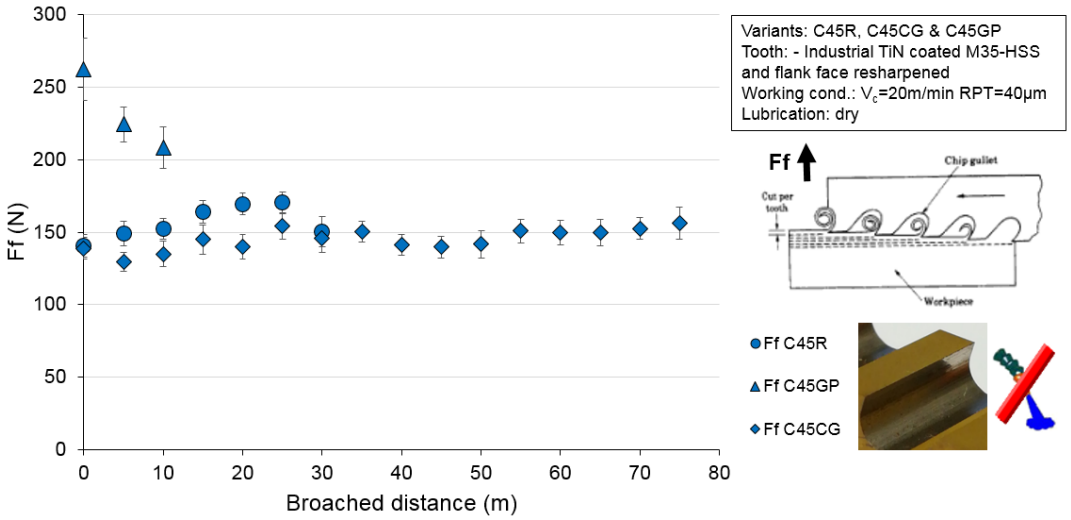

Annex figure 13. Feed forces obtained during the tool life tests.

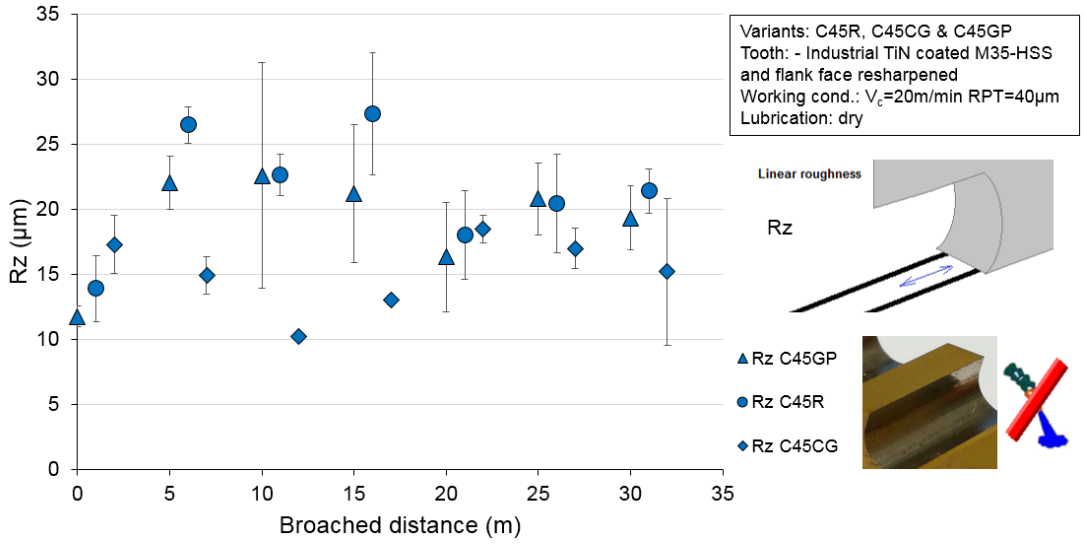

Annex figure 14. Linear Rz roughness obtained during the tool life tests.

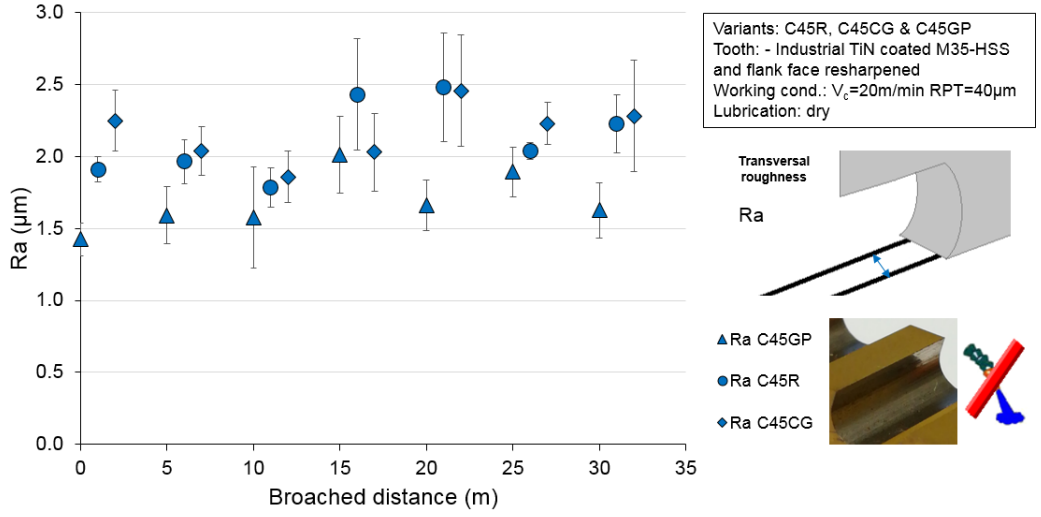

Annex figure 15. Transversal Ra roughness obtained during the tool life tests.

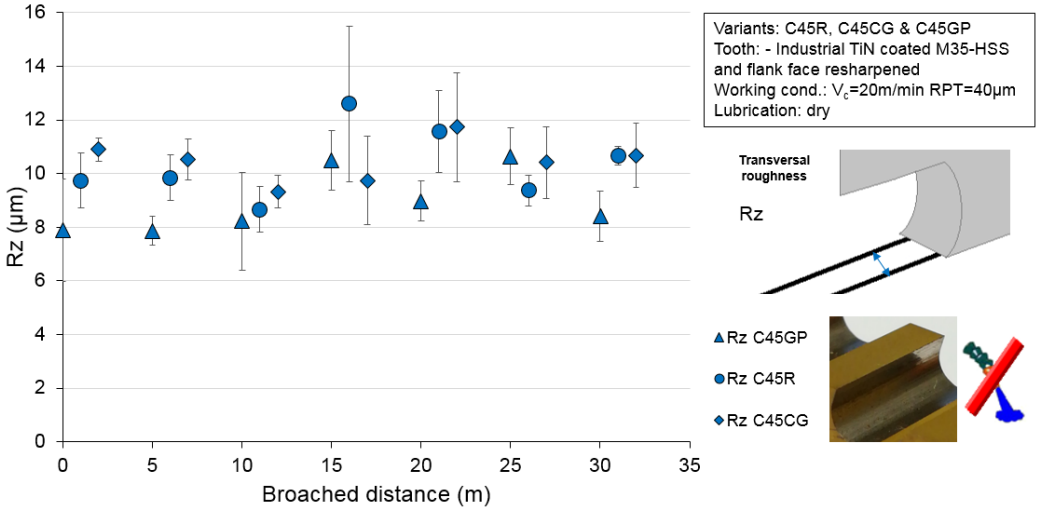

Annex figure 16. Transversal Rz roughness obtained during the tool life tests.

Friction coefficient and forces comparison

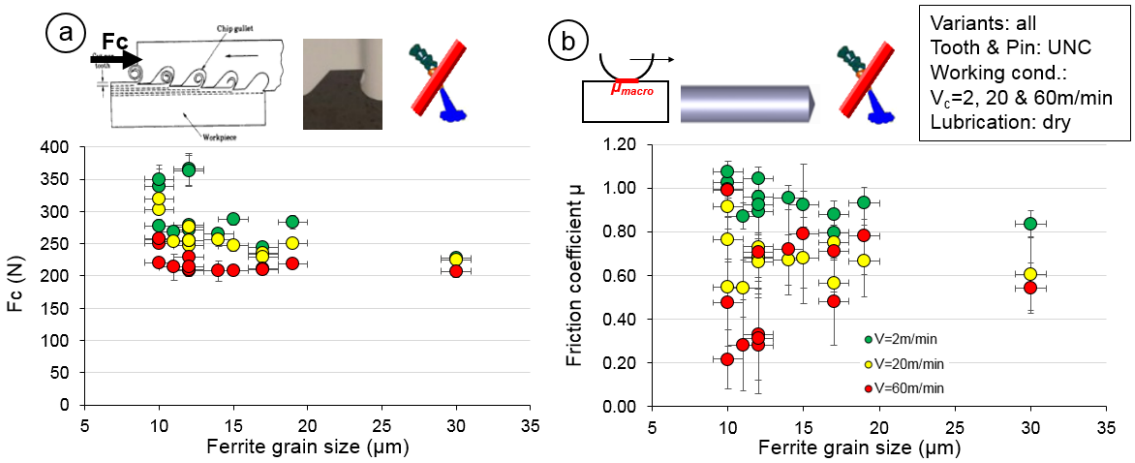

Annex figure 17. Cutting forces and friction coefficients comparison versus ferrite grain size.

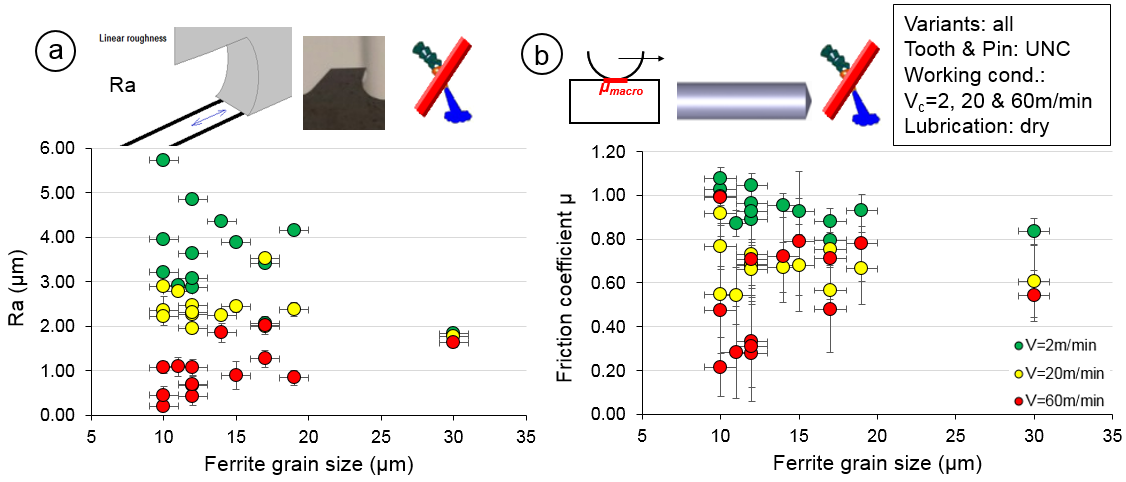

Annex figure 18. Roughness and friction coefficients comparison versus ferrite grain size.

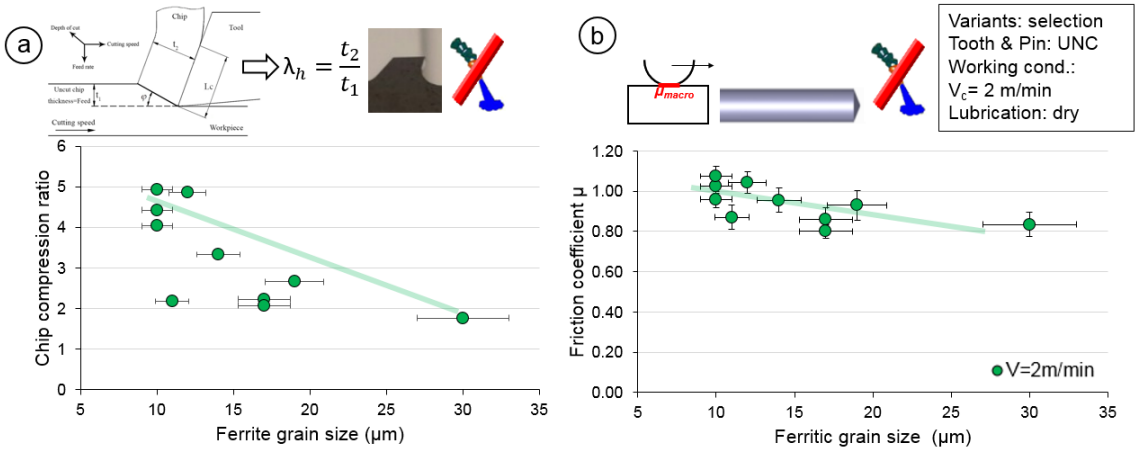

Annex figure 19. Chip compression ratio and friction coefficients comparison versus ferrite grain size.